
Optimal statistical experiment design for
detecting and locating light atoms
using quantitative high resolution
(scanning) transmission electron microscopy

Proefschrift voorgelegd tot het
behalen van de graad van
Doctor in de Wetenschappen
aan de Universiteit Antwerpen te
verdedigen door

Julie Gonnissen

Promotoren:

Prof. Dr. Sandra Van Aert
Prof. Dr. Jan Sijbers

FEBRUARY 2017

Doctoral Committee

Chairman

Prof. Dr. Joris Dirckx, University of Antwerp, Belgium

Promotors

Prof. Dr. Sandra Van Aert, University of Antwerp, Belgium

Prof. Dr. Jan Sijbers, University of Antwerp, Belgium

Members

Prof. Dr. Nick Van Remortel, University of Antwerp, Belgium

Prof. Dr. Ir. Arnold J. (Arjan) den Dekker, University of Antwerp, Belgium and
Delft University of Technology, The Netherlands

Dr. Wouter Van den Broek, Humboldt University of Berlin, Germany

Dr. Lewys Jones, University of Oxford, England, United Kingdom

Contact information

Julie Gonnissen

University of Antwerp - Department of Physics

EMAT - Electron Microscopy for Materials Science

Groenenborgerlaan 171

B-2020 Antwerp

Belgium

Julie.Gonnissen@uantwerpen.be



*To my beloved husband Thomas
and our dear children Samuel, Eveline
& the lovely kicking feet we'll soon be able to meet*

Summary

In the last decade, visualising light atoms like lithium and hydrogen has gained serious interest, as they play a key-role in many industrial applications, such as lithium batteries or energy storage materials. Therefore, the optimisation of different techniques in Transmission Electron Microscopy (TEM) for such applications has become an important issue. However, it is extremely difficult to visualise materials containing light elements and quantify their structure and chemical composition at the atomic-scale, since the interaction with the electron beam weakens for lighter atoms. The main goal of this PhD research was to optimise the experiment design of the electron microscope in order to characterise nanostructures containing light atoms, using advanced and new techniques in quantitative TEM. The purpose is then to retrieve the atomic structure of light atom nanocrystals from experimental images.

Atoms can be visualised using High Resolution Scanning Transmission Electron Microscopy (HRSTEM) using a High Angle Annular Dark Field (HAADF) detector. In this technique, a focused electron probe scans over a material, which is transparent for the incoming electrons. When using an annular detector with a high inner angle, (almost) exclusively incoherently scattered electrons are detected. The thus obtained signal scales approximately with the atomic number Z squared, and is therefore relatively highly sensitive for the chemical composition. However, a direct qualitative interpretation of experimental images gives unreliable results, if the difference in atomic number Z of neighbouring atom columns is small or when the signal-to-noise ratio (SNR) of the images is low. Thus, quantitative methods are necessary in order to characterise the chemical composition of crystals containing light elements. Statistical parameter estimation theory in combination with detection theory is therefore used.

Observations from HR(S)TEM experiments fluctuate around expectation values. The expectation model, i.e. the model of expectation values, is a physical func-

tion of the unknown parameters that have to be measured. In this thesis, the parameters that have to be estimated are the atom types present (or absent) in the structure, the position coordinates of the projected atom columns, and the number of atoms in the projected atom columns (i.e. the column thickness). In order to estimate continuous structure parameters, such as the atom column positions, use can be made of the so-called *Cramér-Rao lower bound*, which is a measure for the attainable precision of the estimates. Detection theory provides an alternative approach for estimating discrete parameters, such as the atomic number Z , as the Cramér-Rao lower bound is not defined in this case. Using detection theory, an estimation problem can be formulated as a binary or multiple hypothesis test in which the hypotheses correspond, for example, to different possible atomic numbers Z . The probability to assign the wrong hypothesis, the so-called *probability of error* can be quantified and minimised as a function of the experimental settings. The goal is then to find the optimal experiment design that minimises this probability of error or maximises the attainable precision. Both conventional TEM and STEM will be investigated and compared for detecting and locating light atoms, and for counting the number of atoms in a projected atom column. For HRSTEM, the annular detector inner and outer angle will be optimised, while in the case of HRTEM, the optimal values for the defocus and spherical aberration will be derived.

For detecting and locating light atoms, it is found that HRSTEM outperforms HRTEM, when using the same incoming electron dose. Moreover, a single optimal detector design is found for both the detecting and locating problem of light atoms in HRSTEM. Next, it is found that HRSTEM is the optimal imaging mode for atom-counting when using the same incoming electron dose and using the optimal detector settings, if scattering cross-sections are used as performance measure in STEM and peak intensities in TEM, as proposed in literature. However, when the decision is based on the so-called joint probability function of all pixel values in the HR(S)TEM image, it is found that HRTEM outperforms HRSTEM for atom-counting.

As a practical application in the research to quantitatively characterise light atom structures, the local oxygen-octahedral coupling at perovskite heterostructural interfaces in different epitaxial thin films is determined. Furthermore, the domain wall in a LiNbO_3 crystal is quantified, and the atomic shift of the domains next to the domain wall is determined as well as the width of the transition region between both domains, using statistical parameter estimation theory.

Contents

Summary	v
Contents	vii
1 Introduction	1
1.1 The role of light atoms in modern technology	1
1.2 Imaging in High Resolution (S)TEM	5
1.3 From CTEM to Aberration-Corrected STEM	10
1.4 From Qualitative toward Quantitative Electron Microscopy	13
1.5 What to expect in this thesis?	16
2 Electron-Specimen Interaction	21
2.1 Introduction	21
2.2 Specimen potential	22
2.3 Electron-specimen interaction	23
2.4 Weak phase object approximation	23
2.5 Thick specimen foils	25
2.6 Multislice method	28
2.7 Thermal vibration of the specimen atoms	30
2.7.1 Frozen phonon approximation	30
2.7.2 Absorptive potential method	32
2.8 Imaging in HRSTEM	34
2.9 Imaging in HRTEM	37
2.10 Conclusions	40
3 Statistical Experiment Design	41
3.1 Introduction	41
3.2 Parametric statistical model of the observations	44

3.2.1	Parametric statistical model for a weak phase object	46
3.3	Attainable precision	48
3.3.1	Fisher information	48
3.3.2	Cramér-Rao Lower Bound	49
3.3.3	Hammersley-Chapman-Robbins Bound	50
3.4	Maximum Likelihood estimator	50
3.4.1	The uniformly weighted least squares estimator	52
3.4.2	Maximum likelihood estimation of atomic numbers	53
3.5	Statistical detection theory	54
3.5.1	Binary hypothesis testing	54
3.5.2	Sum of Kullback-Leibler divergences	62
3.5.3	Multiple hypothesis testing	64
3.6	Conclusions	67
4	Statistical Experiment Design for Atomic Number Estimation	69
4.1	Introduction	69
4.2	Atomic number estimation of a single isolated atom	70
4.3	Analytical expression for the probability of error	76
4.4	Atomic number estimation of an atom column in a specimen	77
4.5	Conclusions	81
5	Statistical Experiment Design to Detect and Locate Light Atoms	83
5.1	Introduction	83
5.2	Detecting the lightest element H	84
5.3	Detecting versus locating light atoms in HRSTEM	88
5.3.1	Practical implementation of the CRLB	88
5.3.2	Detecting and locating Li in LiV_2O_4	89
5.3.3	Detecting and locating O in SrTiO_3	95
5.3.4	Detecting versus locating	103
5.3.5	Effect of the incoming electron dose	103
5.4	Detecting versus locating light atoms in HRTEM	107
5.5	Conclusions	112
6	Statistical Experiment Design for Nanoparticle Atom-Counting	115
6.1	Introduction	115
6.2	Results from binary hypothesis testing	117
6.3	Results from multiple hypothesis testing	120

6.3.1	Simulation parameters	120
6.3.2	Results for peak intensities and scattering cross-sections . .	123
6.3.3	Results for image intensities on a pixel by pixel basis	125
6.4	Discussion	127
6.4.1	Results for peak intensities and scattering cross-sections . .	127
6.4.2	Results for image intensities on a pixel by pixel basis	131
6.5	Conclusions	131
7	Experimental Applications	133
7.1	Introduction	133
7.2	Efficient fitting algorithm	134
7.3	Estimating the atomic column positions	135
7.4	Estimating the B-O-B bond angle	138
7.5	Domain wall quantification in LiNbO_3	140
7.6	Conclusions	150
8	General Conclusions	151
	Appendix A	155
	Bibliography	159
	List of Symbols and Abbreviations	181
	Samenvatting	189
	List of publications	193
	Dankwoord	197

1 Introduction

1.1 The role of light atoms in modern technology

Light atoms, such as lithium, oxygen, and hydrogen, play a key-role in a range of industrial applications, such as lithium batteries or hydrogen-storage materials. Lithium batteries conquered the portable market because of their light weight and higher energy density as compared to other batteries [1–3]. The performance of lithium-ion batteries is determined by the diffusion behaviour of lithium ions in the cathode, anode, and electrolyte regions. During the charging process, lithium ions move from the cathode to the anode through the electrolyte by being forced to carry electrons from the cathode to the anode. In the discharging process, they return to the cathode through the electrolyte due to a certain potential difference and in this way an electronic power is generated between both electrodes by following this movement of lithium ions. Thus, understanding this movement of lithium ions at the interface between the electrode and electrolyte and also inside the electrodes, which is called the diffusion behaviour, is an essential step to develop lithium-based batteries with improved charging rate, capacity or life time [4–6]. The diffusion channel of lithium ions in an Li_xFePO_4 crystal was visualised at the atomic scale by neutron diffraction [6], and has been further examined by X-ray diffraction [7]. By in situ electron microscopy, lithium ion diffusion has been found to induce local structural and compositional changes [8] in electrodes such as dendrite growth [5]. Detecting individual lithium ions at the atomic scale is an important issue to understand local diffusion behaviour in composite materials with chemical inhomogeneity and defects at the atomic level [3]. Visualisation of lithium atomic columns has been achieved by retrieving the exiting wave phase of a specimen from a focal series of high-resolution transmission electron microscopy (HRTEM) images (phase retrieval method [9]) for LiCoO_2 crystals [10] and Al_3Li crystals [11].

However, only recently, direct imaging of the light lithium atom (with atomic number $Z_{\text{Li}} = 3$) columns in LiV_2O_4 [12] has been succeeded by using scanning transmission electron microscopy (STEM) with an annular bright field (ABF) detector, i.e. a detector located within the illumination cone of the probe as to detect both transmitted and scattered electrons. Other studies also showed this technique to be appropriate for detecting lithium in different materials [3, 13, 14]. Nowadays, lithium-rich layered oxides of general formula $\text{LiNi}_{1/3}\text{Co}_{1/3}\text{Mn}_{1/3}\text{O}_2$ display the highest capacity ($\approx 200 \text{ mAh g}^{-1}$) of all positive-electrode materials used so far [15, 16]. However, these layered structures suffer from a large reduction in average cell voltage during cycling, which prevents their successful implementation in practical cells [17–19]. In [15], a better understanding of this voltage decay phenomenon is provided, and it is shown that this effect is linked to the trapping of metal ions in tetrahedral sites that seem to favour the stability of delithiated structures [15]. Hopefully, the obtained deeper insight in the voltage decay process of these promising oxide layered structures can offer chemists new clues for identifying new formulations in the near future to explore all advantages present in this class of high-capacity electrodes.

The lightest atom of all, hydrogen ($Z_{\text{H}} = 1$), has also become more and more important during the last decades for industrial applications since it can be used in hydrogen storage applications. Hydrogen storage is a key enabling technology for the improvement of hydrogen and fuel cell technologies that can provide energy for a wide range of applications, including both stationary and portable power, and transportation. Also, hydrogen can be used as a medium to store energy created by intermittent renewable power sources (e.g., wind and solar) during periods of high availability and low demand, increasing the utilisation and benefits of the large capital investments in these installations [20]. The stored hydrogen can be used during peak hours, as system backup, or for portable, transportation, or industrial applications. Extensive research is also performed in order to develop onboard vehicular hydrogen storage systems that will allow for a driving range of 480 kilometres or more, while meeting packaging, cost, safety, and performance requirements to be competitive with conventional vehicles. The driving range must be achievable across the range of light-duty vehicle platforms and without compromising space, performance or cost. There is a host of early or near-term power applications in which fuel cell technologies are expected to achieve wide-scale commercialisation, prior to light-duty vehicles. The early market applications can generally be categorised into three segments [20]:

- stationary power (such as backup power for telecommunications towers, emergency services, and basic infrastructure),
- portable power (such as personal laptop battery rechargers, portable generator sets, or mobile lighting),
- material handling equipment (such as forklift trucks, airport baggage and pushback tractors, etc.).

Currently, these applications are suggested to be the largest markets for fuel cells until light-duty fuel cell vehicles are commercialised [21]. Therefore, a lot of effort has been put in addressing the hydrogen storage technology gaps for these applications [20]. Also of interest is to analyse and define the economic feasibility of hydrogen as an energy storage medium to expand the use of renewable energy generation. Materials-based approaches that are currently being investigated include reversible metal hydrides, hydrogen sorbents, and regenerable chemical hydrogen storage materials. Furthermore, for regenerable hydrogen storage materials, it is essential that there are cost effective and energy efficient spent fuel regeneration technologies available to complete the fuel cycle [20]. The current research for materials-based hydrogen storage technology is focused on developing materials that have the potential to meet the ultimate light-duty vehicle system targets by 2020 [20]. Specifically, research on metal hydride materials focuses on improving the volumetric and gravimetric capacities, hydrogen adsorption and desorption kinetics, and reaction thermodynamics of potential material candidates. Sorbent materials research, on the other hand, focuses on increasing the dihydrogen binding energies, optimising the materials pore size, increasing pore volume and surface area, and investigating effects of material densification. Finally, research on chemical hydrogen storage materials focuses on improving volumetric and gravimetric capacity, transient performance, and the efficient regeneration of the spent storage material [20]. As it is of great importance to retrieve information on the atomic scale about the different possible materials that can be used for these applications, HRTEM is an appropriate technique to visualise and investigate these materials of interest. However, as hydrogen only yields a very low scattering intensity it is not possible to detect, while in the presence of heavier scatterers, using conventional TEM (CTEM or TEM for simplicity) or STEM imaging modes when applying a high angle annular dark field (HAADF) detector. Recently, however, it has been shown to be possible to detect the lightest hydrogen element using aberration corrected

STEM in combination with an ABF detector [22–24].

The importance of oxygen atoms in modern technological applications is even broader as compared to lithium and hydrogen, as this atom type appears in a much wider range of technologically interesting materials, such as perovskite structures, all metal oxides containing porous materials like zeolites, low dimensional oxide crystals, and so on. Metal oxides can be used in lots of important industrial applications, for example, for catalysis or gas absorption [25]. In recent years, a whole range of fascinating phenomena have been found in oxide materials, or their surfaces or interfaces. These include, among many others [26]:

- novel electric transport properties at heterophase or internal interfaces [27–31],
- unusual magnetic phenomena at heterophase interfaces [32–35],
- stabilisation of unusual phases and resulting novel properties in oxide thin films [36–38],
- construction of new morphotropic phase boundaries in a wide range of ferroelectric materials [38–41],
- creation of multiferroic oxides combining permanent magnetic and polarisation orderings [42–46],
- control of bulk properties through interface chemistry [47, 48].

These are just a few examples from the dynamic field of functional oxides, and for a more complete and comprehensive review, the interested reader is referred to the report of Martin et al. [49] and the references therein. Although oxygen atoms are also still light ($Z_{\text{O}} = 8$) they have been observed by advanced techniques, such as exit wave reconstruction [50], spherical aberration corrected TEM [51, 52], and high voltage HRTEM [53]. Although these methods show concepts to locate where the oxygen columns would be, their utilisation is limited due to the small scattering intensity of light elements. Advanced results are mainly retrieved on the direct imaging of oxygen columns in structures derived from thermodynamically stable, high-temperature perovskites, characterised by negligible beam sensitivity [53, 54]. In catalysis and energy conversion, however, metastable and specifically beam-sensitive phases exhibiting defects and

distortions in the metaloxygen polyhedra are mostly used. Therefore, intensive research has been done in the past decade in order to find new techniques for the direct imaging of this light element.

As already mentioned before, using an ABF detector in combination with STEM has been shown appropriate in order to detect different light atoms [23, 55–57]. Recently, also atomic resolution BF STEM has been shown to be appropriate to measure oxygen octahedra tilt angles in $\text{Li}_{0.5-3x}\text{Nd}_{0.5+x}\text{TiO}_3$ (LNT), a member of a family of perovskite-related, solid-solution phases that is amongst the best Li-ion conductors [58]. By colour-coding tilt-angle magnitudes onto individual octahedra, a striking diamond-shaped domain pattern has been revealed, which aligned spatially with the contrast associated with the superstructure which could be visualised using LAADF STEM imaging [58]. This result has provided the first real-space evidence of the correlation between octahedral tilt modulation and the diamond-type domain structure with associated strain in LNT.

Both imaging techniques, conventional TEM and STEM will be further explained in the next section, including different possible detector settings in STEM. Thereafter a brief overview will be given on the evolution of transmission electron microscopy during the years, based on the review given by MacLaren and Ramasse in [26]. Finally, it will also be discussed how electron microscopy has evolved during the last decades from a purely qualitative toward a quantitative technique, aiming at accurate and precise measurements of parameters of interest.

1.2 Imaging in High Resolution (Scanning) Transmission Electron Microscopy

Most of the interesting phenomena in light-atomic materials described in the beginning of this chapter arise at the atomic scale and therefore, atomic resolution characterisation of the structure and chemistry is fundamental for a full understanding of the origins of such phenomena. Only atomic resolution TEM techniques seem to be appropriate to provide local information to the atomic scale, since electrons interact sufficiently strongly with materials [59, 60]. Furthermore, atomic-scale structural and chemical characterisation of materials has become possible in the past few years thanks to the development of new techniques for the correction of the lens aberrations in the probe-forming lenses, which has led to major advances in (scanning) transmission electron microscopy [26]. In Figure

1.1, a schematic setup of both (conventional) TEM and STEM is shown. For a detailed overview on TEM, the interested reader is referred to [61–63]. In TEM, the specimen is illuminated in one shot by a parallel incident electron beam. The electron-specimen interaction results in a complex electron wave function at the exit plane of the specimen, i.e. the so-called exit wave. If the specimen is oriented along a crystallographic main zone axis and the neighbouring columns are not too close to each other, it is shown that a one-to-one correspondence exists between the exit wave and the projected structure of the specimen [64, 65]. After the electron-specimen interaction, the resulting exit wave is magnified by a set of apertures and magnetic lenses. The magnified wave then propagates further to the image plane where it forms the so-called image wave. As already mentioned above, the microscope's lenses are not perfect, which causes distortions in the exit wave by lens aberrations such as spherical aberration, defocus, and chromatic aberration while propagating to the image plane. Therefore, the image wave is more difficult to interpret in terms of structural information. In a final step, the image wave is recorded using, for example, a fluorescent screen, or nowadays usually a charge coupled device (CCD), which detects the electrons reaching the camera. As only the intensity is recorded, the phase of the image wave is lost. Furthermore, TEM is a coherent imaging mode which means that contrast reversals can occur due to the lens aberrations and multiple elastic scattering of the electrons.

When a focused electron probe is used instead of a parallel electron beam, this probe can be scanned over the specimen in a raster pattern by exciting scanning deflection coils, as shown on the right side of Figure 1.1. The scattered electrons are then detected and their intensity is plotted as a function of the probe position. This technique is referred to as scanning transmission electron microscopy (STEM), about which more details are given in [66, 67]. For each probe position, a so-called convergent beam electron diffraction (CBED) pattern is formed in the back focal plane, where an annular detector is located. Different detector geometries are nowadays available [68–70]. It is possible to detect a bright-field signal by placing the central (i.e., the transmitted) beam on a bright-field detector, while an annular dark-field detector around the bright-field detector collects the signal from (some of) the diffracted beams. Which diffracted beams (or rather, which range of diffraction angles) are being collected on the dark-field detector depends on the camera length of the diffraction pattern. At low camera lengths the collected angles are large and the dark-field detector is a high-angle annular dark-field detector, while at higher camera lengths the angles are smaller. As an

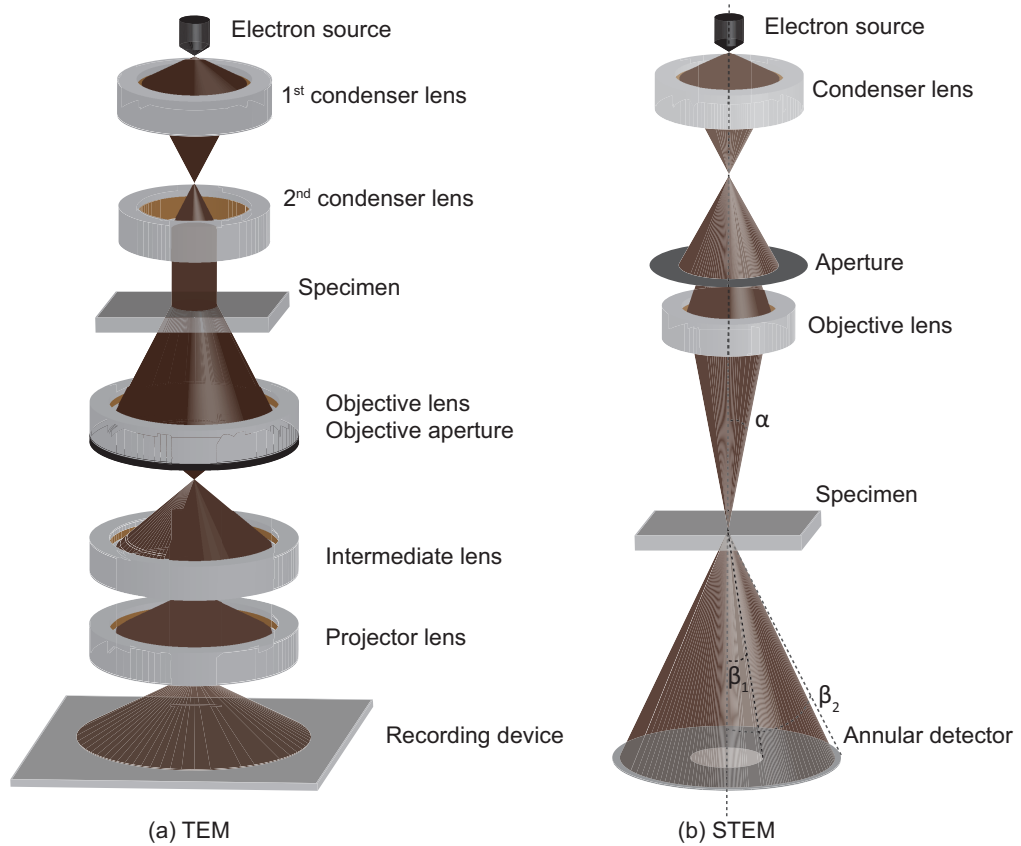


Figure 1.1: (C)TEM and STEM setup. In TEM, a plane wave is projected onto the sample after which the exit wave is projected onto a fluorescent screen or a camera. In STEM, a convergent probe is scanned over the sample and for each probe position, the intensity of the scattered electrons is recorded on the annular STEM detector.

example, the interested reader is referred to Appendix A, where a table is given of the different possible camera lengths with the corresponding detector angles for two TEM/STEM instruments available at EMAT, the FEI X-Ant-EM and the FEI QU-Ant-EM. Depending on the collection range of the detector, the contrast and signal-to-noise ratio (SNR) of the image will be different.

For example, an annular dark field (ADF) detector is an annular detector (usually a scintillator-photomultiplier detector [26]) whose inner and outer angles (β_1 and β_2) may be varied, although limited by physical dimensions and positioning in the column. Typically, the outer angle β_2 is taken very large (200 mrad or more), and is in practice only limited by physical restrictions in the column, such as shadowing from the set of probe-forming lenses. Varying the inner angle will allow different mechanisms to contribute to the detected signal. If the inner angle of the ADF detector is much larger than the probe semi-convergence angle α (typically three times larger), this will yield a dark-field image. A typical probe semi-convergence angle α equals 15 – 30 mrad. Only the electrons that are scattered under high angles are then collected by the detector, which is referred to as high angle ADF (HAADF) detector. This signal comes from Rutherford scattering of electrons by the atomic nuclei and is considered to be purely incoherent. Furthermore, the resulting image contrast strongly depends on the atomic number or the number of atoms in a column, varying approximately as Z^2 for isolated atoms. Therefore, HAADF imaging is often referred to as Z -contrast imaging, which makes these images directly interpretable in terms of crystal structure. Due to the Z -dependency, HAADF STEM can also provide chemical information [71–74], and when applying statistical methods even the number of atoms can be determined [75–77]. For smaller inner angles, coherent diffraction effects contribute to the overall signal recorded by the detector, which is then referred to as medium or low angle ADF (MAADF or LAADF) imaging. When the inner angle β_1 is approximately twice the probe semi-convergence angle this is referred to as MAADF STEM. LAADF STEM corresponds to an inner angle which is only slightly larger than the probe semi-convergence angle. MAADF STEM has been shown to be appropriate for strain measurements and is more sensitive to lighter elements as compared to HAADF STEM [78–80]. One of the great advantages of HAADF and MAADF STEM is the possibility to collect simultaneously some analytical signals. For example, one can perform electron energy-loss spectroscopy (EELS) and/or energy dispersive X-ray (EDX) spectroscopy in combination with HAADF or MAADF imaging, which makes it possible to obtain elemental and chemical information at the atomic scale [81–83].

Another signal that is straightforward to collect is the bright field (BF) signal, which is simply recorded using an axial detector centred at the optic axis. The detector range is then lying within the illumination cone of the probe and the detected signal is mainly formed by elastically scattered electrons. The contrast on

this BF detector is principally phase contrast, especially at very low angles. It can be shown by reciprocity that BF STEM images are (almost) equivalent to conventional broad-beam TEM images. BF contrast is thus also critically dependent on sample thickness and defocus, and can show contrast inversions [26].

One recently developed related detector is the annular BF (ABF) detector, whereby an annular detector is used with the detector collection range lying within the cone of illumination (the direct-scattered region). The typically used detector range is then from half of the probe semi-convergence angle upto the semi-convergence angle ($\alpha/2 - \alpha$). Small-angle scattering occurs at the edge of the atoms where all elements have comparable scattering factors. Thus the scattering intensities of light and heavy elements are more balanced [84], which allows ABF STEM to visualise light atoms in the presence of heavier scatterers [56, 85, 86]. On the other hand, high-angle scattering occurs deep within the atom, close to the nucleus, where the unscreened nuclear charge is very different for different elements, giving rise to the Z-contrast behaviour. For thin specimen thicknesses, the contrast formation mechanism of ABF STEM has been explained in a simple way using the s-state channelling model [85]. Findlay et al. have shown that ABF STEM performs well to detect light elements [55, 85]. Another strength of ABF STEM is that both light and heavy atom columns are visible simultaneously, in contrast to high angle annular dark field (HAADF) STEM, which tends to render light elements invisible when in proximity to heavier scatterers [87, 88]. This effect can be understood since the ADF contrast, the so-called Z-contrast, is based on the scattering amplitude, while the ABF phase-contrast is based on wave-interference, so that it only requires the atoms to alter the phase of the electron wave [89]. As direct imaging of light elements is necessary for the full determination of crystal structures, such as cathode materials for lithium-ion batteries, this topic has recently become very important and a lot of research has been done in this field in the past few years. Not only the identification of individual lithium atoms [3, 12, 57, 90], but also the direct imaging of other light elements, such as carbon, oxygen or nitrogen [56, 69, 85, 86] and even hydrogen [22, 23] has been shown to be possible using the ABF STEM detector setting.

1.3 From Conventional TEM to Aberration-Corrected STEM: a brief overview

Ever since its invention by Knoll and Ruska [91] back in the 1930s, the electron microscope has been a widely used instrument in understanding the micro- and nanoscale structure of materials. The classic broad-beam techniques which were pioneered in Ruska and Knolls instrument have been dominant in science for a long time in the history of transmission electron microscopy. Nevertheless, already back in the 1930s, both Knoll [92] and von Ardenne [93] were experimenting with a fine probe of electrons scanning across a specimen and retrieving an image in a serial fashion. However, this technique was not really popular by that time and only stepped up again in the 1960s and 1970s thanks to the work of Albert Crewe [94, 95]. Furthermore, the use of cold field emission guns (CFEGs) for electrons, ultra-high vacuum chambers, and the introduction of annular detectors led to a massive step forwards. Imaging of single heavy atoms with the Chicago STEM [96] can be considered as the culmination of this progress. As a result of this improvement, several companies including Hitachi, AEI, Siemens and Vacuum Generators (VG) started with the production of commercial CFEG dedicated STEMs and these were installed in a number of laboratories. In particular, these instruments have been used for applications in high spatial resolution electron energy-loss spectroscopy (EELS) and energy dispersive X-ray (EDX) spectroscopy of materials [97]. Still, the world of transmission electron microscopy kept being dominated by broad-beam techniques, and the majority of electron microscopy laboratories were focussed on (C)TEM. However, already many of these institutions had STEM-capable TEMs available, which were mainly meant for use on analytical studies.

Only in the mid to late 1990s, the revolution of STEM really started. It had already been known for years from the work of Otto Scherzer that geometric distortions of the wavefront because of spherical and chromatic aberrations were inherent to electron microscopy, when using conventional round electron lenses [98]. This is because of the fact that no diverging round lenses for electrons exist, unlike for visible light, where aberration correction is much simpler. Scherzer's research contributed significantly to understanding the limits of resolution in conventional lenses, and to maximising the possible resolution by which is known as the Scherzer defocus [99]). Furthermore, he made several proposals for aberration correction [99, 100]. This stimulated a great effort to develop an aberration

tion corrector for the round lenses in electron microscopes, not only in Scherzers group [101–103] but also in other laboratories [104–106]. The two earliest proposals have used combinations of multipole electromagnetic lenses (either quadrupole octupole-, or multiple sextupole-based designs [107]) in order to make an effective compound lens with an overall negative spherical aberration. Unfortunately, most of the early attempts failed at practical realisation of an aberration-corrected microscope, not only because of electrical or mechanical instabilities but also because of the lack of automated alignment schemes, as computers were not readily available.

Only in the 1990s, Zach and Haider managed to realise a working practical implementation of an aberration corrector in a scanning electron microscope [107] based on a design proposed by Rose, one of Scherzers former students. This was very fast succeeded by the aberration correction of a transmission electron microscope's objective lens [108] and the achievement of 1 Å and even better resolution in HR TEM, at conventional accelerating voltages of 200 kV [54, 109]. Krivanek, Dellby and Lupini developed contemporarily new techniques which led to the correction of the aberrations in the probe-forming lens of a STEM [110]. Thanks to these new developments, it was already immediately demonstrated that the newest generation of aberration-corrected instruments could obtain a point resolution of the order of 100 pm in TEM and 50 pm in STEM, at moderate accelerating voltages [111–115]. The point resolution represents the smallest detail that can be interpreted visually in experimental images. Of course, this had a huge and prompt impact on the world of electron microscopy research, namely that atomic structures of many materials could now be easily interpreted visually.

In TEM, further improvements of the point resolution can be obtained by using higher accelerating voltages. Recently, a point resolution of 43 pm has been reported for an aberration corrected 1.2-MV cold field-emission TEM [116]. However, such high voltages lead to radiation damage in the specimen, which limits the use of high voltages for the analysis of light-element structures and catalytic nanoparticles. Another resolution measure can also be considered in TEM, i.e. the so-called information limit. The information limit represents the smallest detail that is transferred from the specimen to the image, or in other words the smallest detail that can be resolved by the microscope. This limit is inversely proportional to the highest spatial frequency that is transferred from the specimen to the image. By using image processing techniques, the interpretable resolution can be pushed down from the point resolution to the information limit. Methods for exit wave reconstruction from a focal series of images, for example, achieve

this goal [117–122]. Since, ideally, the exit wave is free from imaging artefacts, the visual interpretation can be considerably enhanced as compared to the original images, especially in the case of thin specimen. In this way, imaging with a resolution of 50 pm is possible in TEM [50, 123–125].

Based on classical resolution criteria, it is often concluded that the directly interpretable resolution from a single image is higher in incoherent ADF STEM as compared to coherent TEM, when the same imaging system is used in both imaging modes. Lord Rayleigh proved in 1896 that the resolution for incoherent imaging is a factor of two higher as compared to coherent imaging [126]. Therefore it could be expected that the achievement of sub-Å resolution was indeed achieved earlier in STEM than in TEM at intermediate accelerating voltages [127, 128]. However, if images are interpreted quantitatively instead of qualitatively, classical resolution criteria, such as Rayleigh's are no longer appropriate [129], and then an alternative criterion is needed to compare coherent and incoherent imaging systems objectively. Such a criterion is proposed in [129] and relates resolution to statistical measurement precision. In terms of precision, it has been found that HRTEM is usually preferable, except for fields of view smaller than a few squared nanometers [129].

Nevertheless, a great advantage of typical annular dark field (ADF) STEM images, is the fact that the contrast can be directly interpreted in terms of atomic positions, when observing crystalline samples aligned to a specific zone axis, where a bright spot corresponds to an atom column, almost irrespective of sample thickness [71, 130]. Since the introduction of these early aberration-corrected STEM instruments, further developments have been made in order to make instruments more user-friendly, to improve the sample mounting and ease of tilting, and to better couple spectrometers to the microscope to allow for efficient collection of spectroscopic signals. Nowadays, all major TEM manufacturers produce aberration-corrected STEM instruments. From the situation in the mid 1990s where most TEMs sold were principally broad-beam TEM instruments, possibly with a STEM capability as an add-on, we are now in a situation where the majority of new installations in materials or physical sciences are combined TEM/STEM instruments with excellent STEM capabilities, very often with aberration correction in the probe-forming optics. Moreover, STEM is becoming the standard technique for quantitative nano- or atomic-scale materials based on image resolution criteria. However, since resolution is not unambiguously defined, a measure for the statistical precision provides a more objective criterion to evaluate different imaging systems if images are interpreted quantitatively [129].

1.4 From Qualitative toward Quantitative Electron Microscopy

Coming to the point at which the resolution is fundamentally limited by the intrinsic “width” of the atom itself, determined by the electrostatic potential and thermal motion of the atom [131], the focus in TEM research has moved gradually from obtaining a better *point resolution* to improving the *precision* with which structural and chemical information can be extracted from TEM data [60, 132]. It should be noted that there is a clear difference between resolution and precision. Resolution, as defined by the classical resolution criteria such as the Rayleigh resolution criterion [133, 134], expresses the ability to visually distinguish neighbouring components, while precision corresponds to the variance with which (structure) parameters can be measured from the observed data. Van Dyck was among the first to emphasise the importance of precise structure determination for materials science and technology [135]. This importance can be motivated as follows [132]. A complete understanding of the relation between the properties of nanomaterials and their structure, combined with recent progress in building nanomaterials atom by atom, will enable materials science to evolve into materials design. Quantum mechanical *ab initio* calculations allow one to predict relations between structure and physical properties of nanomaterials, but validation and further improvement of these calculations are only possible by interaction with experiments. This requires experimental characterisation methods yielding local structure information with sufficiently high precision. In fact, atom positions have to be measured with a precision of the order of 1 pm, since a displacement of the atoms over such a length may have a considerable effect on the material’s properties [136, 137]. For example, strain induced by the lattice mismatch between a substrate and the superconducting layer grown on top may double its critical temperature [138]. As already mentioned before, TEM is the most appropriate technique to provide the required precision, since from all possible imaging particles, electrons interact most strongly with matter [59, 60].

The first studies on the feasibility of precise structure determination through TEM were based on simplified models and simulations [135, 139, 140]. These studies showed that TEM has indeed the potential to provide structure characterisation with a precision that is orders of magnitude better than the resolution of the microscope, but this requires a quantitative model-based interpretation of

the images. A merely visual interpretation is inadequate. The methodology for the quantitative approach required is provided by *statistical parameter estimation theory*. Meanwhile, the feasibility of this approach has been demonstrated not only in simulations, but also in practice [75, 141–143]. The starting point of the quantitative approach mentioned above is the notion that we are not so much interested in the electron microscopy images as such, but rather in the information - structural and chemical - of the sample under study. Image quality and resolution are therefore of subordinate importance. Images are to be considered as data planes, from which sample structure parameters, such as atom positions, particle sizes and fiber diameters, have to be estimated as precisely as possible. For this, we need a parametric model of the images that includes all ingredients to perform a computer simulation of the images (such as electron-specimen interaction, microscope transfer and image detection). If first principles based models cannot be derived, or are too complex for their intended use, simplified models may be used. The model is parametric in the unknown sample structure parameters, which are estimated by fitting the model to the experimental images using a criterion of goodness of fit, such as least squares or maximum likelihood [144]. Structure determination thus becomes a parameter estimation problem. Using this statistical parameter estimation based methodology, not only structural information, but also chemical information can be extracted from electron microscopy data. Indeed, it has been shown to be possible to quantify electron energy loss (EELS) spectra [145] and to relatively quantify the chemical composition of atom columns from HAADF STEM images [146] using the same methodology. The quantification of HAADF STEM images in terms of chemical composition could efficiently be solved using a simple parametric incoherent imaging model to describe the image intensities. The parameters of this model are then estimated using least squares estimation and interpreted in terms of total intensities scattered by the atom columns. Recent work has shown that such scattered intensities can be further explored in order to count the number of atoms that are present in an atom column [76, 77]. Quantifying larger fields of view of experimental HAADF STEM images can nowadays be performed using the StatSTEM program [147], were an efficient algorithm is implemented that suits this purpose.

Ultimately, the precision with which the parameters can be estimated is limited by counting statistics. Indeed, due to noise, the pixel values that constitute the experimental images will fluctuate randomly from experiment to experiment.

These pixel values, which we will from now on refer to as observations, can therefore be modelled as random variables, characterised by a joint probability *density* function (PDF) (in the case of continuous observations) or a joint probability function (PF) (in the case of discrete observations, such as the Poisson counting results). Use of the concept of Fisher information [148] allows one to derive an expression for the highest attainable precision with which the structure parameters of the sample under study can be estimated unbiasedly. This expression defines a lower bound on the parameter variance. This bound, which is known as the Cramér-Rao lower bound (CRLB), can be derived from the P(D)F of the observations. The CRLB relies on weak regularity conditions on the P(D)F of the observations [148]. One of these conditions is that the P(D)F should be continuously differentiable with respect to the parameters. The CRLB is generally a function of the sample parameters, the microscope parameters, and the electron dose. It provides quantitative insight into what precision might be achieved from the available image(s). It also provides insight into the sensitivity of the precision to the parameter values. An important application for which the CRLB can be used is statistical experiment design. Experiment design is the selection of free variables in an experiment to improve the precision of the estimated parameters. By calculating the CRLB as a function of the microscope settings, these experimental settings can be optimised so as to attain the highest precision [132, 139, 140, 149–155]. The approach for experiment design also provides the possibility to decide if new instrumental developments result in significantly higher attainable precisions. In this sense, it provides the framework to improve the balance between precision on the one hand and cost, complexity and size of the instrument on the other hand. For example, in this thesis, the inner and outer detector angles of the STEM detector have been optimised, where exact optimal values for both angles are proposed for detecting and locating light elements. In practice, however, the camera length of the diffraction pattern determines the range of collected diffraction angles, which is a restricted parameter in the microscope as only a discrete number of camera lengths are available. Manufacturers of new microscopes could therefore consider to optimise the instrument by making the camera length a continuously variable parameter, which in theory is possible by tuning the lens currents of the diffraction and projector lenses.

The CRLB, as already mentioned above, requires the P(D)F of the observations to be continuously differentiable with respect to the parameters. However, when

estimating a so-called restricted (or, discrete) parameter from a HR(S)TEM image, such as the atomic number (Z), or the number of atoms in a projected atom column, this condition is no longer satisfied and hence the CRLB is not defined. Therefore, an alternative approach is developed for estimating discrete parameters using the principles of detection theory [156–159]. This framework allows one to formulate a discrete parameter estimation problem as a binary or multiple hypothesis test, where each hypothesis corresponds, for example, to the assumption of a specific Z value or a specific number of atoms in the column. Furthermore, statistical detection theory provides the tools to compute the probability to assign an incorrect hypothesis. This so-called probability of error can be computed as a function of the experimental settings and hence can be used instead of the CRLB to optimise the experiment design for discrete parameter estimation problems.

1.5 What to expect in this thesis?

So far, studies on the precision of atomic scale measurements from HRTEM images considered the estimation of the position [60, 129, 132, 135, 139–141, 144, 150, 151, 160] and thickness [161] of atoms (or atom columns in projection). In this thesis, we will quantitatively obtain the optimal experiment design to detect and locate light atoms and to count the number of atoms in a projected atom column from HRTEM and HRSTEM images.

We will start in a simple way by studying the problem of estimating the atomic number Z from a HRSTEM image of a single isolated atom, using the principles of detection theory [156–159]. In the problem of identifying the atomic number Z , a priori knowledge concerning possible solutions for the different hypotheses is usually available. In such cases, the question reduces to distinguishing between a finite plausible set of values for the atomic numbers Z , given the experimental HR(S)TEM observations. Detection theory provides the tools to decide between 2 or more hypotheses - where each hypothesis corresponds to the assumption of a specific Z value or a specific thickness - and to compute the experimental settings minimising the probability to assign an incorrect hypothesis. In this way the probability of error can be computed in order to optimise the experiment design. In particular, we will start by analysing the detection performance to the inner detector radius when deciding between two different atomic numbers Z for a single atom. In the beginning of this thesis, we were only able to calculate the

probability of error by performing numerous noise realisations and computing the fraction of correctly assigned hypotheses, as no analytical expression for the probability of error was derived yet. Therefore, an alternative criterion, the Kullback-Leibler divergence was first proposed, circumventing the need of successive noise realisations.

In a second step of this research, an analytical expression for the probability of error was obtained, for different possible performance measures that can be used, i.e. peak intensities, scattering cross-sections or HR(S)TEM images on a pixel by pixel basis. This analytical expression is then used as an optimality criterion to optimise the experiment design, first to identify the atomic number Z of an atom in a crystalline specimen, and later to detect light atoms from realistic HR(S)TEM image simulations. In particular, the inner and outer detector angles of the annular STEM detector are both optimised, first to determine the chemical composition at the interface of a crystalline specimen, and also for the detection of light atoms. One can not only investigate the optimal detector design in order to identify the atomic number Z , or detect light atoms, but also derive the optimal detector settings to optimise the precision with which the atom column positions can be estimated. The attainable precision with which unknown continuous structure parameters can be estimated, can be obtained using the concept of Fisher information. The ultimate precision is given by the lowest possible variance with which an unknown parameter can be estimated from a set of observations of which the probability distribution function is assumed to be known [148, 162, 163]. An expression for this lower bound on the variance with which the atom column positions can be estimated from HR(S)TEM images can be determined and is given by the so-called Cramér-Rao lower bound (CRLB) [148, 160, 163–165]. Since the CRLB is independent of the used estimation method, it gives the intrinsic limit to the precision that can be obtained. This lower bound is a function of the microscope settings, of which at least some are adjustable, like the annular STEM detector and probe settings. The optimal statistical experiment design of a HR(S)TEM experiment for locating light atoms is then given by the microscope settings that minimise the CRLB [132, 151]. In particular, the inner and outer detector angles of the annular STEM detector are optimised for detecting and locating light atoms. This provides us not only the optimal detector region, but moreover the precise optimal detector angles. The use of recently developed pixelated detectors enables a high flexibility in the choice of detector settings [70, 166, 167] and allow one to collect the scattered signal (CBED pattern) for each probe position.

The result is a 4D-dataset (2D CBED - 2D image scan), which contains all the information about the electron-sample interaction for the scanned area. Another very recently developed and promising technique is atomic resolution electron ptychography [168]. This technique enables the reconstruction of phase-contrast images in STEM under zero-aberration conditions required for optimal simultaneous incoherent Z-contrast imaging. The phase image can be reconstructed from the 4D-dataset acquired with a recently developed high-speed pixelated detector [70]. As the analysis of such 4D-datasets will require a sufficient amount of time, it is appropriate to know which area in the detector plane is the most sensitive and contains the most information in order to detect and locate light atoms.

In a third step, the probability of error for multiple hypothesis testing is used to optimise the experiment design for nanoparticle atom-counting. Hereby, the aim of this research was to investigate which imaging technique is optimal in terms of obtaining the lowest probability to miscount the number of atoms: HRTEM or HRSTEM. In this comparison, the incoming electron dose is kept constant as it is a limiting factor in both imaging modes. In the case of HRSTEM, the detector design is optimised, while in the case of HRTEM the spherical aberration and defocus are the optimised parameters.

Furthermore, statistical parameter estimation theory has been applied in order to obtain precise results for the atom column positions in different practical applications. The estimated atom column positions are then used in the quantification of a domain wall in a LiNbO_3 crystal, and for calculating the angle between the B-site atoms and the oxygen atoms in perovskite heterostructures.

The outline of this thesis is as follows. In chapter 2, the electron-specimen interaction is described as well as the different simulation methods applied for the HRTEM and HRSTEM image simulations performed in this thesis. In chapter 3, the basic principles of statistical experiment design are given, where the probability of error and the attainable precision are proposed as quantitative performance measures for discrete and continuous estimation problems, respectively. Both quantities allow one to evaluate, optimise and compare different experimental settings for different research purposes. In chapter 4, the probability of error is used to optimise the experiment design in order to identify the chemical composition, i.e. by estimating the atomic number Z from HRSTEM images, both of a single isolated atom as well as of an atom at the interface in a crystalline

specimen. In chapter 5, the optimal experiment design is investigated in order to detect and locate light atoms from HR(S)TEM images using the probability of error and the concept of Fisher information as an optimality criterion, respectively. Hereby, it is investigated if a single optimal design is obtained for both the detection and locating problem of light atoms. In chapter 6, the probability of error is used to optimise the experiment design of a HRTEM and HRSTEM experiment in order to count the number of atoms from a projected atom column. Furthermore, in this chapter it is investigated which imaging mode is optimal for nanoparticle atom-counting, using different possible performance measures, HRTEM or HRSTEM. Some practical applications using statistical parameter estimation theory are presented in chapter 7, and finally in chapter 8, conclusions are drawn.

Electron-Specimen Interaction 2

2.1 Introduction

In this chapter, the quantum mechanical description of the electron-specimen interaction will be given, based on derivations given in chapters 3, 5 and 6 of [169] and chapter 10 of [62]. For more details, we would therefore like to refer the interested reader to these two books. Although the electron-specimen interaction only occurs in a very limited trajectory of the electrons inside the microscope, it is the most difficult part to calculate due to the strong interaction with the specimen's potential. Depending on the thickness and the atom types present in the specimen, the electrons can be scattered many times when passing through the specimen. The electron-specimen interaction is called *kinematical* if the electron scatters only once while it passes the specimen, otherwise the scattering is called *dynamical*.

In principle, the electrons behave relativistically at the beam energies used in the electron microscope (50-300 keV), which means that it is not correct to describe them with the Schrödinger equation. Instead, the Dirac equation would be the correct wave equation describing relativistic electrons, however, it is significantly more difficult to work with mathematically. Therefore, it has become traditional to simply use the non-relativistic Schrödinger equation, in which the correct relativistic electron wavelength and mass are being substituted. This approach has been compared to more accurate calculations using the Dirac equation and it has been shown by Fujiwara [170], Ferwerda [171,172], and Jagannathan *et al.* [173,174] that this is usually accurate enough in the typical energy ranges used in the electron microscope. In particular, the influence of using the Dirac equation only leads to a difference below 0.1% in normalised scattering amplitude, as compared to simulations using the non-relativistic Schrödinger equation [175]. Only for energies of the order of 1,000 keV or higher, this approximation may

introduce small errors [169]. As this approach is much easier to work with, only the Schrödinger equation will be introduced in this chapter.

The mathematical description of the electron-specimen interaction requires the knowledge of the specimen potential seen by the incident electron beam. Therefore, in the next section, the approximation of the specimen potential will be presented.

2.2 Specimen potential

If we consider a specimen instead of a single, isolated atom, the incident electrons interact with the total electrostatic Coulomb potential of the specimen as a whole. Simulating an electron microscope image requires knowledge of the position of all atoms in the specimen, along with their atomic numbers. The question is then how the atomic potentials of the individual atoms can be combined to obtain the total potential of the specimen. The most simple approach is a linear superposition of all spherically symmetric atomic potentials which are contained in the specimen [169]:

$$V(\mathbf{r}) = \sum_{i=1}^N V_i(\mathbf{r} - \mathbf{r}_i), \quad (2.1)$$

where $\mathbf{r} = (x, y, z)$ is a three-dimensional coordinate vector and $\mathbf{r}_i = (x_i, y_i, z_i)$ corresponds to the coordinate vector of atom i in the crystal unit cell, with its corresponding atomic potential $V_i(\mathbf{r})$. Throughout this thesis we will always use bold symbols to denote vectors. For single atoms separated by a distance that is large as compared to the atom size this linear superposition approximation would be exact. The effective root-mean-square size of the atoms as determined by the projected atomic potential is about two ångströms in diameter [169]. Note that the effective full-width-half-maximum of a single atom image may be smaller because of the strong potential near the nucleus of each atom. In a realistic solid specimen, however, the atoms are bound together, causing their outer valence electrons to have been rearranged slightly. The primary interaction resulting in high angle scattering is the interaction between the incident electrons and the atomic nucleus' electrostatic Coulomb potential.

Knowing the expression for the total specimen potential, the electron-specimen interaction can be described mathematically.

2.3 Electron-specimen interaction

If we assume that the potential of the specimen is stationary, then the wave function of the electron in the specimen can be calculated using the time-independent Schrödinger equation

$$\frac{-\hbar^2}{2m}\Delta\Psi(\mathbf{r}) - eV(\mathbf{r})\Psi(\mathbf{r}) = E_0\Psi(\mathbf{r}), \quad (2.2)$$

with $\hbar = h/2\pi$ being Planck's constant divided by 2π , m the relativistic mass of the electron, e the magnitude of the electron charge, Δ the three-dimensional Laplacian operator, $V(\mathbf{r})$ the electrostatic potential in the specimen, \mathbf{r} a three-dimensional coordinate vector and $E_0 = eV_0$ the kinetic energy of the incident electrons. Only elastic processes will be considered so the energy will remain constant. The wave vector k_0 and the kinetic energy of the incident wave are respectively given by:

$$E_0 = \frac{h^2k_0^2}{2m}, \quad (2.3)$$

$$k_0 = \frac{1}{\lambda} \quad (2.4)$$

where λ corresponds to the relativistically corrected electron wavelength. Substitution of equation (2.3) into the Schrödinger equation (2.2) gives

$$\left(\Delta + 4\pi^2k_0^2 + \frac{2me}{\hbar^2}V(\mathbf{r})\right)\Psi(\mathbf{r}) = 0. \quad (2.5)$$

We will first consider the electron-specimen interaction of a (weak) phase object in the kinematical approximation.

2.4 Weak phase object approximation

In the weak phase object approximation, dynamical scattering of the electrons in the specimen foil is neglected and therefore, this approximation is not valid for most of the practical specimens used in the electron microscope. Although in principle correct quantitative information cannot be retrieved using this approximation, it can give a good qualitative insight in the electron-specimen interaction and moreover, it provides a good starting point for more advanced methods, such as the multislice method, which is able to describe multiple

scattering of electrons in a thick specimen foil.

If we now consider a specimen that is sufficiently thin, we can neglect the propagator term, Δ , in equation (2.5), and project the specimen onto a single plane. A solution then has to be found of the following equation:

$$\left(4\pi^2 k_0^2 + \frac{2me}{\hbar^2} V(\mathbf{R})\right) \Psi(\mathbf{R}) = 0. \quad (2.6)$$

A formal solution of this equation is known as the *phase object approximation* and can be expressed as follows [62]:

$$\Psi(\mathbf{R}) = T(\mathbf{R})\psi_0(\mathbf{R}), \quad (2.7)$$

with

$$T(\mathbf{R}) = e^{i\sigma v_z(\mathbf{R})} \quad (2.8)$$

$$v_z(\mathbf{R}) = v_z(x, y) = \int_{-\infty}^{+\infty} V(x, y, z) dz \quad (2.9)$$

$$\sigma = \frac{2\pi me\lambda}{\hbar^2}, \quad (2.10)$$

and where $\psi_0(\mathbf{R})$ equals the wave function of the incident electron, $T(\mathbf{R})$ is the transmission operator, $v_z(\mathbf{R})$ is the projected electrostatic atomic potential along the optical axis z and σ denotes the interaction parameter. As a small change in the wavelength is equivalent to a phase shift of the electron as it passes through the sample, it can be seen that a thin specimen acts as a phase shifting layer or a *phase grating* [62].

If the phase change is small (much smaller than a radian), the exponential in the exit wave function of equation (2.7) can be approximated by its Taylor expansion [169]:

$$\Psi(\mathbf{R}) \approx (1 + i\sigma v_z(\mathbf{R}) + \dots)\psi_0(\mathbf{R}) \quad (2.11)$$

which is known as the so-called *weak phase object approximation*. To simulate a single, isolated atom with low to medium atomic number, the weak phase approximation is an appropriate method.

The weak phase object approximation can be used to describe theoretically the interaction between electrons and a very thin specimen, or a thin specimen consisting of light atoms. In general, the specimen must be substantially thinner than the mean free path of all the inelastic scattering events, which depends on the atom types present in the specimen. In practice, specimens consisting of heavy scatterers meet this criterion only for a thickness below a few nm, but biological samples, for example, may reach thicknesses up to 50 nm and still behave as a weak phase object [176]. The weak phase object approximation will be used in chapter 4 where, as a first proof of concept, the estimation of the atomic number of a single isolated atom in HRSTEM will be investigated. However, this approximation is not valid for realistic specimen thicknesses used in a HR(S)TEM. Therefore, one needs more elaborate theories to describe the dynamical electron-specimen interaction of thicker specimens, such as the multislice method.

2.5 Thick specimen foils

We will now look at the electron-specimen interaction of thick specimen foils. The kinetic energy of the incident electrons is known to be much larger than the electrostatic potential of the specimen foil $V(\mathbf{r})$. Therefore, the electron motion will be predominantly in the forward direction and the specimen might be considered as a small perturbation on the electron's motion. The electron wave function can then be regarded as a modulated plane wave:

$$\Psi(\mathbf{r}) = \psi(\mathbf{r})e^{2\pi i\mathbf{k}_0 \cdot \mathbf{r}}, \quad (2.12)$$

with \mathbf{k}_0 the three-dimensional wave vector of the incident plane wave defined by $k_0^2 = k_x^2 + k_y^2 + k_z^2 = \frac{1}{\lambda^2}$, with \mathbf{k}_x and \mathbf{k}_y one-dimensional wave vectors perpendicular to the optical axis and \mathbf{k}_z the one-dimensional wave vector parallel to the optical axis, z . Substitution of equation (2.12) in equation (2.5) requires the calculation of $\Delta\Psi(\mathbf{r})$, which can be done by using the following Laplacian identity:

$$\Delta(UV) = U\Delta(V) + 2(\nabla U) \cdot (\nabla V) + V\Delta U, \quad (2.13)$$

for U and V being three-dimensional functions.

This leads to:

$$\Delta\Psi(\mathbf{r}) = \left(\Delta\psi(\mathbf{r}) + 4\pi i\mathbf{k}_0 \cdot \nabla\psi(\mathbf{r}) - 4\pi^2 k_0^2 \psi(\mathbf{r}) \right) e^{2\pi i\mathbf{k}_0 \cdot \mathbf{r}}. \quad (2.14)$$

Therefore, equation (2.5) can be rewritten as

$$\left(\Delta\psi(\mathbf{r}) + 4\pi i \mathbf{k}_0 \cdot \nabla\psi(\mathbf{r}) + \frac{2me}{\hbar^2} V(\mathbf{r})\psi(\mathbf{r}) \right) e^{2\pi i \mathbf{k}_0 \cdot \mathbf{r}} = 0. \quad (2.15)$$

As this must hold for any position \mathbf{r} , it follows that

$$\Delta\psi(\mathbf{r}) + 4\pi i \mathbf{k}_0 \cdot \nabla\psi(\mathbf{r}) + \frac{2me}{\hbar^2} V(\mathbf{r})\psi(\mathbf{r}) = 0. \quad (2.16)$$

The three-dimensional gradient operator ∇ and the Laplacian operator Δ can now be split into components parallel and perpendicular to the optical axis, which allows to rewrite equation (2.16) as:

$$\left(\frac{\partial^2}{\partial z^2} + 4\pi i k_z \frac{\partial}{\partial z} + \Delta_{xy} + 4\pi i \mathbf{k}_{xy} \cdot \nabla_{xy} + \frac{2me}{\hbar^2} V(\mathbf{r}) \right) \psi(\mathbf{r}) = 0, \quad (2.17)$$

where Δ_{xy} and ∇_{xy} are the two-dimensional Laplacian and gradient operators, respectively, and \mathbf{k}_{xy} is the two-dimensional vector given by $(\mathbf{k}_x, \mathbf{k}_y)$. To solve this equivalent form of the Schrödinger equation, knowledge of two boundary conditions, at the entrance ($z=0$) and exit ($z = \varepsilon$) planes of the specimen is required. As this equation appears hardly solvable when the crystal is not perfect and simple, approximate solutions have to be sought.

High energy electrons are generally assumed to have a motion that is predominantly in the forward z direction, resulting in a large component of the wave vector k_z and a slow change of $\psi(\mathbf{r})$ with z , meaning that

$$\left| \frac{\partial^2 \psi(\mathbf{r})}{\partial z^2} \right| \ll \left| 4\pi i k_z \frac{\partial \psi(\mathbf{r})}{\partial z} \right|. \quad (2.18)$$

Equation (2.17) can therefore be approximated as:

$$\left(4\pi i k_z \frac{\partial}{\partial z} + \Delta_{xy} + 4\pi i \mathbf{k}_{xy} \cdot \nabla_{xy} + \frac{2me}{\hbar^2} V(\mathbf{r}) \right) \psi(\mathbf{r}) = 0. \quad (2.19)$$

Ignoring the term containing the second derivative with respect to z is sometimes referred as ignoring backscattered electrons or *forward scattering approximation* which is appropriate for high energy electrons [177–179]. This approximation is probably better known as the paraxial approximation of the Schrödinger equation. D. Van Dyck [178] has showed that the error introduced by neglecting the

second order derivative term, consists of two parts: the first one arises from the omission of backscattered electrons, which is shown to be negligible. The second part is due to a slight modification of the wave vector of the transmitted electrons, which becomes important for highly dynamical diffraction in thicker crystals. The latter effect causes the approximation to be only valid for crystal thicknesses up to a few tens of nanometers.

The Schrödinger equation for fast electrons travelling along the wave vector \mathbf{k}_0 can now be written as first order differential equation in z :

$$\frac{\partial\psi(\mathbf{r})}{\partial z} = \left(\frac{i}{4\pi k_z} \Delta_{xy} - \frac{\mathbf{k}_{xy}}{k_z} \cdot \nabla_{xy} + \frac{\mathbf{k}_0}{k_z} i\sigma V(\mathbf{r}) \right) \psi(\mathbf{r}). \quad (2.20)$$

In the case of parallel illumination along the optical axis ($\mathbf{k}_{xy} = \mathbf{0}$) this reduces to

$$\frac{\partial\psi(\mathbf{r})}{\partial z} = \left(\frac{i\lambda}{4\pi} \Delta_{xy} + i\sigma V(\mathbf{r}) \right) \psi(\mathbf{r}), \quad (2.21)$$

where the interaction parameter σ is defined in equation (2.10). It should be noticed that equation (2.21) is of the same form as the time-dependent Schrödinger equation in two-dimensional space, where the depth z plays the role of time t .

The theory of dynamical scattering has been studied by many scientists over the years, in principle the main purpose is solving the differential equation (2.5), or in the approximated form equation (2.19) which becomes (2.21) in the case where $\mathbf{k}_{xy} = \mathbf{0}$. The two most popular groups of methods solving this equation are the Bloch wave and the multislice methods. All these methods solve the Schrödinger equation under certain approximations.

Bethe (1928) [180] was the first to describe the dynamical scattering theory in the context of electron diffraction. He started from the Schrödinger equation and performed a Fourier expansion on the specimen potential and the electron wave function, with components that match the underlying periodicity of the crystal lattice. In this way, he obtained a set of coupled linear dispersion equations for the plane wave expansion coefficients that can be put in a matrix form and, in the forward scattering approximation, can be expressed as an eigenvalue problem. The Fourier components of the wave function have since become known as Bloch waves in analogy with Bloch's theorem in solid state physics. Since Bethe's original approach, several many-beam electron diffraction theories have been developed which are in fact all reformulations of the original Bethe

theory. Howie and Whelan [181] used a different starting point but ended up with a set of coupled first order differential equations similar to the Bloch wave method. Van Dyck [182] and Jap and Glaeser [183] have independently developed a Feynman path integral formulation of the dynamical scattering theory, which shows the equivalence between the multislice formula and the Howie and Whelan equations. The history of the development of the theory of dynamical diffraction of electrons has been given by Cowley [184], Self *et al.* [185], Van Dyck [186], and Watanabe [187].

Cowley and Moodie [188] considered the dynamical scattering problem by starting from a physical optics point of view and derived a method that has become known as the multislice method. In this method the specimen is divided into two-dimensional thin slices along the direction of the optical axis. The electron beam alternately transverses a slice and propagates to the next slice. If each slice is thin enough it can be regarded as a phase object and the propagation between slices is given by the Fresnel diffraction equation, describing propagation of waves in the near field [189]. Goodman and Moodie [190] later expanded the multislice theory into an accessible form appropriate for numerical implementation on a computer and showed how various theories of dynamical scattering were related.

The methods that have been used to simulate electron microscopy images in this thesis are based on the multislice theory. Therefore, only the applied multislice methods are further discussed in the next section.

2.6 Multislice method

The multislice approach, which was first proposed by Cowley and Moodie [188], gives a solution of the Schrödinger equation in the paraxial approximation, given by equation (2.21). In this approximation it is assumed that the high-energy electrons move predominantly in the forward z direction. Here we will follow the derivation according to Kirkland [169] to come to the general multislice formula. The starting point of the multislice approach states that the 3D atomic potential of the specimen can be approximated by a set of 2D projections. Then, the specimen's potential will be subdivided in n slices in which the atomic potentials of the different atoms in each slice of the specimen are being projected. In this case,

every slice of the specimen will act as a pure phase plate or *phase-grating* and will only modify the phase of the incident electron wave $\psi(x, y, z) = \psi(\mathbf{R}, z)$. After the interaction with a certain slice, the wave function will propagate to the next slice. The multislice algorithm then consists of these two succeeding steps - transmission through a slice and propagation to the next slice - until the wave function reaches the specified thickness z of the specimen on the exit plane of the last slice. A schematic scheme of the multislice decomposition of a thick specimen is shown in Figure 2.1.

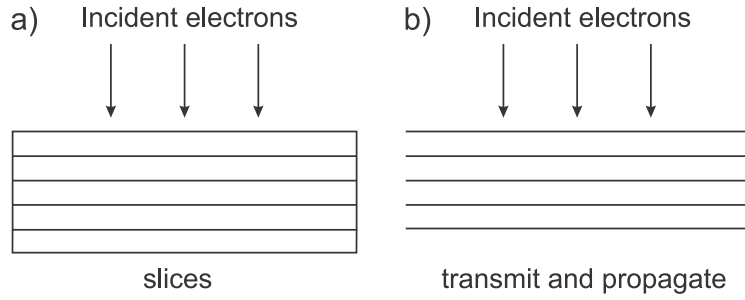


Figure 2.1: Schematic scheme of the multislice decomposition of a thick specimen. (a) The specimen divided in thin slices, and (b) each slice is treated as a transmission step (solid line) and a propagation step (vacuum between the slices).

This process is mathematically described as follows [169]

$$\psi(x, y, z + \Delta z) = p(x, y, \Delta z) \otimes [t(x, y, z)\psi(x, y, z)] + \mathcal{O}(\Delta z^2), \quad (2.22)$$

in which

$$t(x, y, z) = \exp\left(i\sigma \int_z^{z+\Delta z} V(x, y, z') dz'\right) \quad (2.23)$$

and

$$p(x, y, \Delta z) = \exp\left(\frac{i\lambda\Delta z}{4\pi} \Delta_{xy}\right), \quad (2.24)$$

correspond to the transmission function and propagation function of the electron wave, respectively. The convolution product of two functions, represented by the symbol \otimes is defined as

$$f(\mathbf{r}) \otimes h(\mathbf{r}) = \int f(\mathbf{r}')h(\mathbf{r} - \mathbf{r}')d\mathbf{r}'. \quad (2.25)$$

We can now label the different potential slices as $n = 0, 1, 2, \dots$ for a corresponding depth z_n , which enables us to rewrite equation (2.22) as follows:

$$\psi_{n+1}(x, y) = p_n(x, y, \Delta z) \otimes [t_n(x, y)\psi_n(x, y)] + \mathcal{O}(\Delta z^2), \quad (2.26)$$

with $\psi_n(x,y)$ being the electron wave function at the entrance of slice n , with its corresponding transmission function $t_n(x,y)$ and propagation function $p_n(x,y,\Delta z)$.

2.7 Thermal vibration of the specimen atoms

In a crystal, atoms are constantly vibrating, even at temperature $T = 0K$ [191]. Due to this thermal movements, the atoms are displaced from their ideal crystal positions. This leads to the fact that the atomic potential, when averaged over time, is blurred, which results in a decrease of the atomic scattering potential. In the first place, this damping of the atomic potential causes the intensities of diffracted beams to become smaller. However, there is also a second effect of thermal vibration of the atoms. The resulting disorder in the crystal lattice gives rise to the fact that some electrons are ‘lost’ for Bragg reflection. These electrons neither stay in the undiffracted beam, nor are they being diffracted into a Bragg reflection. As they ‘diffuse’ this is known as *thermal diffuse scattering*, or simply TDS [192].

In STEM images, a substantial amount of the intensity is formed by TDS electrons, caused by the thermal vibration of the atoms in the specimen [169]. At room temperature, the atoms in the specimen vibrate slightly. The atomic vibrations are small as compared to the typical interatomic distance so this effect is expected to be small, but it can nevertheless lead to some interesting effects. TDS particularly leads to a diffuse background intensity in the diffraction pattern and shows peaks at the atomic column positions [193].

Appropriate methods to include TDS in HR(S)TEM image simulations are either the frozen phonon approximation or the absorptive potential method [194], which have both been used within the multislice approach in this thesis. For the simulation of HRTEM images, the frozen phonon method is used, while the absorptive potential method is applied for the simulation of the HRSTEM images in this thesis. Both methods will be further explained in the following subsections.

2.7.1 Frozen phonon approximation

In principle, we should treat the electron-phonon scattering based on a many-body quantum mechanical framework, which treats the thermal scattering as a quantum excitation of the crystal [195]. However, under the single elastic

scattering approximation, the rigorous quantum mechanical description is equivalent to the frozen phonon model [169, 196]. Furthermore, multiple scattering of TDS electrons can be neglected for STEM image simulations as elastic scattering mainly constitutes small angle scattering and therefore only leads to an insignificant redistribution of intensity in the diffraction plane [194].

The frozen phonon model is based on the rather classical idea that the time that the electrons in the microscope interact with the specimen (about 7.1 fs) is much shorter than the vibration period of an atom (0.1 to 1 ps for optical phonons and higher for acoustic phonons) [62, 169]. This is a result of the fact that the electron beam moves at about 0.6 times the speed of light [62]. Therefore, when the imaging electron is inside the specimen, it will see the atoms being frozen at displaced positions. Typically, the current in the microscope is small enough such that the time between two successive imaging electrons passing through the specimen is long, as compared to the oscillation period of the thermal phonons in the specimen. Therefore, each successive imaging electron sees a slightly different displacement configuration of atoms in the specimen. All different atom configurations are uncorrelated with each other so during the exposure time (some ms in the case of TEM), many of these configurations are averaged incoherently.

In principle, this method uses the multislice algorithm, applied to a crystal supercell containing atoms at statistically displaced positions, where the different displacement configurations are caused by thermal motion. Many of these calculations have to be performed for different displacement configurations, which are then incoherently averaged to give the resulting intensity pattern. Van Dyck proved [197] that the frozen phonon method is fully equivalent to a full quantum mechanical treatment of the inelastic phonon scattering model.

The frozen phonon approach can be numerically implemented by performing repeated multislice simulations for different atomic coordinate configurations. These different configurations are either taken as outcome of realistic phonon calculations, retrieved from *ab initio* (density functional theory) calculations or molecular dynamic calculations, or as outcome of calculations using the approximated Einstein model in which the atoms vibrate independently, neglecting any correlation of atomic displacements. The latter is also often referred to as the frozen lattice or uncorrelated phonon approximation. Muller *et al.* showed that frozen lattice approximation leads to results that are in good agreement with the

complete frozen phonon model [198]. The final image or diffraction pattern is the averaged intensity over the different displacement configurations. For all the frozen phonon simulations that are performed in this thesis the Einstein model was used.

2.7.2 Absorptive potential method

The largest drawback of the frozen phonon method, is that the computation of the image intensity for a large number of configurations (100-500) is time-consuming. Certainly in the case of HRSTEM, where every scanned pixel is computed in a serial way the frozen phonon method is time-consuming. Therefore, a computationally less-intensive multislice algorithm has been used for the HRSTEM image simulations in this thesis, while the HRTEM simulations are performed using the frozen phonon model.

This computationally less-intensive method is based on the fact that the inelastically scattered electrons are being distributed at angles other than the Bragg angles; thus, they are considered to be effectively absorbed by the crystal as long as the elastically scattered wave is concerned. This is the reason that the loss of electrons caused by TDS can be described as an *absorption* effect in the imaging of Bragg reflected electrons, which can be taken into account by a complex crystal potential, as was first proposed by Allen *et al.* [199] and Ishizuka [200].

The main approximation that is made in the absorptive potential method is the assumption that the TDS scattered electrons directly propagate towards the detector, without further interaction with the specimen. For small specimen thicknesses (up to about 50 nm) and for light atoms, this approximation is quite accurate and deviates less than 4% from the frozen phonon approximation [201].

In practice the effect of TDS in the absorptive potential method is implemented within the multislice approach by adding the imaginary component V_{TDS} , the TDS-absorptive potential, to the electrostatic Coulomb potential $V_{Coul}(\mathbf{R})$, which is then the real component of the total projected potential of the crystal slice $V_p(\mathbf{R})$ [201]:

$$V_p(\mathbf{R}) = V_{Coul}(\mathbf{R}) + iV_{TDS}(\mathbf{R}). \quad (2.27)$$

The TDS-absorptive potential is defined by [194, 199, 200]:

$$V_{TDS}(\mathbf{R}) = FT_{\mathbf{g} \rightarrow \mathbf{R}}^{-1} \left[\frac{\sigma \Delta z}{\Omega} \sum_n e^{2\pi i \mathbf{g} \cdot \mathbf{R}_n} \int f_S^n f_{S-\mathbf{g}}^n e^{-B_n \mathbf{g}^2} (1 - e^{-2B_n [S^2 - \mathbf{S} \cdot \mathbf{g}]}) d^2 S \right], \quad (2.28)$$

where n counts the number of atoms with corresponding 2D coordinate vectors \mathbf{R}_n within the centre plane of the slice, σ is the interaction constant, Ω is the volume of the crystal unit cell, \mathbf{g} is a reciprocal lattice vector, $B_n = 2\pi\langle\mathbf{u}_n(t)\rangle^2$ is the Debye-Waller factor related to the atomic displacement vectors \mathbf{u}_n , $f_{\mathbf{q}}^n$ is the scattering factor of atom n with scattering vector \mathbf{q} , and the integration is performed over all possible scattering vectors \mathbf{S} . The inverse Fourier transform $FT_{\mathbf{g}\rightarrow\mathbf{R}}^{-1}$ and the forward Fourier transform $FT_{\mathbf{R}\rightarrow\mathbf{g}}$ are defined as follows:

$$FT_{\mathbf{R}\rightarrow\mathbf{g}}[f(\mathbf{R})] = \mathcal{F}(\mathbf{g}) = \int_{-\infty}^{\infty} f(\mathbf{R})e^{-i2\pi\mathbf{g}\cdot\mathbf{R}}d\mathbf{R} \quad (2.29)$$

$$FT_{\mathbf{g}\rightarrow\mathbf{R}}^{-1}[\mathcal{F}(\mathbf{g})] = f(\mathbf{R}) = \int_{-\infty}^{\infty} \mathcal{F}(\mathbf{g})e^{i2\pi\mathbf{g}\cdot\mathbf{R}}d\mathbf{g}. \quad (2.30)$$

TDS electrons play a major role in STEM when using an HAADF detector which mainly collects TDS electrons and inelastically scattered electrons. In contrast to HRTEM imaging, simulation of STEM imaging with TDS electrons can be performed with a simple multislice approximation [199, 200, 202, 203] using an absorptive potential computed from e.g. the parametrization of Weickenmeier and Kohl [204]. This is possible in STEM imaging since multiple scattering of TDS electrons does not need to be taken into account and the interaction of TDS electrons with the crystal potential can be neglected. In [194] it is shown how a modified multislice approach using TDS-*emission* potentials can be used to obtain an approximation for the TDS intensity in HRTEM images using plane wave illumination.

In the absorptive potential multislice calculation, V_p as given in equation (2.27) is used to describe the dynamical interaction of the electron beam with the projected potential as follows:

$$\Psi(\mathbf{R}) = e^{i\sigma\Delta zV_p(\mathbf{R})}\psi_0(\mathbf{R}) \quad (2.31)$$

For slice n , the intensity of the TDS scattered electrons that reach the detector is then given by:

$$I_{TDS}^{(n)} = \int_{detector} I^{(n)}(\mathbf{R})V_{TDS}^{(n)}(\mathbf{R})d^2\mathbf{R}, \quad (2.32)$$

for $I^{(n)}$ being the intensity of the wave function entering slice n and $V_{TDS}^{(n)}$ the TDS potential as defined in equation (2.28) of the atoms in slice n . Recall that the TDS signal leads to a smooth background in the diffraction plane and only gives small contributions to the Bragg reflections. If electron waves from different point sources of different atoms would be coherent, the TDS intensity would lead to peaks at positions of Bragg reflections. Therefore, it is assumed to be a good approximation to treat electron waves coming from different TDS point sources as being incoherent [194]. The total TDS intensity on the detector can then be obtained by incoherently summing up the contributions of all slices as follows:

$$I_{TDS}^{(total)} = \sum_n I_{TDS}^{(n)} \quad (2.33)$$

The absorptive potential method is used within the multislice approach for all HRSTEM simulations that have been performed in this thesis.

2.8 Imaging in HRSTEM

The image simulation process when using the multislice approach, is schematically shown in Figure 2.2 for a HRSTEM simulation of a SrTiO_3 crystal as an example.

The imaging process starts with the incident electron wave function $\psi(x, y, 0) = \psi_0(x, y)$ at position (x_p, y_p) . The specimen potential of the SrTiO_3 crystal is subdivided in two different types of slices, corresponding to the different atom planes in the unit cell: a slice containing the projected potentials of the Sr and O atoms, and a slice including the projected Ti and O potentials at their respective crystal coordinates. In a first step ($n = 1$), the incident wave function transmits through the first slice, containing Sr and O, while interacting with the corresponding projected atomic potentials. Then, it propagates to the next slice where it interacts with the projected atomic potentials of the Ti and O atoms ($n = 2$), to propagate again to interact with the Sr-O slice ($n = 3$). These succeeding steps of propagation and transmission or interaction, follow each other up until the electron wave function reaches the exit plane of the crystalline specimen. The resulting exit wave function $\psi_{n+1}(x, y) = \psi(x, y, z)$ carries the information of the electron-specimen interaction.

After the electron beam passed through the specimen, the scattered electrons propagate further towards the annular detector. Since the ADF detector is placed in the diffraction plane, it is the Fourier transform of the exit wave function that reaches the detector. The integrated intensity is then given by the squared absolute wave function in reciprocal space, multiplied with the detector function $D(\mathbf{g})$. This integrated intensity denotes the total amount of scattered electron signal at the probe position (x_p, y_p) , and is assigned to a pixel value in the simulated image. For all different positions of the scanning probe, this calculation is performed in order to simulate the complete HRSTEM image.

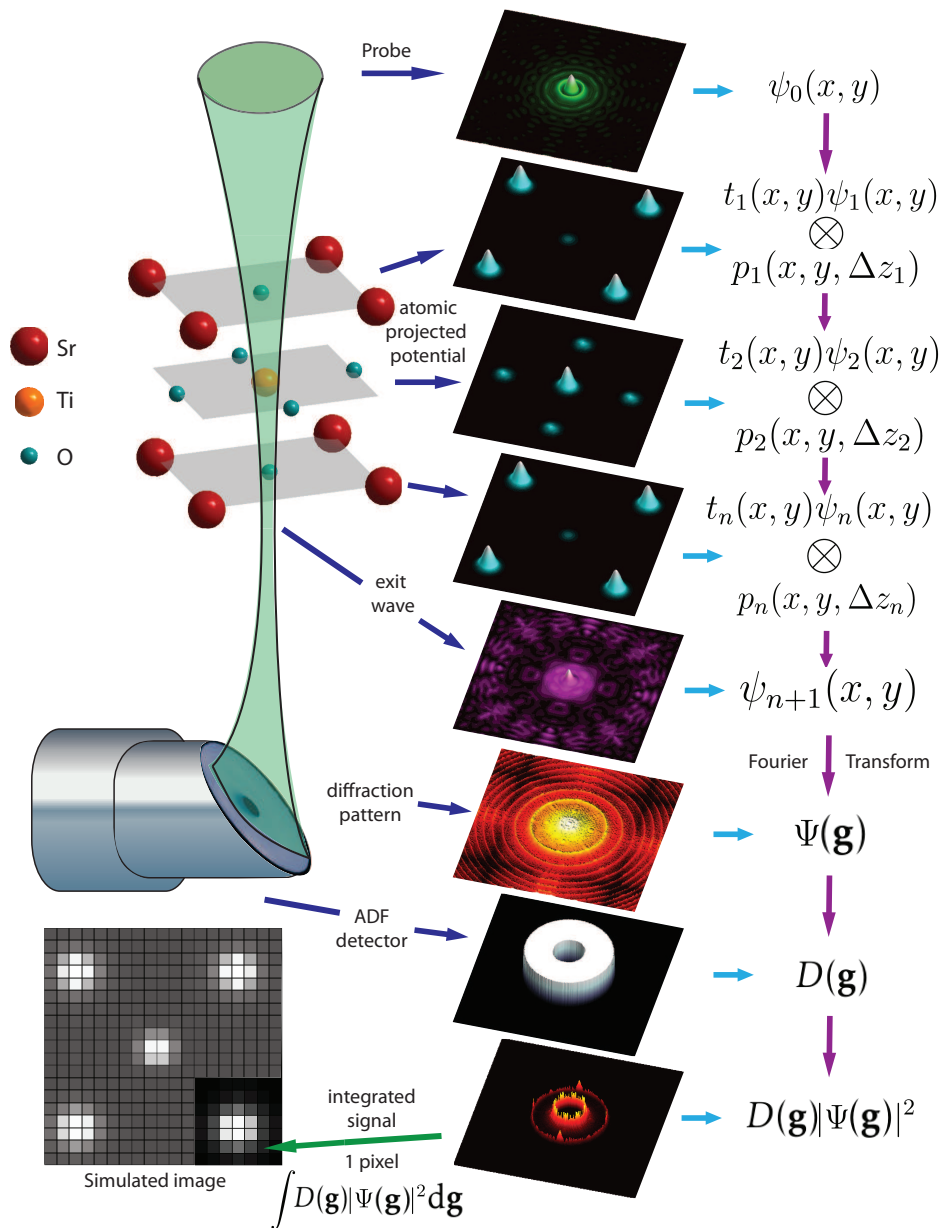


Figure 2.2: Schematic representation of the image simulation process where the multislice decomposition of a SrTiO₃ unit cell is performed to calculate the electron-specimen interaction. This figure is reproduced with permission from Martinez (2015) [205].

2.9 Imaging in HRTEM

In HRTEM, after the electron beam has interacted with the specimen, it passes through the lens system of the microscope. The exit wave is then magnified by the objective lens and the intermediate lenses and transferred to the image plane. Ideally, the electron beam is parallel to the optical axis, fully coherent, and the electron lenses are aberration-free. However, in practice, the imaging process is limited by spatial and temporal incoherence effects, which causes it to become only a partially coherent process. Spatial incoherence is caused by the fact that the illuminating beam is not perfectly parallel, and it will always have a small distribution of angles. This is a result of the fact that the electron source has a finite area. Temporal incoherence results from fluctuations in the energy of the thermally emitted electrons and small instabilities in lens current supplies. A small spread in energy of the incident electron is equivalent to a small (incoherent) spread in defocus values due to the chromatic aberration of the objective lens.

If there is a significant spread in illumination angles and the specimen is thick, then each illumination angle incident on the specimen may interact differently with the specimen. Different illumination angles may satisfy different diffraction conditions in the specimen. The correct way to include a spread in illumination angles and a spread in beam energy and lens currents in a thick specimen is to perform a multislice simulation for each angle in the condenser aperture, then integrate over a range of defocus values and finally sum the results incoherently [206]. If \mathbf{g}_β is one angle in the condenser aperture then the initial wave function is given by:

$$\psi_0(\mathbf{R}) = e^{2\pi i \mathbf{g}_\beta \cdot \mathbf{R}} \quad (2.34)$$

This incident wave function interacts with the specimen foil yielding a wave function that explicitly depends of \mathbf{g}_β , $\Psi(\mathbf{R}, \mathbf{g}_\beta)$. Each of these wave functions should be convolved with the point spread function $T(\mathbf{R}, f + \delta_f)$ and incoherently summed over a range of illumination angles and defocus values to give the final image intensity:

$$I(\mathbf{R}) = \iint \int p(\mathbf{g}_\beta) p(\delta_f) |\Psi(\mathbf{R}, \mathbf{g}_\beta) \otimes T(\mathbf{R}, f + \delta_f)|^2 d^2 \mathbf{g}_\beta d\delta_f, \quad (2.35)$$

in which $p(\mathbf{g}_\beta)$ and $p(\delta_f)$ are the normalised distribution functions of the different illumination angles and defocus values, respectively. The integration over \mathbf{g}_β

is time-consuming and computationally demanding as it is included in the wave function $\Psi(\mathbf{R}, \mathbf{g}_\beta)$. Therefore, a multislice simulation is required for every different orientation of the illumination angle. In comparison, the integration over the defocus spread δ_f is relatively quick since it is included in the point spread function, which is only convolved with the exit wave function after the electron-specimen interaction (and thus after the multislice simulations). Equation (3.14) gives the general expression for the image intensity of a HRTEM image. As numerically integrating over both the defocus spread and the illumination angle spread is computationally demanding, approximate solutions are often used in practice.

In the case where the specimen is thin enough (in the phase object approximation), so that its geometrical extent along the optic axis can be ignored, the illumination angle can be included in either the specimen or the transfer function of the objective lens [169], which means that

$$|\Psi(\mathbf{R}, \mathbf{g}_\beta) \otimes T(\mathbf{R}, f + \delta_f)| = |\Psi(\mathbf{R}) \otimes T(\mathbf{R}, f + \delta_f, \mathbf{g}_\beta)| \quad (2.36)$$

The great advantage is then that one does not need to repeat the multislice calculation over the different orientations of the illumination angles any more. Thus, for a phase object, equation (2.35) can be rewritten as follows [169]:

$$I(\mathbf{R}) = \iint_{\mathbf{g}_\beta} \int_{\delta_f} p(\mathbf{g}_\beta) p(\delta_f) |\Psi(\mathbf{R}) \otimes T(\mathbf{R}, f + \delta_f, \mathbf{g}_\beta)|^2 d^2 \mathbf{g}_\beta d\delta_f. \quad (2.37)$$

In the *perfectly coherent* case, $\mathbf{g}_\beta = 0$ and $\delta_f = 0$, which means that the integrals in equation (2.37) will disappear. As a result, the image intensity for a thin specimen in the perfectly coherent case is given by [62]

$$I(\mathbf{R}) = [\Psi(\mathbf{R}) \otimes T(\mathbf{R})][\Psi^*(\mathbf{R}) \otimes T^*(\mathbf{R})], \quad (2.38)$$

where $\Psi^*(\mathbf{R})$ and $T^*(\mathbf{R})$ are the complex conjugates of the exit wave and the coherent point spread function, respectively. After taking the Fourier transform of this expression and using the convolution and multiplication theorems one can then write [169]:

$$\begin{aligned} I(\mathbf{g}) &= [\Psi(\mathbf{g})T(\mathbf{g})] \otimes [\Psi^*(-\mathbf{g})T^*(-\mathbf{g})] \\ &= \int \Psi(\mathbf{g}')T(\mathbf{g}')\Psi^*(\mathbf{g}' + \mathbf{g})T^*(\mathbf{g}' + \mathbf{g})d\mathbf{g}' \\ &\equiv \int T_{cc}(\mathbf{g}', \mathbf{g}' + \mathbf{g})\Psi(\mathbf{g}')\Psi^*(\mathbf{g}' + \mathbf{g})d\mathbf{g}'. \end{aligned} \quad (2.39)$$

The new function, T_{cc} , is the so-called *transmission cross coefficient* or in short TCC, which depends on the two spatial frequency vectors \mathbf{g}' and $\mathbf{g}' + \mathbf{g}$. This function expresses that each spatial frequency \mathbf{g}' in the exit wave function will interfere with every other spatial frequency $\mathbf{g}' + \mathbf{g}$ in order to result in the final image intensity. The TCC describes the strength of this pairwise interference. The coherent expression for the TCC is the following:

$$T_{cc}^{coh}(\mathbf{g}, \mathbf{g}') \equiv T(\mathbf{g})T^*(\mathbf{g}') = A(\mathbf{g})A(\mathbf{g}')e^{-i[\chi(\mathbf{g})-\chi(\mathbf{g}')]}, \quad (2.40)$$

where $A(\mathbf{g})$ denotes the aperture function defining an outer cut-off value for the reciprocal vectors that are being included, and $\chi(\mathbf{g})$ describes the phase shift of the electron wave in the back focal plane of the objective lens, resulting from the lens aberrations:

$$\chi(\mathbf{g}) = \pi f \lambda g^2 + \frac{\pi}{2} C_s \lambda^3 g^4 + \frac{\pi}{3} C_5 \lambda^5 g^6, \quad (2.41)$$

where f denotes the expected defocus value, C_s the 3rd-order spherical aberration and C_5 the 5th-order spherical aberration.

In practice, however, we need to include the effects of partial coherence now. This means that integration over both spread functions, resulting from the spatial and temporal incoherence effects, have to be included in the expression for the perfectly coherent TCC for thin specimens, given by equation (2.40) [169]:

$$T_{cc}^{pc}(\mathbf{g}, \mathbf{g}') = \iint_{\mathbf{g}_\beta} \int_{\delta_f} p(\mathbf{g}_\beta) p(\delta_f) T_{cc}^{coh}(\mathbf{g} + \mathbf{g}_\beta, \mathbf{g}' + \mathbf{g}_\beta, f + \delta_f) d\mathbf{g}_\beta d\delta_f. \quad (2.42)$$

The image intensity for partially coherent imaging can then be obtained by substituting this expression for the partially coherent TCC in equation (2.39). However, this is not a trivial integral as in practice a large number of defocus values and beam directions have to be included. The integral cannot be solved analytically and numerically it is still very time-consuming. Therefore, it has often been approximated for a *weak* phase object to save computation time and effort.

For a *weak phase object*, in order to obtain an analytical expression for the the partially coherent TCC given by equation (2.42), both spread functions are assumed

to be Gaussian distributions, given by [169]:

$$p(\mathbf{g}_\beta) = \frac{1}{\pi k_\beta^2} e^{-g_\beta^2/k_\beta^2} \quad (2.43)$$

$$p(\delta_f) = \frac{1}{\sqrt{\pi}\Delta} e^{-\delta_f^2/\Delta^2}. \quad (2.44)$$

In these expressions, k_β and Δ are the $1/e$ half-width values of the Gaussian distributions, corresponding to the spread in illumination angles and the defocus spread, respectively. k_β equals β/λ , for β being the beam semi-divergence angle. By considering the spread functions one at a time and using a Taylor expansion for the aberration function $\chi(\mathbf{g})$, the following approximate expression can be found for the microscope's partially coherent TCC [62]:

$$T_{cc}^{pc}(\mathbf{g}, 0) = A(\mathbf{g}) e^{-i\chi(\mathbf{g})} \exp\left[-\frac{(\pi\lambda\Delta)^2}{4u} g^4\right] \exp\left[-\frac{\pi^2\beta^2}{\lambda^2 u} (C_s\lambda^3 g^3 - f\lambda g)^2\right], \quad (2.45)$$

where $u = 1 + (\pi\beta\Delta)^2 g^2$. Although this is an approximated expression, it is very useful to work with since the temporal and spatial envelope functions both appear in the form of multiplicative factors. In order to obtain the full not-approximated expression, we would need to numerically integrate equation (2.35) without applying Taylor expansions for the aberration function. However, since nowadays the values of k_β and Δ are sufficiently small, the approximation is valid for most of the modern microscopes. For the HRTEM simulations in this thesis, the exit wave has been simulated using the STEMsim software developed by Prof. Dr. Andreas Rosenauer [201], which is then combined with the approximated expression (2.45) of the microscope transfer function for partially coherent imaging, to result in the final image intensity.

2.10 Conclusions

In this chapter, the theory of the electron-specimen interaction and the usual approximations to include thermal diffuse scattering are described. The solution of the Schrödinger equation that has been used for the HR(S)TEM image simulations in this thesis, i.e. the multislice method, has been discussed. Also for thin specimens, the weak phase object approximation has been derived and discussed. Both methods will be used in chapter 4 for the estimation of the atomic number in a thin specimen, and the detection and location problem of light elements in a thicker specimen, respectively.

Statistical Experiment Design

3.1 Introduction

The performance of a HR(S)TEM experiment is often evaluated qualitatively, which means in terms of direct visual interpretability. For this purpose, the image contrast and signal-to-noise ratio (SNR) are useful criteria. However, as already mentioned in the introduction of this thesis, electron microscopy has evolved toward a quantitative technique in the last few years, aiming at accurate and precise numbers for the parameters of interest. Therefore, images are interpreted quantitatively, and a measure for the attainable precision is derived using the principles of *statistical experiment design* [129]. These principles may be applied to a wide range of sciences, where unknown parameters need to be measured as precisely as possible from a certain experiment. In this thesis, the experiments are quantitative HR(S)TEM measurements, which may be regarded as a set of observations, characterised by the electron counting results made, for example, with an annular STEM detector or a charged coupled device (CCD) camera in the case of TEM. From those electron counting results, the unknown structure parameters of the object under study have to be determined. In particular, the atom column positions, the chemical composition of the specimen (i.e., the atomic numbers Z) and the number of atoms in a projected atom column, will have to be estimated in this thesis.

Typically, measurements will occur in the presence of fluctuations or noise, which will fundamentally limit the precision with which the unknown parameters can be measured. The goal of statistical experiment design is to derive the particular set of experimental settings that will result in the highest possible precision with which unknown parameters can be determined. These settings will then correspond to the *optimal statistical experiment design*. Using *statistical parameter estimation theory*, these optimal settings can be derived

straightforwardly [60, 141, 144, 148, 150, 160, 207]. Another proposed method to derive the optimal statistical experiment design, makes use of *statistical detection theory* [156–158, 208, 209]. In this case, a statistical estimation problem will be formulated as a hypothesis test in which the hypotheses can correspond, for example, to the different possible atomic numbers Z of a specific projected atom column. Furthermore, statistical detection theory provides the tools to calculate the probability to choose the wrong hypothesis, both for binary and for multiple hypothesis testing. It will then not be the *precision* with which the unknown parameters can be determined that is optimised, but the probability to choose the wrong hypothesis or the so-called *probability of error*. The experiment design for which the precision and/or probability of error is optimal does not necessarily correspond to the experimental settings leading to the highest SNR or the best image contrast. Therefore, optimising the experiment design by means of statistical methods is necessary. Furthermore, statistical experimental design provides the electron microscopist with insight in which precision may be obtained at which microscope settings. In this way, it shows the possible benefit of the optimal settings as compared to the usual settings. The electron microscopist may then decide whether it is advantageous to modify these usual settings or not. Optimising the experiment design is a procedure that consists of different steps.

To start, a *statistical parametric model of the observations* has to be defined. Since the experimental HR(S)TEM image pixel values fluctuate randomly about their expectation values, due to the presence of inherent noise, they can be modelled as stochastic variables. By definition, a stochastic variable is characterised by its *probability (density) function*, whereas a set of stochastic variables is characterised by their *joint probability (density) function* [210]. The joint probability (density) function defines both the expectation values of the observations, and the fluctuations of these observations about their expectation values. The expectation values are being described by a physical expectation model, that is parametric in the unknown structure parameters. In quantitative HR(S)TEM, the expectation model corresponds to the expected number of electron counts in the detected image. It is a physical function of the experimental parameters, which contains the electron-object interaction, the electron transfer in the microscope, and the final image detection. In this thesis, the investigated parameters of the expectation model are the projected atom column positions, the atom type, and the number of atoms in a projected atom column (i.e. the thickness).

When the expectation model of the observations is known, the next step in the procedure of optimising the experiment design, is to specify the optimality criterion. Since the purpose of the experiment is to estimate the unknown parameters with the highest possible precision, the optimality criterion is preferably the precision of the estimated parameters. Precision corresponds to the variance, or the square root of the variance, i.e. the standard deviation, with which structure parameters can be estimated. Therefore, the precision first has to be quantified, which is possible for *continuous* parameters by using statistical parameter estimation theory. The attainable precision can be derived from the parametric statistical model of the observations, that is, the lower bound on the variance with which the unknown parameters can be estimated unbiasedly [148, 162]. It can be shown that the so-called *Cramér-Rao lower bound* (CRLB) is a lower bound for the class of unbiased estimators. An estimator is called *unbiased* if its expectation value is equal to the true parameter value, in other words, an unbiased estimator does not have any systematic error. The CRLB is a function of the experimental settings, and therefore, the lower bound on the variance of each unknown parameter could be considered as optimality criterion to be minimised. However, simultaneous minimisation of the set of lower bounds corresponding to the entire set of unknown parameters is usually impossible. Therefore, an appropriate scalar measure, that is, a function of the matrix elements of the CRLB, has to be chosen as optimality criterion according to the experimenter's specific purpose [154]. An overview of different possible scalar measures is given in [152]. For an electron microscopist, a specific purpose might be to measure the atom column positions as precisely as possible, irrespective of the precision of the object thickness or of the atom numbers. Thus, a possible optimality criterion is the sum of the lower bounds on the variance of the position coordinates.

In the case where the estimated parameter is *discrete*, such as, the atom type or the number of atoms in a projected atom column, statistical detection theory allows the derivation of the probability of error, which can then be used as optimality criterion, instead of the attainable precision. This approach has first been proposed in [157] to be further worked out for different research goals in [158, 208, 209]. The probability of error itself does not provide us knowledge on the attainable precision, but gives a way to derive those experimental settings for which it is most probable that the unknown parameter is being determined correctly.

In a final step to optimise the experiment design, the chosen optimality criterion has to be computed and evaluated for a whole range of different experimental parameters, which can be done by performing HR(S)TEM image simulations under different imaging settings.

The organisation of this chapter is as follows. In section 3.2, the parametric statistical model of the observations is derived, and the derivation of the attainable precision from such a model is given by the Cramér-Rao lower bound which is derived in section 3.3. The maximum likelihood estimator, that achieves the Cramér-Rao lower bound asymptotically, that is, for an increasing number of observations, is here also discussed in section 3.4. In section 3.5, the concept of statistical detection theory is explained and discussed as a quantitative tool to optimise the experiment design for discrete estimation problems, and finally in section 3.6 conclusions are drawn.

3.2 Parametric statistical model of the observations

Every HR(S)TEM experiment will contain certain inherent fluctuations. Therefore, different sets of pixel observations will always slightly differ, although they are made under the same imaging conditions. To describe this stochastic behaviour, we can model the observations as stochastic variables. A set of pixel observations can be represented by a column vector of length $K \times L$:

$$\mathbf{w} = (w_{kl} | k = 1 \dots K; l = 1 \dots L)^T. \quad (3.1)$$

The index kl refers to the x - and y -coordinates (x_k, y_l) of a set of $K \times L$ pixel observations, which corresponds to the position of the probe in the case of HRSTEM. In the case of HRTEM, the index kl refers to the position $(x_k, y_l) \equiv (x_1 + (k-1)\Delta x, y_1 + (l-1)\Delta y)$ of the recorded image, with $k = 1, \dots, K$ and $l = 1, \dots, L$ and (x_1, y_1) represents the pixel in the bottom left corner of the field of view (FOV). Each set of observations is, by definition, characterised by its joint probability (density) function (P(D)F) [148]:

$$p(\boldsymbol{\omega}) = p(\omega_{kl} | k = 1 \dots K; l = 1 \dots L). \quad (3.2)$$

This joint probability (density) function describes the probability for a set of given observations which are modelled as stochastic variables $\boldsymbol{\omega}$. The expectation value and variance of a continuous stochastic variable are defined by the joint probabil-

ity density function:

$$\mu = \mathbb{E}(\omega) = \int_{-\infty}^{+\infty} \omega p(\omega) d\omega, \quad (3.3)$$

$$\sigma^2 = \text{var}(\omega) = \mathbb{E}[(\omega - \mu)^2] = \int_{-\infty}^{+\infty} (\omega - \mu)^2 p(\omega) d\omega \quad (3.4)$$

For discrete variables, the integration needs to be replaced by a summation. The expectations of the observations are described by the *expectation model*, which is a function of the unknown parameters that have to be measured. In this thesis, the parameters that are estimated are the atom types that are present (or absent) in the structure, the position coordinates of the projected atom columns, and the number of atoms in the projected atom columns. The set of unknown parameters are represented by the $(R \times 1)$ -column vector θ containing the r unknown parameters to be measured. The expectation value of the pixel (k, l) is then given by:

$$\mathbb{E}(\omega_{kl}) = \lambda_{kl}(x_k, y_l; \theta) = \lambda_{kl}, \quad (3.5)$$

For HR(S)TEM images, the observation at the pixel (k, l) is denoted as w_{kl} . When assuming that the HR(S)TEM observations are statistically independent electron counting results, they can be accurately modelled as Poisson distributed random variables [210, 211]:

$$\frac{\lambda_{kl}^{\omega_{kl}}}{\omega_{kl}!} \exp(-\lambda_{kl}). \quad (3.6)$$

For a Poisson distributed random variable, the expected value equals the variance:

$$\mathbb{E}(\omega_{kl}) = \text{var}(\omega_{kl}) = \lambda_{kl}, \quad (3.7)$$

Assuming that the pixel observations in a HR(S)TEM image are statistically independent, the joint probability function of a set of pixel observations which are modelled as Poisson distributed random variables, equals the product of the probabilities given by equation (3.6):

$$p(\omega) = \prod_{k=1}^K \prod_{l=1}^L \frac{\lambda_{kl}^{\omega_{kl}}}{\omega_{kl}!} \exp(-\lambda_{kl}). \quad (3.8)$$

In sections 5.4 and 6.3, in the comparison between the performance of both imaging modes, HRTEM and HRSTEM, the incoming electron dose, $N(e^-/\text{\AA}^2)$, will be kept the same as both imaging modes are bound by the same physical constraint

of radiation sensitivity. Certainly in the case of beam-sensitive specimens, the dose is a critical parameter that limits the performance of both imaging modes, in order to determine unknown structure parameters. In HRSTEM, the incoming electron dose per probe position corresponds to $D_{STEM} = N \cdot \Delta x \Delta y$ with $\Delta x \Delta y$ the pixel area, while in HRTEM, the total number of incident electrons is $D_{TEM} = N \cdot FOV$ with FOV the field of view. The expectation values for the pixel intensities are therefore given by

$$\begin{aligned} \lambda_{kl}^{TEM} &= p_{kl,TEM} \cdot D_{TEM} \quad \text{and} \\ \lambda_{kl}^{STEM} &= p_{kl,STEM} \cdot D_{STEM} \quad \text{respectively,} \end{aligned} \quad (3.9)$$

with

$$\begin{aligned} p_{kl,TEM} &= \frac{f_{kl}(\boldsymbol{\theta})}{\sum_{k=1}^K \sum_{l=1}^L f_{kl}(\boldsymbol{\theta})} \quad \text{and} \\ p_{kl,STEM} &= f_{kl}(\boldsymbol{\theta}), \end{aligned} \quad (3.10)$$

corresponding to the probability that an electron hits a pixel with coordinates (x_k, y_l) in a HRTEM or HRSTEM experiment, respectively. In these expressions, f_{kl} is the fraction of detected intensity at pixel (k, l) which can be obtained using software that allows one to simulate (S)TEM images. In this work, the STEMsim software developed by Prof. Dr. A. Rosenauer was used [201].

3.2.1 Parametric statistical model for a weak phase object

The weak phase object approximation has been discussed in chapter 2, and will be used in chapter 4 for the estimation of the atomic number of a single isolated atom in HRSTEM. Here, the analytic expression for the expectation model that is used for this estimation problem, under the weak phase object approximation, will be derived.

In the case of HRSTEM, the exit wave $\Psi(\mathbf{R})$ is modulated by the probe function $p(\mathbf{R})$, yielding:

$$\Psi(\mathbf{R}) = (1 + i\sigma v_z(\mathbf{R}))p(\mathbf{R} - \mathbf{R}_0), \quad (3.11)$$

with \mathbf{R}_0 corresponding to the probe position and \mathbf{R} a two-dimensional coordinate vector. In the detector plane, the Fourier transform of the exit wave equals:

$$\Psi(\mathbf{g}) = P(\mathbf{g})e^{2\pi i \mathbf{g} \cdot \mathbf{R}_0} + i\sigma V(\mathbf{g}) \otimes P(\mathbf{g})e^{2\pi i \mathbf{g} \cdot \mathbf{R}_0}, \quad (3.12)$$

in which \mathbf{g} is a two-dimensional vector in Fourier space, $V(\mathbf{g})$ equals the Fourier transformed projected potential $v_z(\mathbf{R})$ and $P(\mathbf{g})$ equals the Fourier transformed probe function $p(\mathbf{r})$. The intensity that is then detected is given by the square modulus of the exit wave:

$$|\Psi(\mathbf{g})|^2 = |P(\mathbf{g})|^2 + \sigma^2 |V(\mathbf{g}) \otimes P(\mathbf{g}) e^{2\pi i \mathbf{g} \cdot \mathbf{R}_0}|^2 + \text{linear terms.} \quad (3.13)$$

The integrated intensity over the detector $D(\mathbf{g})$, for the electron probe at position \mathbf{R}_0 is calculated as follows:

$$I(\mathbf{R}_0) = \int |\Psi(\mathbf{g})|^2 D(\mathbf{g}) d\mathbf{g}. \quad (3.14)$$

The detector function $D(\mathbf{g})$ is assumed to be equal to one in the detected field and to zero elsewhere. The fraction of detected intensity with respect to the incoming electron beam equals:

$$f(\mathbf{R}_0) = \frac{I(\mathbf{R}_0)}{\int |\Psi(\mathbf{g})|^2 d\mathbf{g}}, \quad (3.15)$$

where the normalisation factor corresponds to the integrated intensity over the whole detector range ($D(\mathbf{g}) = 1$). The number of expected electrons at probe position $\mathbf{R}_0 = (x_k, y_l)$ is then given by the expectation value λ_{kl} :

$$\lambda_{kl} = \lambda(\mathbf{R}_0) = D_{STEM} f(\mathbf{R}_0), \quad (3.16)$$

for D_{STEM} the number of incident electrons per probe position. This expectation model of the observations depends on the atomic number Z through the projected atomic potential. For the estimation of the atomic number of a single isolated atom in HRSTEM in chapter 4, the following parametrised expression of the projected atomic potential was used [169]:

$$\begin{aligned} v_z(\mathbf{R}) = v_z(x, y) &= \int_{-\infty}^{+\infty} V(x, y, z) dz \\ &= 4\pi^2 a_0 e \sum_{i=1}^3 a_i K_0(2\pi R \sqrt{b_i}) + 2\pi^2 a_0 e \sum_i \frac{c_i}{d_i} \exp(-\pi^2 R^2 / d_i), \end{aligned} \quad (3.17)$$

with $R^2 = \sqrt{x^2 + y^2}$, $V(x, y, z)$ equals the single isolated atom's potential and $K_0(x)$ the modified Bessel function of zeroth order, a_0 the Bohr Radius, and a_i, b_i, c_i and d_i form a set of 12 parameters for every atomic number Z , parametrising the

projected atomic potential.

The probe function in equation (3.13) is defined as follows:

$$P(\mathbf{g}) = A(\mathbf{g})e^{-i\chi(\mathbf{g})}, \quad (3.18)$$

where $A(\mathbf{g})$ denotes the aperture function defining an outer cut-off value for the reciprocal vectors that are being included, and $\chi(\mathbf{g})$ describes the phase shift of the electron wave in the back focal plane of the objective lens, resulting from the lens aberrations, which is defined in equation (2.41).

3.3 Attainable precision

In this section, the Fisher information matrix and the attainable precision for the estimation of continuous structure parameters, given by the CRLB, will be derived from the parametrised probability function of the observations. For more detailed information about these concepts, the reader is referred to [148,162,163].

3.3.1 Fisher information

Consider $p(\boldsymbol{\omega}; \boldsymbol{\theta})$, the joint probability (density) function of a set of observations $\mathbf{w} = (w_{kl}|k = 1 \dots K; l = 1 \dots L)^T$. An example of this function is given by equation (3.8) for the pixel intensities in a HR(S)TEM image. The so-called *Fisher information matrix* measuring the amount of information that an observable random variable carries about an unknown parameter vector $\boldsymbol{\theta} \in \mathbb{R}^R$, can then be defined as follows:

$$F = -\mathbb{E} \left[\frac{\partial^2 \ln p(\boldsymbol{\omega}; \boldsymbol{\theta})}{\partial \boldsymbol{\theta} \partial \boldsymbol{\theta}^T} \right], \quad (3.19)$$

which is an $(R \times R)$ -matrix. The expression between square brackets gives the Hessian matrix of the logarithm of the joint probability (density) function of which the (r, s) th element is given by $\partial^2 \ln p(\boldsymbol{\omega}; \boldsymbol{\theta}) / \partial \theta_r \partial \theta_s$.

The Fisher information represents the expected value of the observed information and is defined as the variance of the so-called score function, i.e. the derivative of the log-likelihood function with respect to the unknown parameters. In this way it is a measure for the physical fluctuations of the stochastic observations.

For the pixel intensities in a HR(S)TEM image, it follows from equations (3.7) and

(3.8), that the (r, s) th element of the Fisher information matrix reduces to:

$$F_{rs} = \sum_k \sum_l \frac{1}{\lambda_{kl}} \frac{\partial \lambda_{kl}}{\partial \theta_r} \frac{\partial \lambda_{kl}}{\partial \theta_s}, \quad (3.20)$$

where the parameter λ_{kl} is defined in equation (3.9) for both HRTEM and HRSTEM.

3.3.2 Cramér-Rao Lower Bound

Use of the concept of Fisher information allows one to determine the highest precision, that is, the lowest variance, with which a parameter can be estimated unbiasedly. It is proven that for the class of unbiased estimators, the ultimate precision is given by a lower bound on their variance, the CRLB [148, 163–165]. Suppose that $\widehat{\boldsymbol{\theta}}$ is any unbiased estimator of $\boldsymbol{\theta}$, that is, $\mathbb{E}[\widehat{\boldsymbol{\theta}}] = \boldsymbol{\theta}$. Then it can be shown [162] that under general conditions the covariance matrix $\text{cov}(\widehat{\boldsymbol{\theta}})$ of $\widehat{\boldsymbol{\theta}}$ satisfies

$$\text{cov}(\widehat{\boldsymbol{\theta}}) \geq F^{-1}, \quad (3.21)$$

so that $\text{cov}(\widehat{\boldsymbol{\theta}}) - F^{-1}$ is positive semi-definite and consequently its diagonal elements cannot be negative. This means that the diagonal elements of $\text{cov}(\widehat{\boldsymbol{\theta}})$, that is, the actual variances of $\widehat{\theta}_1, \dots, \widehat{\theta}_R$ are larger than or equal to the corresponding diagonal elements of F^{-1} :

$$\text{var}(\widehat{\theta}_r) \geq [F^{-1}]_{rr}, \quad (3.22)$$

where $r \in \{1, \dots, R\}$, with R the number of components of $\widehat{\boldsymbol{\theta}}$ and $[F^{-1}]_{rr}$ the r th diagonal element of the inverse of the Fisher information matrix. In this sense, F^{-1} represents a lower bound for the variances of all unbiased estimators $\widehat{\boldsymbol{\theta}}$. The matrix F^{-1} is called the *Cramér-Rao lower bound* on the variance of $\widehat{\boldsymbol{\theta}}$.

The CRLB can be generalised in order to include unbiased estimators of column vectors of functions of the parameters, instead of the proper parameters. Let $\boldsymbol{\gamma}(\boldsymbol{\theta})$ be the $(Q \times 1)$ -column vector $(\gamma_1(\boldsymbol{\theta}), \dots, \gamma_Q(\boldsymbol{\theta}))^T$ of functions of the proper $(R \times 1)$ -parameter vector $\boldsymbol{\theta}$, and let $\widehat{\boldsymbol{\gamma}}$ be an unbiased estimator of $\boldsymbol{\gamma}(\boldsymbol{\theta})$. Then, it can be shown that [162]

$$\text{cov}(\widehat{\boldsymbol{\gamma}}) \geq \frac{\partial \boldsymbol{\gamma}}{\partial \boldsymbol{\theta}^T} F^{-1} \frac{\partial \boldsymbol{\gamma}^T}{\partial \boldsymbol{\theta}}, \quad (3.23)$$

where $\frac{\partial \boldsymbol{\gamma}}{\partial \boldsymbol{\theta}^T}$ is the $(Q \times R)$ -Jacobian matrix, whose (qr) th element is given by $\partial \gamma_q / \partial \theta_r$.

3.3.3 Hammersley-Chapman-Robbins Bound

An alternative measure for the attainable precision may be given by the so-called *Hammersley-Chapman-Robbins bound*, which is a generalisation of the Cramér-Rao lower bound in the sense that it is both tighter and does not require regularity assumptions, such as, the probability (density) function of the observations to be differentiable [212, 213]. Therefore, it is applicable to a wider range of problems as compared to the Cramér-Rao lower bound. However, it is often much more complicated to compute.

Suppose that $\widehat{\delta}$ is any unbiased estimator of an arbitrary scalar function $g : \mathbb{R}^n \rightarrow \mathbb{R}$ of $\boldsymbol{\theta}$, i.e. $\mathbb{E}[\widehat{\delta}] = g(\boldsymbol{\theta})$ for all $\boldsymbol{\theta}$. The Hammersley-Chapman-Robbins bound is then defined as [213]:

$$\text{var}(\widehat{\delta}) \geq \sup_{\Delta} \frac{(g(\boldsymbol{\theta} + \Delta) - g(\boldsymbol{\theta}))^2}{\mathbb{E}\left[\frac{p(\boldsymbol{\omega}; \boldsymbol{\theta} + \Delta)}{p(\boldsymbol{\omega}; \boldsymbol{\theta})} - 1\right]^2}. \quad (3.24)$$

It has been shown that the Hammersley-Chapman-Robbins bound is applicable in many cases, where the Cramér-Rao lower bound is inapplicable [214]. Besides, it is also applicable in cases that satisfy the Cramér-Rao inequality. Chapman and Robbins have shown in 1951 [213] that their lower bound is at least as tight as the Cramér-Rao lower bound, for all $\boldsymbol{\theta}$. An elaborate effort has been made to compute the Hammersley-Chapman-Robbins bound for the discrete estimation problem of distinguishing between two different atom types under the weak phase object approximation. However, since the implementation of this lower bound is not straightforward and did not lead to consistent results, a different approach was proposed for discrete estimation problems using statistical detection theory, which is introduced in section 3.5.

3.4 Maximum Likelihood estimator

In the previous section, the concept of Fisher information and the CRLB have been introduced. The meaning of this CRLB is as follows. In general, different estimators may be used to estimate unknown parameters. An estimator is a function of the stochastic observations and therefore a stochastic variable itself. Therefore, its precision is represented by its variance (or by its standard deviation, which equals the square root of the variance). In the previous subsection,

it is already mentioned that the variance of the class of unbiased estimators will never be lower than the CRLB. It can be shown that there exists an estimator that achieves the CRLB at least asymptotically, that is, for an increasing number of observations. This estimator is the Maximum Likelihood (ML) estimator [157]. In electron microscopy, the number of observations is usually sufficiently large for the asymptotic properties of the ML estimator to apply, and the use of this estimator is therefore highly recommended in quantitative electron microscopy [144]. Furthermore, the existence of the ML estimator justifies the choice of the CRLB as optimality criterion.

The ML estimates are obtained by following the next steps:

1. The probability (density) function $p(\boldsymbol{\omega}, \boldsymbol{\theta})$ depends through the expectation model $f(\boldsymbol{\theta})$ on the unknown parameters $\boldsymbol{\theta}$, like e.g. in equation (3.8). In this P(D)F, the independent variables $\boldsymbol{\omega} = (\omega_{kl} | k = 1 \dots K; l = 1 \dots L)^T$ are first replaced by the available observations $\mathbf{w} = (w_{kl} | k = 1 \dots K; l = 1 \dots L)^T$, in order to obtain

$$p(\mathbf{w}, \boldsymbol{\theta}). \quad (3.25)$$

2. Then, the hypothetical true parameters $\boldsymbol{\theta} = (\theta_1 \dots \theta_R)^T$ are replaced by the independent variables $\mathbf{t} = (t_1 \dots t_R)^T$. The logarithm of the resulting function is called the *log-likelihood function*:

$$\ln L(\mathbf{t}) := \ln p(\mathbf{w}, \mathbf{t}), \quad (3.26)$$

with $L(\mathbf{t})$ being the likelihood function.

3. The ML estimates $\widehat{\boldsymbol{\theta}}_{ML}$ of the elements of the parameter vector $\boldsymbol{\theta}$, are then defined by the values of the elements of \mathbf{t} that maximise $L(\mathbf{t})$:

$$\widehat{\boldsymbol{\theta}}_{ML} = \arg \max_{\mathbf{t}} L(\mathbf{t}) = \arg \max_{\mathbf{t}} \ln L(\mathbf{t}). \quad (3.27)$$

The joint probability (density) function evaluated at the maximum likelihood estimates $p(\mathbf{w}, \widehat{\boldsymbol{\theta}}_{ML})$ generates the observations with a larger probability than if it would be evaluated at any other set of parameters $p(\mathbf{w}, \mathbf{t})$ [215].

The ML estimator has some interesting properties, of which the most important ones are the following [148]:

- *Consistency*: The ML estimator is consistent in the sense that it converges toward the true value of the parameters for an increasing number of observations.
- *Asymptotic normality*: For an increasing number of observations, the P(D)F of the ML estimator asymptotically tends to a normal distribution, having the parameters θ as expectation values (i.e. mean values) and the CRLB as its covariance matrix.
- *Asymptotic efficiency*: For an increasing number of observations, the CRLB is achieved by the ML estimator, meaning that its covariance matrix asymptotically equals the CRLB. In this sense, the ML estimator is most precise.
- *Invariance property*: If $\widehat{\theta}_{ML}$ are the ML estimates for the elements of the parameter vector θ , and $\gamma(\theta)$ is a vector of functions of θ , then the ML estimates of $\gamma(\theta)$ are given by $\widehat{\gamma}_{ML}(\theta) = \gamma(\widehat{\theta}_{ML}) = (\gamma_1(\widehat{\theta}_{ML}), \dots, \gamma_Q(\widehat{\theta}_{ML}))^T$.

3.4.1 The uniformly weighted least squares estimator

In HR(S)TEM, the pixel observations are assumed to be statistically independent electron counting results and therefore, they can be modelled as a Poisson distribution. For an increasing number of expected electron counts per pixel, i.e. an increasing expectation value $\mathbb{E}[\omega_{kl}] = \lambda_{kl}$, the Poisson distribution tends to a normal distribution with both expectation value $\mathbb{E}[\omega_{kl}] = f_{kl}(\theta)$ and variance $\text{var}(\omega_{kl})$ equal to λ_{kl} of the Poisson distribution [216]. This approximation is valid if the number of observations is large as compared to the square root of this number [217]. Moreover, if the contrast in the images is low, the deviations of the observations from their expectations may be supposed to be identically distributed, i.e. $\text{var}(\omega_{kl}) = \sigma_{kl}^2 \approx \sigma^2 = \text{cte}$ [218]. Under these conditions, the joint probability density function of the observations equals:

$$p(\omega, \theta) = \prod_{k=1}^K \prod_{l=1}^L \frac{1}{\sqrt{2\pi}\sigma} \exp\left(-\frac{(\omega_{kl} - f_{kl}(\theta))^2}{2\sigma^2}\right). \quad (3.28)$$

The log-likelihood function can be derived from this joint probability density function:

$$\ln L(\mathbf{t}) = -\frac{N}{2} \ln 2\pi - N \ln \sigma - \frac{1}{2} \sum_{k=1}^K \sum_{l=1}^L \left(-\frac{\omega_{kl} - f_{kl}(\mathbf{t})}{\sigma}\right)^2. \quad (3.29)$$

The ML estimates for the statistically independent and identically normally distributed observations are then given by:

$$\hat{\boldsymbol{\theta}}_{ML} = \arg \max_{\boldsymbol{t}} \ln L(\boldsymbol{t}) = \arg \min_{\boldsymbol{t}} \sum_{k=1}^K \sum_{l=1}^L (w_{kl} - f_{kl}(\boldsymbol{t}))^2. \quad (3.30)$$

The right-hand side of equation 3.30 are the uniformly weighted *least squares (LS) estimates*, $\hat{\boldsymbol{\theta}}_{LS}$ of the unknown parameters $\boldsymbol{\theta}$. As we may assume that the conditions in HR(S)TEM are appropriate to consider the pixel observations to be independent and identically normally distributed, we will use the least squares estimator in this thesis in order to estimate unknown structure parameters. In [147], it is shown that even for a very low incoming electron dose the parameters of interest are obtained with the highest possible precision when using the uniformly weighted least squares estimator as implemented in the efficient model estimation algorithm of StatSTEM [147]. Therefore, implementation of the maximum likelihood estimator would have no extra benefit. In particular in chapter 7, the LS estimator is used to estimate the atom column positions in several experimental applications.

3.4.2 Maximum likelihood estimation of atomic numbers

As a second example, we consider the identification (i.e. estimation) of the atomic number Z of a single atom from a HRSTEM image. As shown in section 3.2, the joint PF for such an experiment is given by equation (3.8) where the expectations are described by equation (3.16). In this example, the unknown parameter θ is given by the atomic number Z . Following equation (3.27), the ML estimator is then given by:

$$\hat{Z}_{ML} = \arg \max_Z \ln L(\boldsymbol{t}; Z) = \arg \max_Z \sum_k \sum_l [w_{kl} \ln f_{kl}(Z) - f_{kl}(Z)]. \quad (3.31)$$

As compared to the example discussed in section 3.4.1, the ML estimator \hat{Z}_{ML} can be computed straightforwardly given the discrete nature of the atomic number and the fact that only one parameter is estimated in this example. For that reason, it does not require advanced computing algorithms.

3.5 Statistical detection theory

Statistical detection theory provides the tools to optimise the experiment design by approaching a discrete estimation problem as a statistical hypothesis test [156]. This can be either a binary or multiple hypothesis test, in which every hypothesis corresponds, for example, to a specific atomic number Z or a specific number of atoms in a projected atom column.

The probability to decide the wrong hypothesis, the so-called *probability of error* can be defined and decision rules are determined in such a way, that the probability of error is minimised. In order to optimise the experiment design when measuring discrete parameters, such as, the presence or absence of a specific projected atom column, or the number of atoms in a projected atom column, this probability of error may be used as optimality criterion, by computing it as a function of the experimental settings. The optimal experiment design then corresponds to those experimental settings that result in the lowest probability of error. In contrast to the CRLB, the minimum probability of error does not provide us the value for the attainable precision of the estimated parameter. Nevertheless, it will correspond to the optimal statistical experiment design for which, under the followed assumptions, the unknown parameter is expected to be estimated correctly with the highest probability. In the following, the theory of binary and multiple hypothesis testing will be derived for the investigated purposes in this thesis, i.e. deciding between two different atomic numbers, detecting light elements, and counting the number of atoms in a projected atom column. Different parts of these results have been published in [157–159, 208, 209].

3.5.1 Binary hypothesis testing

A binary hypothesis test is used for three different research goals in this thesis: In the case where we want to decide between two different atom types, if we want to detect a light atom or atom column, or if we want to know whether there are n or $n+1$ atoms in a projected atom column. In these cases, the estimation problem can be described as a binary hypothesis test, in which the hypotheses are respectively given by:

$$\begin{array}{lll} (a) \mathcal{H}_0 : Z = Z_0 & (b) \mathcal{H}_0 : Z = Z_0 & (c) \mathcal{H}_0 : n_{\mathcal{H}_0} = n \\ \mathcal{H}_1 : Z = Z_1 & \mathcal{H}_1 : Z \in \emptyset & \mathcal{H}_1 : n_{\mathcal{H}_1} = n + 1 \end{array} \quad (3.32)$$

where \mathcal{H}_0 is referred to as the null hypothesis and \mathcal{H}_1 as the alternative hypothesis. In case (a), both hypotheses correspond to two different possible atomic numbers, Z_0 and Z_1 , in (b), the hypotheses correspond to whether the light atom is present or absent, and in (c), the hypotheses correspond to two succeeding numbers of atoms in a projected atom column.

It is assumed in the considered binary hypothesis tests, that a priori knowledge assures that only \mathcal{H}_0 or \mathcal{H}_1 is possible, so that one of both hypotheses is always correct. In order to express a prior belief in the likelihood of the hypotheses, the prior probabilities $P(\mathcal{H}_0)$ and $P(\mathcal{H}_1)$ associated with these hypotheses are assumed to be known, with $P(\mathcal{H}_0) + P(\mathcal{H}_1) = 1$. If both hypotheses are equally likely, then it is reasonable to assign equal prior probabilities of $1/2$. In a quantitative approach, the goal is now to minimise the probability of assigning the wrong hypothesis. In a so-called Bayesian approach, this *probability of error* P_e is defined as:

$$\begin{aligned} P_e &= \Pr\{\text{decide } \mathcal{H}_0, \mathcal{H}_1 \text{ true}\} + \Pr\{\text{decide } \mathcal{H}_1, \mathcal{H}_0 \text{ true}\} \\ &= P(\mathcal{H}_0|\mathcal{H}_1)P(\mathcal{H}_1) + P(\mathcal{H}_1|\mathcal{H}_0)P(\mathcal{H}_0) \end{aligned} \quad (3.33)$$

with $P(\mathcal{H}_i|\mathcal{H}_j)$ the conditional probability of deciding \mathcal{H}_i while \mathcal{H}_j is true. Using criterion (3.33), the two possible errors are weighted appropriately to yield an overall error measure. Decision rules are now defined such that the probability of error is minimised. It is shown in [156] that one therefore should decide \mathcal{H}_1 if

$$\frac{p(\mathbf{w}; \mathcal{H}_1)}{p(\mathbf{w}; \mathcal{H}_0)} > \frac{P(\mathcal{H}_0)}{P(\mathcal{H}_1)} = \gamma, \quad (3.34)$$

otherwise \mathcal{H}_0 is decided. In this expression, $p(\mathbf{w}; \mathcal{H}_i)$ is the conditional (joint) probability function $p(\omega; \mathcal{H}_i)$ assuming \mathcal{H}_i to be true, evaluated at the available observations \mathbf{w} . For equal prior probabilities of $1/2$, it is clear that γ in equation (3.34) corresponds to 1. Then, we decide \mathcal{H}_1 if

$$LR(\mathbf{w}) = \frac{p(\mathbf{w}; \mathcal{H}_1)}{p(\mathbf{w}; \mathcal{H}_0)} > 1. \quad (3.35)$$

The function $LR(\mathbf{w})$ is called the likelihood ratio since it indicates for each set of observations \mathbf{w} the likelihood of \mathcal{H}_1 versus the likelihood of \mathcal{H}_0 . This test is therefore also known as the likelihood ratio test. Similarly, decision rule (3.35) corresponds to deciding \mathcal{H}_1 if

$$\ln LR(\mathbf{w}) = \ln p(\mathbf{w}; \mathcal{H}_1) - \ln p(\mathbf{w}; \mathcal{H}_0) > 0. \quad (3.36)$$

Otherwise \mathcal{H}_0 is decided. Following section 3.4, this corresponds to choosing the hypothesis for which the log-likelihood function is maximal. The left-hand side of equation (3.36) is termed the log-likelihood ratio.

The expression for the conditional (joint) probability function depends on the measure that is used to estimate the unknown structure parameters. Three different measures will be compared, i.e., peak intensities (PI), scattering cross-sections (SCS) and all HR(S)TEM image intensities on a pixel by pixel basis. The stochastic variable ω takes a different form for these three performance measures:

$$\begin{aligned} \omega^{\text{Im}} &= [\omega_{11}, \omega_{12}, \omega_{21}, \dots, \omega_{KL}]^T && \text{for (S)TEM images,} \\ \omega^{\text{CS}} &= \sum_{k=1}^K \sum_{l=1}^L \omega_{kl} \cdot \Delta x^2 && \text{for SCSs in STEM,} \\ \omega^{\text{PI}} &&& \text{for PIs,} \end{aligned} \tag{3.37}$$

where ω_{kl} corresponds to the variables describing the pixel intensities of the HR(S)TEM image of the atomic column, Δx equals the pixel size, and ω^{PI} corresponds to the variable describing the pixel intensity at the position of the atomic column. The index kl refers to the x - and y -coordinates $(x_k, y_l)^T$ of a set of KL pixel observations. In the case of HRSTEM, the index kl corresponds to the position of the probe, while in the case of HRTEM, this refers to the position $(x_k, y_l) \equiv (x_1 + (k-1)\Delta x, y_1 + (l-1)\Delta y)$ of the recorded image, with $k = 1, \dots, K$ and $l = 1, \dots, L$ and (x_1, y_1) represents the pixel in the bottom left corner of the field of view (FOV). Based on the definition of ω^{PI} , it is clear that when using PIs one only takes the information of a single pixel into account. On the other hand, the detailed profiles of the images of atomic columns are represented in the multi-dimensional variable ω^{Im} . The scattering cross-section sums the pixel values in a Voronoi cell in the image, which are contained in ω^{Im} , into a single number, as defined by ω^{CS} in equation (3.37). The computation of the probability of error for a binary hypothesis test will now be given for these three performance measures. For the results presented in chapters 4 and 5, only ω^{Im} , i.e. all pixel values in the HR(S)TEM images are used, while in chapter 6 the three different measures are compared.

Peak intensities

As mentioned before, it is known that the pixel observations in a HR(S)TEM image can be considered as statistically independent electron counting results, which can therefore be modelled as a Poisson distribution. The conditional probability function for the pixel intensity at the position of a projected atom column, i.e. the peak intensity, is thus given by:

$$p(\omega^{\text{PI}}; \mathcal{H}_i) = \frac{(\lambda_{\mathcal{H}_i}^{\text{PI}})^{\omega^{\text{PI}}}}{\omega^{\text{PI}}!} \exp(-\lambda_{\mathcal{H}_i}^{\text{PI}}), \quad (3.38)$$

where $\lambda_{\mathcal{H}_i}^{\text{PI}} = \mathbb{E}_{\mathcal{H}_i}[\omega^{\text{PI}}]$ corresponds to the expectation value for the pixel intensity of the HR(S)TEM image at the position of the projected atom column. Since this expectation value depends on which hypothesis \mathcal{H}_i is assumed to be true, also the probability function depends on \mathcal{H}_i . In general, this expectation value can be computed under each hypothesis using software that allows one to simulate a STEM image for a given input material's structure and a given set of microscope parameters [201, 219]. Following the decision rule given in equation (3.34), for equal prior probabilities $P(\mathcal{H}_0) = P(\mathcal{H}_1) = 1/2$, we decide \mathcal{H}_1 for an observation w^{PI} , if:

$$p(w^{\text{PI}}; \mathcal{H}_1) > p(w^{\text{PI}}; \mathcal{H}_0) \quad (3.39)$$

otherwise \mathcal{H}_0 is decided. The probability of error can then analytically be computed using the cumulative distribution function of the Poisson distribution [208]:

$$\begin{aligned} P_e &= \frac{1}{2}P(\mathcal{H}_0|\mathcal{H}_1) + \frac{1}{2}P(\mathcal{H}_1|\mathcal{H}_0) \\ &= \frac{1}{2}F(x^{\text{PI}}; \lambda_{\mathcal{H}_1}^{\text{PI}}) + \frac{1}{2}[1 - F(x^{\text{PI}}; \lambda_{\mathcal{H}_0}^{\text{PI}})] \end{aligned} \quad (3.40)$$

where $F(x^{\text{PI}}; \lambda_{\mathcal{H}_i}^{\text{PI}})$ equals the Poisson cumulative distribution function with parameter $\lambda_{\mathcal{H}_i}^{\text{PI}}$ evaluated at the intersection value x^{PI} , between the two conditional distribution functions $p(w^{\text{PI}}; \mathcal{H}_0)$ and $p(w^{\text{PI}}; \mathcal{H}_1)$, which is given by:

$$x^{\text{PI}} = \frac{\lambda_{\mathcal{H}_0}^{\text{PI}} - \lambda_{\mathcal{H}_1}^{\text{PI}}}{\ln \frac{\lambda_{\mathcal{H}_0}^{\text{PI}}}{\lambda_{\mathcal{H}_1}^{\text{PI}}}}. \quad (3.41)$$

Scattering cross-sections

As a second measure, next to the peak intensities, one can also use scattering cross-sections in the case of HRSTEM to optimise the experiment design. The scattering cross-section values are computed as follows (equation (3.37)) [220]:

$$\omega^{\text{CS}} = \sum_{k=1}^K \sum_{l=1}^L \omega_{kl} \cdot \Delta x^2 \quad (3.42)$$

The integration area for the computation of the scattering cross-sections can be defined using Voronoi cells. A Voronoi cell of an atomic column is the cell formed by the perpendicular bisectors of the direct connections to the neighbouring columns. Here, the atom column positions are assumed to be known, therefore, this definition of the scattering cross-sections is used for simplicity as they can be calculated directly from the simulated HRSTEM images in this way. In the case of (HA)ADF STEM, a parametric model consisting of Gaussian peaks at the atomic column positions is used to describe the pixel intensities in the case of HRSTEM [75–77]. The scattering cross-section then corresponds to the volume under the estimated Gaussian peak. These volumes are equivalent to the computed values from the integration of the Voronoi cells. However, the use of the volumes provides some extra advantages, since the parametric model takes into account overlap between neighbouring atom columns [147].

The expected scattering cross-section value equals:

$$\mathbb{E}_{\mathcal{H}_i}[\omega^{\text{CS}}] = \sum_{k=1}^K \sum_{l=1}^L \lambda_{\mathcal{H}_i,kl} \cdot \Delta x^2 = CS_n \quad (3.43)$$

where $\lambda_{\mathcal{H}_i,kl} = \mathbb{E}_{\mathcal{H}_i}[\omega_{kl}]$ corresponds to the expectation values for the pixel intensities of the HR(S)TEM image of the atom column and CS_n is the expected scattering cross-section for n atoms. A sum of independent Poisson distributed variables is known to be Poisson distributed [216], and thus, the variable

$$\sum_{k=1}^K \sum_{l=1}^L \omega_{kl} \quad (3.44)$$

is also Poisson distributed. The conditional probability distribution for a scattering cross-section taking into account the constant factor Δx^2 , then equals [147]:

$$p(\omega^{\text{CS}}; \mathcal{H}_i) = \frac{\left(\lambda_{\mathcal{H}_i}\right)^{\frac{\omega^{\text{CS}}}{\Delta x^2}}}{\left(\frac{\omega^{\text{CS}}}{\Delta x^2}\right)!} \exp\left(-\lambda_{\mathcal{H}_i}\right), \quad (3.45)$$

where $\lambda_{\mathcal{H}_i}$ is given by:

$$\lambda_{\mathcal{H}_i} = \sum_{k=1}^K \sum_{l=1}^L \lambda_{\mathcal{H}_i,kl}. \quad (3.46)$$

Analogous to the decision rule for the peak intensities of equation (3.39), we decide \mathcal{H}_1 for an observed scattering cross-section w^{CS} , under the assumption of equal priors $P(\mathcal{H}_0) = P(\mathcal{H}_1) = 1/2$, if:

$$p(w^{\text{CS}}; \mathcal{H}_1) > p(w^{\text{CS}}; \mathcal{H}_0), \quad (3.47)$$

otherwise \mathcal{H}_0 is decided. For scattering cross-sections, the probability of error can then be calculated as follows:

$$\begin{aligned} P_e &= \frac{1}{2}P(\mathcal{H}_0|\mathcal{H}_1) + \frac{1}{2}P(\mathcal{H}_1|\mathcal{H}_0) \\ &= \frac{1}{2}F\left(\frac{x^{\text{CS}}}{\Delta x^2}; \lambda_{\mathcal{H}_1}\right) + \frac{1}{2}\left[1 - F\left(\frac{x^{\text{CS}}}{\Delta x^2}; \lambda_{\mathcal{H}_0}\right)\right], \end{aligned} \quad (3.48)$$

where $F\left(\frac{x^{\text{CS}}}{\Delta x^2}; \lambda_{\mathcal{H}_i}\right)$ equals the Poisson cumulative distribution function with parameter $\lambda_{\mathcal{H}_i}$ evaluated at $x^{\text{CS}}/\Delta x^2$ with x^{CS} being the intersection value of the two probability functions $p(w^{\text{CS}}; \mathcal{H}_0)$ and $p(w^{\text{CS}}; \mathcal{H}_1)$, which is given by:

$$x^{\text{CS}} = \frac{(\lambda_{\mathcal{H}_0} - \lambda_{\mathcal{H}_1})\Delta x^2}{\ln \frac{\lambda_{\mathcal{H}_0}}{\lambda_{\mathcal{H}_1}}}. \quad (3.49)$$

The goal is now to optimise the experiment design as a function of the experimental settings in order to have the lowest probability of choosing the wrong hypothesis. The experimental settings for which the probability of error reaches a minimum is then considered as the optimal experiment design.

Image intensities on a pixel by pixel basis

As a third performance measure to optimise the experiment design, the image intensities in the HR(S)TEM images of the atom column may be considered on a pixel by pixel basis. In this case, the decision is based on the conditional *joint* probability function of all the image pixel intensities, which is given by:

$$p(\omega^{\text{Im}}; \mathcal{H}_i) = \prod_{k=1}^K \prod_{l=1}^L \frac{(\lambda_{\mathcal{H}_i,kl})^{\omega_{kl}}}{\omega_{kl}!} \exp(-\lambda_{\mathcal{H}_i,kl}). \quad (3.50)$$

Since we have a joint probability function now for the stochastic variable ω^{Im} of the HR(S)TEM image, it is not possible to compute the probability of error directly from the overlapping areas of $p(\omega^{\text{Im}}; \mathcal{H}_0)$ and $p(\omega^{\text{Im}}; \mathcal{H}_1)$. However, it is possible to calculate this probability of error analytically by reformulating the decision rule using the so-called log-likelihood ratio $\ln LR(\omega^{\text{Im}})$ [158]. The decision rule then becomes to decide \mathcal{H}_1 for an observation \mathbf{w}^{Im} , if

$$\ln LR(\mathbf{w}^{\text{Im}}) \equiv \ln \left(\frac{p(\mathbf{w}^{\text{Im}}; \mathcal{H}_1)}{p(\mathbf{w}^{\text{Im}}; \mathcal{H}_0)} \right) > \ln(1) = 0, \quad (3.51)$$

otherwise \mathcal{H}_0 is decided, for equal prior probabilities. This corresponds to choosing the hypothesis for which the log-likelihood function is maximal. The function $LR(\mathbf{w}^{\text{Im}})$ is called the likelihood ratio since it indicates for each set of observations \mathbf{w}^{Im} the likelihood of \mathcal{H}_1 versus the likelihood of \mathcal{H}_0 . Given the decision rule of equation (3.51), the expression for the probability of error P_e given by equation (3.33), can be rewritten as follows:

$$\begin{aligned} P_e &= \frac{1}{2}P(\mathcal{H}_0|\mathcal{H}_1) + \frac{1}{2}P(\mathcal{H}_1|\mathcal{H}_0) \\ &= \frac{1}{2}P(\ln LR(\mathbf{w}^{\text{Im}}) < 0|\mathcal{H}_1) + \frac{1}{2}P(\ln LR(\mathbf{w}^{\text{Im}}) > 0|\mathcal{H}_0). \end{aligned} \quad (3.52)$$

When using the conditional joint probability function for HR(S)TEM images given by equation (3.50), the log-likelihood ratio defined by equation (3.51) can be rewritten as

$$\ln LR(\mathbf{w}^{\text{Im}}) = \sum_{k=1}^K \sum_{l=1}^L \left(w_{kl} \ln \left(\frac{\lambda_{\mathcal{H}_1,kl}}{\lambda_{\mathcal{H}_0,kl}} \right) - \lambda_{\mathcal{H}_1,kl} + \lambda_{\mathcal{H}_0,kl} \right). \quad (3.53)$$

Following the central limit theorem, the log-likelihood ratio tends to be normally distributed [221]:

$$p(\ln LR(\mathbf{w}^{\text{Im}}); \mathcal{H}_i) = \frac{1}{\sigma_{\mathcal{H}_i} \sqrt{2\pi}} \exp \left(-\frac{(\ln LR(\mathbf{w}^{\text{Im}}) - \mu_{\mathcal{H}_i})^2}{2\sigma_{\mathcal{H}_i}^2} \right) \quad (3.54)$$

For HR(S)TEM images, the expected value $\mu_{\mathcal{H}_i}$ and variance $\sigma_{\mathcal{H}_i}^2$ characterising this normal distribution can then be computed from equation (3.53) when as-

suming \mathcal{H}_i to be true, giving the following results:

$$\begin{aligned}\mu_{\mathcal{H}_i} &= \mathbb{E}_{\mathcal{H}_i} \left[\ln LR(\mathbf{w}^{\text{Im}}) \right] \\ &= \sum_{k=1}^K \sum_{l=1}^L \left(\lambda_{\mathcal{H}_i,kl} \ln \frac{\lambda_{\mathcal{H}_1,kl}}{\lambda_{\mathcal{H}_0,kl}} - \lambda_{\mathcal{H}_1,kl} + \lambda_{\mathcal{H}_0,kl} \right),\end{aligned}\quad (3.55)$$

$$\begin{aligned}\sigma_{\mathcal{H}_i}^2 &= \text{var}_{\mathcal{H}_i} \left[\ln LR(\mathbf{w}^{\text{Im}}) \right] \\ &= \sum_{k=1}^K \sum_{l=1}^L \lambda_{\mathcal{H}_i,kl} \left(\ln \frac{\lambda_{\mathcal{H}_1,kl}}{\lambda_{\mathcal{H}_0,kl}} \right)^2.\end{aligned}\quad (3.56)$$

In this derivation, use is made of the property that the variance of a Poisson distributed variable equals its expectation value, $\mathbb{E}_{\mathcal{H}_i}[\omega_{kl}] = \text{var}_{\mathcal{H}_i}[\omega_{kl}] = \lambda_{\mathcal{H}_i,kl}$. The explicit description of the distribution of the log-likelihood ratio now enables us to unambiguously compute the probability of error given by equation (3.52), resulting in the following general expression:

$$P_e = \frac{1}{2} \left[\Phi \left(\frac{-\mu_{\mathcal{H}_1}}{\sigma_{\mathcal{H}_1}} \right) + \Phi \left(\frac{\mu_{\mathcal{H}_0}}{\sigma_{\mathcal{H}_0}} \right) \right] \quad (3.57)$$

with $\Phi(\pm\mu/\sigma)$ the cumulative distribution function of the standard normal distribution evaluated at $\pm\mu/\sigma$. The meaning of the expected value $\mu_{\mathcal{H}_i}$ and variance $\sigma_{\mathcal{H}_i}^2$ characterising the normal distributions of $\ln LR(\mathbf{w}^{\text{Im}})$ given by equation (3.54) under both hypotheses, is illustrated in Figure 3.1(c) based on HRSTEM images for a Sr column consisting of either 30 or 31 atoms. The decision rule is also clarified: \mathcal{H}_0 is decided for $\ln LR(\mathbf{w}^{\text{Im}}) < 0$, otherwise \mathcal{H}_1 is decided to be correct. The dark grey region denotes the error which is made if \mathcal{H}_0 is chosen while \mathcal{H}_1 is correct, and vice versa for the light grey region. It is clear from this figure that the probability of error corresponds to the overlap between both distributions.

Parameter	Symbol	Value
Defocus	f (Å)	-14.03
Spherical aberration	C_s (mm)	0.001
Spherical aberration of fifth order	C_5 (mm)	0
Slice thickness	z_{slice} (Å)	1.95
Debye-Waller factor	B_{Sr} (Å ²)	0.6214
	B_{Ti} (Å ²)	0.4398
	B_O (Å ²)	0.7323
Acceleration voltage	V_0 (kV)	300
Semi-convergence angle	α (mrad)	20
Probe sampling distance	$\Delta x, \Delta y$ (Å)	0.1562
FWHM of the source image	$FWHM$ (Å)	0.7
Total number of scanned pixels	$K \times L$	25×25

Table 3.1: Parameter values used in the simulation software STEMsim.

3.5.2 Sum of Kullback-Leibler divergences

A tightly connected performance measure that will be investigated as a possible alternative to optimise the design is based on the so-called Kullback-Leibler divergence [222, 223]. This measure quantifies the difference between two probability distributions. Here, the Kullback-Leibler divergence will be discussed for a general stochastic variable ω , which can then be replaced by the variable corresponding to peak intensities, scattering cross-sections or the image intensities on a pixel by pixel basis. The Kullback-Leibler divergence from $p_{\mathcal{H}_1} = p(\omega; \mathcal{H}_1)$ to $p_{\mathcal{H}_0} = p(\omega; \mathcal{H}_0)$ is defined as

$$D(p_{\mathcal{H}_1}, p_{\mathcal{H}_0}) \equiv \mathbb{E}_{\mathcal{H}_1} \left[\ln \frac{p(\omega; \mathcal{H}_1)}{p(\omega; \mathcal{H}_0)} \right] = \mathbb{E}_{\mathcal{H}_1} [\ln LR(\omega)]. \quad (3.58)$$

It corresponds to the expected or mean log-likelihood ratio assuming \mathcal{H}_1 to be true. Similarly the Kullback-Leibler divergence from $p_{\mathcal{H}_0}$ to $p_{\mathcal{H}_1}$ equals

$$D(p_{\mathcal{H}_0}, p_{\mathcal{H}_1}) = \mathbb{E}_{\mathcal{H}_0} \left[\ln \frac{p(\omega; \mathcal{H}_0)}{p(\omega; \mathcal{H}_1)} \right] = -\mathbb{E}_{\mathcal{H}_0} \left[\ln \frac{p(\omega; \mathcal{H}_1)}{p(\omega; \mathcal{H}_0)} \right] = -\mathbb{E}_{\mathcal{H}_0} [\ln LR(\omega)]. \quad (3.59)$$

From equations (3.58) and (3.59), it follows that

$$D(p_{\mathcal{H}_1}, p_{\mathcal{H}_0}) + D(p_{\mathcal{H}_0}, p_{\mathcal{H}_1}) = \mathbb{E}_{\mathcal{H}_1} [\ln LR(\omega)] - \mathbb{E}_{\mathcal{H}_0} [\ln LR(\omega)]. \quad (3.60)$$

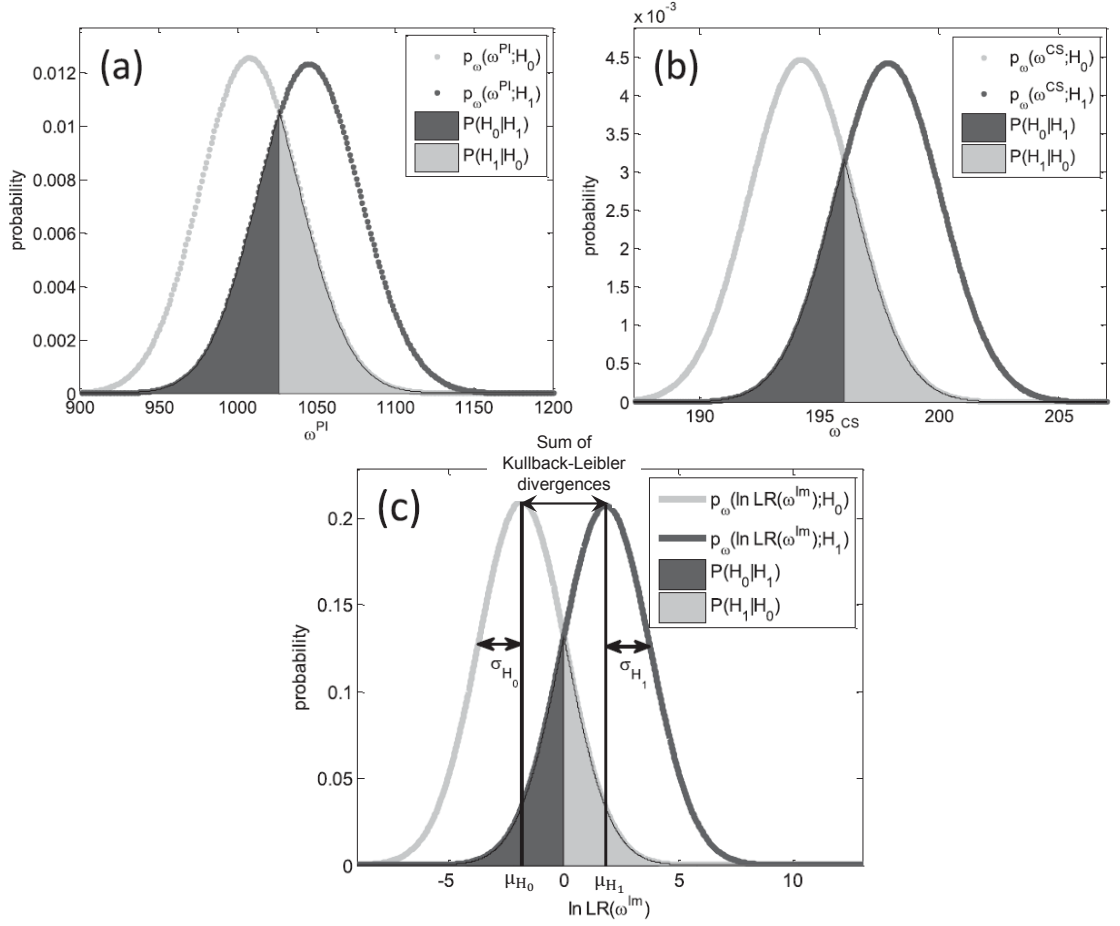


Figure 3.1: Calculation of the probability of error for a binary hypothesis test for (a) peak intensities ω^{PI} ($D = 10^6 e^-/\text{\AA}^2$ and $n_{\mathcal{H}_0} = 15$), (b) scattering cross-sections ω^{CS} ($D = 10^5 e^-/\text{\AA}^2$ and $n_{\mathcal{H}_0} = 30$), and (c) images ω^{Im} ($D = 10^5 e^-/\text{\AA}^2$ and $n_{\mathcal{H}_0} = 30$) of a Sr column with a detector collection range of 60-100 mrad and settings of Table 3.1.

The sum of Kullback-Leibler divergences thus corresponds to the difference between the mean log-likelihood ratio under \mathcal{H}_1 and the corresponding value when assuming \mathcal{H}_0 to be true, as is also illustrated in Figure 3.1(c). We have investigated if this measure can be used as an alternative of the above mentioned probability of error to compute the optimal experiment design. Indeed, based on decision rule (3.36), which can be used to choose between \mathcal{H}_1 and \mathcal{H}_0 , it follows that the probability to assign the wrong hypothesis will decrease when the distributions

of the log-likelihood ratio under these hypotheses are better separated. A measure of this separation is given by equation (3.60). For that reason, it is likely to assume that the probability to assign a wrong hypothesis will decrease when the sum of Kullback-Leibler divergences increases.

An explicit expression for equation (3.60) can be derived from equation (3.53) and using the fact that the expectations of the observations are described by means of their expectation model:

$$D(p_{\mathcal{H}_1}, p_{\mathcal{H}_0}) + D(p_{\mathcal{H}_0}, p_{\mathcal{H}_1}) = \left(\mathbb{E}_{\mathcal{H}_1}[\omega] - \mathbb{E}_{\mathcal{H}_0}[\omega] \right) \left(\ln \mathbb{E}_{\mathcal{H}_1}[\omega] - \ln \mathbb{E}_{\mathcal{H}_0}[\omega] \right). \quad (3.61)$$

In chapter 4, this expression will be calculated explicitly for a linear imaging model in the weak phase object approximation, in order to distinguish between two different atom types. It will be investigated if an increase of the sum of Kullback-Leibler divergences leads to a decrease of the probability of error. In this way, it will be possible to decide if this measure can be used as an alternative performance measure to optimise the experiment design. The sum of Kullback-Leibler divergences, however, only takes into account the separations between the distributions of the log-likelihood ratio whereas the probability of error also takes into account the width of the distributions.

3.5.3 Multiple hypothesis testing

If different choices of the two hypotheses lead to different designs, a binary hypothesis test is no longer adequate. Therefore, the approach of binary hypothesis testing for atom-counting is extended towards multiple hypothesis testing. The multiple hypothesis test will first be described for a general observation \mathbf{w} and then be further derived for both scattering cross-sections, which are often used in practice in HRSTEM [75, 76, 208], and peak intensities.

Suppose we want to decide among M possible hypotheses:

$$\{\mathcal{H}_0, \mathcal{H}_1, \dots, \mathcal{H}_{M-1}\}. \quad (3.62)$$

For atom-counting, the number of hypotheses typically equals the maximum number of atoms in a column which should be considered for the sample under study. The decision rule is now defined such that the probability of error is minimised. The minimum probability of error decision rule for an observation \mathbf{w} , is then to decide \mathcal{H}_k if

$$p(\mathbf{w}|\mathcal{H}_k)P(\mathcal{H}_k) > p(\mathbf{w}|\mathcal{H}_i)P(\mathcal{H}_i) \quad \forall i \neq k. \quad (3.63)$$

This decision rule is termed the *maximum a posteriori probability* (MAP) decision rule [156]. In this expression, $p(\mathbf{w}|\mathcal{H}_i)$ is the conditional (joint) probability (density) function (P(D)F) $p(\omega|\mathcal{H}_i)$ assuming \mathcal{H}_i to be true, evaluated at the available observations \mathbf{w} . For equal prior probabilities $P(\mathcal{H}_i) = 1/M$, the decision rule given in equation (3.63) simplifies to

$$p(\mathbf{w}|\mathcal{H}_k) > p(\mathbf{w}|\mathcal{H}_i) \quad \forall i \neq k. \quad (3.64)$$

This is then the M -ary maximum likelihood (ML) decision rule [156]. In the case of a multiple hypothesis test, the probability of error is defined in the following way:

$$P_e = \sum_{i=0}^{M-1} \sum_{j=0}^{M-1} \delta_{ij} P(\mathcal{H}_i|\mathcal{H}_j) P(\mathcal{H}_j), \quad (3.65)$$

where $P(\mathcal{H}_i|\mathcal{H}_j)$ is the conditional probability of deciding \mathcal{H}_i when \mathcal{H}_j is true, and

$$\delta_{ij} = \begin{cases} 1 & i \neq j \\ 0 & i = j \end{cases}. \quad (3.66)$$

The number of terms for the calculation of the probability of error used in equation (3.65) equals $M(M-1)$. Therefore, it is more efficient to calculate $P_c = 1 - P_e$, where P_c is the probability of a correct decision. In this case, the number of terms in the summation reduces to M :

$$P_c = \sum_{i=0}^{M-1} P(\mathcal{H}_i|\mathcal{H}_i) P(\mathcal{H}_i), \quad (3.67)$$

where $P(\mathcal{H}_i|\mathcal{H}_i)$ corresponds to the probability that hypothesis \mathcal{H}_i is decided assuming this hypothesis to be correct, and this is weighted by its prior probability $P(\mathcal{H}_i)$.

When the decision for a certain hypothesis between M different hypotheses is completely random, the probability for a correct decision equals $1/M$ when assuming equal prior probabilities. As a consequence, for a multiple hypothesis test with M different hypotheses, the maximum possible probability of error for which the correct hypothesis can not be decided equals $(M-1)/M$.

Expression (3.67) will now be calculated analytically; (1) for scattering cross-sections and (2) for peak intensities in HR(S)TEM images, for which the conditional probability functions are given by equation (3.45) and (3.38), respectively.

For equal prior probabilities $P(\mathcal{H}_i) = 1/M$, the probability of a correct decision for scattering cross-sections in HRSTEM images then corresponds to:

$$\begin{aligned}
 P_c = \frac{1}{M} & \left[F\left(\frac{x^{\text{CS}_{0,1}}}{(\Delta x)^2}, \lambda_{\mathcal{H}_0^s}\right) + \right. \\
 & F\left(\frac{x^{\text{CS}_{1,2}}}{(\Delta x)^2}, \lambda_{\mathcal{H}_1^s}\right) - F\left(\frac{x^{\text{CS}_{1,0}}}{(\Delta x)^2}, \lambda_{\mathcal{H}_1^s}\right) + \\
 & F\left(\frac{x^{\text{CS}_{2,3}}}{(\Delta x)^2}, \lambda_{\mathcal{H}_2^s}\right) - F\left(\frac{x^{\text{CS}_{2,1}}}{(\Delta x)^2}, \lambda_{\mathcal{H}_2^s}\right) + \\
 & \dots + \\
 & \left. \left(1 - F\left(\frac{x^{\text{CS}_{M-1,M-2}}}{(\Delta x)^2}, \lambda_{\mathcal{H}_{M-1}^s}\right)\right) \right], \tag{3.68}
 \end{aligned}$$

where \mathcal{H}_i^s denotes the sorted hypotheses according to the expected values of the scattering cross-sections, and $x^{\text{CS}_{i,j}} = x^{\text{CS}_{j,i}}$ corresponds to the intersection between two neighbouring probability functions. This intersection is given by

$$x^{\text{CS}_{i,j}} = \frac{\left(\lambda_{\mathcal{H}_i^s} - \lambda_{\mathcal{H}_j^s}\right)(\Delta x)^2}{\ln \frac{\lambda_{\mathcal{H}_i^s}}{\lambda_{\mathcal{H}_j^s}}}. \tag{3.69}$$

In this expression, $\lambda_{\mathcal{H}_i^s} = \sum_{k=1}^K \sum_{l=1}^L \lambda_{\mathcal{H}_i^s,kl}$ equals the sum over the expected values of the pixel intensities in a Voronoi cell of the atomic column, and $F\left(\frac{x^{\text{CS}_{i,j}}}{(\Delta x)^2}, \lambda_{\mathcal{H}_i^s}\right)$ is the Poisson cumulative distribution function with parameter $\lambda_{\mathcal{H}_i^s}$ evaluated at $x^{\text{CS}_{i,j}}/\Delta x^2$. The expected pixel intensities $\lambda_{\mathcal{H}_i^s,kl}$ can in practice be obtained by using software for HR(S)TEM image simulations [201, 219].

A similar expression for the probability of a correct decision can now be found for peak intensities [159]:

$$\begin{aligned}
 P_c = \frac{1}{M} & \left[F\left(x^{\text{PI}_{0,1}}, \lambda_{\mathcal{H}_0^s}\right) + \right. \\
 & F\left(x^{\text{PI}_{1,2}}, \lambda_{\mathcal{H}_1^s}\right) - F\left(x^{\text{PI}_{1,0}}, \lambda_{\mathcal{H}_1^s}\right) + \\
 & F\left(x^{\text{PI}_{2,3}}, \lambda_{\mathcal{H}_2^s}\right) - F\left(x^{\text{PI}_{2,1}}, \lambda_{\mathcal{H}_2^s}\right) + \\
 & \dots + \\
 & \left. \left(1 - F\left(x^{\text{PI}_{M-1,M-2}}, \lambda_{\mathcal{H}_{M-1}^s}\right)\right) \right], \tag{3.70}
 \end{aligned}$$

where the intersection between the different probability functions is given by

$$x^{\text{PI},j} = \frac{\left(\lambda_{\mathcal{H}_i^s} - \lambda_{\mathcal{H}_j^s}\right)}{\ln \frac{\lambda_{\mathcal{H}_i^s}}{\lambda_{\mathcal{H}_j^s}}}, \quad (3.71)$$

and $\lambda_{\mathcal{H}_i^s}$ corresponds to $\lambda_{\mathcal{H}_i^s, \text{PI}} = \mathbb{E}_{\mathcal{H}_i^s}[\omega^{\text{PI}}]$, the expected pixel value at the atomic column position.

When a decision is based on the joint probability function of the image pixel values, which are defined by ω^{Im} in equation (3.37), the probability of error given by equation (3.65), can not be calculated analytically anymore. In that case, the probability of error can only approximately be calculated using repetitive noise realisations, which is computationally intensive. By using the decision rule given by equation (3.64), the probability of error is then given by the fraction of miscounted numbers of atoms from a large set of noise realisations.

3.6 Conclusions

In this chapter, it has been shown how statistical experiment design can be optimised in order to derive unknown continuous or discrete structure parameters either with the highest precision, or the lowest probability of error, respectively. The optimisation process can be summarised as follows:

- First, a parametric statistical model of the observations has to be derived. This is a physics-based model that both defines the expectations of the observations and the fluctuations of the observations about these expectations. The expectations of the observations can, in general, be computed using software to simulate HR(S)TEM images [201, 219].
- Second, an optimality criterion is chosen, which depends on the purpose of the experimenter. For the estimation of continuous parameters, a function of the elements of the CRLB is chosen, while for a discrete estimation problem, statistical detection theory allows one to calculate the probability of error as optimality criterion. Since the parametric statistical model of the observations is a function of the experimental settings, both (a function of) the CRLB and the probability of error are functions of these settings as well.

- Third, the chosen optimality criterion is evaluated and optimised with respect to the experimental settings. The settings corresponding to either the highest precision or lowest probability of error are suggested as the optimal statistical experiment design. In the remainder of this thesis, this procedure will be applied to quantitatively optimise and compare HRTEM and HRSTEM for detecting and locating light elements, and for counting the number of atoms in a projected atom column.

Statistical Experiment Design for Atomic Number Estimation from HRSTEM images

4.1 Introduction

In the previous chapter, the theoretical tools to derive the limits to the precision with which unknown structure parameters can be estimated from HR(S)TEM images are discussed. In this chapter, these quantitative tools will be applied to explore the optimal statistical experimental settings for identifying the atomic number from HRSTEM images. The possibilities and limitations are investigated by using the probability of error and the Kullback-Leibler divergence as alternative quantitative criteria to optimise the STEM detector settings, in terms of identifying the chemical composition, i.e. by estimating the atomic number Z ¹. It is expected that the probability of error is minimised by the same optimal experimental settings that maximise the sum of Kullback-Leibler divergences, and that the sum of Kullback-Leibler divergences is less computationally intensive and faster to calculate as compared to the probability of error.

These quantitative criteria are applied when considering the problem of identifying the atomic number Z , both for a single isolated atom and for atom columns lying on the interface of a crystalline specimen². Note that chemical theory restricts the atomic number to be a positive integer, which makes it a so-called restricted or discrete parameter. A priori knowledge about the atom types that may be present in a sample and their concentration ratios is usually available. In such cases, the question reduces to distinguishing between a finite plausible

¹Part of the results presented in this chapter is published in A. J. den Dekker, J. Gonnissen, A. De Backer, J. Sijbers, and S. Van Aert, Estimation of unknown structure parameters from high-resolution (S)TEM images: What are the limits?, *Ultramicroscopy* 134, 34-43 (2013).

²Part of the results presented in this chapter are published in J. Gonnissen, A.J. den Dekker, A. De Backer, G.T. Martinez, A. Rosenauer, J. Sijbers and S. Van Aert, Optimal experimental design for the detection of light atoms from high-resolution STEM images, *Applied Physics Letters*, 105, 6 (2014).

set of values for the atomic numbers, given the experimental STEM observations. Here we restrict to the problem of deciding between two hypotheses, where each hypothesis corresponds to the assumption of a specific Z value, given by the first case in equation (3.32): $\mathcal{H}_0 : Z = Z_0$ and $\mathcal{H}_1 : Z = Z_1$. In a first step, the probability of error, given by equation (3.33), was calculated using the decision rule defined by equation (3.36). This was possible by performing repetitive image simulations which is very time-consuming. Next, the sum of Kullback-Leibler divergences, which corresponds to the difference of the expected or mean log-likelihood ratio under \mathcal{H}_1 and the corresponding value when assuming \mathcal{H}_0 to be true, is computed for the same experimental settings as the probability of error. Both measures have been investigated and compared as criteria to optimise the detector design in an HRSTEM experiment. In a second step, an analytical expression for the probability of error was found which made the use of the sum of Kullback-Leibler divergences unnecessary.

This chapter is organised as follows. In section 4.2, minimising the probability of error is used in order to optimise the experiment design for identifying the atomic number Z of a single isolated atom, which is compared to the result of the sum of Kullback-Leibler divergences. In section 4.3, the probability of error is computed for the investigated isolated atom cases with the obtained analytical expression, and compared with the results based on multiple noise realisations. The analytical expression of the probability of error is then used in section 4.4 to optimise the detector design in HRSTEM in order to identify the atomic number at the interface of a crystalline specimen. In section 4.5, conclusions are drawn.

4.2 Statistical experiment design for identifying the atomic number of a single isolated atom

As a first experimental case study to show the practical use of both the probability of error and the Kullback-Leibler divergence for the optimisation of the experiment design, the optimal inner detector radius of an annular detector is derived when deciding between the presences of an Al or Ti atom in HR STEM images, based on an earlier problem considered in [224]. This estimation problem can be formulated as a binary hypothesis test with hypotheses $\mathcal{H}_0 : Z = 12$ (Al) and $\mathcal{H}_1 : Z = 22$ (Ti). The probability of error is then computed using repetitive image simulations under both hypotheses. Therefore, the simplified discrete parametric model of an isolated atom derived in section 3.2.1 is assumed. Given

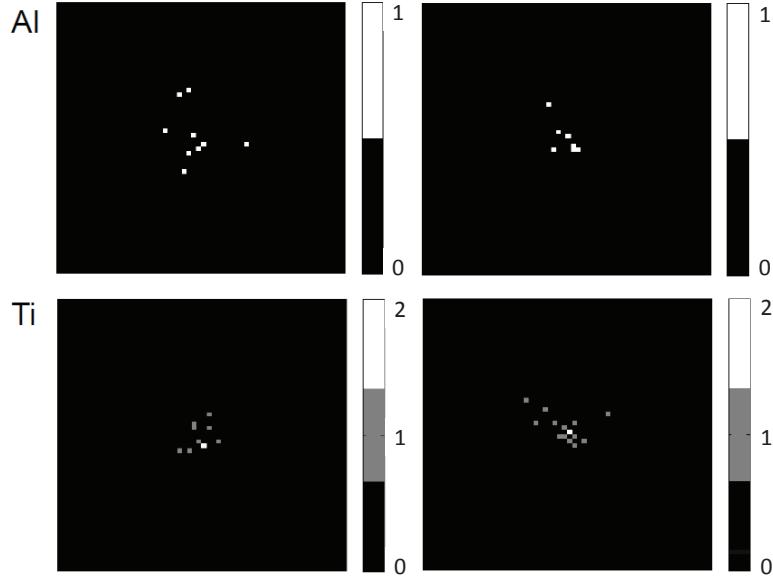


Figure 4.1: The electron counting results for two different Poisson noise realisations simulated under the same settings, for an Al and Ti atom.

the simulation parameters listed in Table 4.1, the expectation models described by equation (3.16) have been computed for a single Al and Ti atom. Next, Poisson distributed observations \mathbf{w} have been generated following the joint PF given by equation (3.50). As an example, two different noise realisations for each isolated atom are shown in Figure 4.1. In total 10000 simulations have been made under \mathcal{H}_0 and another 10000 under \mathcal{H}_1 . For every simulation experiment, the log-likelihood ratio $\ln LR(\mathbf{w})$ has been calculated. From equation (3.31) it follows that $\ln LR(\mathbf{w})$ can be written as follows for the single-atom HRSTEM model given by equation (3.16):

$$\ln LR(\mathbf{w}) = \sum_k \sum_l [w_{kl} (\ln f_{kl}(Z_1) - \ln f_{kl}(Z_0)) + (f_{kl}(Z_0) - f_{kl}(Z_1))]. \quad (4.1)$$

In this way, the results shown in Figure 4.3 are obtained for three different inner detector radii (13 mrad, 21 mrad and 47 mrad). The histograms shown in blue and red result from simulations assuming the presence of an Al and Ti atom, respectively. The histograms are computed for a whole HRSTEM image and not only for the probe positioned at the centre of the grid, corresponding to the position of the atom.

Parameter	Symbol	Value
Defocus	f (nm)	-8.301
Spherical aberration	C_s (mm)	0.035
Spherical aberration of fifth order	C_5 (mm)	0
Acceleration voltage	V_0 (kV)	300
Semi-convergence angle	α (mrad)	21
Probe sampling distance	Δx (Å)	0.1
Incident electron dose	N ($e^-/\text{Å}^2$)	100
Total number of scanned pixels	$K \times L$	60×60
Electron wavelength	λ (Å)	0.0197
Interaction parameter	σ (rad $\text{kV}^{-1} \text{Å}^{-1}$)	0.53

Table 4.1: Microscope parameter values used in the simulation study of a single, isolated atom.

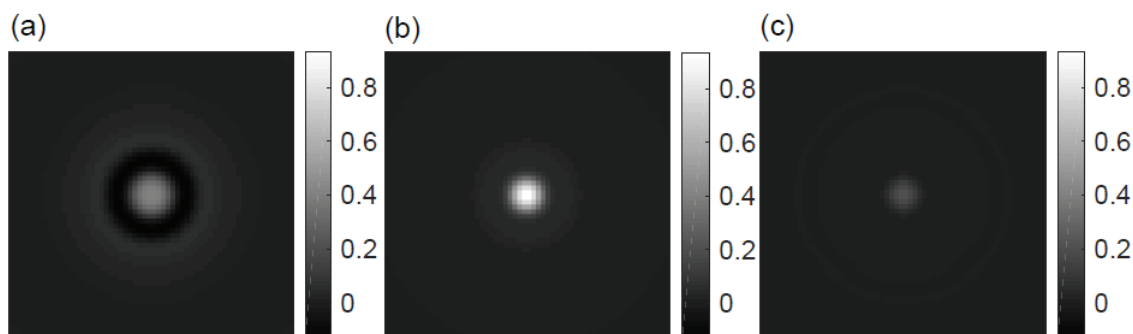


Figure 4.2: The difference between simulated STEM images of a Ti and an Al atom for an inner detector radius of (a) 13 mrad, (b) 21 mrad and (c) 47 mrad, on a fixed contrast scale.

Based on the computed log-likelihood ratios, hypothesis \mathcal{H}_1 or \mathcal{H}_0 is decided following decision rule (3.36) for each simulation experiment, using expression (4.1) for the log-likelihood ratio. From the fraction of wrongly assigned atomic numbers, the probability of error, given by equation (3.52), can then be estimated. The goal is now to minimise the probability of error and maximise the sum of Kullback-Leibler divergences (equation (3.61)) as a function of the inner radius

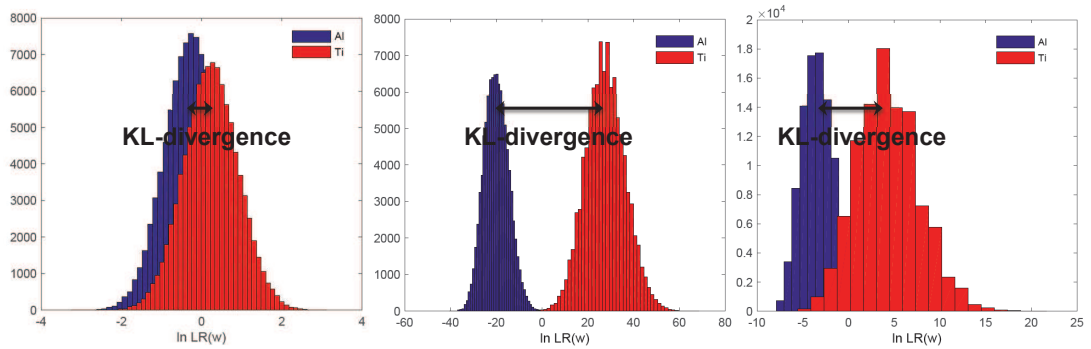


Figure 4.3: Histograms of the log likelihood ratio for an inner detector radius of (a) 13 mrad, (b) 21 mrad and (c) 47 mrad, for the presence of an Al (blue) and Ti (red) atom.

of an annular detector, assuming a constant infinitely large outer detector radius. The inner detector radius will be varied over a broad range, covering the ABF to the HAADF regime. This means that in equation (3.14) all contributions outside the so-formed detector hole are summed up. It is found that the sum of Kullback-Leibler divergences and the probability of error provide consistent results. Indeed, the probability to assign the wrong hypothesis decreases when the distributions of the log-likelihood ratio under the considered hypotheses are better separated, and thus when the sum of Kullback-Leibler divergences increases. It is seen in Figure 4.4 that a minimum for the probability of error is found for the inner detector radius maximising the sum of Kullback-Leibler divergences, namely for 21 mrad. For a probe semi-convergence angle of 21 mrad, this setting corresponds to the LAADF STEM regime. We see in Figure 4.3 that for this inner detector radius the log-likelihood functions under both hypotheses are separated the most. This is a first indication for the Kullback-Leibler divergence to be an efficient alternative performance measure to the probability of error to optimise the experiment design. From the histograms shown in Figure 4.3(c) it can also be seen that the curves come closer again for a larger inner detector radius, which can be understood since the detected dose decreases for an increasing inner detector radius. This is also clear from the results shown in Figure 4.2, where the difference between the simulated HRSTEM image of a Ti and an Al atom is shown for the same three inner detector radii.

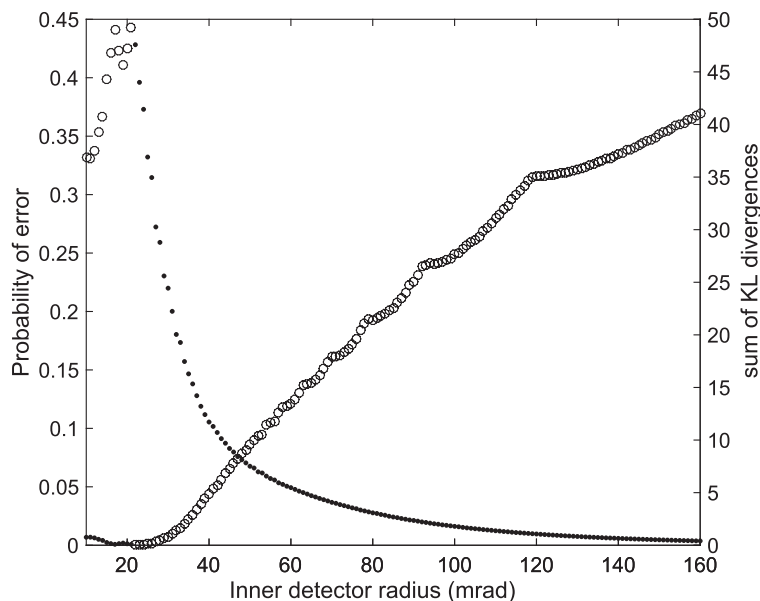


Figure 4.4: The probability of error (open circles) and the sum of Kullback-Leibler divergences (dots) for identifying either Al or Ti, both as a function of the inner detector radius.

Our second study is based on a problem which was previously considered in [146], where the question was to decide between the presence of Ti and Mn atom columns at an interface. In that case, the difference in atomic number Z is only 3. Because of this small difference in Z , in combination with the presence of heavy atomic columns surrounding the Ti and Mn columns, this question could not be solved visually. Instead, statistical parameter estimation theory can be used. Here we will reconsider this problem in terms of optimising the STEM detector settings for the simplified problem of deciding between the presence of a single Ti or Mn atom at the interface. The hypotheses of interest can therefore be formulated as $\mathcal{H}_0 : Z = Z_0 = 22$ and $\mathcal{H}_1 : Z = Z_1 = 25$. If we assume that the probabilities of the presence of a Ti atom or Mn atom are equal, an expression for the probability of error is given by equation (3.52). Furthermore, the sum of Kullback-Leibler divergences, for which an expression is given by equation (3.61), will be computed for the given hypotheses and maximised as a function of the inner detector radius. As discussed in section 3.5, the detector radius minimising the probability of error indeed corresponds to the radius maximising the sum of Kullback-Leibler divergences. In the same way as for deciding between an Al and Ti atom and using the

same simulation parameters as listed in Table 4.1, the results are obtained for Ti and Mn and presented in Figure 4.5. From the results shown in Figure 4.5 it can

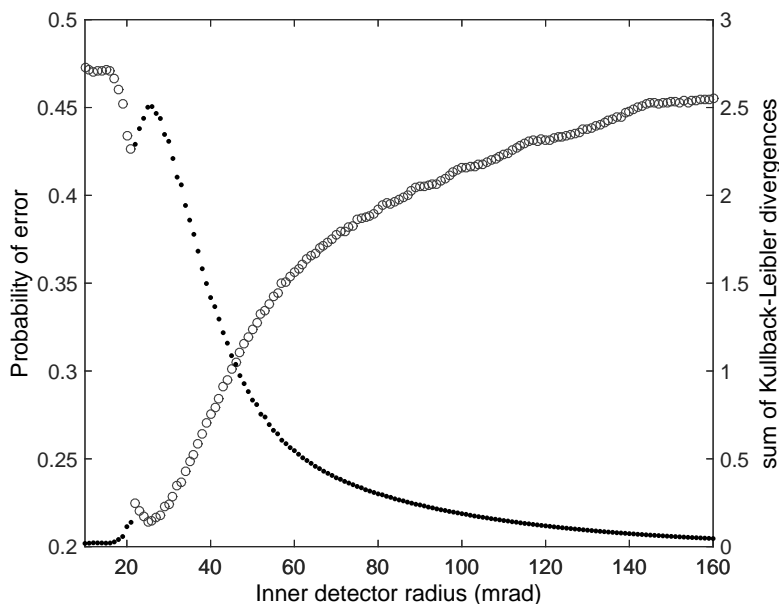


Figure 4.5: The probability of error (open circles) and the sum of Kullback-Leibler divergences (dots) for identifying either Ti or Al, both as a function of the inner detector radius.

be seen that a minimum for the probability of error is found for the inner detector radius that is maximising the sum of Kullback-Leibler divergences, which corresponds to 24 mrad in this case. For a probe semi-convergence angle of 21 mrad this still corresponds to the LAADF STEM regime.

Both in Figures 4.4 and 4.5, it is seen that the probability of error shows some small peaks at certain values for the inner detector radius. The reason for this behaviour is not understood so far. However, as one will notice in the next section the analytical expression for the probability of error, which is used further on in this thesis, varies smoothly with the inner detector radius and therefore this effect has not been further examined.

4.3 Analytical expression for the probability of error

In Figures 4.4 and 4.5, the probability of error is computed using repetitive image simulations under both hypotheses. From both results it is clear that the sum of Kullback-Leibler divergences yields consistent results, and moreover, it is much easier to compute since it does not require multiple noise realisations. However, if we look closer to both results, we can also see that although the probability of error is similar for both cases, the sum of Kullback-Leibler divergences is much larger in the case where we want to distinguish between Al and Ti as compared to the case where we want to decide between the presence of a Ti or Mn atom. This can be understood from the greater difference in atomic number between Al and Ti, as compared to Ti and Mn. The distance between the mean values of the log-likelihood ratios under both hypotheses is consequently expected to be larger in the case of Al and Ti. However, the value of the Kullback-Leibler divergence does not give us any quantitative information on how likely the correct decision between both elements can be made. Comparing the sum of Kullback-Leibler divergences for different hypothesis tests would not give useful quantitative information on how well the different atoms can be distinguished, without comparing with the corresponding probabilities of error.

Therefore, effort has been put in the derivation of an analytical expression for the probability of error, which was derived in chapter 3 and is given by equation (3.57) for binary hypothesis testing in HRSTEM images on a pixel by pixel basis. The fact that this analytical expression was found, enabled us to calculate the probability of error in a fast and straightforward way, without the need for multiple noise realisations. In fact, this also made the Kullback-Leibler divergence unnecessary as it provides less information. Indeed, the probability of error takes into account the overlap between consecutive probability distributions, while the sum of Kullback-Leibler divergence only gives a measure for the distance between the mean values, or expected values of these distributions. In Figure 4.6, the result of the probability of error is compared for both deciding between Al and Ti, and between Ti and Mn, when using 100.000 noise realisations or using the analytical expression given by equation (3.57). It can be seen that both results match very well, and that there are only some small variations due to the limited number of included noise realisations. This is also a verification that it is justified to apply the central limit theorem for the number of considered pixels and consider the log-likelihood ratio, defined in equation (3.53) to be normally distributed.

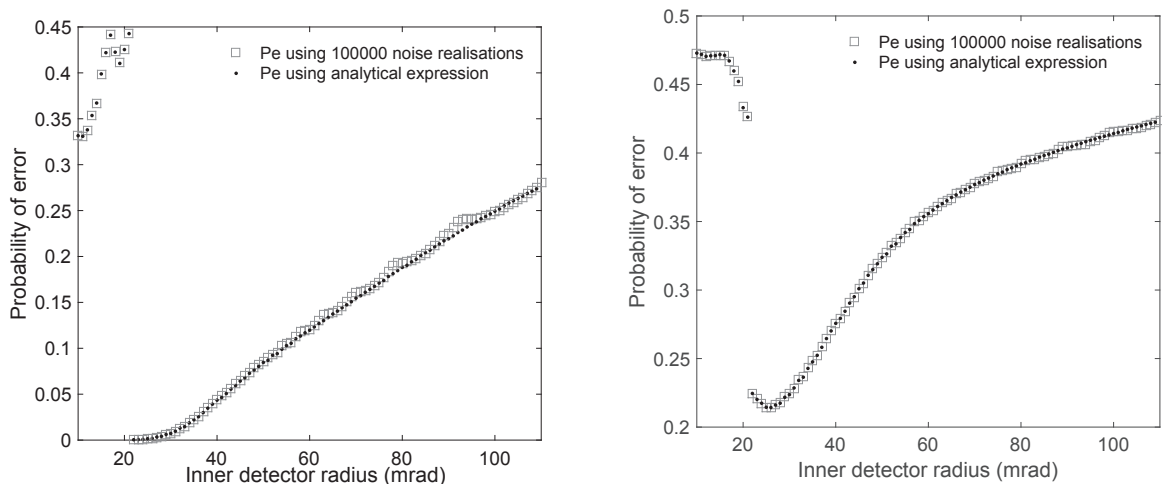


Figure 4.6: The probability of error for identifying either Al and Ti (left) or Ti and Mn (right) as a function of the inner detector radius, calculated using the analytical expression and using noise realisations.

4.4 Statistical experiment design for identifying the atomic number of atom columns in a specimen

In the previous examples it was shown that the tools of statistical detection theory can be applied to optimise the experiment design for identifying the atomic number for a single isolated atom in HRSTEM. Therefore, the next goal was to investigate if our quantitative method is also applicable for identifying atoms in a crystal. As a further application to demonstrate our method, we looked at the interface of a $\text{SrTiO}_3/\text{LaAlO}_3$ substrate, which is an interesting case study since such interfaces are known to exhibit a plethora of exceptional properties [224]. If we want to decide whether there is a Ti or Al atom column at the interface, we can describe this problem using the same binary hypothesis test as for the isolated atom cases, with hypotheses: $\mathcal{H}_0 : Z = \text{Al}$ and $\mathcal{H}_1 : Z = \text{Ti}$. Since nowadays, simulations are sufficiently accurate to describe experimental images [76,78,225,226], we demonstrate our method through realistic simulations of the interface which are performed by the simulation software STEMsim developed by Prof. Dr. A. Rosenauer [201]. The crystal interface is simulated using the multislice approach and TDS is taken into account using the absorptive potential method described in section 2.7.2.

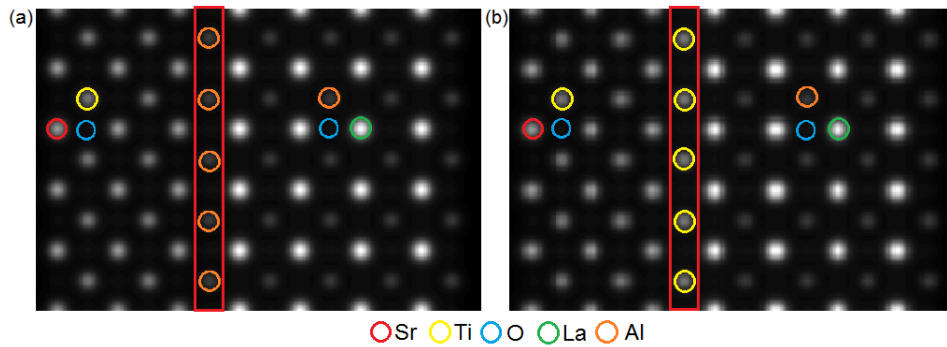


Figure 4.7: Simulated HRSTEM images of the $\text{SrTiO}_3/\text{LaAlO}_3$ compound with (a) Al atoms or (b) Ti atoms at the interface for the optimal detector collection range of 23-100 mrad.

Similar as before, the STEM detector settings can be optimised in order to minimise the probability to choose the wrong hypothesis. A 1.6 nm thick crystal is simulated with either Al or Ti atoms at the interface. The simulation parameters are listed in Table 4.3 and an example of the expectation model is shown in Figure 4.7 for an annular detector collection range of 23-100 mrad. Using equation (3.57), the probability of error can be calculated for different detector settings. Now, we computed the probability of error as a function of not only the inner, but also the outer radius of the annular STEM detector. The inner detector radius is varied from 0-99 mrad, while the outer detector radius is varied between 1-100 mrad. The results are presented in Figure 4.8.

Based on this figure we find that the suggested optimal detector setting lies in the low angle annular dark field (LAADF) regime, with the inner detector angle just larger than the probe forming angle (from 23-100 mrad). Hovden and Muller [69] also found that for well-resolved and atomically-thin specimens, the LAADF detector can provide a significant increase in SNR over other common detector geometries including ABF and BF. The values of the probability of error in the different optimal regions are summarised in Table 4.2.

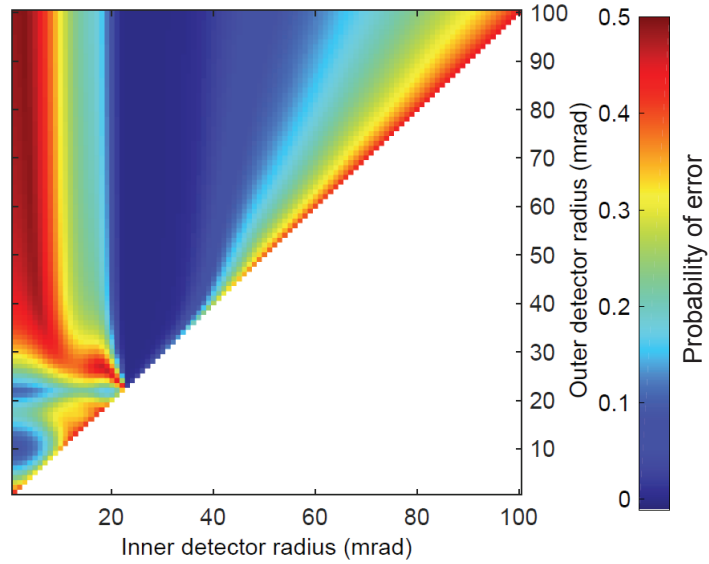


Figure 4.8: P_e as a function of the inner and outer detector angle at Scherzer conditions for an incoming electron dose of $2000 e^-/\text{\AA}^2$ at 300 kV and a probe semi-convergence angle of 21.8 mrad for identifying Al or Ti at the interface of a 1.6 nm thick $\text{SrTiO}_3/\text{LaAlO}_3$ compound.

Optimum (mrad)	P_e
1-10	0.0865
1-22	0.1074
23-25	0.00047
23-100	5.11 e-09

Table 4.2: Values for the probability of error at different detector ranges.

Parameter	Symbol	Value
Defocus	f (nm)	-8.301
Spherical aberration	C_s (mm)	0.035
Slice thickness	z_{slice} (Å)	0.975
Debye-Waller factor	B_{Sr} (Å ²)	0.6214
	B_{Ti} (Å ²)	0.4398
	B_{Al} (Å ²)	0.604
	B_{La} (Å ²)	0.8563
	B_O (Å ²)	1.152
Acceleration voltage	V_0 (kV)	300
Semi-convergence angle	α (mrad)	21.7
Probe sampling distance (x -direction)	Δx (Å)	0.061
Probe sampling distance (y -direction)	Δy (Å)	0.057
Incident electron dose	N (e ⁻ /Å ²)	2000
FWHM of the source image	$FWHM$ (Å)	0.7
Total number of scanned pixels	$K \times L$	400 × 250

Table 4.3: Parameter values used in the STEMsim software for the simulation of the SrTiO₃/LaAlO₃ interface.

4.5 Conclusions

In this chapter, we first compared two quantitative criteria which were proposed in chapter 3, i.e. the probability of error and the Kullback-Leibler divergence, in order to estimate the atomic number of a single isolated atom. Both criteria gave consistent results, however, in contrast to the Kullback-Leibler divergence, the probability of error contains also information on the overlap between different probability distributions and is therefore a more preferable measure. The analytical expression of the probability of error makes the need for an alternative criterion redundant, and it is then applied to optimise the STEM detector design in order to estimate the atomic number of atoms at the interface of a crystalline specimen. In the case of deciding between the presence of two different atom types, both for a single isolated atom or for atom columns at an interface of a thin crystal, the LAADF STEM detector setting is proposed as optimal annular detector setting based on our quantitative approach. This detector setting was also suggested elsewhere based on visual interpretation [69]. Not only the optimal detector regime is found using this quantitative approach, but even optimal detector angles follow from the proposed method.

In conclusion, our quantitative method can be applied to a wide range of materials applications in order to provide objective suggestions for the inner and outer angle of the annular STEM detector for atomic number estimation with the lowest probability of error.

5 Statistical Experiment Design to Detect and Locate Light Atoms

5.1 Introduction

The theoretical tools to derive the limits to the precision with which unknown structure parameters can be estimated from HR(S)TEM images are derived in chapter 3. In chapter 4, these quantitative tools have been used in order to identify the chemical composition, i.e. by estimating the atomic number Z , of both a single isolated atom and of atom columns in a crystalline specimen. Here, the same quantitative approach will be applied to explore some other interesting research goals, more precisely to investigate the optimal statistical experimental settings in order to detect and locate light atom columns from HR(S)TEM images¹. In the case of HRSTEM, this will provide us information on where in the detector plane the most sensitive region is located, while in the case of HRTEM the optimal values for the spherical aberration and defocus are derived, for detecting and locating light atom columns.

Since light elements play a key role in many technologically important materials, such as lithium-battery devices or hydrogen storage applications, much effort has been made to optimise the STEM technique in order to detect light elements. Therefore, classical performance criteria, such as contrast or signal-to-noise ratio, are often discussed hereby aiming at improvements of the direct visual interpretability. However, when images are interpreted quantitatively, one needs alternative criteria based on statistical detection theory or the concept of Fisher information, which will be evaluated and compared in this chapter for different applications. Using realistic simulations of technologically important materials,

¹Part of the results presented in this chapter is published in *J. Gonnissen, A. De Backer, A.J. den Dekker, J. Sijbers and S. Van Aert, Detecting and locating light atoms from High Resolution Scanning Transmission Electron Microscopy images: The quest for a single optimal design, *Ultra-microscopy*, 170, 128-138 (2016).*

we demonstrate the benefits of the proposed methods and compare the results with existing approaches.

This chapter is organised as follows. In section 5.2, binary hypothesis testing is applied to optimise the detector design in HRSTEM in order to both detect the lightest H atom. Next, it is investigated if the same optimal experiment design is found in order to detect and locate light elements from HRSTEM images in section 5.3, and from HRTEM images in section 5.4. In section 5.5, conclusions are drawn.

5.2 Detecting the lightest element H

In the previous chapter, results are presented for the optimal statistical experimental settings for identifying the atomic number from HRSTEM images, more precisely in the case where one needs to distinguish between two different atomic numbers. The next step in this research was then to investigate if the applied quantitative approach could also be useful to optimise the experiment design to detect light elements in HRSTEM images. For this application, the hypotheses in the binary hypothesis test had to be reformulated in such a way that the question to investigate became whether there is an atom present or not. Both hypotheses are then given by $\mathcal{H}_0 : Z = Z_0$ and $\mathcal{H}_1 : Z \in \emptyset$. Translated into a binary hypothesis test, this gives us the second case in equation (3.32).

As a first test for this research goal, the crystal YH_2 was investigated, which is referred to as one of the most thermodynamically stable hydrides [23]. Yttrium hydride is a material which exists in several forms, the most common being a metallic compound with formula YH_2 . YH_2 has a face centred cubic structure, and is a metallic compound. Under great pressure, extra hydrogen can combine to yield an insulator with a hexagonal structure, with a formula close to YH_3 [227]. In 1996, it was shown that the metal-insulator transition when going from YH_2 to YH_3 can be used to change the optical state of windows from non-transparent to transparent [228], which caused a wave of research on metal hydride-based chromogenic materials [229].

For this material we consider the problem of optimising the annular STEM detector in order to detect the lightest H atom. One has been able to experimentally detect H in this material using ABF STEM detector settings [23], and it was our

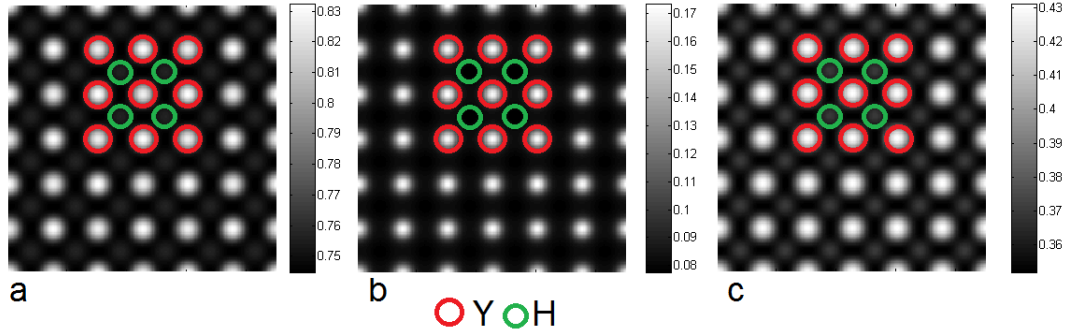


Figure 5.1: Simulated HRSTEM images of a YH_2 unit cell viewed from the $[010]$ direction, for annular detector collection ranges of (a) 11-53 mrad, (b) 22-53 mrad = ADF and (c) 11-17 mrad = ABF.

goal to find out if we would obtain the same optimal detector type, or even better the exact optimal detector angles, using our quantitative approach. The expectation models are simulated using STEMsim [201] both for the crystal in the presence and absence of hydrogen, corresponding to the hypotheses $\mathcal{H}_0 : Z = 1$ and $\mathcal{H}_1 : Z \in \emptyset$. The used simulation parameters are listed in Table 5.1, and examples of simulated HRSTEM images are shown in Figure 5.1 for three different detector settings. Note that in Figure 5.1(c) the contrast is not reversed, as one would maybe expect for the considered detector range. However, the contrast in the ABF STEM regime only inverts when the coherent contribution to the signal is higher as compared to the incoherent signal, which depends on several parameters like the crystal thickness, the atom types present in the crystal and the exact inner and outer detector angles.

The log-likelihood ratio $\ln LR(\mathbf{w})$ defined by equation (3.53) is calculated for the probability distributions under both hypotheses. The log-likelihood ratio distributions are shown in Figure 5.2 for detector collection angles of (a) 11-53 mrad, (b) 22-53 mrad, and (c) 11-17 mrad in case of the presence (red) and absence (green) of H in YH_2 . The red and green coloured areas correspond to the probability of deciding \mathcal{H}_0 while \mathcal{H}_1 is true and the probability of deciding \mathcal{H}_1 while \mathcal{H}_0 is true, respectively, and the sum of both areas represents the probability of error. Using the analytical expression defined by equation (3.57), the probability of error was computed as a function of the inner and outer detector angle.

Results of the probability of error for the detection of H in YH_2 are shown in Figure 5.3. As an optimal detector setting, the ABF STEM regime is indeed found when following our quantitative approach with a detector ranging from 11 to 17

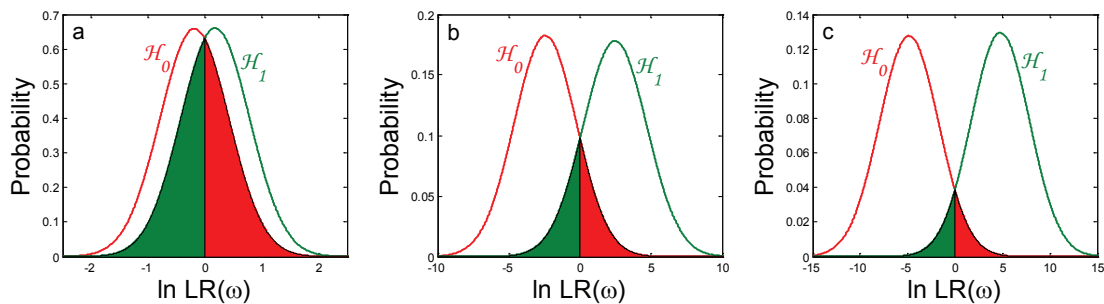


Figure 5.2: Log-likelihood ratio distributions for detector collection angles of (a) 11-53 mrad, (b) 22-53 mrad or ADF and (c) 11-17 mrad or ABF, for the presence (red) and absence (green) of H in YH_2 .

mrad. Also a local optimum is observed in the LAADF regime with both inner and outer detector radius larger than the probe semi-convergence angle (for 23-28 mrad).

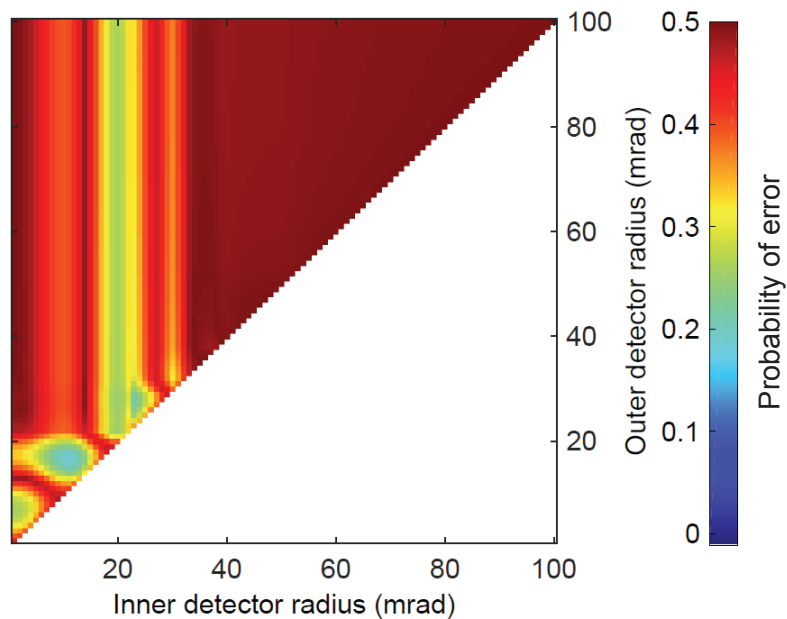


Figure 5.3: P_e as a function of the inner and outer detector angle at Scherzer conditions for an electron dose of $2000 e^-/\text{\AA}^2$ at 300 kV and a probe semi-convergence angle of 21.8 mrad for the detection of H in a 2.6 nm thick YH_2 crystal.

Parameter	Symbol	Value
Defocus	f (nm)	-8.301
Spherical aberration	C_s (mm)	0.035
Slice thickness	z_{slice} (Å)	2.6
Debye-Waller factor	B_Y (Å ²)	0.6
	B_H (Å ²)	1.5
Acceleration voltage	V_0 (kV)	300
Semi-convergence angle	α (mrad)	21.7
Probe sampling distance (x -direction)	Δx (Å)	0.069
Probe sampling distance (y -direction)	Δy (Å)	0.069
Incident electron dose	N ($e^-/\text{Å}^2$)	2000
FWHM of the source image	$FWHM$ (Å)	0.7
Total number of scanned pixels	$K \times L$	75×75

Table 5.1: Parameter values used in the STEMsim software for the simulation of YH₂.

5.3 Detecting versus locating light atoms in HRSTEM

The next interesting question in our research was to investigate if both detecting light atoms with the lowest probability of error and locating them with the highest possible precision, would lead to the same optimal experiment design. To illustrate the concept, the problem of suggesting optimal detector settings to detect the lithium atoms in LiV_2O_4 is considered, as well as detecting the oxygen in SrTiO_3 . Therefore, a binary hypothesis test is performed where both hypotheses correspond to either the presence or absence of the oxygen or lithium atoms in the crystal. The probability of error can then be calculated as a function of the experimental settings, in order to derive the optimal statistical experiment design. After optimal experiment designs have been obtained for the detection of the oxygen and lithium columns, a detailed simulation study is performed for the same crystals LiV_2O_4 and SrTiO_3 , where the question is for which detector design the lithium and oxygen columns can be located from HR STEM images with ultimate precision. This analysis is based on the Cramér-Rao lower bound, defined in section 3.3.2. The precision with which the atomic column coordinates can be measured is represented by the diagonal elements of the CRLB. Since both diagonal elements of the CRLB are equivalent for the investigated crystals in this section, as the x - and y -axes are convertible, the first one which corresponds to the lower bound on the variance of the x -coordinate of the atomic column position, is chosen as optimality criterion. The highest precision to locate a column is then given by the lower bound on the standard deviation of the estimated atomic column position, defined by the square-root of the criterion that is minimised, $\sqrt{\text{CRLB}_{11}}$.

Furthermore, both research questions are investigated as a function of the incoming electron dose. This allows one to investigate which electron dose is ultimately required to detect and locate light atoms with sufficient statistical significance.

5.3.1 Practical implementation of the CRLB

To calculate the partial derivatives in the expression for the Fisher information matrix, given by equation (3.20), different HR(S)TEM images for the LiV_2O_4 and SrTiO_3 crystals are simulated, where the central lithium or oxygen column in the field of view is shifted both in the x - and y -direction. The partial derivatives are

then approximated using the finite difference method:

$$\frac{\partial \lambda_{kl}}{\partial \theta} \approx \frac{\lambda_{kl}(\theta) - \lambda_{kl}(\theta - h)}{h}. \quad (5.1)$$

The order of magnitude of the shift h is chosen to be of the same order as the root-mean-square displacement u , which can be calculated since the Debye-Waller factors B are known. For the lithium atoms in LiV₂O₄, B_{Li} equals 1.10 Å² [3], and for the oxygen atoms in SrTiO₃, B_O equals 0.7323 Å² [230, 231]. The root-mean-square displacement is then given by [232]:

$$u = \sqrt{\frac{B}{8\pi^2}}. \quad (5.2)$$

In the case of locating lithium in the crystal LiV₂O₄, the value for the shift h in equation (5.1) is set to 0.1648 Å in the x -direction and 0.1665 Å in the y -direction, corresponding to the x - and y -dimension of the pixel size of the simulated LiV₂O₄ crystal. For a lower value of the shift h , the numerical approximation of the derivative did not improve any further. In the case of locating oxygen in the crystal SrTiO₃ the value for the shift h is analogously set to 0.1562 Å, which equals the x - and y -dimension of the pixel size of the simulated crystal.

5.3.2 Detecting and locating Li in LiV₂O₄

As a first interesting application, we look at the material LiV₂O₄, where we want to investigate if the same optimal detector settings are found for both detecting and locating the light lithium atoms from HRSTEM experiments.

Rechargeable lithium-ion batteries are key components of many electronic applications. As lithium ions are inserted into or extracted from host materials during battery operation, the spinel structure of LiM₂O₄, for M being a transition metal ion like vanadium, could provide an appropriate three-dimensional tunnel for lithium diffusion [233, 234] and therefore it has potential as a cathodic material for batteries. However, implementation of such a material has been delayed due to its limited cycling and unsatisfactory storage performance at elevated temperatures [1]. In order to be able to improve battery performance, it is a necessary step to investigate these materials and the behaviour of lithium atoms in and around these host materials.

Several studies have shown that ABF STEM made it possible to visualise the lithium atom columns in LiV₂O₄ (space group of $F_{d\bar{3}m}$ and lattice constant of

0.824 nm) [3, 12, 57, 90] and therefore, it was our goal to investigate if we would find the same optimal detector range for detecting and locating lithium in this material, using our quantitative approach.

Detecting Li in LiV_2O_4

In [3], individual lithium columns could be visualised using ABF STEM for an acceleration voltage of 300 kV and a sample thickness of 2.9 nm. In order to compare with these results, we optimised detector settings for an accelerating voltage of 300 kV and the same crystal thickness. In addition, since one could prefer to perform this experiment at a lower voltage in order to reduce beam damage, we also optimised the design for an accelerating voltage of 80 kV. The commonly used accelerating voltage of 300 kV and the lower value of 80 kV were selected as they have also been used before in literature to experimentally image individual lithium columns [11]. For this crystal the two hypotheses in the performed binary hypothesis test, $\mathcal{H}_0 : Z = 3$ and $\mathcal{H}_1 : Z \in \emptyset$, now correspond to the presence of a lithium atom and the absence of an atom of any type, respectively.

The expectation models under both hypotheses are simulated for a probe semi-convergence angle of 21.7 mrad, an electron dose of $2000 e^-/\text{\AA}^2$, a spherical aberration of 1 micron with Scherzer defocus and an acceleration voltage of 300 kV. Simulations at 80 kV are also performed for a probe forming aperture angle of 21.7 mrad, a spherical aberration of 1 micron and Scherzer conditions for the defocus. Source size broadening is taken into account by convoluting point source images with a Gaussian function with FWHM = 0.7 Å. All other parameters used for the simulation of LiV_2O_4 , viewed from the [110] direction, are listed in Table 5.2. Simulated HRSTEM images of a crystal unit cell of LiV_2O_4 are shown in Figure 5.4 for three different detector settings. Note that the scale is different for the three detector settings, since the amount of signal changes with the detection area.

The probability of error for the detection of the light lithium atom column in a LiV_2O_4 crystal was computed for a whole range of detector inner and outer angles (0-99 mrad and 1-100 mrad, respectively), for three different crystal thicknesses of 1.17 nm, 2.91 nm and 4.66 nm, corresponding to a column of respectively 2, 5 and 8 Li atoms thick, and an incoming electron dose of $10^5 e^-/\text{\AA}^2$, for both considered accelerating voltages of 300 kV and 80 kV. As the behaviour of the probability of error did not seem to change significantly after an outer detector radius

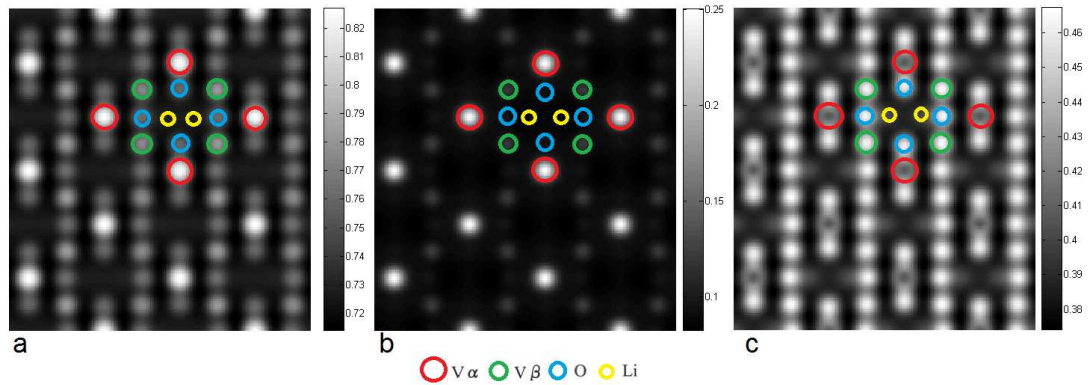


Figure 5.4: Simulated HRSTEM images of a LiV_2O_4 unit cell viewed from the $[110]$ direction, for annular detector collection ranges of (a) 12-53 mrad, (b) 22-53 mrad = ADF and (c) 12-18 mrad = ABF.

of 100 mrad, calculations have only been performed up to this outer detector angle in order to limit the computation time. This can be understood as scattering to the high detector angles is dominated by inelastic TDS scattering, which varies smoothly with the detector range at high angles. The results of the probability of error for the detection of lithium in LiV_2O_4 at 80 and 300 kV are shown in Figure 5.5. In Figure 5.5, the optimal inner and outer detector angles to detect the lithium column are determined by the blue region where the probability of error is minimal. From the results shown in Figure 5.5, we can see that the same optimal detector range is obtained for the three thicknesses under study. It can also be seen that the optimal range of low probability of error becomes broader for detecting atomic columns in a thicker sample region, which means that it becomes less critical to optimise the detector settings to detect a lithium column when the sample region becomes thicker, what could be expected. Furthermore, when the results of both accelerating voltages are compared, it is remarkable that the range of low probability of error is much broader when working at a lower incoming electron dose. At the accelerating voltage of 80 kV, the optimal detector range covers an overlapping region of ABF and LAADF, with an inner detector angle smaller than the probe semi-convergence angle, and an outer detector angle larger than the probe forming angle. Also for this lower accelerating voltage, the optimal detector range broadens when detecting lithium in a thicker sample region. From these results, it follows that a lower accelerating voltage is favourable if one wants to detect the light lithium atoms in LiV_2O_4 .

In general, the results of the probability of error show us which area in the detec-

Parameter	Symbol	Value
Defocus	f (nm)	-1.4 (or -2.04)
Spherical aberration	C_s (mm)	0.001
Slice thickness	z_{slice} (Å)	1.46
Debye-Waller factor	B_{Li} (Å ²)	1.1
	B_V (Å ²)	0.01
	B_O (Å ²)	0.48
Acceleration voltage	V_0 (kV)	300 (or 80)
Semi-convergence angle	α (mrad)	21.7
Probe sampling distance (x -direction)	Δx (Å)	0.165
Probe sampling distance (y -direction)	Δy (Å)	0.167
Incident electron dose	N (e ⁻ /Å ²)	10 ⁵
FWHM of the source image	$FWHM$ (Å)	0.7
Total number of scanned pixels	$N \times M$	50 × 35

Table 5.2: Parameter values used in the STEMsim software for the simulation of LiV₂O₄.

tion plane is most sensitive for detecting light elements. From the results shown in Figure 5.5, it is clear that the overall optimal detector range for the detection of lithium at 300 kV is the LAADF STEM regime, where the inner detector radius is slightly larger than the probe semi-convergence angle of 21.7 mrad. Here, also local optima are found in the ABF STEM regime, where the inner and outer detector radii are both lying within the illumination cone. This was also suggested elsewhere [3, 12, 23, 56, 57, 85, 158]. For the acceleration voltage of 80 kV, the optimal range becomes broader and both covers inner angles that lie in the LAADF and ABF STEM regime.

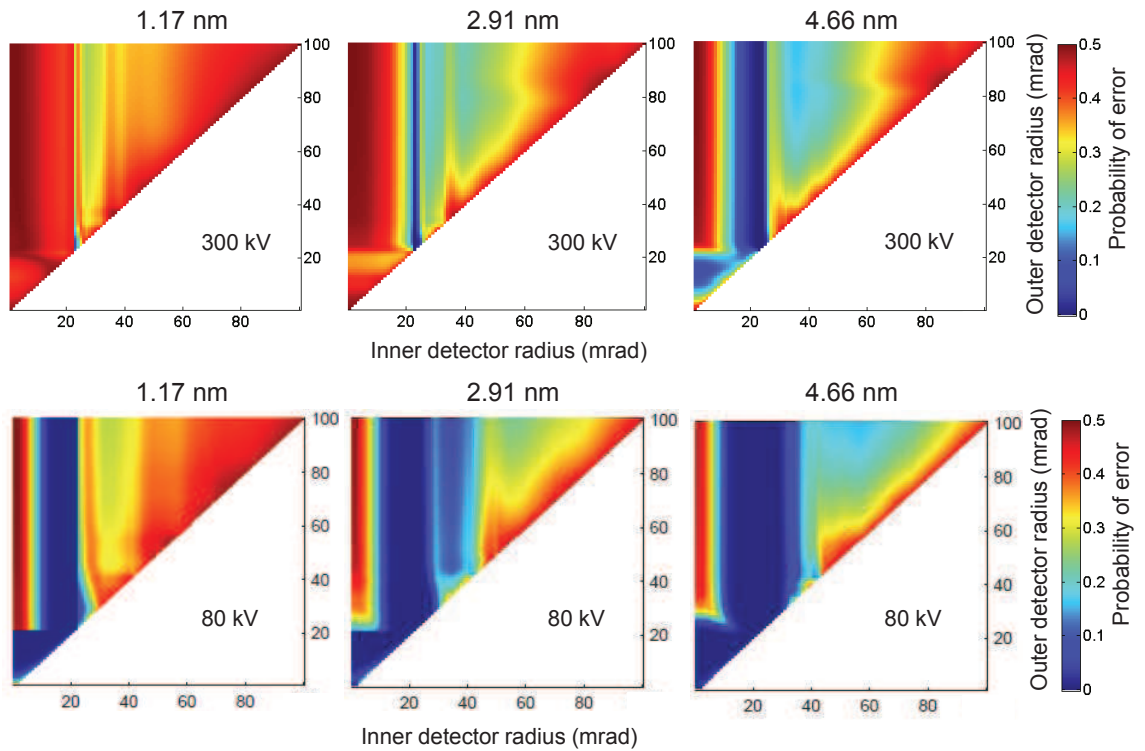


Figure 5.5: The probability of error to detect Li in a 1.17 nm, 2.91 nm and 4.66 nm thick LiV_2O_4 crystal respectively using a binary hypothesis test, for an incoming electron dose of $10^5 e^-/\text{\AA}^2$ and accelerating voltage of 300 kV (upper row) and 80 kV (lower row). On the horizontal axes, the inner detector radius is shown and on the vertical axes the outer detector radius, both in mrad.

Locating Li in LiV_2O_4

The ultimate precision with which the position of the pure lithium column in LiV_2O_4 can be determined was calculated for an accelerating voltage of 300 kV, an incoming electron dose of $10^5 e^-/\text{\AA}^2$, for an inner STEM detector radius going from 0-99 mrad and an outer STEM detector radius varying from 1-100 mrad. All other simulation parameters are given in Table 5.2. This electron dose was chosen in order to retrieve an ultimate precision that lies in the picometre range, as desired. The detector settings leading to the minimum value of the $\sqrt{\text{CRLB}_{11}}$ result in the ultimate precision to locate the lithium column. Results for this ultimate precision are shown in Figure 5.6 for the same thicknesses that were investigated for the detection problem of lithium in the previous section.

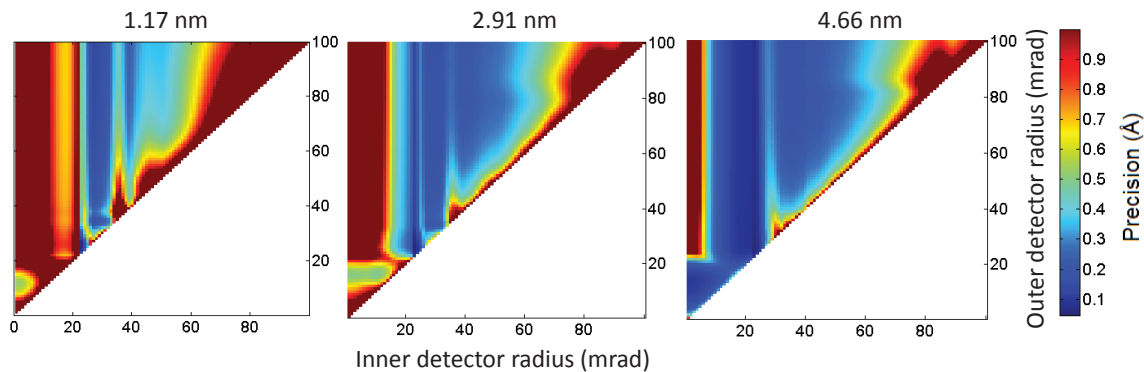


Figure 5.6: The precision with which the pure Li column can be located in LiV_2O_4 for the three different crystal thicknesses of 1.17 nm, 2.91 nm and 4.66 nm, respectively and the same incoming electron dose of $10^5 e^-/\text{\AA}^2$. On the horizontal axes, the inner detector radius is shown and on the vertical axes the outer detector radius, both in mrad. Note that the maximum value of the colourbar is set to 1 Å in order to visualise the optimal region.

From the results shown in Figure 5.6, it is clear that the overall optimal detector collection range to locate light atomic columns is LAADF STEM, which was also the optimal detector range for the detection of light elements. Local optima are again found in the ABF STEM regime for the different investigated thicknesses. From Figure 5.6 it is also clear that a better precision can be obtained for locating an atomic column in a thicker sample region. This can intuitively be understood since it is easier to determine the position of a column with a higher contrast. In addition to the result shown in Figure 5.6, a line scan is plotted of the attainable precision as a function of thickness at the optimal detector design, to better visualise the attained picometre range precision. This line scan is shown in Figure 5.7 for the same electron dose that was used in Figure 5.6.

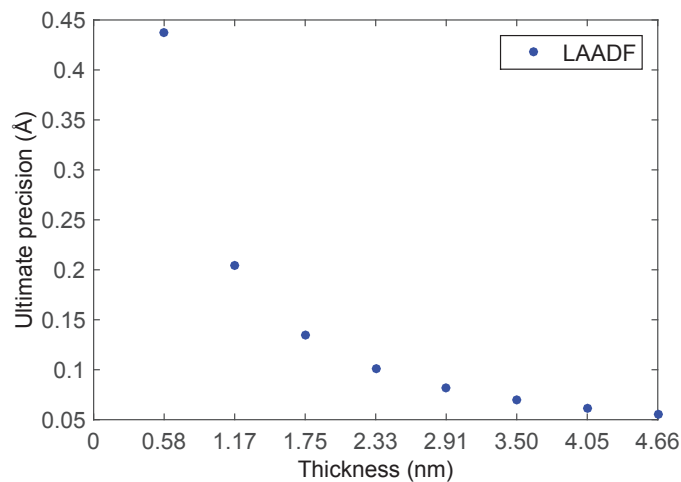


Figure 5.7: The ultimate precision to locate a Li column in LiV₂O₄ for an incoming electron dose of $10^5 e^-/\text{Å}^2$ as a function of thickness, at the optimal detector settings for detecting and locating the Li column.

5.3.3 Detecting and locating O in SrTiO₃

In the past few years, aberration-corrected STEM imaging using an annular detector located within the bright field region has been reported to visualise not only light lithium atoms like in the previous section, but also oxygen, strontium and titanium oxide columns in a SrTiO₃ crystal [56]. This ABF imaging has been shown appropriate for imaging light atom columns which are located near columns of heavy elements. Since SrTiO₃ is an excellent substrate for epitaxial growth of high-temperature superconductors and many oxide-based thin films, it is a widely studied material and an interesting crystal to investigate with our quantitative approach. The goal of this section was thus to optimise the STEM detector design to detect and locate the light oxygen atoms in SrTiO₃.

Detecting O in SrTiO₃

In the same way as for the LiV₂O₄ crystal, statistical detection theory can be applied to determine the probability of error for the detection of the light oxygen atoms in SrTiO₃. The binary hypothesis test that we then evaluate is given by the following hypotheses: $\mathcal{H}_0 : Z = 8$ and $\mathcal{H}_1 : Z \in \emptyset$ and the probability of error can again be computed as a function of the experiment design, and minimised in order to obtain the optimal STEM detector settings. The simulation param-

eters which are used for SrTiO₃ for a spherical aberration-corrected microscope are listed in Table 5.3.

Parameter	Symbol	Value
Defocus	f (nm)	-1.4
Spherical aberration	C_s (mm)	0.001
Slice thickness	z_{slice} (Å)	1.95
Debye-Waller factor	B_{Sr} (Å ²)	0.6214
	B_{Ti} (Å ²)	0.4398
	B_O (Å ²)	0.7323
Acceleration voltage	V_0 (kV)	300
Semi-convergence angle	α (mrad)	20
Probe sampling distance (x - and y -direction)	$\Delta x, \Delta y$ (Å)	0.075
Incident electron dose	N ($e^-/\text{Å}^2$)	10^4
FWHM of the source image	$FWHM$ (Å)	0.7
Number of scanned pixels for detecting O	$N \times M$	52×52
Number of scanned pixels for positioning O	$N \times M$	25×25

Table 5.3: Parameter values used in the STEMsim software for the simulation of SrTiO₃.

The results for the probability of error using a binary hypothesis test in order to detect oxygen in the crystal SrTiO₃ from a HRSTEM image are shown in Figure 5.8 for three different thicknesses and for an incoming electron dose of $10^4 e^-/\text{Å}^2$. From the results shown in Figure 5.8, it is clear that for thin crystals the optimal detector collection range corresponding to the regime of minimum probability of error is LAADF STEM, which means that the optimal inner detector angle is only slightly larger than the probe semi-convergence angle. There is also a local optimum in the ABF STEM region, where both the inner and outer detector radius are lying within the illumination cone. For thicker crystals, we can see that the optimal region broadens and the optima in the ABF and LAADF STEM regions start to overlap. Moreover, it can be seen that for the thicker crystal, there is a broader range where the probability of error is very low and does not change significantly, which indicates that it becomes less critical to optimise the detector design if one wants to detect an atomic column in a thicker sample region.

Thickness (nm)	Optimum (mrad)	P_e
1.95	2-13	0.18
	22-24	0.05
	22-100	$\propto e^{-09}$
3.91	11-20	0.051
	22-24	0.00017
	22-100	$\propto e^{-16}$
29.29	0-5	$\propto e^{-120}$
	17-21	$\propto e^{-35}$
	17-100	$\propto e^{-29}$

Table 5.4: Values for the probability of error at different detector ranges for the three investigated thicknesses.

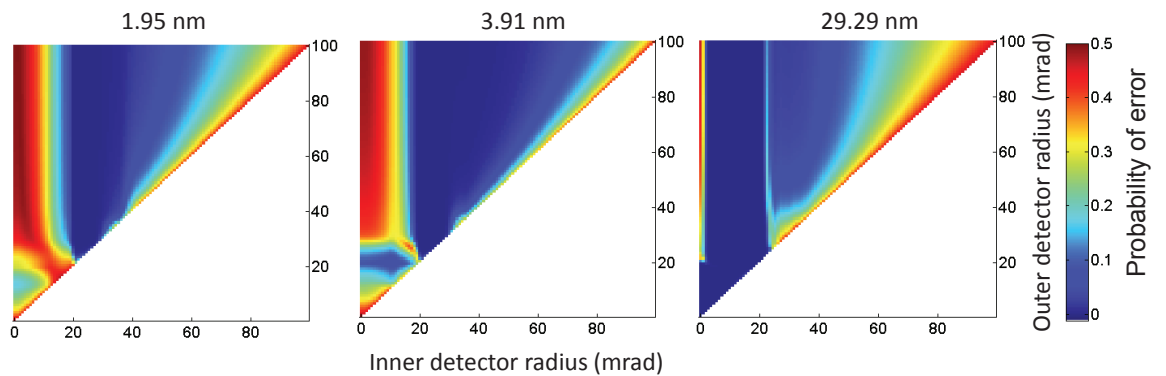


Figure 5.8: The probability of error to detect O in a 1.95 nm, 3.91 nm and 29.29 nm thick SrTiO₃ crystal using a binary hypothesis test, for an incoming electron dose of $10^4 e^-/\text{\AA}^2$. On the horizontal axes, the inner detector radius is shown and on the vertical axes the outer detector radius, both in mrad.

In order to have more insight in the results of the probability of error for detecting the light O column in SrTiO₃ shown in Figure 5.8, we show the radial integrated intensity of the CBED pattern at the position of the O column for a 3.91 nm thick SrTiO₃ crystal in Figure 5.9. In this figure, the radial integrated intensity is plot-

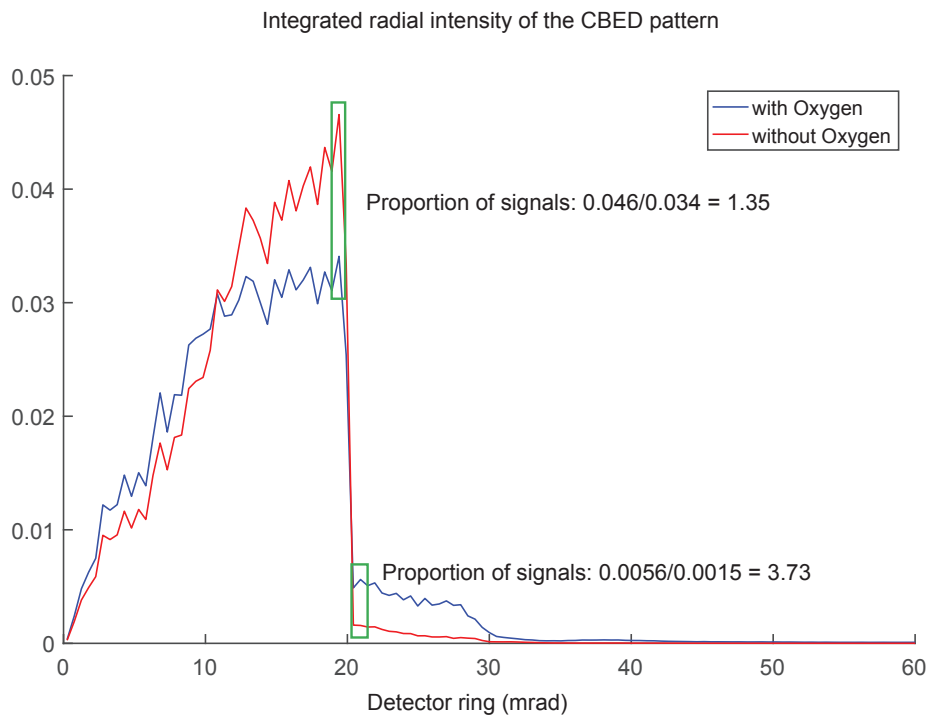


Figure 5.9: The radial integrated intensity of the CBED pattern at the position of the O column, both for the simulated model with and without O at 300 kV for a 3.91 nm thick SrTiO₃ crystal.

ted both for the model in the presence and the absence of the O column. Although only the information of one pixel of the simulated images under both hypotheses is included, this result can already provide more insight in the behaviour of the probability of error as the models under both hypotheses will differ the most at this pixel. From Figure 5.9, it is clear that the intensity shows different peaks in the ABF STEM regime, while it drops down after the detector angle has reached the probe semi-convergence angle. This is expected as from this angle on only scattered intensity will reach the detector and therefore the detected dose decreases significantly. By comparing the radial integrated intensity curves of the CBED patterns under both hypotheses, it is clear that the detector rings for which both signals are more separated correspond to the different optimal regions in the probability of error shown in Figure 5.8. In the LAADF regime, the proportion of both signals is the largest, which can explain the global minimum for the probability of error for this detector setting. Indeed, as we use purely Poisson statistics

a high proportion in signal means that the expectation values or mean values are more separated. Furthermore, the low intensity in this LAADF regime gives rise to a lower expectation value and thus also a lower variance of the probability functions under both hypotheses, resulting in a low probability of error. Note that all other results of the probability of error for detecting light atom columns in this thesis can be explained in an equivalent way. As a further illustration to understand the result of the probability of error for detecting O in a 3.91 nm thick SrTiO₃ crystal, simulated Poisson noise realisations are shown for different detector settings in Figure 5.10, for an incoming electron dose of $N = 10^4 e^-/\text{\AA}^2$.

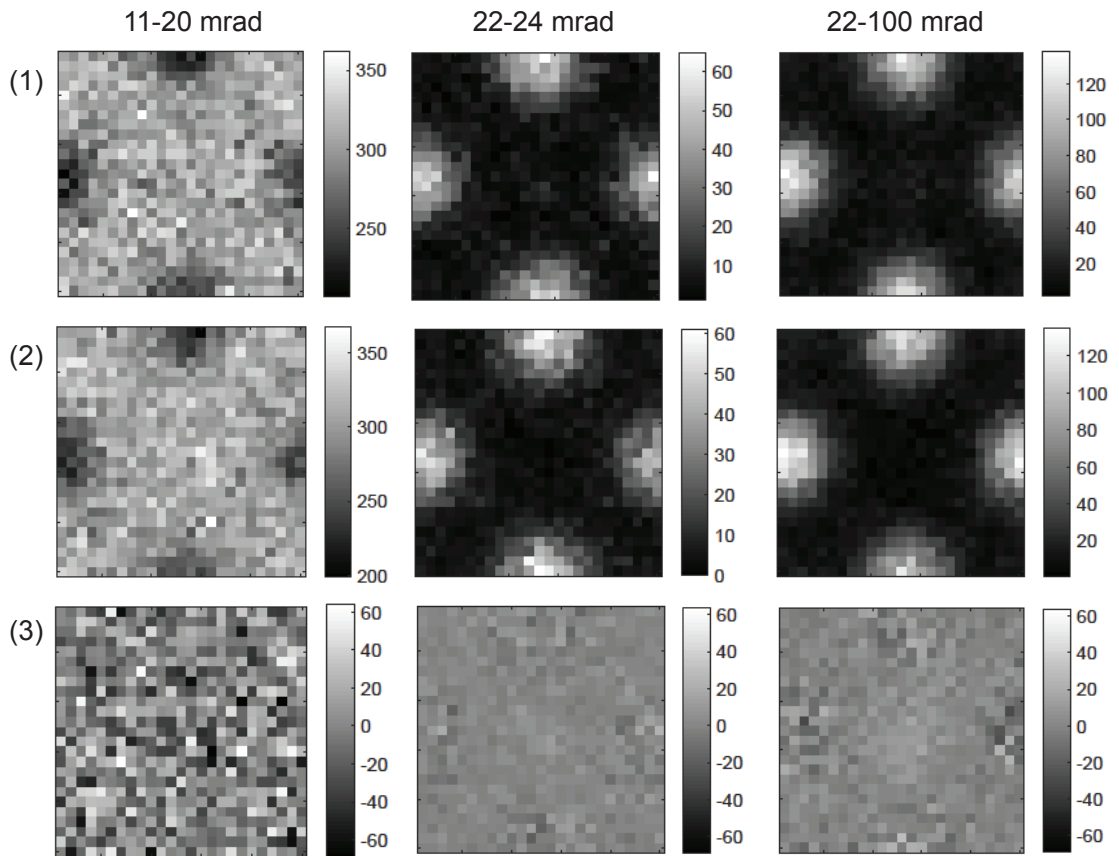


Figure 5.10: Poisson noise realisations of a 3.91 nm thick SrTiO₃ crystal (1) in the presence and (2) absence of the central O column, for an incoming electron dose of $N = 10^4 e^-/\text{\AA}^2$ and for three different detector settings. (3) Difference images of the model with and without O are shown on the same gray scale.

It is clear from the images shown in Figure 5.10 that there is still some detected dose for the small detector ring of 22-24 mrad, if the incoming electron dose is sufficiently high. However, the true optimal setting of 22-100 mrad gives a much higher detected dose which results in a much lower probability of error as compared to the 22-24 mrad setting (see Table 5.4). Furthermore, it is important to note that, even though the small detector ring of 22-24 mrad visually seems to obtain the same low probability of error as the 22-100 mrad ring for detecting O in a 3.91 nm thick SrTiO₃ crystal (Figure 5.8), the colors in the plot of the probability of error drastically scale with the incoming electron dose. This is further demonstrated in Figure 5.11, where the probability of error is shown for two lower incoming electron doses as compared to the results in Figure 5.8. For example, for a 10 times smaller incoming electron dose than for the results shown in Figure 5.8 $P_e = 0.13$ for the small ring of 22-24 mrad, while we still obtain a low value of $P_e = 0.0039$ for the setting of 22-100 mrad in this case.

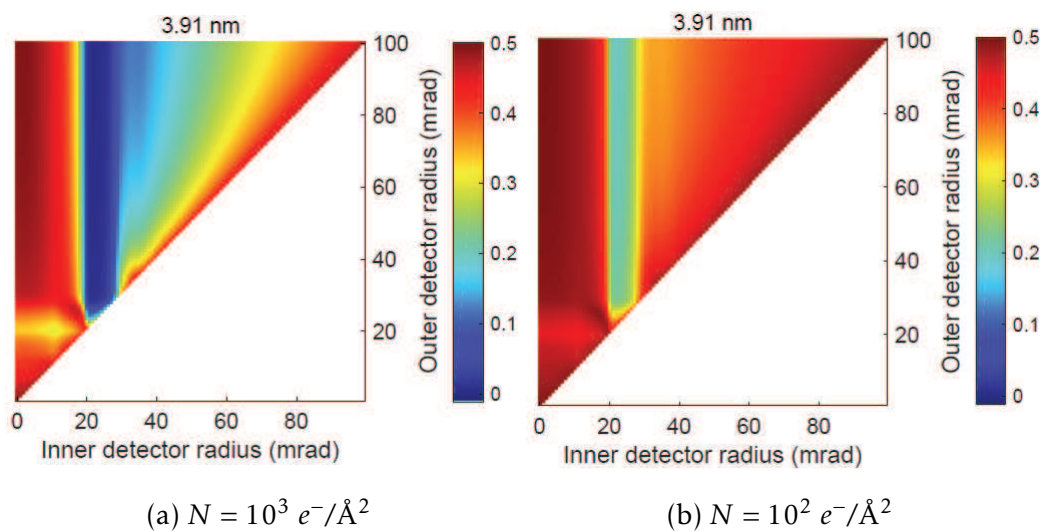


Figure 5.11: The probability of error to detect O in a 3.91 nm thick SrTiO₃ crystal using a binary hypothesis test, for two different incoming electron doses. On the horizontal axes, the inner detector radius is shown and on the vertical axes the outer detector radius, both in mrad.

Locating O in SrTiO₃

The ultimate precision with which the position of the pure oxygen column in SrTiO₃ can be determined, was calculated for an incoming electron dose of $10^4 e^-/\text{\AA}^2$, for a whole range of inner and outer detector angles for the annular STEM detector. The inner radius was varied from 0-99 mrad and the outer radius from 1-100 mrad. A lower dose as compared to the case of locating lithium in LiV₂O₄ suffices in order to obtain picometre precision, since oxygen is a heavier atom and thus gives a higher scattered intensity as compared to lithium.

In Figure 5.12 it can be seen that the overall optimal detector range is again LAADF STEM, while local optima are present in the ABF STEM regime, at least up to a thickness of 4 nm. For thicker sample regions however, both regimes broaden and start to overlap and the true optimum becomes ABF STEM. From the results shown in Figure 5.12, we can also see that a better precision can be obtained when locating an atomic column in a thicker sample region. The optimal detector settings that are obtained from the results shown in Fig. 5.12, together with the corresponding values for the ultimate precision, are given in Table 5.5.

Thickness (nm)	Optimum (mrad)	Precision (\AA)
1.95	21.7-100	0.0800
3.91	20.8-100	0.0611
29.29	0.1-6.4	0.0141

Table 5.5: Results from Figure 5.12 for the optimal detector settings for positioning O in the crystal SrTiO₃, together with the corresponding values for the ultimate precision with which the O column can be positioned for an electron dose of $10^4 e^-/\text{\AA}^2$.

In Figure 5.13 the ultimate precision is plotted to locate the pure O column in SrTiO₃ as a function of thickness, at the two optimal settings that were derived for the different considered crystal thicknesses, and for the same electron dose that was used for the results in Figure 5.12. It can be seen from this figure that from a thickness of 5 nm and larger, the optimal detector setting shifts from LAADF STEM to ABF STEM.

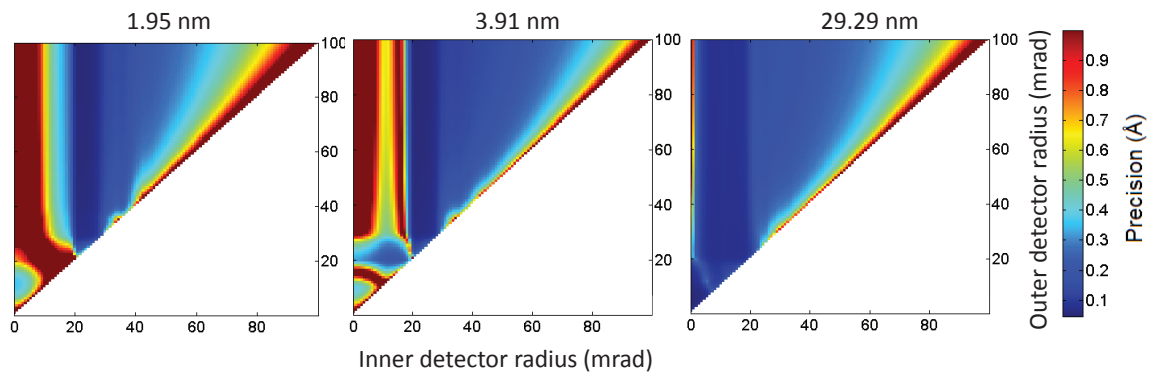


Figure 5.12: The ultimate precision to locate the pure O column in a 1.95 nm, 3.91 nm and 29.29 nm thick SrTiO₃ crystal from HRSTEM images, for an incoming electron dose of $10^4 e^-/\text{Å}^2$. On the horizontal axes, the inner detector radius is shown and on the vertical axes the outer detector radius, both in mrad. Note that the maximum value of the colourbar is set to 1 Å in order to visualise the optimal region.

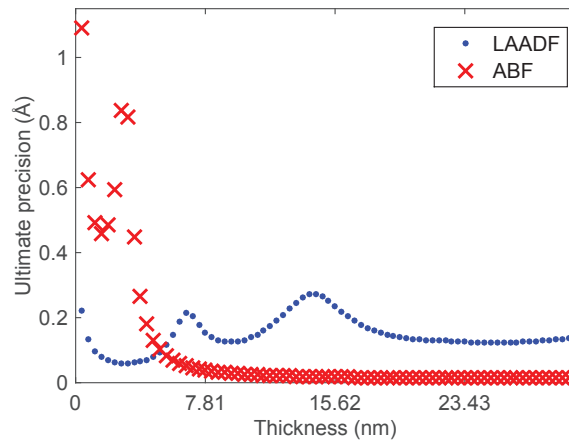


Figure 5.13: The ultimate precision to locate an O column in SrTiO₃ for an incoming electron dose of $10^4 e^-/\text{Å}^2$ as a function of thickness, at the optimal detector settings for detecting and locating the O column.

5.3.4 Detecting versus locating

Although a single optimum is found for both simulation studies in order to detect and locate light atoms, it can be seen by comparing either Figures 5.5 and 5.6 or Figures 5.8 and 5.12, that the optimal detector region becomes broader in the results of the precision, as compared to the optimal detector region where the probability of error is minimal. This suggests that it is more critical to optimise the experiment design for detecting than for locating light atoms. Therefore, as soon as the experiment design is optimised in order to detect light atomic columns, these columns can also be located with a high precision.

5.3.5 Effect of the incoming electron dose

The detectability of atomic columns as well as the precision to locate them do not only depend on the detector settings, but also on the number of incident electrons. Although the optimal detector settings are independent of the electron dose, the probability of error and the attainable precision can be further analysed as a function of the incident electron dose, both for detecting and locating atomic columns. Especially for light element crystals, the effect of radiation damage is almost unavoidable and therefore one might be interested to investigate the lowest possible incident electron dose, for which the detectability as well as the precision for locating the light atoms are sufficiently high.

From the previous results of the probability of error and the ultimate precision, we obtained a single optimal detector design to both detect and locate a lithium column in LiV_2O_4 , as desired. In Figure 5.14, results of the probability of error and the ultimate precision as a function of incoming electron dose are shown, both at the respective optimal detector settings for the different thicknesses. From the results shown in Figure 5.14(a), it is clear that the probability to choose the wrong hypothesis decreases for an increasing electron dose, as expected. If one finds a maximum probability of error of 10% acceptable, an incident electron dose of about $5500 e^-/\text{\AA}^2$ would be sufficient when using the optimal detector settings for detecting Li in LiV_2O_4 for a column of 4.66 nm. From Figure 5.14(a), it can also be seen that a higher incoming electron dose is necessary if one wants to detect a lithium column in a very thin sample region with a sufficiently low probability of error. About 7900 incoming electrons per \AA^2 are therefore necessary to detect a lithium column of 2.91 nm thick, in order to still obtain a maximum probability of error of 15 %.

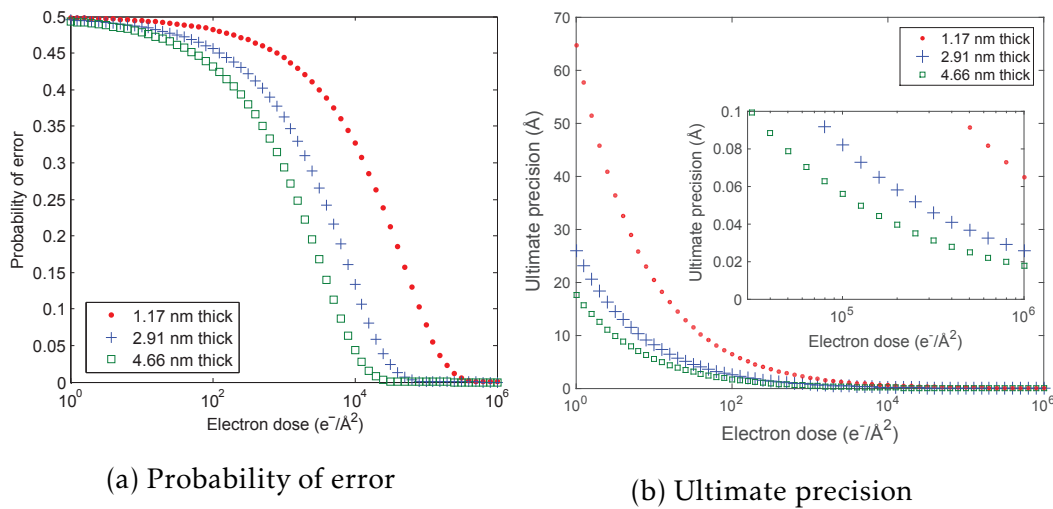


Figure 5.14: (a) The probability of error to detect a Li column in LiV_2O_4 and (b) the ultimate precision to locate a lithium column in LiV_2O_4 , both as a function of the electron dose for three different crystal thicknesses: 1.17 nm, 2.91 nm and 4.66 nm at the optimal detector settings for detecting and locating Li.

Also, for locating the lithium columns in LiV_2O_4 one can look at the effect of the electron dose on the attainable precision. Therefore, for the three different thicknesses the ultimate precision is investigated as a function of the electron dose at the optimal detector settings. Results are shown in Figure 5.14(b). It can be seen that for an electron dose of $10^5 e^-/\text{\AA}^2$, the ultimate precision lies in the picometre range as desired when the optimal detector setting for the respective crystal thicknesses is applied. If we compare Figures 5.14(a) and 5.14(b), we propose $10^5 e^-/\text{\AA}^2$ as optimal incoming electron dose. Indeed, at this incoming dose picometre precision for locating the lithium column in LiV_2O_4 is obtained, at least for thicknesses of 2.91 nm or larger. At the same time, for an electron dose of $10^5 e^-/\text{\AA}^2$ a very low probability of error of maximum 15% is found for the detection of lithium, even for a column in a very thin sample region.

For the simulation study of SrTiO_3 , the probability of error and the attainable precision can also be investigated as a function of the incident electron dose. In the same way as for the LiV_2O_4 crystal, results are shown in Figures 5.15(a) and 5.15(b) for respectively the probability of error and the ultimate precision as

functions of incoming electron dose, under the optimal detector settings for the different investigated crystal thicknesses.

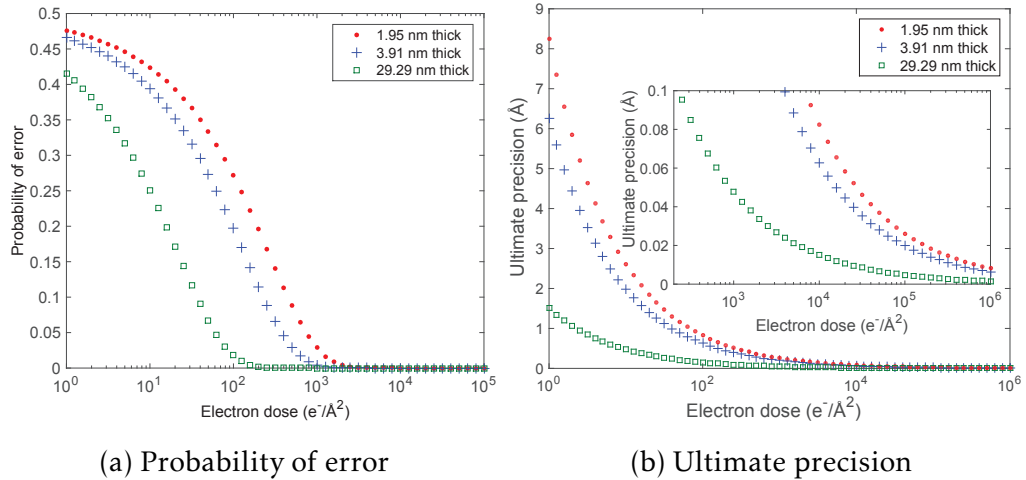


Figure 5.15: (a) The probability of error to detect the central O column in SrTiO₃ and (b) the ultimate precision to locate the O column in SrTiO₃, both as a function of the electron dose for three different crystal thicknesses: 1.95 nm, 3.91 nm and 29.29 nm at the optimal detector settings for detecting and locating O.

For detecting and locating the central O column, the probability of error and the ultimate precision both lead to the same optimal detector range as desired. Both quantities also decrease as a function of the incoming electron dose. From the results shown in Figure 5.15, it is clear that a very low probability of error is already obtainable for an incoming dose of about $10^3 e^-/\text{Å}^2$. However, a higher dose of $10^4 e^-/\text{Å}^2$ is necessary if one also wants to have picometre precision for the oxygen column position in the SrTiO₃ crystal.

From these results, it can be shown that one can tune the incoming electron dose in such a way that a sufficiently low probability of error is attained in order to detect a light atomic column, and moreover a high precision on the atomic column position is retrieved. From the results shown in Figures 5.14 and 5.15 it can also be seen that the thicker the sample region, the easier it is to detect and locate the atomic column, which is an expected result.

Note that in this work, the fundamental counting-statistics limit is established, while in a real experiment the presence of scan noise and other instabilities occur

which will make this ideal situation unlikely to be routinely realised. Indeed, environmental or instrumental disturbances such as acoustic, mechanical, or electromagnetic interference can cause all kinds of distortions in the experimental images recorded by an aberration-corrected STEM [235]. Both SNR and resolution performance are reduced due to these distortions. In addition, sample or stage drift can cause the images to appear warped which will result in unreliable lattice parameters being exhibited. Therefore, several image reconstruction codes have been developed through the years in order to correct for these features appearing in all scanning microscope techniques [235–238]. In [235], a detailed study of the origins, characteristics, and effects of imaging distortions is presented. Nowadays, different methods to compensate for scan and drift distortions exist and can be used in order to correct the recorded images. In chapter 7 of this thesis, the Smart Align code [239] is applied, which allows robust rigid and non-rigid registration of scanning microscope data using the image's numerical gradients to calculate transformations. Another proposed method to remove the damaging effects of sample drift is the Revolving STEM (RevSTEM) technique. Here, scan rotation between successive rapid frame acquisitions is introduced, as well as the projective standard deviation (PSD) method in order to track lattice vector angle distortions [240]. Very recently, another approach has been reported to compensate for non-linear effects in scanning microscope images. This method uses orthogonal scan pairs to align each measurement line-by-line along the slow scan direction, by fitting contrast variation along the lines [241]. In conclusion, different approaches are available to first compensate for scan and/or drift distortions in HRSTEM images, which will result in more precise results when applying statistical parameter estimation theory in order to derive unknown structure parameters from the corrected images.

In order to test the effect of scan noise on the result of the probability of error, a test study has been performed in which the probability of error was calculated for the detection of O in SrTiO₃ using simulated images containing both scan and Poisson noise. However, as our analytical expression for the probability of error assumes only Poisson noise to be present, the inclusion of scan noise was only possible using repetitive noise realisations which is very time-consuming. Since all image pixel values in the simulated HRSTEM images under both hypotheses are being used in the calculation of the probability of error for detecting light atom columns, only a high amount of scan noise results in a loss of information in the simulated images and therefore in an increase of the probability of error. It was found that the overall behaviour of the probability of error as a function

of the inner and outer STEM detector angles remained the same when including scan noise in the simulated images, and thus the same detector setting was found to be optimal. Therefore, all results for the probability of error in this thesis were calculated using the efficient analytical expression for the probability of error, taking only the presence of Poisson noise into account. Note, however, that when using a different performance measure than all pixel values in the HRSTEM images, such as peak intensities or scattering cross-sections, the effect of scan noise (or other image distortions) is expected to have a more significant effect on the result of the probability of error.

5.4 Detecting versus locating light atoms in HRTEM

In comparison with the results presented in the previous section, where the limits to detect and position light elements in HRSTEM have been investigated, the performance of HRTEM has been examined for the same research goals and for the same material, SrTiO₃. In the comparison between HRTEM and HRSTEM the incoming electron dose, $N(e^-/\text{\AA}^2)$, was kept the same as it is a limiting factor in both imaging modes. Certainly if one wants to detect or locate light elements from a HR(S)TEM image, the dose is a limiting parameter for the performance of both imaging modes.

In the case of HRTEM, the spherical aberration (C_s) and defocus (f) were considered as the most influencing experimental parameters, in contrast to the inner and outer detector angles of the annular STEM detector in the case of HRSTEM. The experiment design was therefore optimised by computing the probability of error and the ultimate precision as a function of spherical aberration and defocus. The optimal experiment design then corresponds to the settings that minimise the probability of error and/or the ultimate precision to locate the pure oxygen column.

Frozen lattice calculations were performed for the HRTEM image simulations, using the phase contrast transfer function for partially coherent imaging [62,169], for a whole range of spherical aberration and defocus values. The simulation parameters that were used are listed in Table 5.6, and the investigated thicknesses are the same than the ones in section 5.3, 1.95 nm, 3.91 nm and 29.29 nm.

Parameter	Symbol	Value
Debye-Waller factor	B_{Sr} (\AA^2)	0.6214
	B_{Ti} (\AA^2)	0.4398
	B_O (\AA^2)	0.7323
Zone orientation	[uvw]	[100]
Acceleration voltage	V_0 (kV)	300
Size of the supercell	$N_a \times N_b$ (nm ²)	4.3×4.3
Number of FP configurations	N	$9 \times 9 \times 4 \times 30$
Slice thickness	z_{slice} (\AA)	1.95
Focal spread	Δ (nm)	2.9
Semi-convergence angle of the partial coherence envelopes	β (mrad)	0.03
Pixel size	$\Delta x, \Delta y$ (\AA)	0.046488
Incident electron dose	N ($e^-/\text{\AA}^2$)	10^4
Number of pixels in the unit cell	$K \times L$	84×84

Table 5.6: Parameter values used for the TEM simulations of SrTiO₃.

Detecting O in SrTiO₃

Results of the probability of error for the detection of the pure oxygen atom column are presented in Figure 5.16, for the same three crystal thicknesses that were investigated for the optimisation of HRSTEM.

From the results shown in Figure 5.16, it is clear that detection of a light atom column in a thin sample region is hardly possible in HRTEM for the considered values for spherical aberration and defocus. However, if the sample region is thicker, the probability of error decreases significantly. The optimal statistical experiment design changes for different thicknesses. The derived optima for the three investigated thicknesses correspond to the following settings: $f = 100 \text{ \AA}$, $C_s = -0.05 \text{ mm}$ ($P_e = 0.4226$); $f = -70 \text{ \AA}$, $C_s = -0.04 \text{ mm}$ ($P_e = 0.3273$) and $f = -70 \text{ \AA}$, $C_s = 0 \text{ mm}$ ($P_e = 1.4 \text{ e-}17$), for a 1.95 nm, 3.91 nm and 29.29 nm thick SrTiO₃ crystal, respectively. As an illustration the contrast transfer function is shown in Figure 5.17 at the optimal settings for a thickness of 3.91 nm, as compared to the settings for zero defocus and spherical aberration. As expected there is no contrast transfer in the case of zero aberrations as the phase contrast imaging in TEM requires at least some aberrations (certain value for defocus and

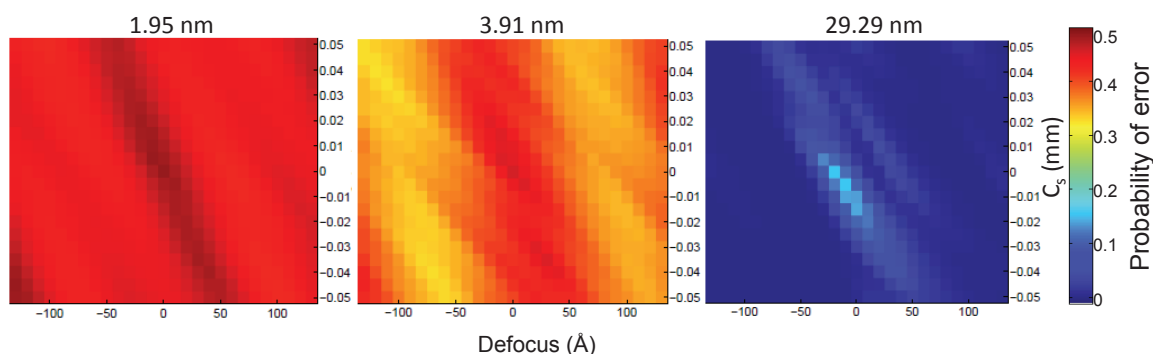


Figure 5.16: The probability of error to detect the central O column in a 1.95 nm, 3.91 nm and 29.29 nm thick SrTiO_3 crystal from HRTEM images, using a binary hypothesis test, for an incoming electron dose of $10^4 e^-/\text{\AA}^2$. On the horizontal axes, the defocus is shown and on the vertical axes the spherical aberration.

spherical aberration) in order to be able to shift the phase of the electron beam. A phase shift per se does not give rise to an image. Only the superposition of the undisturbed wave with the scattered wave leads to interference and thus to changes in intensity, which can be measured.

When comparing the results presented in Figure 5.16 with the corresponding probabilities of error for the detection of oxygen from HRSTEM, presented in Figure 5.8, we see that for the detection of oxygen in thin sample regions the probability of error is much larger in HRTEM than in HRSTEM, for the same incoming electron dose. This suggests that it is advantageous to use HRSTEM in order to be able to detect light atom columns in thin sample regions.

Locating O in SrTiO_3

To investigate the precision with which the light oxygen column can be located in a HRTEM image, use is made of the concept of Fisher information as in the previous section. The first diagonal element of the CRLB is evaluated as a function of a range of spherical aberration values and different defocus values, and gives a measure of the ultimate precision with which the unknown parameter can be estimated. The optimal statistical experiment design then corresponds with those experimental settings minimising the CRLB, or in other words maximising the ultimate precision.

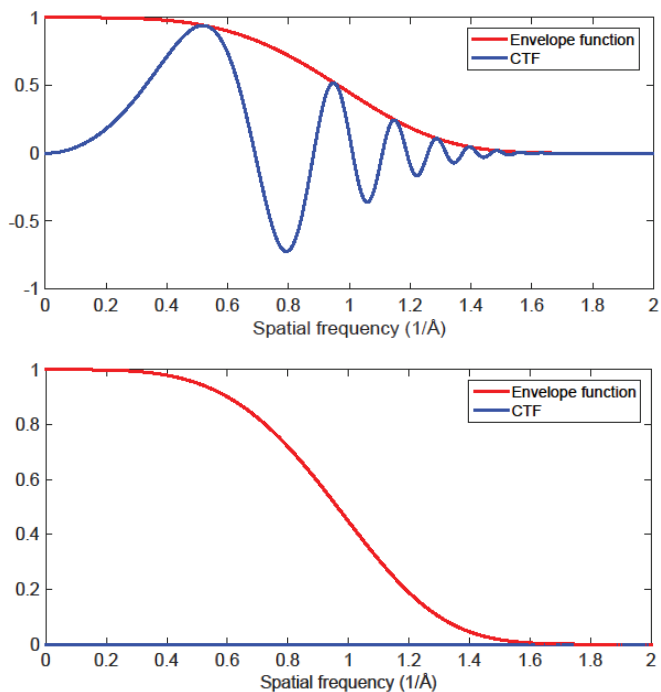


Figure 5.17: The contrast transfer function (CTF) at zero aberrations and at the optimal settings ($f = -70 \text{ \AA}$, $C_s = -0.04 \text{ mm}$) for detecting the O column in a 3.91 nm thick SrTiO_3 crystal from HRTEM images.

Results of the ultimate precision to locate the pure oxygen column in SrTiO_3 as a function of spherical aberration and defocus are shown in Figure 5.18.

From the results shown in Figure 5.18 it is clear that, in the same way as for detecting the oxygen column, the ultimate precision is much better when the light atom column is located in a thicker sample region. This can intuitively be understood since we look at the precision to locate the whole column and not a single atom within the column. As the column becomes thicker, it becomes easier to locate and thus the precision will improve. What is also shown in this Figure, is that the optimal experimental settings deviate for the different investigated crystal thicknesses. Furthermore, when comparing with the result for locating the oxygen column from HRSTEM presented in Figure 5.12, it is clear that the obtainable precision is much better in HRSTEM as compared to HRTEM for locating the oxygen column in thinner sample regions. Only for thicker sample regions, an equivalent high precision is obtained for both imaging modes. As the

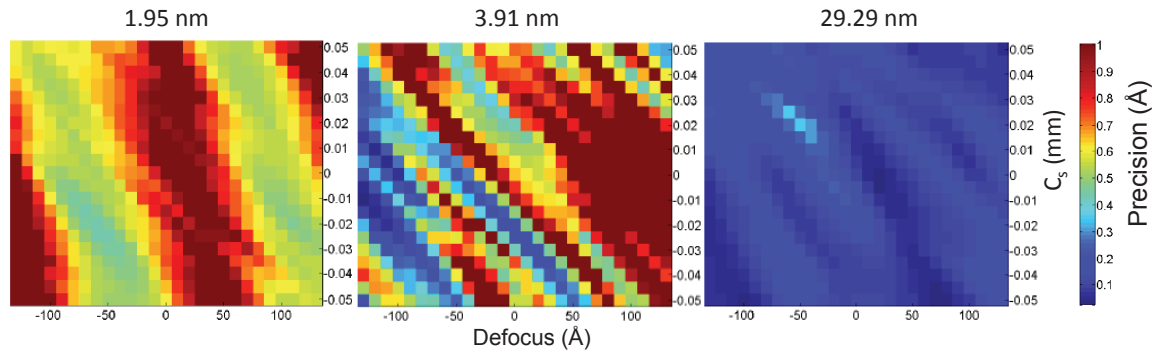


Figure 5.18: The ultimate precision to locate the pure O column in a 1.95 nm, 3.91 nm and 29.29 nm thick SrTiO_3 crystal from HRTEM images, for an incoming electron dose of $10^4 e^-/\text{\AA}^2$. On the horizontal axes, the defocus is shown and on the vertical axes the spherical aberration.

optimal settings are critical in HRTEM in order to obtain an acceptable precision, and as they deviate for different thicknesses, it is also more difficult to optimise the experiment design in practice if one would want to locate light atom columns from a HRTEM experiment, as compared to HRSTEM. The derived optima for the three investigated thicknesses correspond to the following settings: $f = -60 \text{ \AA}$, $C_s = -0.02 \text{ mm}$ ($\sqrt{\text{CRLB}} = 0.5412$); $f = -110 \text{ \AA}$, $C_s = -0.01 \text{ mm}$ ($\sqrt{\text{CRLB}} = 0.4267$) and $f = 20 \text{ \AA}$, $C_s = 0 \text{ mm}$ ($\sqrt{\text{CRLB}} = 0.0342$), for a 1.95 nm, 3.91 nm and 29.29 nm thick SrTiO_3 crystal respectively.

For HRTEM, it is found after comparing the results of Figures 5.16 and 5.18 that no single optimal setting was obtained for both detecting and locating the oxygen column in SrTiO_3 , even not for exactly the same crystal thickness. For an incoming electron dose of $10^4 e^-/\text{\AA}^2$, the probability of error was much higher as compared to HRSTEM for detecting the light column in thin specimen regions. In order to obtain a sufficiently low probability of error and picometre range precision for the detection and location problem, respectively, a higher dose would be required in the case of HRTEM. Of course, this would not always be convenient in practice, definitely not for detecting and locating light elements.

5.5 Conclusions

In this chapter, we first proposed a method based on detection theory to find the optimal experimental settings for the detection of light elements. To study the optimal design to locate these light elements, use is made of the concept of Fisher information. When combining these statistical tools, the most sensitive regions in the detection plane could be investigated for both research questions in the case of HRSTEM, which can be useful for experimentalists when choosing the appropriate camera length for their experiment. In the case of HRTEM, the most appropriate settings for spherical aberration and defocus could be derived for both detecting and locating the light oxygen column in SrTiO_3 images.

When detecting the lightest hydrogen atom, ABF STEM has been found to be the optimal detector setting, with the detection range lying within the illumination cone of the probe. Based on qualitative criteria, such as visual contrast, this setting was already suggested elsewhere for the detection of light atoms [3, 12, 23, 56, 57, 85].

Next, the crystals LiV_2O_4 and SrTiO_3 have been investigated in order to optimise the experiment design to detect and locate either a light lithium or oxygen column respectively.

For HRSTEM, the optimal detector design depends on the investigated material and the crystal thickness and corresponds to either LAADF STEM for thin specimens, or ABF STEM. When the sample region becomes thicker, both optimal regions start to overlap and, furthermore, it becomes easier to detect the light atom columns. The optimal settings obtained for locating the light atom columns using the attainable precision as optimality criterion, have been found to be consistent with the optimal settings for the detection of these light atom columns for HRSTEM imaging.

In the case of HRTEM, different optima are found for the detection of the light oxygen column in SrTiO_3 for the three investigated thicknesses. Only for the detection of light elements in thicker sample regions, optimisation of the spherical aberration and defocus becomes less critical and the optimal region broadens. However, no single optimum has been retrieved for the detection and locating problem for HRTEM imaging. Therefore, this imaging technique seems inappropriate if one wants to detect and locate light atom columns with the lowest probability of error and the highest possible precision, respectively, from a single image. Using a focal series of HRTEM images and by performing exit

wave reconstruction, precise quantitative results might be obtained, but this was not investigated in this thesis.

In addition, the minimum needed incoming electron dose has been derived for which light atoms can be detected and located with a sufficiently low probability of error and a high precision, respectively. In the case of HRSTEM, a single optimal incoming electron dose has been found for which the light elements can be detected with a low probability of error and also located with a precision in the picometre range. This optimal incoming electron dose depends on the crystal structure and thickness. For detecting and locating either Li in LiV_2O_4 or O in SrTiO_3 from HRSTEM images, an incoming electron dose of the order of $10^5 e^-/\text{\AA}^2$ or $10^4 e^-/\text{\AA}^2$ has been proposed respectively, under the optimal detector settings. It is clear that a lighter element results in a lower scattering intensity and therefore requires a higher incoming electron dose to retrieve the same ultimate precision as compared to a heavier element. Note, however, that in practice this will not always be possible as lighter elements are more beam-sensitive and will only tolerate a lower incoming electron dose.

Statistical Experiment Design for Nanoparticle Atom-Counting

6.1 Introduction

In modern technology, nanoparticles play an important role because of their unique properties, which are determined by their 3D atomic structure. The quest to find new materials with improved applications has therefore driven research the past few years to develop methods to characterise nanostructures in three dimensions with high precision. Significant advances have been made in quantitative electron microscopy, for example, by combining ADF STEM with atom-counting [75, 242–244]. Until now, different kinds of methods have been proposed and investigated to count the number of atoms of a crystalline nanostructure from HAADF STEM images. As a first attempt to solve the counting problem, Erni *et al.* [245] proposed to measure the absolute value of the intensity differences between neighbouring atom columns. LeBeau *et al.* [225, 246–249] compared simulated atom column intensities with normalised experimentally measured atom column intensities in order to count the number of atoms. Van Aert *et al.* [76] developed a new quantitative, statistical model-based method to count the number of atoms from HAADF STEM images of a structure viewed along a zone-axis. This approach may help determine the three-dimensional (3D) arrangement of atoms in crystalline nano-particles [75, 242, 243, 250, 251]. Indeed, by applying this statistical counting method and combining the results for different viewing directions, the 3D atomic structure can be attained using discrete tomography [250, 251]. Moreover, single atom sensitivity is shown to be feasible in practice using this statistical model-based method, when taking some aspects into consideration that affect the accuracy and precision with which the atoms in a column can be estimated, such as the number of atom columns available in the observed STEM image, the number of different thicknesses that has to be taken into account, and the amount of noise [77]. Combining

statistical parameter estimation theory with *ab initio* calculations [243] or Monte Carlo simulations [252] has also been shown to enable atomic resolution 3D reconstructions.

In the present chapter, we will explore the theoretical limits to the precision with which the number of atoms in a column can be estimated from HR(S)TEM images. Therefore, HR(S)TEM images are interpreted quantitatively and the optimal experiment design to count the number of atoms in a column is investigated using the principles of detection theory, which are introduced in chapter 3. The probability of error will then be evaluated as a function of the experiment design in order to optimise the experimental settings for atom-counting. In the first part of this chapter, the annular STEM detector is optimised for atom-counting from HRSTEM images based on a binary hypothesis test ¹. However, when different optimal designs are obtained for a different choice of hypotheses, one needs to move on towards multiple hypothesis testing. Therefore, in the second part of this chapter, the statistical experiment design in both HRTEM and HRSTEM is optimised for atom-counting using multiple hypothesis testing, and the possibilities and limitations of both imaging techniques are investigated and compared ².

For atom-counting, one needs a criterion that enables one to distinguish between different numbers of atoms in an atomic column. In previous work, it was shown that the total intensity of scattered electrons, the so-called scattering cross-section (SCS) is an appropriate measure for atom-counting [75–77, 146, 208]. The SCS is a more robust measure as compared to the peak intensity (PI), since it is much less affected by a small mistilt of the sample, the defocus, source coherence and other residual aberrations [220, 253]. In HRTEM, it has been shown that the number of atoms in a projected atomic column can be counted using negative spherical aberration imaging [254]. In [254], atoms were counted from HRTEM image PIs of a thin MgO crystal. The PIs in this work were extracted from small areas of 100 image pixels by fitting a Gaussian peak function to local intensity distributions around the maxima. By then comparing simulated images in an iterative

¹Part of the results presented in this chapter is published in A. De Backer, A. De wael, J. Gonnissen and S. Van Aert, Optimal experimental design for nano-particle atom-counting from high-resolution STEM images, *Ultramicroscopy*, 151, 46-55 (2015).

²Part of the results presented in this chapter is published in J. Gonnissen, A. De Backer, A.J. den Dekker, J. Sijbers and S. Van Aert, Atom-counting in High Resolution Electron Microscopy: TEM or STEM - that's the question, *Ultramicroscopy*, (2016), accepted manuscript.

best-fitting procedure with the experimental images, a quantitative comparison of the experimental and simulated peak intensities was performed in order to determine the different column thicknesses of the MgO crystal.

Ultimately, the pixel values in a HR(S)TEM image are Poisson distributed because of the presence of inherent counting noise, which sets fundamental limits to the precision with which the number of atoms can be determined. Our quantitative approach using the principles of detection theory is used to investigate the capabilities of HRTEM and HRSTEM for atom-counting. In statistical detection theory, the so-called probability of error, P_e , can be calculated as a function of the experimental parameters when comparing two or more hypotheses using a binary or multiple hypothesis test, respectively. For the atom-counting problem, the hypotheses correspond to different possible column thicknesses [208]. For the computation of this probability to miscount the number of atoms, realistic simulations describing the experimental images can be used [78, 201, 219, 225, 226, 255], together with knowledge about the statistics of the image pixel values. The experimental settings leading to the lowest probability to miscount the number of atoms then correspond to the optimal experiment design for atom-counting. To compare the probability of error for both HRTEM and HRSTEM, simulations are performed for a thin MgO crystal, as well as for a thicker SrTiO₃ crystal and a heavier Au crystal for varying experimental settings in both imaging modes.

6.2 Results from binary hypothesis testing

In this section, binary hypothesis testing is used to investigate the optimal inner detector radius of an annular STEM detector for atom-counting. The hypotheses then correspond to two succeeding column thicknesses, as in case (c) of equation (3.32): $\mathcal{H}_0 : n_{\mathcal{H}_0} = n$ and $\mathcal{H}_1 : n_{\mathcal{H}_1} = n + 1$. In Figure 6.1 the results for the probability of error from a binary hypothesis test with equal prior probabilities, defined by equation (3.33) are shown as a function of the number of atoms $n_{\mathcal{H}_0}$ in a Sr column for two different incident electron doses. The expectation models of the Sr column under the different hypotheses, i.e. for different column thicknesses, are simulated using the parameters listed in Table 6.1. The dose only changes the value of the probability of error; for a higher electron dose, the probability of error becomes lower. From the result shown in Figure 6.1, it can be seen that the probability of error increases for an increasing number of atoms. This means that it is easier to differentiate between two atomic columns containing 1 and

2 atoms than to differentiate 75 and 76 atoms in a column. Another important conclusion that can be drawn from this figure concerns the different results for the three measures which we consider. The probability of error for the scattering cross-sections (red dots) using equation (3.48) approximates well the probability of error for the STEM images on a pixel by pixel basis (blue squares) for which equation (3.57) is used, whereas the probability of error for the peak intensities (green crosses), computed using equation (3.40) is larger. This means that the scattering cross-sections contain almost the same amount of information as the images themselves in terms of atom-counting. Thus, the differences in profile of the atomic columns do not add a significant amount of extra information for atom-counting. These differences can only be detected when using the images, since the scattering cross-sections sum all the pixel values in the image into one number. This result is very beneficial since the scattering cross-sections are now often used as a measure to analyse the number of atoms in an atomic column and in addition the scattering cross-sections are far more robust to compare with simulations. Scattering cross-sections are independent of the FWHM of the source size used, the defocus etc. [220, 253].

In Figure 6.2 the probability of error is shown for the optimisation of the inner detector radius with a fixed outer detector radius of 100 mrad. In Figure 6.2(a), results for P_e are shown for $n_{\mathcal{H}_0} = 1$ for the three different measures for a Sr column. From this, we can conclude that the optimal inner detector radius equals 21 mrad since the probability of error reaches a minimum here, suggesting that imaging in the LAADF STEM regime is optimal for atom-counting. However, when choosing $n_{\mathcal{H}_0} = 75$, the optimal inner detector radius increases to 28 mrad, which can be seen in Figure 6.2(b). For this value of $n_{\mathcal{H}_0} = 75$, 21-100 mrad can definitely not be considered as an optimum, whereas for $n_{\mathcal{H}_0} = 1$ an inner detector radius of 28 mrad is near-optimal for atom-counting. Because the optimal detector design clearly depends on which two hypotheses are chosen, we should move on toward multiple hypothesis testing for atom-counting.

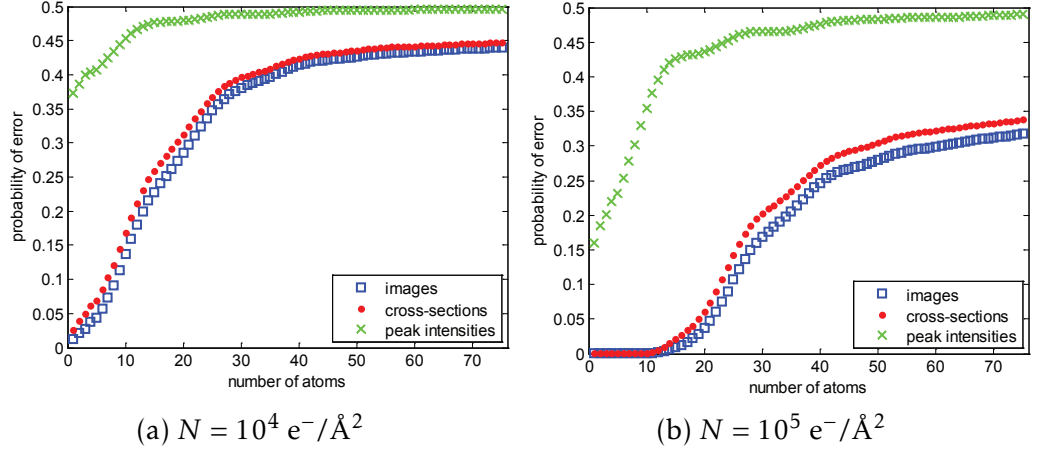


Figure 6.1: Probability of error as a function of the number of atoms in a Sr column for a detector collection range of 60 – 100 mrad and two different incoming electron doses, using a binary hypothesis test.

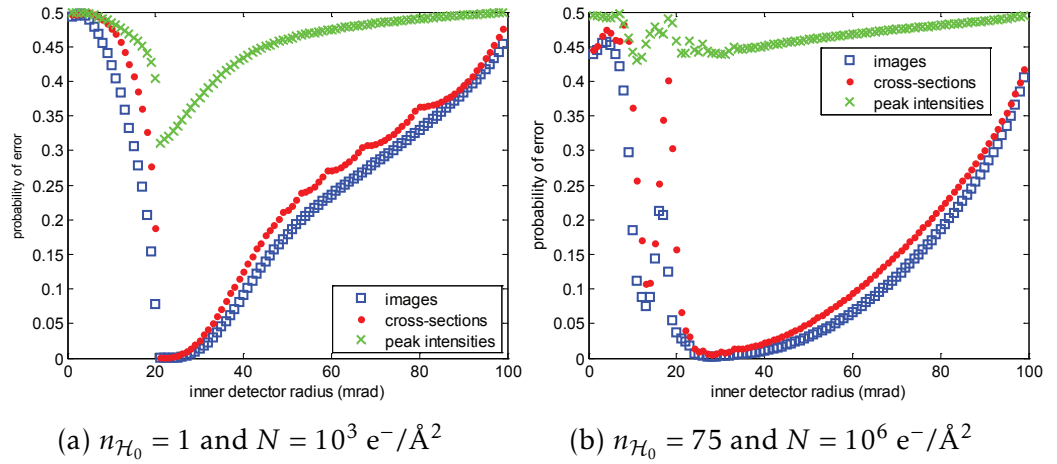


Figure 6.2: Probability of error for a Sr column as a function of the inner detector angle with a fixed outer detector radius (100 mrad) using a binary hypothesis test.

6.3 Results from multiple hypothesis testing

In this section, multiple hypothesis testing will be used to compare the capabilities of both HRTEM and HRSTEM for atom-counting. In a first comparison between both imaging techniques, the atom-counting decision was either based on the PF of the PIs for HRTEM as proposed in [254], or on the PF of the SCSs for HRSTEM as suggested in [75–77, 208, 239]. After comparing both currently used methods, it was interesting to compare with the ‘ultimate’ situation using all image intensities on a pixel by pixel basis, although this would require a much more complex atom-counting procedure. In the comparison between HRTEM and HRSTEM the incoming electron dose, $N(e^-/\text{\AA}^2)$, was kept the same as it is a limiting factor in both imaging modes. Certainly, if one wants to count the number of atoms from a HR(S)TEM image of a beam-sensitive material, the dose is a critical parameter that limits the atom-counting performance. The dose is included in the expectation models using equations (3.9) and (3.10).

6.3.1 Simulation parameters

A detailed simulation study was performed for three investigated crystals: MgO, SrTiO₃ and Au. In the case of HRTEM, the spherical aberration (C_s) and defocus (f) were considered as the most influencing experimental parameters, while for HRSTEM the inner and outer detector angles of the annular STEM detector were assumed to affect the atom-counting performance the most. The experiment design was therefore optimised by computing the probability of error as a function of either spherical aberration and defocus, or inner and outer detector angle for HRTEM and HRSTEM, respectively. The optimal experiment design then corresponds to the settings that minimise the probability of error. Absorptive potential multislice calculations were used to simulate the HRSTEM images, using settings for an aberration-corrected microscope under Scherzer defocus, for an inner STEM detector radius varying from 0-99 mrad and the outer detector radius varying from 1-100 mrad. Frozen lattice calculations were performed for the HRTEM image simulations, using the phase contrast transfer function for partially coherent imaging [62, 169], for a whole range of spherical aberration and defocus values. The absorptive potential method is used for the HRSTEM image simulations in order to save computation time, since otherwise a number of frozen phonon configurations would have to be calculated for every probe position in the scanned region. Moreover, in [209] it was shown that, for the thicknesses that we

consider here, frozen phonon and absorptive potential calculations give equivalent results, which was also shown by Rosenauer et al. in [226].

Both imaging modes will be compared in this work using detailed simulation studies. As we only perform a theoretical study under the optimal conditions, we only assume Poisson noise to be present, while scan noise is not taken into account. Furthermore, a uniform detector is assumed in the case of STEM and no modulation transfer function (MTF) or detective quantum efficiency (DQE) of the camera is taken into account for TEM. The latter is a good approximation when using Direct Detection Devices (DDD) in counting mode, as for this new generation of detectors, both the MTF and DQE are significantly improved as compared to conventional CCD cameras [256, 257]. Furthermore, in order to give HRTEM the best possible chance and make the considered assumptions more acceptable, a very small pixel size is used in the HRTEM image simulations (see Table 6.1). If one would like to compare the simulated images with experimental results, the DQE and MTF of the camera should however be taken into account in the case of TEM [258], as well as the correct exact phonon model [259–261]. In the case of STEM, the detector sensitivity should be considered and the images have to be corrected for drift and scan distortions.

The used simulation parameters are listed in Table 6.1 for MgO, SrTiO₃ and Au.

	Symbol	MgO	SrTiO ₃	Au
General parameters				
Debye-Waller factor	B (Å ²)	$B_{Mg} = 0.30$ $B_O = 0.34$	$B_{Sr} = 0.6214$ $B_{Ti} = 0.4398$ $B_O = 0.7323$	$B_{Au} = 0.6198$
Zone orientation	[uvw]	[001]	[100]	[001]
Acceleration voltage	V_0 (kV)	300	300	300
Size of the supercell	$N_a \times N_b$ (nm ²)	3.8×3.8	4.3×4.3	3.3×3.3
STEM parameters				
Slice thickness	z_{slice} (Å)	2.106	1.95	2.0391
Defocus	f (Å)	-83.01	-14.03	-83.01
Spherical aberration	C_s (mm)	0.001	0.001	0.001
Spherical aberration of 5th order	C_5 (mm)	0	0	0
Semi-convergence angle	α (mrad)	21.7	20	21.7
Pixel size	Δx (Å)	0.2106	0.1562	0.20391
FWHM of the source image	$FWHM$ (Å)	0.7	0.7	0.7
Number of pixels in the unit cell	$K \times L$	20×20	25×25	20×20
TEM parameters				
Number of FP configurations	N	$7 \times 7 \times 4 \times 30$	$9 \times 9 \times 4 \times 30$	$7 \times 7 \times 4 \times 30$
Slice thickness	z_{slice} (Å)	2.106	1.95	2.039
Focal spread	Δ (nm)	2.9	2.9	2.9
Semi-convergence angle of the partial coherence envelopes	β (mrad)	0.03	0.03	0.03
Pixel size	Δx (Å)	0.0165	0.046488	0.03186
Number of pixels in the unit cell	$K \times L$	256×256	84×84	128×128

Table 6.1: Parameter values used for the STEM and TEM simulations of MgO, SrTiO₃ and Au.

6.3.2 Results for peak intensities and scattering cross-sections

The optimal experiment design was investigated for realistic simulation experiments, using the analytical expressions for the probability of error for atom-counting in HRTEM and HRSTEM, given by equation (3.65). In this section, the probability of error was calculated when the decision was based on the PF of the SCSs in HRSTEM, and on the PF of the PIs in HRTEM, for which the probabilities for a correct decision are given by equations (3.68) and (3.70), respectively. Therefore, a first detailed simulation study of MgO was performed for counting up to 12 atoms (i.e. 6 unit cells) corresponding to a column thickness of 2.5 nm, like in [254]. The probability of error for atom-counting was then calculated as a function of the experimental parameters for PIs in HRTEM and SCSs in HRSTEM, for incoming electron doses of $10^4 e^-/\text{\AA}^2$ and $10^7 e^-/\text{\AA}^2$.

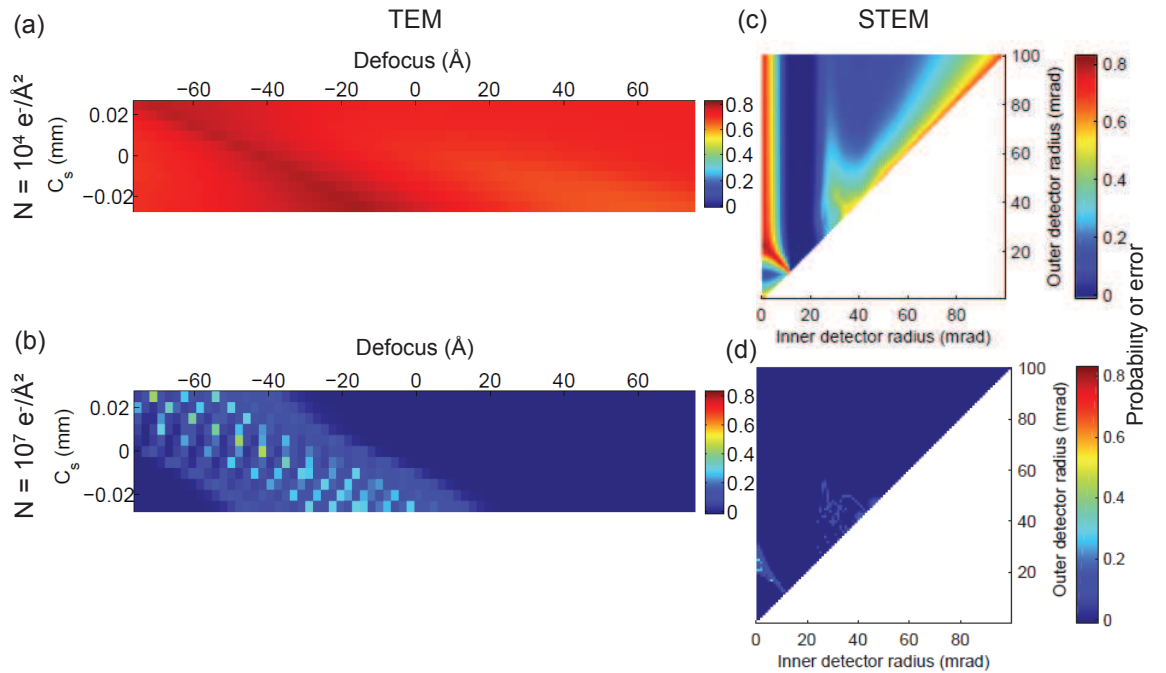


Figure 6.3: P_e for atom-counting using PI in HRTEM (a and b) and SCS in HRSTEM (c and d) for a MgO column up to 12 atoms thick, for $N = 10^4 e^-/\text{\AA}^2$ (a and c) and $N = 10^7 e^-/\text{\AA}^2$ (b and d).

Results of the probability of error for PIs in HRTEM are shown in Figure 6.3(a) and 6.3(b). From these figures, it is clear that for the investigated values for

the spherical aberration and defocus, P_e reaches high values for the incoming electron dose of $N = 10^4 e^-/\text{\AA}^2$, while it is substantially lower for $N = 10^7 e^-/\text{\AA}^2$. In Figure 6.3(a), the result for the lower incoming electron dose of $10^4 e^-/\text{\AA}^2$ is presented, where P_e is minimal for the setting $C_s = -0.025$ mm and $f = 57$ \AA. For this setting, however, the probability to miscount the number of atoms is high and equals 66%. For the higher incoming electron dose of $10^7 e^-/\text{\AA}^2$, there is a large dark-blue region visible in Figure 6.3(b) corresponding to a very low probability of error, that is optimal for atom-counting in HRTEM. For this electron dose P_e is minimised and close to 0 for the setting $C_s = -0.025$ mm and $f = 49$ \AA. As expected, this indicates that the atom-counting precision becomes much better for a higher incoming electron dose.

Results of P_e when the decision was based on the PF of the SCSs in HRSTEM are shown in Figures 6.3(c) and 6.3(d), for the same two incoming electron doses that were used for HRTEM. A clear optimal detector range is obtained for both incoming electron doses in the Annular Bright Field (ABF) STEM regime for a detector range of 13 – 20 mrad, visible as the dark-blue region where the probability of error is close to 0. Local optima are also found in the Low Angle ADF (LAADF) STEM regime for both incoming electron doses, as well as in the BF regime (0 – 10 mrad) where the probability of error is about 10%. It can be seen that P_e for atom-counting is much lower for HRSTEM as compared to HRTEM, even for a low incoming electron dose.

Next, a detailed simulation study for a SrTiO_3 crystal was performed for a thickness up to 75 atoms, corresponding to a column thickness of about 30 nm. The results for P_e for atom-counting from HRTEM and HRSTEM are shown in Figure 6.4 for the Sr column in SrTiO_3 . In this figure, decision rules were again based on the PFs of the performance measures that currently have been used in practice, i.e. the PIs and SCSs for HRTEM and HRSTEM, respectively. Based on the results shown in Figure 6.4, it is clear that P_e for atom-counting in HRTEM is high as compared to HRSTEM. In HRTEM, P_e is minimised for the setting $C_s = -0.035$ mm and $f = -80$ \AA. However, for this setting the probability to miscount the number of atoms is still high and equals 48%. In HRSTEM, for a thickness of 75 atoms, the optimal detector range that minimises P_e equals 27-100 mrad, for which the probability of error is 0.5%. For a probe semi-convergence angle of 21.7 mrad, this optimal detector design corresponds to LAADF STEM. Note, however, that when not all column thicknesses have to be considered in the multiple hypothesis test, for example if only a certain range of possible column thicknesses can be

assumed from prior knowledge about the sample, a different optimum might be found for atom-counting.

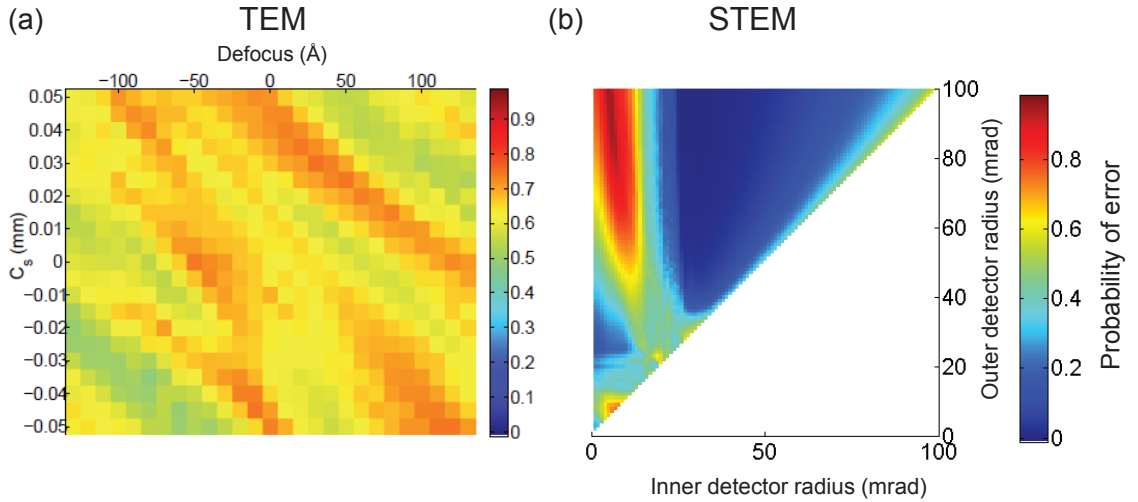


Figure 6.4: P_e for atom-counting using (a) PIs in HR TEM and (b) SCSs in HR STEM for a Sr column with a thickness up to 75 atoms and $N = 10^6 e^-/\text{Å}^2$.

6.3.3 Results for image intensities on a pixel by pixel basis

So far, two currently used methods for atom-counting were compared, but in this section, the ‘ultimate’ situation when the decision is based on the joint PF of the image pixel values was investigated. Although this requires a more complex framework, it was interesting to investigate and compare the limits of both imaging techniques in this case. As was mentioned before, equation (3.65) can only be computed approximately following the decision rule given in equation (3.64) using multiple noise realisations, when the atom-counting decision is based on the joint PF of the image pixel values. The experimental parameters were varied and optimised in the same way as before, for an incoming electron dose of $10^4 e^-/\text{Å}^2$. Results for PF’s of PIs and SCSs were compared with results when using all image intensities on a pixel by pixel basis for a Sr column in SrTiO_3 up to 30 atoms thick, as well as for a heavier Au column up to 50 atoms thick. Results of the probability of error for atom-counting in HRTEM and HRSTEM are shown in Figure 6.5 for the Sr column and in Figure 6.6 for the Au column, for the different performance measures.

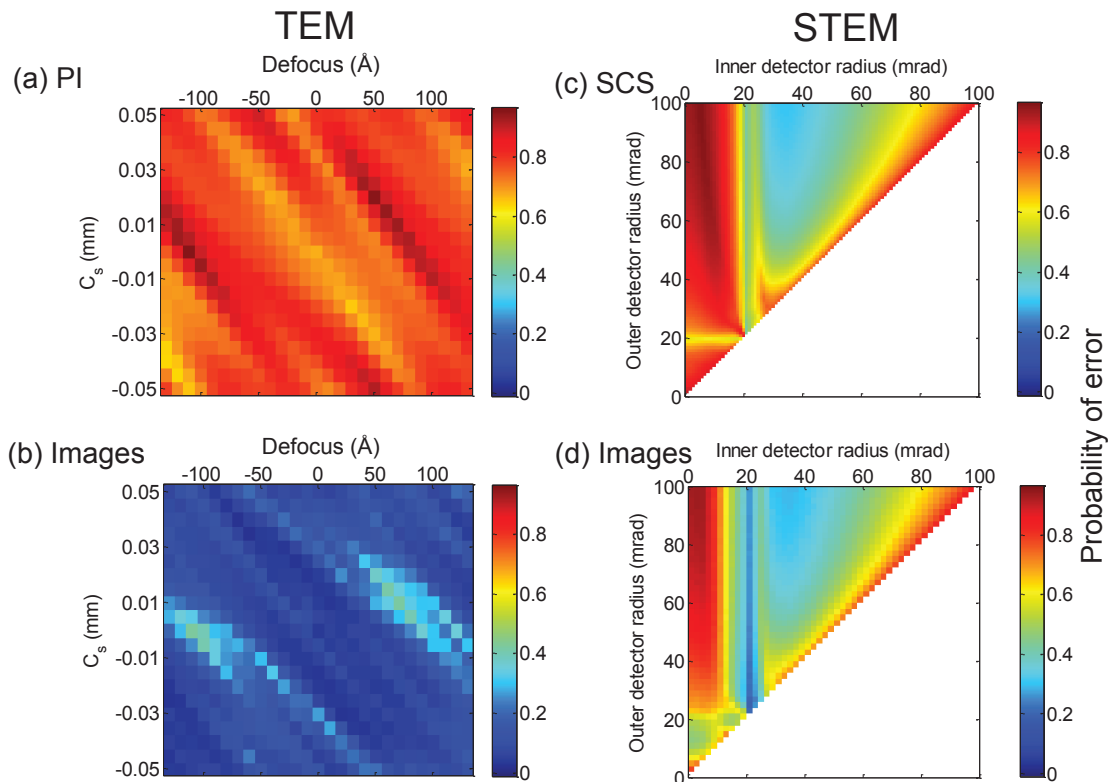


Figure 6.5: P_e for atom-counting using (a) PIs in HRTEM, (b) image intensities on a pixel by pixel basis in HRTEM, or (c) SCSs in HRSTEM and (d) image intensities on a pixel by pixel basis in HRSTEM, for a Sr column with a thickness up to 30 atoms, and $N = 10^4 e^-/\text{\AA}^2$.

When comparing Figures 6.5(a) and 6.5(b), it is evident that the probability of error decreases significantly when the decision is based on the joint PF of all HRTEM image pixel values, as compared to the result based on the PF of the PIs. For HRSTEM, there is only a slight decrease in probability of error, which can be seen when comparing Figures 6.5(c) and 6.5(d). For the Au column, similar results were found which are presented in Figures 6.6(c) and 6.6(d). In section 6.2, it was already shown for a binary hypothesis test that the probability of error for the SCSs approximately equals the probability of error when using all image intensities on a pixel by pixel basis. From the results shown here, it can be seen that this is also true for a multiple hypothesis test.

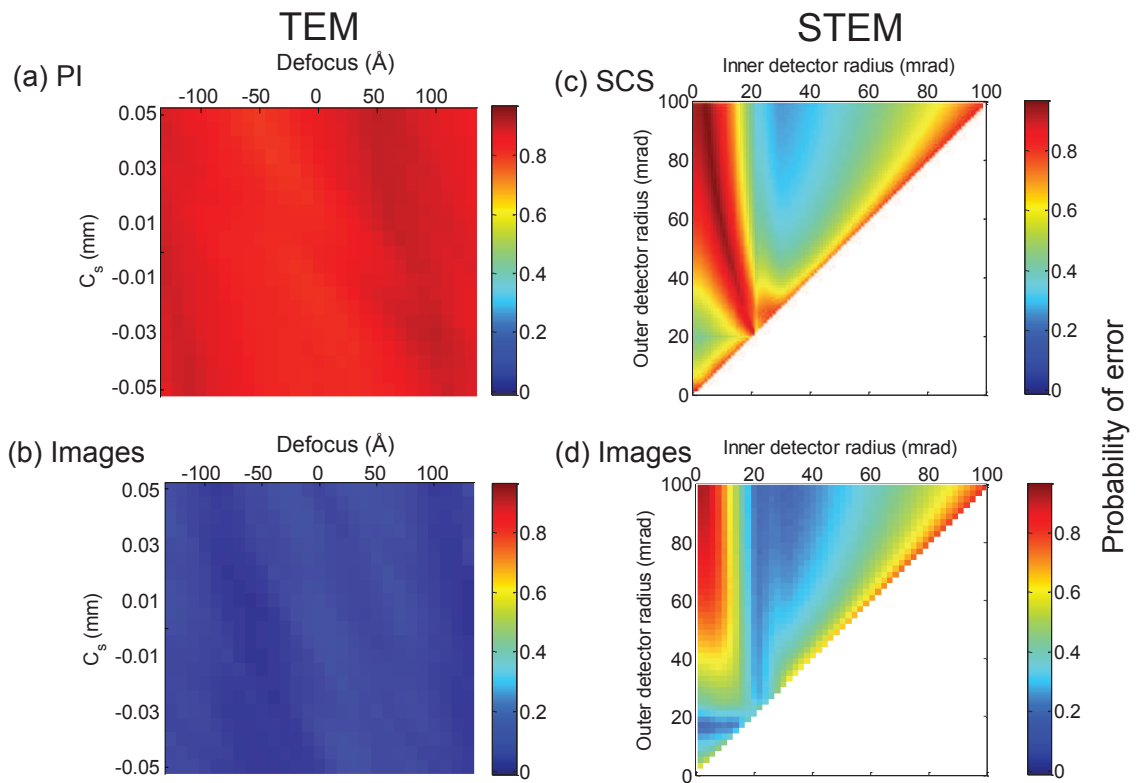
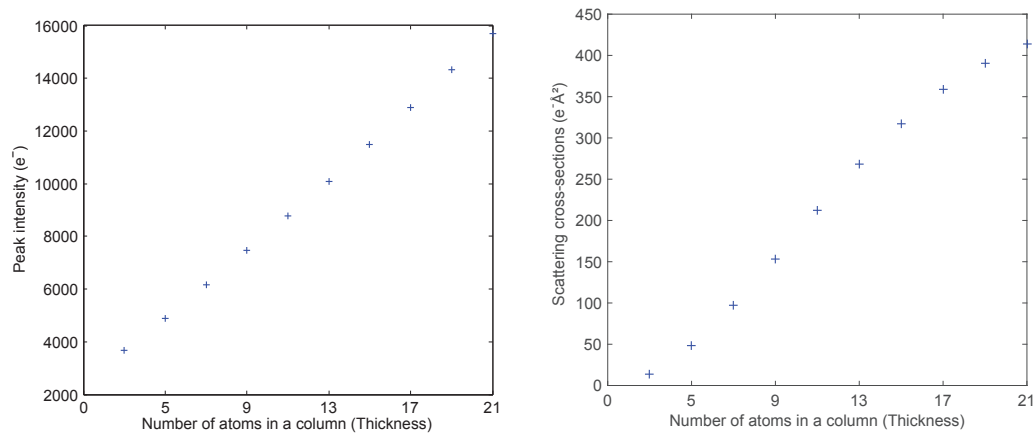


Figure 6.6: P_e for atom-counting using (a) PIs in HRTEM, (b) image intensities on a pixel by pixel basis in HRTEM, or (c) SCSs in HRSTEM and (d) image intensities on a pixel by pixel basis in HRSTEM, for a Au column with a thickness up to 50 atoms, and $N = 10^4 e^-/\text{\AA}^2$.

6.4 Discussion

6.4.1 Results for peak intensities and scattering cross-sections

The difference in probability of error between HRTEM and HRSTEM for the MgO column, of which the results are shown in Figure 6.3, can be understood by investigating the performance measures as a function of thickness. In Figure 6.7, both the PIs for HRTEM and the SCSs for HRSTEM are plotted as a function of the number of atoms, at the optimal experimental settings. From the results shown in Figure 6.7, it can be seen that both the PIs and the SCSs increase almost linearly with the thickness under the optimal settings, which allows us to distinguish between different numbers of atoms. However, in Figure 6.3, a much



(a) PIs in HRTEM for $C_s = -0.015$ mm and $f = 51$ Å (b) SCSs in HRSTEM for detector range = 13-100 mrad

Figure 6.7: The used performance measures for a MgO column as a function of thickness, both at the optimal experimental settings and for $N = 10^4 e^-/\text{Å}^2$.

lower probability of error was obtained for atom-counting in HRSTEM as compared to HRTEM. This can be understood by looking at the succeeding PFs of the respective performance measures for the different column thicknesses, which are presented in Figure 6.8. In Figure 6.8(a), it is shown that the difference between the mean values of the PFs of consecutive PIs is small as compared to their standard deviation at the lower incoming electron dose of $10^4 e^-/\text{Å}^2$, which results in highly overlapping PFs. The large overlap results in a high probability of error, which makes it hard to distinguish between the different column thicknesses in the case of HRTEM. In Figures 6.8(b) and 6.8(d), it is visible that the precision of the SCSs and PIs improves significantly with the incoming electron dose. Therefore, a higher incoming electron dose decreases the probability of error both in HRTEM and HRSTEM. For HRSTEM at the lower incoming electron dose, the difference between the mean values of the PFs of consecutive SCS values was already large as compared to their standard deviation, which follows from Figure 6.8(c). The different column thicknesses in HRSTEM can therefore easily be distinguished, even at the lower incoming electron dose of $10^4 e^-/\text{Å}^2$.

For SrTiO_3 also a high probability of error was found in the results presented in Figure 6.4, when using PIs in HR TEM as compared to SCSs in HR STEM, for counting the number of atoms in a Sr column with a thickness up to 75 atoms.

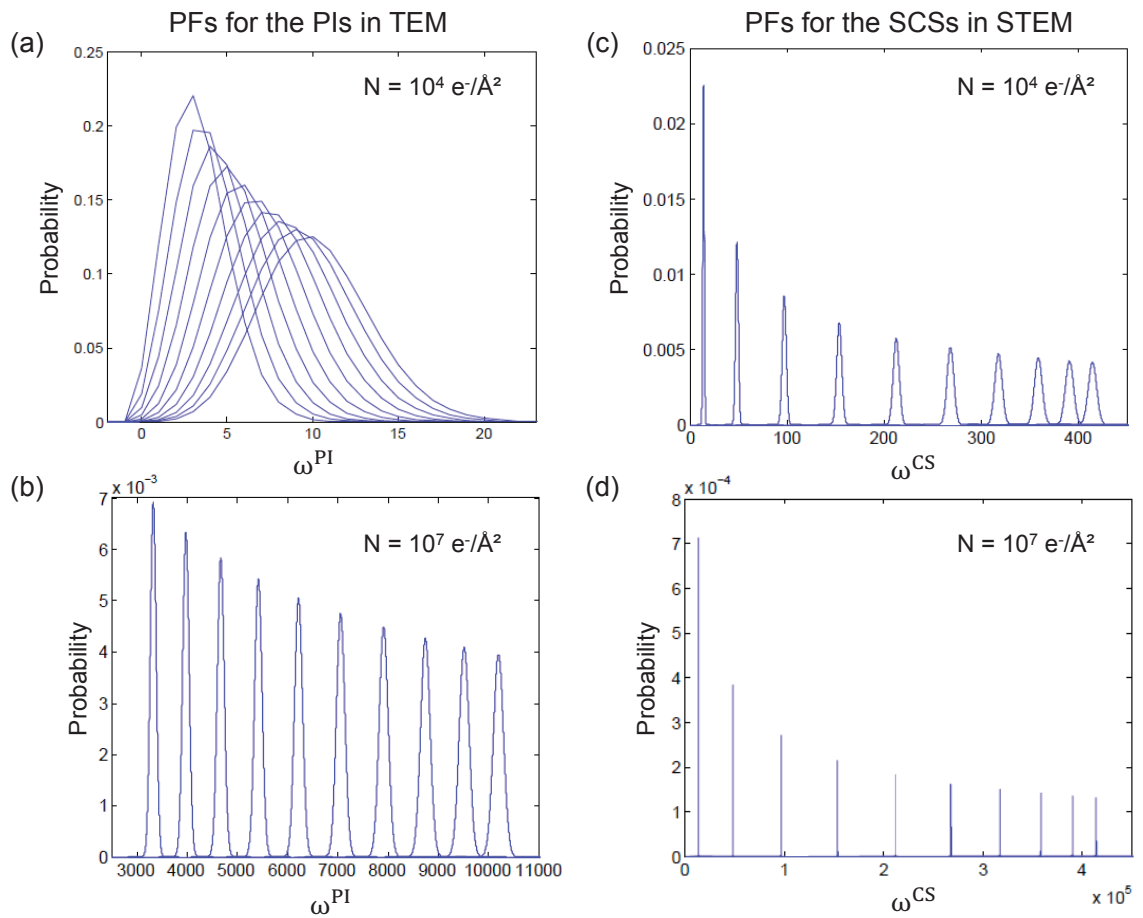


Figure 6.8: The PDFs for the succeeding PIs in HRTEM and SCSs in HRSTEM of a MgO column up to a thickness of 10 unit cells, for two different incoming electron doses.

This result can now be understood since PIs oscillate for thicker crystals depending on the atomic column type, as shown in Figure 6.9. This oscillating behaviour is a result of inherent electron channelling, which depends on both the atomic type and the atomic column thickness [65]. To make this more clear, a simulated Sr column as a function of thickness is shown in Figure 6.10, where the oscillation in intensity is visible in the case of TEM.

It is impossible to assign PIs in HRTEM unambiguously to a specific number of atoms when they oscillate as a function of thickness as shown in Figure 6.9(a).

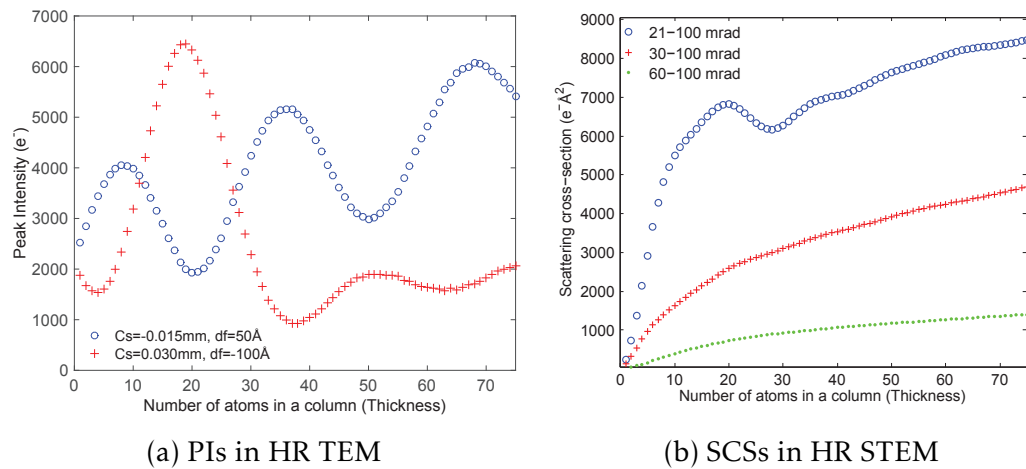


Figure 6.9: The used performance measures plotted as a function of thickness using different experimental settings for a Sr column with a thickness up to 75 atoms and $N = 10^6 e^-/\text{Å}^2$.

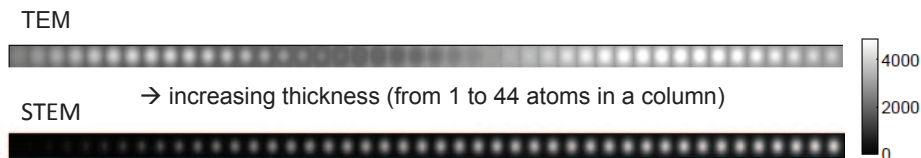


Figure 6.10: Simulated images of a Sr column in SrTiO_3 for increasing thickness (from left to right), both for TEM ($C_s = -0.015 \text{ mm}$ and $f = 49 \text{ Å}$) and STEM (30-100 mrad). The oscillation due to the channelling effect in the case of TEM is clearly visible.

Therefore, in the presence of noise, columns of different thickness cannot be distinguished using PIs as a performance measure, even not at relatively large electron doses. In HRSTEM, however, there are no contrast oscillations at the optimal detector settings. Furthermore, the standard deviation of the PFs of the SCSs in HRSTEM is small as compared to the difference between the mean values of PFs of consecutive SCSs, in contrast to the PFs of PIs in HRTEM for the same incoming electron dose. As was already discussed in [208], it can be seen in Figure 6.9(b) that the Low Angle Annular Dark Field (LAADF) STEM regime (21-100 mrad) is only appropriate for atom-counting up to a thickness of about 20 atoms

in the column, due to the higher coherent contribution to the SCS for this detector setting. The same reasoning applies when counting the number of Au atoms.

6.4.2 Results for image intensities on a pixel by pixel basis

On the one hand, the results that are shown in Figures 6.5 and 6.6 suggest that it is advantageous to use HRTEM for atom-counting, when using all image intensities on a pixel by pixel basis. In this case the probability of error for HRTEM decreases significantly as compared to the result when using PIs, and it becomes even lower than the probability of error for atom-counting in HRSTEM. Note, however, that in practice the use of the joint PF of all image intensities would require a rather complex procedure. Indeed, one would then need to know the behaviour of all pixel values in the image as a function of thickness, and therefore also all imaging parameters. Recall that in the followed quantitative approach, all imaging parameters were assumed to be known exactly. Moreover, it was assumed that the spherical aberration and defocus can be tuned precisely in the case of HRTEM, which is obviously not an evident matter. In fact, the spherical aberration and defocus will be estimated parameters too, which in practice will increase the probability of error for atom-counting mostly in HRTEM, as this imaging technique is less robust with respect to these parameters as compared to HRSTEM.

On the other hand, for atom-counting in HRSTEM, it is clear from Figures 6.5 and 6.6, that the probability of error based on the PF of the SCSs is a good approximation for the probability of error when the decision is based on the joint PF of the image pixel intensities. This is a great advantage of atom-counting using HRSTEM, since SCSs are a robust measure for many imaging parameters, including defocus, source coherence, convergence angle [220], and also for crystal tilt [262].

6.5 Conclusions

In a first part of this chapter, binary hypothesis testing has been worked out for atom-counting. In this way the limits to the precision with which the number of atoms in a projected atomic column can be estimated are investigated. Using binary hypothesis testing, the experiment design of the annular detector in a HRSTEM experiment is optimised for atom-counting. It is pointed out that the

use of scattering cross-sections, which were already proposed in [76, 146, 220], is afforded in the quantitative analysis of HRSTEM images when the goal is to count the number of atoms with the lowest probability of error, since they perform equally well as the HRSTEM images on a pixel by pixel basis of a projected atomic column and they even outperform peak intensities.

Furthermore, optimising the experiment design for atom-counting using multiple hypothesis testing is worked out, where the possibilities and limitations of both HRTEM and HRSTEM were investigated in a quantitative way. Three different crystals were simulated; MgO, SrTiO₃ and Au, in order to investigate and compare the probability of error for atom-counting in both imaging modes. By calculating the probability of error as a function of the experimental settings, the experiment design was optimised. For HRSTEM, the annular inner and outer detector angles were optimised, whereas for HRTEM the spherical aberration and defocus were optimised.

We can conclude that when comparing the currently used approaches, HRSTEM is in general applicable for atom-counting when using an appropriate detector range, where the SCSs monotonically increase with thickness, and where the overlap between the PFs of consecutive SCSs is small. When the decision is based on the PF of PIs, atom-counting in HRTEM is only possible in projected atom columns in a very thin sample region at optimal imaging conditions, and using a sufficiently high incoming electron dose. The PIs oscillate as a function of thickness, depending on the atom column type due to the inherent electron channelling. The probability of error at the optimal settings for HRTEM, when the atom-counting decision is based on the PF of PIs is larger as compared to the optimal probability of error for HRSTEM, for the same incoming electron dose. Under the assumption that one can make the atom-counting decision based on the joint PF of all image pixel intensities, the probability of error decreased significantly in the case of HRTEM, and became lower as compared to HRSTEM. Note, however, that such atom-counting procedure would require the behaviour of all image pixel intensities to be known accurately as a function of thickness, which is not a trivial matter. In HRSTEM, both for binary and multiple hypothesis testing, the probability of error based on the joint PF of the image pixel values is well approximated by the probability of error for SCSs, for which an appropriate and practical framework exists [75–77]. In conclusion, HRTEM may in theory result in a lower probability of error for atom-counting when using image intensities on a pixel by pixel basis, but the commonly used SCSs for atom-counting in STEM lead to a high performance and have been shown to work in practice.

Experimental Applications 7

7.1 Introduction

In the previous chapters, the statistical experiment design to detect and locate light atoms from an HR(S)TEM experiment was investigated. In practice, however, the unknown structure parameters, such as the precise atom column positions will have to be estimated from experimental images whatever the experiment design. In this chapter, some experimental results for different applications are given which have been obtained by using statistical parameter estimation theory. Therefore, an efficient model-based fitting algorithm for the estimation of atom column positions and intensities from atomic resolution (S)TEM images is used, which is implemented in the StatSTEM program [147]. After estimating the atom column positions from an experimental image, different structure characteristics have been obtained, such as the relative tilt angle near the interface of a metal oxide heterostructure, the B-O-B bond angle between the B site atoms and the oxygen atoms in such heterostructure, and also atom displacements with respect to a domain wall in the crystal LiNbO_3 .

To visualise the oxygen atoms in order to calculate the B-O-B bond angle in the metal oxide heterostructures, the ABF STEM setting was experimentally found to be the optimal design, as was proposed in chapter 5 for the detection of light atoms. For the other applications, only the heavy atomic column positions were needed and therefore, HAADF STEM was an appropriate imaging mode.

This chapter is organised as follows. In section 7.2, the efficient fitting algorithm applied to retrieve the atom column positions is introduced. In section 7.3, the estimated atom column positions from HAADF STEM images of metal oxide heterostructures are used to estimate the relative unit cell tilt angle near the interface

¹, and in section 7.4, the B-O-B bond angle of the oxygen octahedra and the B site atoms are obtained from atomic resolution ABF STEM images. In section 7.5, the results are presented of an elaborate study where the domain wall in LiNbO₃ is quantified ² and finally in section 7.6, conclusions are drawn.

7.2 Efficient fitting algorithm

Statistical parameter estimation theory can be used to estimate unknown structure parameters with high accuracy and precision from experimental images [141, 144]. Nowadays, this methodology has become the optimal method for quantitative electron microscopy. In this theory, the (S)TEM image is considered as a data plane from which the unknown structure parameters are being estimated. The starting point of this method is then a statistical parametric model describing the expectations of the experimental measurements. In HR(S)TEM images, the projected atom columns are peaked at the atomic column positions, which can therefore be modelled as a superposition of Gaussian functions [61, 263]. Recently an efficient algorithm has been developed by co-workers from the University of Antwerp which has been implemented within the StatSTEM program [147]. By fitting a model of a superposition of Gaussian functions to the experimental images using a criterion of goodness of fit, the unknown structure parameters can be estimated. The least squares estimator can be used for this purpose in an iterative optimisation process. The ML estimator as defined in equation (3.30) equals the least squares estimator for independent normally distributed observations. A direct implementation of this estimator in which all parameters are estimated at the same time is computationally very intensive and is only feasible for (S)TEM images containing a limited number of projected atomic columns, i.e. a limited field of view. A more efficient algorithm is therefore proposed and implemented in the StatSTEM program, which enables

¹The results of this analysis are published in Z. L. Liao, R. J. Green, N. Gauquelin, S. Macke, L. Lin, J. Gonnissen, R. Sutarto, E. P. Houwman, Z. Zhong, S. Van Aert, J. Verbeeck, G. A. Sawatzky, M. Huijben, G. Koster, G. Rijnders, Long-Range Domain Structure and Symmetry Engineering by Interfacial Oxygen Octahedral Coupling at Heterostructure Interface, *Advanced Functional Materials*, (2016) Wiley Online Library.

²The results of this analysis are published in J. Gonnissen, D. Batuk, G.F. Nataf, L. Jones, A.M. Abakumov, S. Van Aert, D. Schryvers and E.K.H. Salje, Direct Observation of Ferroelectric Domain Walls in LiNbO₃: Wall-Meanders, Kinks, and Local Electric Charges, *Advanced Functional Materials* (2016), Wiley Online Library

one to analyse large fields of view. The basic idea of the new algorithm is the segmentation of the HR(S)TEM image into smaller sections containing individual columns without ignoring overlap between neighbouring columns. In this way, only the parameters corresponding to a single atom column are estimated simultaneously, instead of all parameters of the parametric model. In this thesis, the StatSTEM program has been applied in order to obtain precise results for the estimated atom column positions from different experimental STEM images.

7.3 Estimating the atomic column positions in transition metal oxide heterostructures

As a first practical application in our research to find new techniques to quantitatively characterise nanostructures consisting of light atoms, the local oxygen octahedral coupling (OOC) at perovskite heterostructural interfaces is investigated in different epitaxial thin films. In [48], it is unravelled how this local oxygen octahedral coupling strongly influences the domain structure and symmetry of the epitaxial films resulting in design rules to induce various structures in thin films using carefully selected combinations of substrate/buffer/film. In ABO_3 perovskites, the crystal symmetry resides in the oxygen octahedral (BO_6) network [264–267]. These symmetries, or oxygen octahedral rotation (OOR) patterns in perovskite heterostructures, are often engineered by epitaxial strain [268]. The short range impact of the OOC on the tilt angle was recently further demonstrated for the $La_{2/3}Sr_{1/3}MnO_3$ (LSMO)/ $NdGaO_3$ (NGO) heterostructure, in which the OOC driven novel anisotropic properties only emerge in LSMO thinner than 8 unit cells (UC) [269]. The limited propagation of the interface induced octahedral tilt into the film currently restricts the engineering of perovskite heterostructures with unique functional properties. Changing the strain or substrate symmetry are two well known strategies to long range engineer the lattice structures and in most situations they cooperatively affect the film structures [270–274]. However, how exactly the substrate symmetry plays a role distinguished from strain is still an open question. By systematically investigating the effect of substrate symmetry on film structures, while keeping the lattice strain constant, the important role of interfacial OOC in determining the film domain structure was investigated [48]. Furthermore, it was shown that if the OOC effect at a heterosymmetric interface is strong enough to induce a different OOR pattern in a film near the interface to match the substrate OOR, the initiated different symmetry can propagate away

from the interface into the full thickness of the films [48]. An example is the structure of an LSMO film on an NGO (110) orthorhombic substrate. The bulk LSMO is rhombohedral, but due to the strong OOC effect at the LSMO/NGO interface, the near interface LSMO becomes orthorhombic [269]. Although the effect of OOC on the magnitude of the octahedral tilt decays steeply within 4 UC [269], the characteristic orthorhombic structure still survives over an extensive thickness range, resulting in an orthorhombic structure in thick LSMO films.

To understand the configuration growth of different heterostructures, HAADF STEM images of both a layered LSMO/NGO and a LSMO/STO/NGO structure are investigated, and showed that the unit cell of LSMO is relatively tilted with respect to the NGO unit cell (see Figure 7.2). Using statistical parameter estimation theory [141, 144, 146, 157], the 2D coordinates of each atomic column of the LSMO/NGO heterostructure have been determined from the HAADF STEM image shown in Figure 7.1(a).

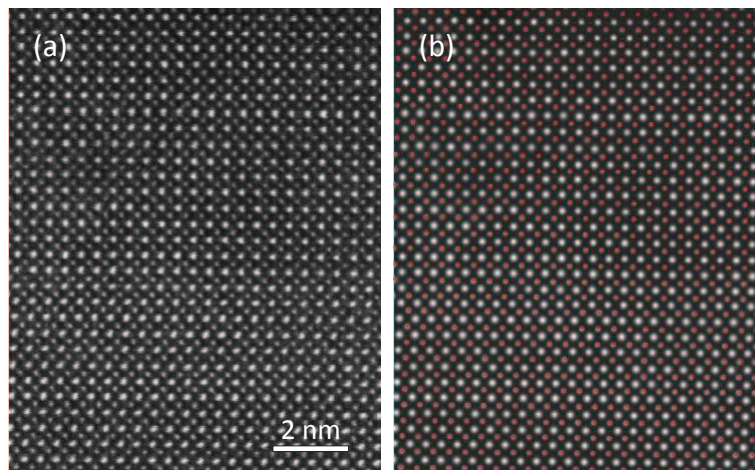


Figure 7.1: Gaussian model fitting of the HAADF image. (a) HAADF-STEM image of LSMO/NGO cross-section. (b) Fitted model of the STEM image with the red dots indicating the B site atomic column positions (Ga, Mn).

A parametric model in which projection images of the atomic columns are described using Gaussian peaks has been assumed. The parameters of this model, including the positions, height, and width of the intensity peaks, were determined using the least-squares estimator with the StatSTEM program [147].

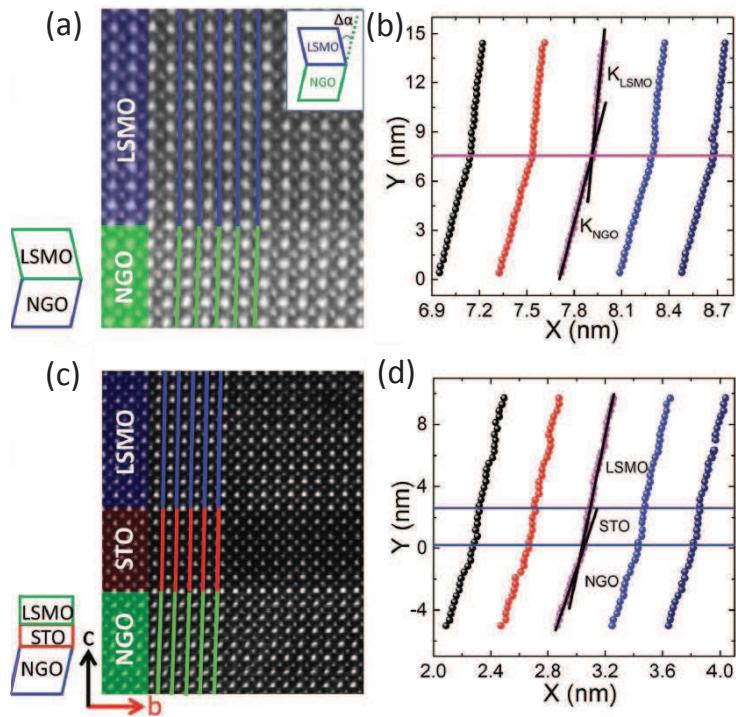


Figure 7.2: Tailoring structure by interface symmetry engineering. HAADF image of 30 UC LSMO films a) with and c) without 6 UC STO buffer layer. Inset image at top-right corner of (a) indicates the definition of relative unit cell tilt angle $\Delta\alpha$. b) The positions (X, Y) of the B site atoms from five columns marked by lines in panel (a). K represents the slope of the curve. d) The positions (X, Y) of B site atoms from five columns marked by lines in panel (c).

The refined model, evaluated at these estimated parameters is shown in Figure 7.1(b). From the refined model, the position of the atoms, such as positions of the B site atomic columns (Ga, Mn) could be obtained, which are indicated in red dots in Figure 7.1(b). The relative tilt angle defined by $\Delta\alpha$ as shown in the inset of Figure 7.2(a), could then be estimated from the B site positions. As shown in the plot of B site (X, Y) positions in Figure 7.2(b), a sudden change of the slope occurs at the interface which cannot be due to image drift and is therefore ascribed to different monoclinic tilt angles in LSMO and NGO. A relative tilt of $\Delta\alpha = \tan^{-1}(K_{\text{LSMO}}) - \tan^{-1}(K_{\text{NGO}}) \approx 0.96 \pm 0.06^\circ$ is obtained from the STEM image, which agrees well with the value of 1° extracted from X-ray reciprocal space mapping [48].

7.4 Estimating the B-O-B bond angle

Recently it has been shown that the oxygen octahedral rotation (OOR) pattern in LSMO films can be tuned by direct coupling to the oxygen octahedral rotation pattern of the underlying substrate [269]. NGO substrates provide a specific octahedral tilt angle, and corresponding orbital overlap, which can be reduced by an increased thickness of the LSMO layer as well as by incorporation of a SrTiO₃ (STO) buffer layer.

In [275], the oxygen octahedral rotation pattern across a 20 UC LSMO/NGO

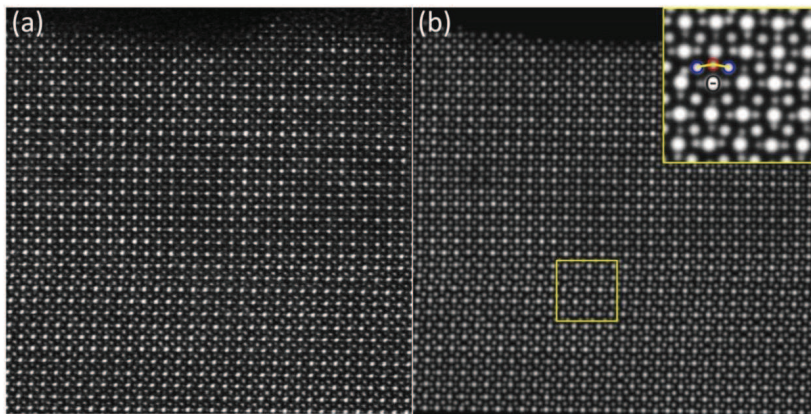


Figure 7.3: (a) Inversed ABF STEM image of a 20 unit cells LSMO film on an NGO (110) substrate. (b) Refined model of the ABF image after least-square estimation of the parametric model. Inset at right-top corner shows the zoomed-in image of the yellow square region.

interface was imaged by annular bright field STEM (ABF STEM), as is shown in Figure 7.3(a). The MnO₆ octahedra are shown to follow the tilt angle of NGO in the interface region due to the oxygen octahedral coupling (OOC) effect [269,276], which progressively decays away from the interface and is already negligible in the 4th unit cell. Figure 7.4 shows the profile of the projected B-O-B bond angle θ in the (001) plane, which is determined using statistical parameter estimation theory [141, 144, 146, 157]. As before, a refined model could be obtained which is shown in Figure 7.3(b).

From the results shown in Figure 7.4(b), it is clear that the bond angle θ in

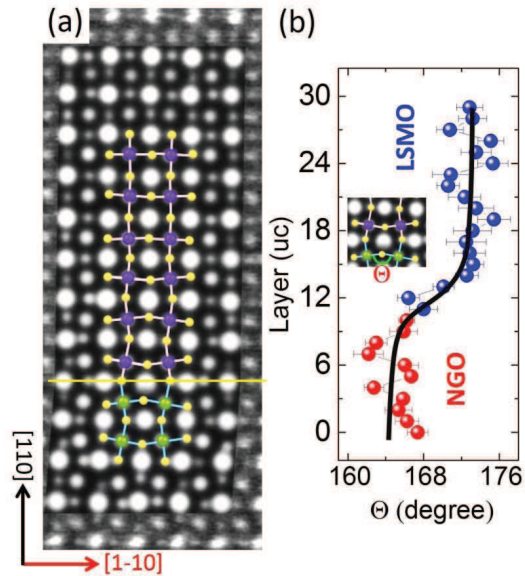


Figure 7.4: Relaxation of octahedra induced thickness-properties correlation. a) ABF-STEM image of LSMO/NGO cross-section. The intensity (I) is rescaled to $-I^{1/4}$ for better oxygen contrast. Inset shows the refined parametric model using statistical parameter estimation. The coloured atoms and bonds highlight the relaxation of octahedral and B-O-B bond angle. b) The layer position dependent [1-10] directional and (001) plane projected B-O-B bond angle θ . Inset shows the definition of θ .

LSMO right at the interface is comparable to the angle in the NGO substrate ($= 165^\circ$) and increases, starting from the interface, up to a saturation value of about 173° above the 4th LSMO unit cell. Further away from the interface, a long range slow relaxation tail of the octahedral rotation pattern should exist, similar to LSMO/STO heterostructures [277]. The plotted errorbar in Figure 7.4(b) is obtained from the standard deviation, averaged over the number of calculated angles per atomic layer.

In [275], it is shown that the reconstructed octahedral rotation pattern due to the OOC effect at the interface, is a nontrivial factor of perovskite oxide interfaces and causes a thickness dependent orbital hybridisation effect. Although LSMO has been used as a prototype material in this study, the results can be applied

to understand thickness related property variations in many other correlated oxide perovskite systems and have deep implications for understanding emergent functionalities in those complex systems.

7.5 Domain wall quantification in LiNbO_3

Ferroic domain walls can be functional elements of a material while the same functionality does not exist in the bulk [278]. Ferroelectric walls in LiNbO_3 are expected to display transport functionality: the walls are locally electrically charged, while the bulk is known not to contain any electric charges besides those related to point defects. These walls are expected to be electrically conducting when the carrier concentration is sufficiently large [279–282]. Ferroelectric walls in LiNbO_3 separate domains with the polarizations pointing in opposite directions (180° walls). The geometrical condition for charged walls is that they are inclined with respect to the equilibrium direction along the ferroelectric polarisation direction [0001] (in the hexagonal setting) [280–282]. Inclined walls generate local strain in the nearby bulk, while walls in mechanical equilibrium are neither charged nor do they strain the lattice. However, LiNbO_3 with macroscopically non-inclined walls still contains significant defect structures [283–286] which decorate the walls [287, 288]. Nataf et al. argued that even ‘straight’ walls should show local inclinations, they ‘meander’, so that head-to-head and tail-to-tail dipolar kink configurations occur locally [289]. Each such configuration represents an increase or decrease of carrier concentrations and hence corresponds to a local charge monopole.

LiNbO_3 has a trigonal structure with the $\overline{R3c}$ space group in the paraelectric phase. With the onset of ferroelectricity at T_c near 1483 K, the structure remains trigonal, but the inversion symmetry of the system is lifted, reducing the symmetry to the $R3c$ space group. LiNbO_3 is hence ferroelectric but not ferroelastic below 1483 K. Domain structures consist exclusively of 180° ferroelectric walls, which are almost strain-free in thermodynamic equilibrium while weak local strains originate from coupling between the polarisation and secondary displacements of the oxygen cages [287, 288]. The crystallographic properties and energetics of domain walls in LiNbO_3 have been described in great detail in [287, 290]. We refer the reader to the excellent review in [287] for further details. In [291], the presence of domain wall meanders has been confirmed, even in LiNbO_3 without

engineered inclined walls and furthermore, it was demonstrated for the first time, that head-to-head configurations exist in a nominally ‘straight’ domain wall. This observation confirms that local charges occur inside domain walls in LiNbO₃.

Results and discussion

LiNbO₃ is a beam-sensitive material. Therefore, both the TEM specimen preparation and the HAADF-STEM image acquisition were optimised in order to obtain most reliable TEM data. In a first step of this research, one was only interested in the Nb lattice, for which HAADF STEM is the optimal detector range. Analysis of ABF STEM images, in which the oxygen columns are visible, would be very interesting for future research work. Multiple detectors could therefore be used, which allows investigating both the HAADF and the simultaneously detected ABF STEM images. The most optimal Focused ion beam (FIB) lamella (Figure 7.5(b)) had a thickness of about 70 nm (estimated using electron energy loss spectroscopy), which is a compromise between the electron transparency and the ion-beam damage during the sample preparation. The HAADF STEM data were collected along the $[1\bar{1}00]$ direction, as a time series of 49 frames with a very short acquisition time of 2.5 s per frame. This mode significantly reduces the dose rate, improving the stability of the material under the electron beam, and minimises the effect of mechanical instabilities of the sample during the experiment. The acquired data were processed using the Smart Align software package [239]. First, all the frames were aligned with respect to each other to compensate for the mechanical drift during the acquisition. Then, each frame was individually corrected for the scan distortions. In the end, the frames were combined into a single image with improved signal-to-noise ratio and minimised scan and drift distortions. A representative fragment of the averaged image is shown in Figure 7.6. The position of the ferroelectric domain wall is marked with a white arrow, and can be seen as a strip with a slightly lower intensity. Also, it creates a weak ripple in the rows of white dots when looking at this image along a grazing incidence from left to right. In the HAADF STEM images the signal is proportional to the chemical composition of the projected atomic columns and scales as $I \propto Z^{1.6-1.9}$, where Z is an average atomic number. Therefore, in the $[1\bar{1}00]$ HAADF STEM images of LiNbO₃, the projected Nb-Li ($Z[\text{Nb}] = 41$, $Z[\text{Li}] = 3$) columns appear as bright dots arranged into a rectangular pattern, while the O ($Z[\text{O}] = 8$) columns are not visible. In the following the Nb-Li columns are referred to as Nb columns since simulations have shown that, as can be expected, the Li atoms are too light

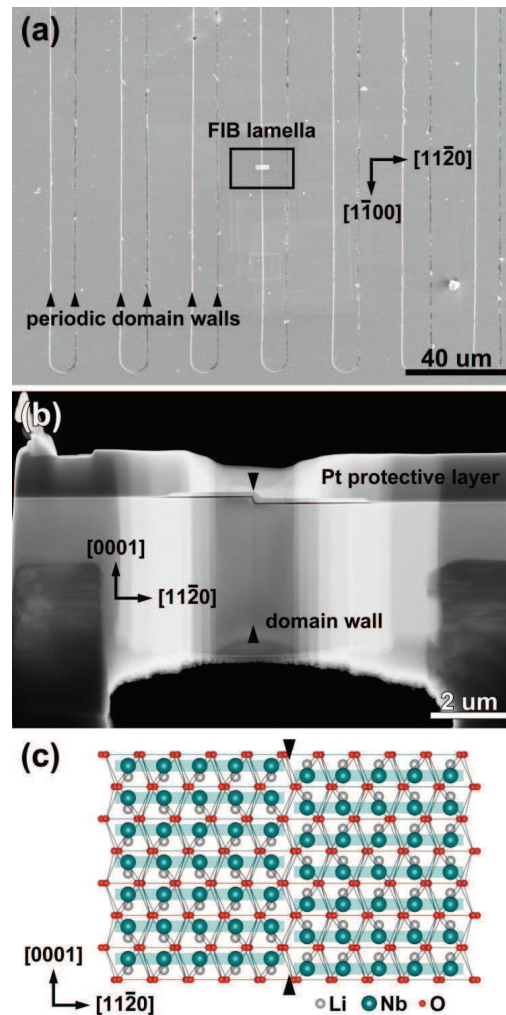


Figure 7.5: (a) Overview SEM image of the investigated LiNbO₃ crystal viewed normal to the surface, i.e., along the [0001] direction. Induced domain walls appear as a set of periodic parallel lines. The site where the FIB specimen was extracted can be seen as a bright narrow strip of the Pt protective layer. (b) Low magnification HAADF-STEM image of an optimised FIB lamella, viewed along the [1 $\bar{1}$ 00] direction. The domain wall can be recognised as a straight line of weaker intensity running perpendicular to the surface and located right under the surface step. (c) Idealised schematic illustration of the domain wall, assuming the oxygen sublattice to remain unchanged when crossing the domain wall. Rows of Nb atomic columns are highlighted with teal stripes.

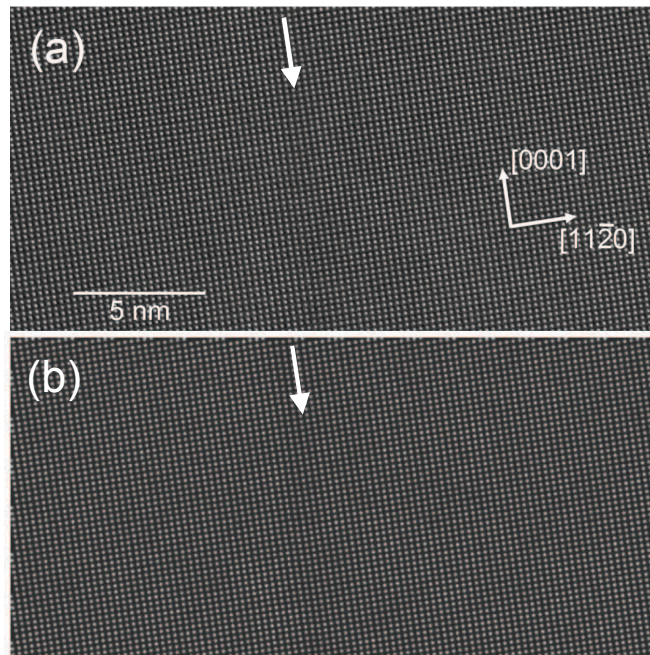


Figure 7.6: (a) The $[1\bar{1}00]$ HAADF STEM image of the ferroelectric domain wall area in the LiNbO₃ sample, averaged over 49 frames and corrected for the drift and scan distortions. (b) The fitted model of the HAADF STEM image. The arrows indicate the direction and location of the interface.

to cause any visible effect in the imaging. To analyse the Nb atomic displacements at the ferroelectric domain wall the projected 2D coordinates of the Nb columns in the averaged $[1\bar{1}00]$ HAADF STEM image were determined using statistical parameter estimation theory as before [141, 144, 146, 157]. The refined model is shown in Figure 7.6(b), where the position of the domain wall is again indicated with a white arrow.

For the determination of the Nb positions we assume that the ferroelectric domain wall does not change the anion sublattice of the structure, but inverts the ferroelectric displacements of the Nb cations. The inverted Li positions cannot be extracted from the images because the weight in the structure factor is much smaller than Nb so that all dipoles are nominally related to Nb. The following procedure was employed to identify the pattern of cation displacements and the exact position of the domain wall along the $[11\bar{2}0]$ direction. First, a region of 90

atomic rows was selected along the [0001] direction, each of which measuring 59 atomic columns along the $[11\bar{2}0]$ direction (this region is the shaded rectangle in Figure 7.7(a)). Then, for each row of 59 columns two reference lines were fitted by linear regression, using the coordinates of the 15 Nb columns at both ends of the row on either side of the wall (green lines in Figure 7.7(b)). In this fit, the slope of the reference lines for a given row at both sides of the domain wall was restricted to be the same, whereas the intercept with the interface was allowed to vary. The slopes for different atomic rows were not restricted.

To calculate the ferroelectric displacements of the Nb atoms, a base line for every $[11\bar{2}0]$ atomic row was then defined midway both reference lines (red line in Figure 7.7(b), which has the same slope as both fitted green reference lines). The red line in Figure 7.7(b) represents the approximate position of Nb in the paraelectric phase. Then, the Nb displacement from the red line was calculated for each Nb column. This displacement represents the approximate ferroelectric shift of Nb. By design this implies that we only measure the displacements of the Nb columns along the [0001] direction, i.e., parallel to the $(11\bar{2}0)$ domain wall. In Figure 7.7 the displacements are represented with the vectors pointing in the direction of the displacement.

The location of the domain wall along the $[11\bar{2}0]$ direction in a given row of Nb atomic columns can be determined as the point where the polar displacements of Nb columns change direction. The location points of the domain wall do not form perfectly straight lines along [0001], but meander back and forth along the $[11\bar{2}0]$ direction. Nevertheless, straight segments of the domain wall can be identified (red lines in Figure 7.7(c)). The overall meanders and local kinks between the wall segments occur within a narrow region of about 7 unit cells along the $[11\bar{2}0]$ direction, represented by the purple full lines in Figure 7.7(c). On a mesoscopic length scale, the domain wall is well confined to the $(11\bar{2}0)$ plane.

Having quantified the off-center displacement of the Nb columns near the ferroelectric domain wall, the width of the wall in each of the 90 selected Nb rows was analysed using a simple parametric model [292]:

$$f(\beta_1, \beta_2, \beta_3, \beta_4) = \beta_1 + \beta_2 \tanh\left(\frac{x - \beta_3}{\beta_4}\right), \quad (7.1)$$

where x represents the coordinates of the fitted atomic columns along $[11\bar{2}0]$ in

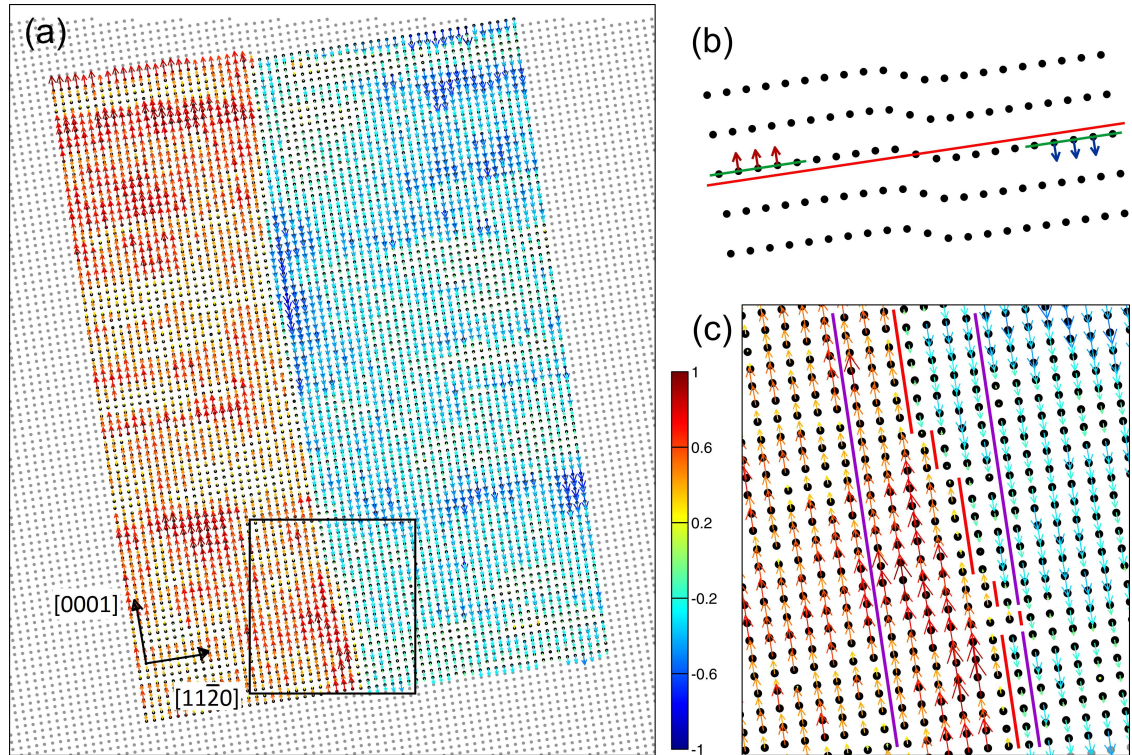


Figure 7.7: (a) The analysed region of 90 reference atomic rows: grey dots correspond to the fitted atom column positions, red and blue arrows indicate the displacement of the fitted atomic positions with respect to the base line and pointing in the direction of the displacement (the larger the displacement, the darker and longer the arrow). (b) Schematic (stretched in the $[0001]$ direction for clarity) showing green reference lines fitted to reference Nb columns in each ferroelectric domain and the red base line midway those reference lines. (c) Enlargement of the squared area in a), where now the straight domain wall segments are indicated in red. Purple lines indicate the transition region, where the Nb displacements are inverted (i.e., the overall width of the domain wall).

a single Nb column row, β_1 corresponds to the position of the domain wall midpoint along the $[0001]$ direction, i.e., the base line of the atomic row (red line in Figure 7.7(b)), β_2 corresponds to the distance between the base line and the corresponding reference lines, β_3 denotes the position of the domain wall midpoint along $[11\bar{2}0]$, and β_4 represents the half-width of the transition region of the domain wall along $[11\bar{2}0]$. In the model, the width of the domain wall corresponds

to $2\beta_4$ and it is independent of the actual location of the interface within the row (β_3).

Analysis of the calculated width of the domain wall for all 90 atomic rows demonstrates that there are two characteristic ranges of the wall widths, which is shown in the corresponding histogram in Figure 7.8(a). Most of the rows have a very narrow width of the domain wall, showing a step-like behaviour of Nb displacements. However, nine rows of the analysed show much wider widths of up to about 20 unit cells, which could be due to a meandering of the interface along the viewing direction.

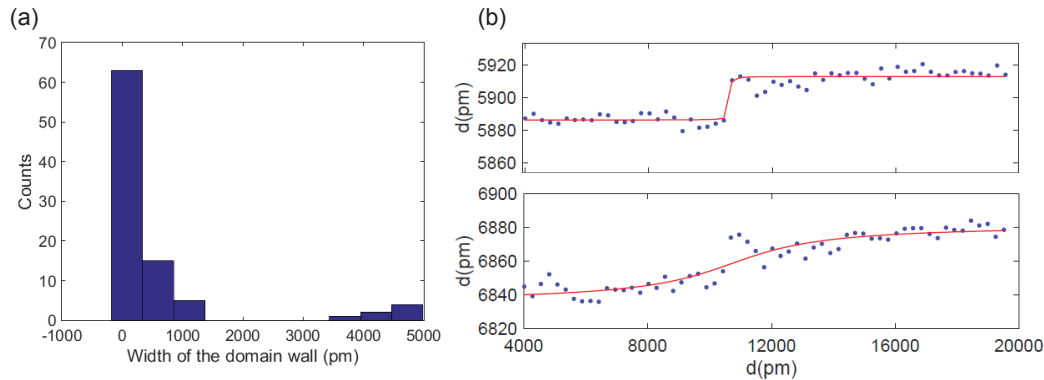


Figure 7.8: (a) Histogram of the estimated widths of the domain wall per row of the Nb columns, showing two clusters, the largest one with very sharp widths, the smallest one with broad widths. (b) Examples of rows with a sharp and a broad domain wall.

Considering only the atomic rows that demonstrate a sharp transition in the Nb off-centre displacements across the domain wall, an average wall width of $174 \text{ pm} \pm 33 \text{ pm}$ was calculated. Alternatively, an averaged master curve for the Nb displacements in the entire region of interest was constructed. Therefore, the atomic rows were first aligned with respect to each other along the $[11\bar{2}0]$ direction, to compensate for the side-ways meanders in the position of the wall. The obtained master curve for the whole region is shown in Figure 7.9. The dots correspond to the averaged atomic column positions for a given row. The curve represents the fitted parametric model, which also estimates the averaged domain wall width as 174 pm. The master curve illustrates that on average the

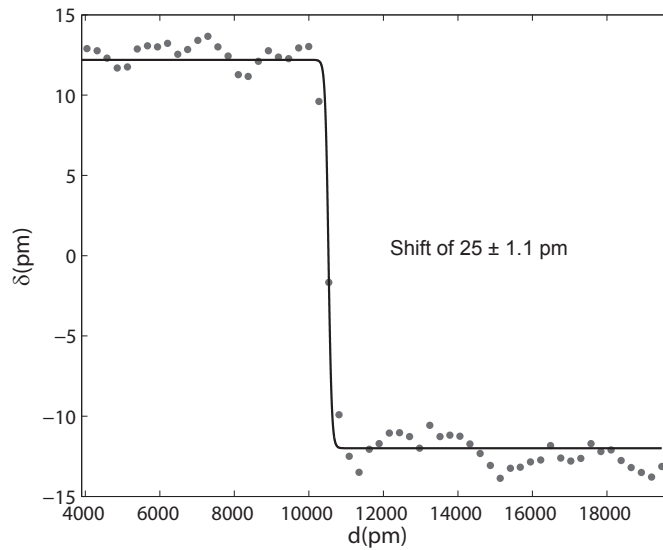


Figure 7.9: The master curve of Nb displacements in the analysed region (dots) and the corresponding fitted parametric model (curve).

domain wall is associated with sharp transitions in the polar displacements of the Nb atoms, accounting for just 3 unit cells along the $[11\bar{2}0]$ direction. Besides, the average displacements of the first atoms on either side of the wall from the base line are estimated as 9.4 pm, which is only slightly lower than the average value of 12.48 pm for the rest of the row and confirms the sharpness of the averaged interface. In a recent work, Wei et al. found a width of 7 pseudocubic unit cells and an averaged lead atom displacement of 8 pm at anti-phase boundaries in PbZrO_3 using negative spherical aberration imaging and averaging over selected atomic rows, but without using parameter estimation theory [293].

The main structural features of the wall in Figure 7.7(c) are the kinks of the displacements by one unit cell. While the overall direction is well defined, one could define the mesoscopic wall width as the distance between the two purple limiting lines (7 unit cells). Over rather long distances, the wall position does not fluctuate beyond this corridor. This situation is very different on a truly atomic scale where kinks with a step of one unit cell are rather common. Only these kinks produce local charges whenever two dipoles with opposite directions meet at a kink of the wall. These kinks can have a high density with 5 kinks over 26

unit cells along the [0001] direction while they are less common in other parts of the sample. If all kinks in the section seen in Figure 3c were oriented in the same direction, the wall would be inclined by a fraction of degree. Such walls were shown to exhibit Cherenkov second harmonic generation (CSHG) and various fine structures of domain walls have been made visible optically [282, 294, 295]. While the macroscopic wall inclination is strictly zero, the local inclinations and hence the number of kinks is large in our sample. This implies that the local wall conductivity (hopping) is large, but we do not expect large distance electronic transport because straight wall segments act as insulators between the kink-rich regions. This picture of local electronic resonances was advocated previously and our results fully support these findings [283, 296]. Our results are also in agreement with the lack of conductivity of domain walls with a macroscopic inclination of zero [281]. Furthermore, the presence of a large number of kinks means that the domain wall is a rough interface and will sensibly affect the CSHG signal.

From the pairs of reference lines for each $[11\bar{2}0]$ row of atomic columns in Figure 7.7, the average shift between the Nb atoms across the domain wall equals $25.0 \text{ pm} \pm 1.1 \text{ pm}$ (i.e., the distance between the stripes of $[11\bar{2}0]$ Nb rows along the [0001] direction in Figure 7.7(c)). The precision on the average shift is calculated by taking the standard deviation for every line, averaged over the 90 rows in the reference region. As compared to our results for the ultimate precision on the oxygen column position in chapter 5, shown in Figure 5.15, this is a very high precision. This can be understood as the thickness of the sample was about 70 nm (which is much thicker than the investigated column thicknesses for the oxygen column, resulting in a higher precision), and furthermore, the precision on the atom column of a heavier atom type is higher as compared to a lighter atom column.

The obtained value for the shift is about half of the expected value of ca. 55 pm calculated from the crystallographic bulk data of LiNbO_3 (see Table S1 in the supporting information). However, the spontaneous polarisation and hence the Nb shift of 24 pm in the TEM sample is that of a thin film prepared by FIB, so it can be expected to be reduced with respect to the bulk value. This effect may be a genuine size effect or related to strain and topological disorder along the beam direction, which could also result in the heterogeneities in the displacements as seen away from the domain wall in Figure 7.7(a). Nevertheless, all topological features of the domain wall appear to be the same as in bulk samples.

To further test whether the patches of small and large displacements visible in Figure 7.7 are due to heterogeneous strain effects, the Nb shifts with respect to the position extrapolated from the four nearest neighbour sites were calculated [297]. This does indeed average the strain variable as seen in Figure 7.10 and thus largely eliminates the heterogeneities.

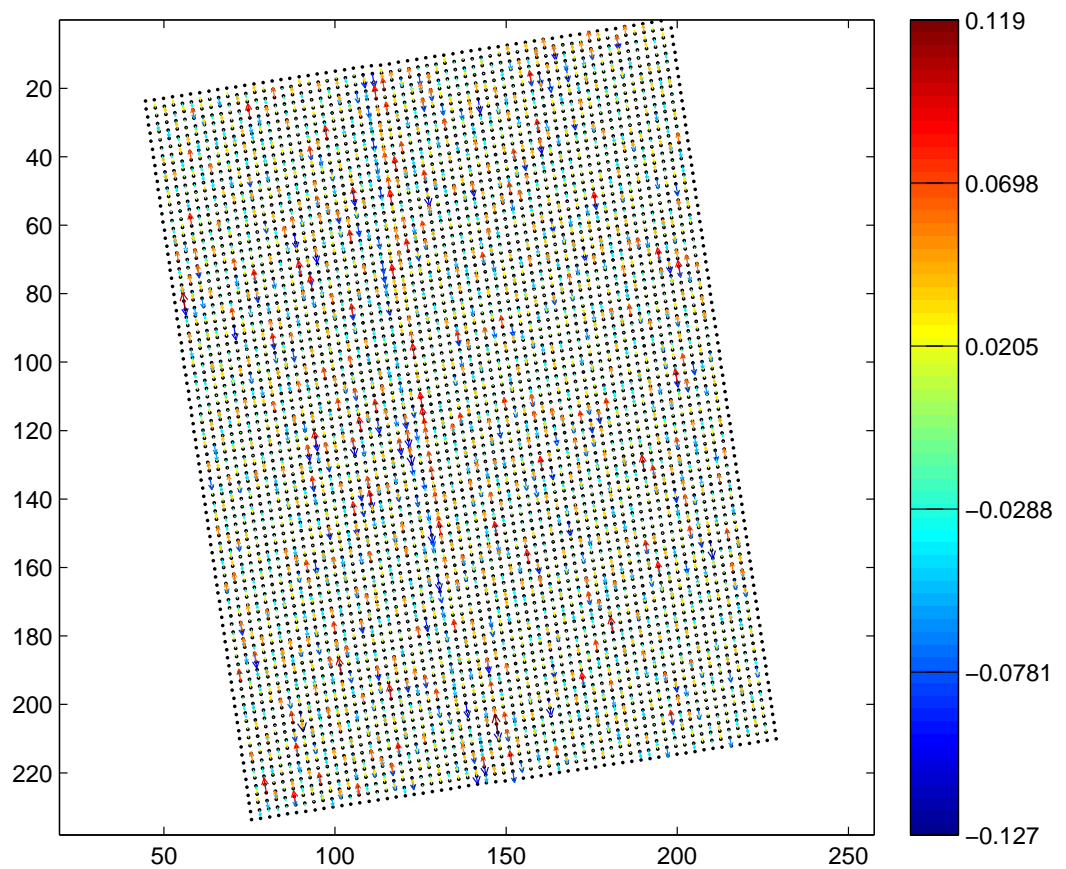


Figure 7.10: Same area as in Figure 7.7 but now the arrows indicate shifts with respect to the positions extrapolated from the four nearest neighbour sites. A more homogeneous distribution is seen, indicating that the patches in Figure 7.7 can be related to local strains.

In conclusion, it is shown that ferroelectric domain walls in LiNbO_3 follow, within experimental resolution, the predictions for 180° walls. Even for equilibrated walls, we found that the wall locally meanders yielding local wall directions inclined with respect to the ferroelectric polarisation. These meanders generate kinks and dipolar configurations where the ferroelectric dipoles are oriented head-to-head or tail-to-tail. These configurations necessarily induce local charges, which do not destabilise the overall wall configuration.

7.6 Conclusions

In this chapter, the least-squares estimator is used in order to estimate the unknown structure parameters within a model-based estimation algorithm, which is implemented in an efficient way in the StatSTEM software [147]. From the estimated atom column positions, different distances, atomic displacements and angles within complex structured materials could be derived from experimental HRSTEM images in a quantitative way.

It is shown that statistical parameter estimation theory can lead to precise results for different applications, which makes it the optimal tool for quantitative electron microscopy. Moreover, the availability of the user-friendly and efficient StatSTEM software will open up new possibilities for quantitative analyses of atomic resolution electron microscopy images.

General Conclusions

In this thesis an innovative method has been proposed in order to optimise the design of quantitative atomic resolution (scanning) transmission electron microscopy experiments. For estimation problems of continuous parameters, such as the atom column positions, the highest attainable precision with which these structure parameters can be obtained has already been shown to be an appropriate optimality criterion. An adequate measure for this precision is given by the so-called Cramér-Rao Lower bound (CRLB), which is a lower bound on the variance of the parameter estimates. Minimising this CRLB as a function of the microscope settings yields the optimal statistical experimental design. However, the CRLB relies on weak regularity conditions on the probability (density) function (P(D)F) of the observations, including that the P(D)F should be continuously differentiable with respect to the parameters. This condition is not satisfied for restricted, or so-called discrete parameters, such as the atomic number Z or the number of atoms in a projected atom column. Therefore, an alternative approach using the principles of detection theory has been proposed in this thesis, in order to optimise the experiment design for discrete parameter estimation problems. An estimation problem can then be formulated as a binary or multiple hypothesis test where every hypothesis corresponds to, for example, a specific atomic number Z , or a number of atoms in a projected atom column. Furthermore, detection theory allows one to compute the probability to assign an incorrect hypothesis, the so-called probability of error. Minimising this probability of error as a function of the microscope settings has been used to optimise the design of a HR(S)TEM experiment in order to identify the chemical composition by estimating the atomic number Z , to detect light atoms, and finally also for nanoparticle atom-counting.

At the start of this PhD research, the optimal detector settings of the annular STEM detector have been investigated for identifying the chemical composition, i.e. for estimating the atomic number Z , using the principles of detection theory. In the case of deciding between the presence of two different atom types, both for individual atoms and for atom columns at an interface of a thin crystal, the LAADF STEM detector setting has been found to be optimal based on our quantitative approach. This detector setting was also suggested elsewhere based on visual interpretation [69]. This optimal setting corresponds to a detector range with the inner detector radius slightly larger than the probe semi-convergence angle of 21 mrad.

In the following step, the HRSTEM detector design has been optimised by using our quantitative approach, in order to detect light atoms. The investigated research question can then be formulated as whether there is an atom column present or not. When detecting the lightest hydrogen atom, ABF STEM has been found to be optimal, with the detection range lying within the illumination cone of the probe. Based on qualitative criteria, such as visual contrast, this setting was already suggested elsewhere for the detection of light atoms [3, 12, 23, 56, 57, 85]. Next, the crystals LiV_2O_4 and SrTiO_3 have been investigated in order to optimise the experiment design to detect and locate either a light lithium or oxygen column respectively. For HRSTEM, the optimal detector design depends on the investigated material and the crystal thickness and corresponds to either LAADF STEM for thin specimens, or ABF STEM. When the sample region becomes thicker, both optimal regions start to overlap and, furthermore, it becomes easier to detect the light atom columns. The optimal settings obtained for locating the light atom columns using the attainable precision as optimality criterion, have been found to be consistent with the optimal settings for the detection of these light atom columns for HRSTEM imaging.

In the case of HRTEM, different optima are found for the detection of the light oxygen column in SrTiO_3 for the three investigated thicknesses. Only for the detection of light elements in thicker sample regions, optimisation of the spherical aberration and defocus becomes less critical and the optimal region broadens. However, no single optimum has been retrieved for the detection and locating problem for HRTEM imaging. Therefore, this imaging technique seems inappropriate if one wants to detect and locate light atom columns with the lowest probability of error and the highest possible precision, respectively, from a single image. Using a focal series of HRTEM images and by performing exit

wave reconstruction, precise quantitative results might be obtained, but this was not investigated in this thesis.

In addition, the incoming electron dose has been optimised in order to detect and locate light atoms. In the case of HRSTEM, a single optimal incoming electron dose has been found for which the light elements can be detected with a low probability of error and also located with a precision in the picometre range. This optimal incoming electron dose depends on the crystal structure and thickness. For detecting and locating either Li in LiV_2O_4 or O in SrTiO_3 from HRSTEM images, an incoming electron dose of the order of $10^5 e^-/\text{\AA}^2$ or $10^4 e^-/\text{\AA}^2$ has been proposed respectively, under the optimal detector settings.

Another application that has been examined in this thesis, using our quantitative approach, is the atom-counting performance of both HRTEM and HRSTEM. By using the principles of detection theory, the limits to the precision with which the number of atoms in a projected atom column can be estimated have been investigated and compared for both imaging modes. The use of scattering cross-sections in HRSTEM, which were already proposed in [76, 146, 220], has been found to be appropriate when the goal is to count the number of atoms with the lowest probability of error. Indeed, they perform equally well as the HRSTEM images on a pixel by pixel basis of a projected atom column and they even outperform peak intensities. By minimising the probability of error as a function of the experimental settings, the experiment design has been optimised for atom-counting. For HRSTEM, the optimal annular inner and outer detector angles have been derived quantitatively, whereas for HRTEM the spherical aberration and defocus have been optimised. We can conclude that when comparing the currently used approaches, HRSTEM is in general applicable for atom-counting when using an appropriate detector range, where the scattering cross-sections monotonically increase with thickness, and where the overlap between the probability functions of consecutive scattering cross-sections is small. When the atom-counting decision is based on the probability function of peak intensities, HRTEM can only be used to count the number of atoms in projected atom columns in a very thin sample region at optimal imaging conditions, and using a sufficiently high incoming electron dose. The peak intensities oscillate as a function of the thickness, depending on the atom column type due to the inherent electron channelling. The probability of error at the optimal experimental settings for HRTEM, when the atom-counting decision is based on the probability function of peak intensities is larger as compared to the optimal probability of error for HRSTEM, when using the same incoming

electron dose. Under the assumption that one can make the atom-counting decision based on the joint probability function of all image pixel intensities, the probability of error decreased significantly in the case of HRTEM, and became lower as compared to HRSTEM. However, such atom-counting procedure would require the behaviour of all pixel values in the image as a function of thickness, and therefore also all imaging parameters. In practice, the spherical aberration and defocus will be estimated parameters too, which will mostly increase the probability of error for atom-counting in HRTEM, as this imaging technique is less robust with respect to these parameters as compared to HRSTEM. In HRSTEM, both for binary and multiple hypothesis testing, the probability of error based on the joint probability function of the image pixel values is well approximated by the probability of error for scattering cross-sections, for which an appropriate and practical framework exists [75–77].

In conclusion, HRTEM may in theory result into a lower probability of error for atom-counting when using image intensities on a pixel by pixel basis, but the commonly used scattering cross-sections for atom-counting in HRSTEM lead to a high performance and have been shown to work in practice.

Finally, experimental images have been analysed for different purposes and the maximum likelihood estimator has been used in order to estimate unknown structure parameters, such as the atom column positions, within a model-based estimation algorithm that is implemented in an efficient way in the StatSTEM software [147]. From the estimated atom column positions, different distances, atomic displacements and angles within complex structured materials have been derived from experimental HRSTEM images in a quantitative way.

In this thesis, statistical experiment design has been used to discover the theoretical limits to quantitative HR(S)TEM. This limit is given by the probability of error in the case of discrete estimation problems, and by the highest attainable precision for the estimation of continuous structure parameters. Furthermore, statistical experimental design allows one to find the optimal microscope settings resulting into the lowest probability of error or the highest attainable precision, respectively. In this way it provides the electron microscopist with insight in which precision may be obtained at which microscope settings. Furthermore, it has been shown that statistical parameter estimation theory can lead to precise results for different applications, which makes it the optimal tool for quantitative electron microscopy.

Appendix A

Camera lengths of the FEI QU-Ant-EM

Camera length (cm)	Inner HAADF (mrad)	Outer HAADF (mrad)
29,5	163	190
37	130	190
46	108	190
58	87	190
73	69	190
91	56	190
115	44	190
145	35	190
185	28	172
230	22	136
285	18	113
360	14	89
460	11	70
580	9	55
720	7	44

Camera lengths of the FEI X-Ant-EM

Camera length (cm)	Inner HAADF (mrad)	Outer HAADF (mrad)
29,5	183.4	144
37	142	147
46	115	157
58	91	157
73	74	157
91	58	197
115	46	215
145	36	215
185	29	174
230	23	142
285	19	117
360	15	95
460	13	78
580	10	63
720	8	50
910	7	41

Camera length (cm)	Inner DF4 (mrad)	Outer DF4 (mrad)	Inner DF2 (mrad)	Outer DF2 (mrad)
37	33,10023	117,3554	16,55012	33,10023
46	26,80653	95,04132	13,40326	26,80653
58	21,21212	75,20661	10,60606	21,21212
73	17,24942	61,15702	8,624709	17,24942
91	13,51981	47,93388	6,759907	13,51981
115	10,72261	38,01653	5,361305	10,72261
145	8,391608	29,75207	4,195804	8,391608
185	6,75	23,93	3,375	6,75
230	5,361305	19,00826	2,680653	5,361305
285	4,428904	15,70248	2,214452	4,428904
360	3,496503	12,39669	1,748252	3,496503
460	3,030303	10,7438	1,515152	3,030303
580	2,331002	8,264463	1,165501	2,331002
720	1,864802	6,61157	0,932401	1,864802
910	1,631702	5,785124	0,815851	1,631702

Bibliography

- [1] J.-M. Tarascon and M. Armand. Issues and challenges facing rechargeable lithium batteries. *Nature*, 414(6861):359–367, 2001.
- [2] A. Du Pasquier, I. Plitz, S. Menocal, and G. Amatucci. A comparative study of Li-ion battery, supercapacitor and nonaqueous asymmetric hybrid devices for automotive applications. *Journal of Power Sources*, 115(1):171–178, 2003.
- [3] S. Lee, Y. Oshima, H. Sawada, F. Hosokawa, and E. Okunishi. Counting lithium ions in the diffusion channel of an LiV_2O_4 crystal. *Journal of Applied Physics*, 109(113530):1–5, 2011.
- [4] M. D. Levi, G. Salitra, B. Markovsky, H. Teller, D. Aurbach, U. Heider, and L. Heider. Solid-State Electrochemical Kinetics of Li-Ion Intercalation into $\text{Li}_{1-x}\text{CoO}_2$: Simultaneous Application of Electroanalytical Techniques SSCV, PITT, and EIS. *Journal of The Electrochemical Society*, 146(4):1279–1289, 1999.
- [5] M. Morcrette, P. Rozier, L. Dupont, E. Mugnier, L. Sannier, J. Galy, and J.-M. Tarascon. A reversible copper extrusion–insertion electrode for rechargeable Li batteries. *Nature Materials*, 2(11):755–761, 2003.
- [6] S. Nishimura, G. Kobayashi, K. Ohoyama, R. Kanno, M. Yashima, and A. Yamada. Experimental visualization of lithium diffusion in Li_xFePO_4 . *Nature Materials*, 7(9):707–711, 2008.
- [7] C. Delmas, M. Maccario, L. Croguennec, F. Le Cras, and F. Weill. Lithium deintercalation in LiFePO_4 nanoparticles via a domino-cascade model. *Nature Materials*, 7(8):665–671, 2008.
- [8] A. Brazier, L. Dupont, L. Dantras-Laffont, N. Kuwata, J. Kawamura, and J.-M. Tarascon. First cross-section observation of an all solid-state lithium-ion “nanobattery” by transmission electron microscopy. *Chemistry of Materials*, 20(6):2352–2359, 2008.
- [9] W. Coene, G. Janssen, M. Op de Beeck, and D. Van Dyck. Phase retrieval through focus variation for ultra-resolution in field-emission transmission electron microscopy. *Physical Review Letters*, 69(26):3743, 1992.
- [10] Y. Shao-Horn, L. Croguennec, C. Delmas, E. C. Nelson, and M. A. O’Keefe. Atomic resolution of lithium ions in LiCoO_2 . *Nature Materials*, 2:464–467, 2003.

- [11] M. D. Rossell, R. Erni, M. Asta, V. Radmilovic, and U. Dahmen. Atomic-resolution imaging of lithium in Al_3Li precipitates. *Physical Review B*, 80(2):024110, 2009.
- [12] Y. Oshima, H. Sawada, F. Hosokawa, E. Okunishi, T. Kaneyama, Y. Kondo, S. Niitaka, H. Takagi, Y. Tanishiro, and K. Takayanagi. Direct imaging of lithium atoms in LiV_2O_4 by spherical aberration-corrected electron microscopy. *Journal of Electron Microscopy*, 59:457–461, 2010.
- [13] S. Lee, Y. Oshima, H. Sawada, F. Hosokawa, E. Okunishi, T. Kaneyama, Y. Kondo, Y. Tanishiro, and K. Takayanagi. Surface imaging by ABF-STEM: Lithium Ions in Diffusion Channel of LIB Electrode Materials. *e-Journal of Surface Science and Nanotechnology*, 10(0):454–458, 2012.
- [14] Y. Oshima, S. Lee, and K. Takayanagi. Visualization of lithium ions by annular bright field imaging. *Microscopy*, pages 1–10, 2016.
- [15] M. Sathiyaa, A. M. Abakumov, D. Foix, G. Rousse, K. Ramesha, M. Saubanère, M. L. Doublet, H. Vezin, C. P. Laisa, A. S. Prakash, D. Gonbeau, G. Van Tendeloo, and J.-M. Tarascon. Origin of voltage decay in high-capacity layered oxide electrodes. *Nature Materials*, 14(2):230–238, 2015.
- [16] T. Ohzuku and Y. Makimura. Layered Lithium Insertion Material of $\text{LiCo}_{1/3}\text{Ni}_{1/3}\text{Mn}_{1/3}\text{O}_2$ for Lithium-Ion Batteries. *Chemistry Letters*, (7):642–643, 2001.
- [17] M. Bettge, Y. Li, K. Gallagher, Y. Zhu, Q. Wu, W. Lu, I. Bloom, and D. P. Abraham. Voltage fade of layered oxides: Its measurement and impact on energy density. *Journal of The Electrochemical Society*, 160(11):A2046–A2055, 2013.
- [18] K. G. Gallagher, J. R. Croy, M. Balasubramanian, M. Bettge, D. P. Abraham, A. K. Burrell, and M. M. Thackeray. Correlating hysteresis and voltage fade in lithium-and manganese-rich layered transition-metal oxide electrodes. *Electrochemistry Communications*, 33:96–98, 2013.
- [19] J. R. Croy, K. G. Gallagher, M. Balasubramanian, Z. Chen, Y. Ren, D. Kim, S.-H. Kang, D. W. Dees, and M. M. Thackeray. Examining Hysteresis in Composite $x\text{Li}_2\text{MnO}_3 \cdot (1-x)\text{LiMO}_2$ Cathode Structures. *The Journal of Physical Chemistry C*, 117(13):6525–6536, 2013.
- [20] U.S. Department of Energy. Multi-Year Research, Development, and Demonstration Plan. 3.3:1–23, 2015.
- [21] U.S. Department of Energy. 2011 Fuel Cell Technologies Market Report. July 2012.
- [22] S. D. Findlay, T. Saito, N. Shibata, Y. Sato, J. Matsuda, K. Asano, E. Akiba, T. Hirayama, and Y. Ikuhara. Direct imaging of hydrogen within a crystalline environment. *Applied Physics Express*, 3(11):116603, 2010.
- [23] R. Ishikawa, E. Okunishi, H. Sawada, Y. Kondo, F. Hosokawa, and E. Abe. Direct imaging of hydrogen-atom columns in a crystal by annular bright field electron microscopy. *Nature Materials*, 10:278–281, 2011.

- [24] Y.-J. Kim, R. Tao, R. F. Klie, and D. N. Seidman. Direct atomic-scale imaging of hydrogen and oxygen interstitials in pure niobium using atom-probe tomography and aberration-corrected scanning transmission electron microscopy. *ACS Nano*, 7(1):732–739, 2012.
- [25] S. D. Jackson and J. S. J. Hargreaves. *Metal oxide catalysis*, volume 1. Wiley Online Library, 2009.
- [26] I. MacLaren and Q. M. Ramasse. Aberration-corrected scanning transmission electron microscopy for atomic-resolution studies of functional oxides. *International Materials Reviews*, 59(3):115–131, 2014.
- [27] A. Ohtomo, D. A. Muller, J. L. Grazul, and H. Y. Hwang. Artificial charge-modulation in atomic-scale perovskite titanate superlattices. *Nature*, 419(6905):378–380, 2002.
- [28] A. Ohtomo and H. Y. Hwang. A high-mobility electron gas at the $\text{LaAlO}_3/\text{SrTiO}_3$ heterointerface. *Nature*, 427(6973):423–426, 2004.
- [29] J. Seidel, L. W. Martin, Q. He, Q. Zhan, Y.-H. Chu, A. Rother, M. E. Hawkrige, P. Maksymovych, P. Yu, M. Gajek, et al. Conduction at domain walls in oxide multiferroics. *Nature Materials*, 8(3):229–234, 2009.
- [30] A. B. Shah, Q. M. Ramasse, S. J. May, J. Kavich, J. G. Wen, X. Zhai, J. N. Eckstein, J. Freeland, A. Bhattacharya, and J. M. Zuo. Presence and spatial distribution of interfacial electronic states in $\text{LaMnO}_3 - \text{SrMnO}_3$ superlattices. *Physical Review B*, 82(11):115112, 2010.
- [31] P. Yu, J.-S. Lee, S. Okamoto, M. D. Rossell, M. Huijben, C.-H. Yang, Q. He, J. X. Zhang, S. Y. Yang, M. J. Lee, et al. Interface ferromagnetism and orbital reconstruction in $\text{BiFeO}_3 - \text{La}_{0.7}\text{Sr}_{0.3}\text{MnO}_3$ heterostructures. *Physical Review Letters*, 105(2):027201, 2010.
- [32] A. B. Shah, Q. M. Ramasse, X. Zhai, J. G. Wen, S. J. May, I. Petrov, A. Bhattacharya, P. Abamonte, J. N. Eckstein, and J.-M. Zuo. Probing interfacial electronic structures in atomic layer LaMnO_3 and SrTiO_3 superlattices. *Advanced Materials*, 22(10):1156–1160, 2010.
- [33] S. Dong, R. Yu, S. Yunoki, G. Alvarez, J.-M. Liu, and E. Dagotto. Magnetism, conductivity, and orbital order in $(\text{LaMnO}_3)_{2n}/(\text{SrMnO}_3)_n$ superlattices. *Physical Review B*, 78(20):201102, 2008.
- [34] A. Brinkman, M. Huijben, M. Van Zalk, J. Huijben, U. Zeitler, J. C. Maan, W. G. Van der Wiel, G. Rijnders, D. H. A. Blank, and H. Hilgenkamp. Magnetic effects at the interface between non-magnetic oxides. *Nature Materials*, 6(7):493–496, 2007.
- [35] H. Yamada, Y. Ogawa, Y. Ishii, H. Sato, M. Kawasaki, H. Akoh, and Y. Tokura. Engineered interface of magnetic oxides. *Science*, 305(5684):646–648, 2004.
- [36] I. MacLaren, Z. L. Wang, H. S. Wang, and Q. Li. Strain-induced crystal structure change in ultrathin films of $\text{Pr}_{0.7}\text{Sr}_{0.3}\text{MnO}_3$. *Applied Physics Letters*, 80(8):1406–1408, 2002.
- [37] Y.-M. Kim, A. Kumar, A. Hatt, A. N. Morozovska, A. Tselev, M. D. Biegalski, I. Ivanov, E. A. Eliseev, S. J. Pennycook, J. M. Rondinelli, et al. Interplay of octahedral tilts and polar order in BiFeO_3 films. *Advanced Materials*, 25(17):2497–2504, 2013.

- [38] R. J. Zeches, M. D. Rossell, J. X. Zhang, A. J. Hatt, Q. He, C.-H. Yang, A. Kumar, C. H. Wang, A. Melville, C. Adamo, et al. A strain-driven morphotropic phase boundary in BiFeO_3 . *Science*, 326(5955):977–980, 2009.
- [39] S. Karimi, I. M. Reaney, Y. Han, J. Pokorny, and I. Sterianou. Crystal chemistry and domain structure of rare-earth doped BiFeO_3 ceramics. *Journal of Materials Science*, 44(19):5102–5112, 2009.
- [40] D. Kan, L. Pálóvá, V. Anbusathaiah, C. J. Cheng, S. Fujino, V. Nagarajan, K. M. Rabe, and I. Takeuchi. Universal Behavior and Electric-Field-Induced Structural Transition in Rare-Earth-Substituted BiFeO_3 . *Advanced Functional Materials*, 20(7):1108–1115, 2010.
- [41] S. Fujino, M. Murakami, V. Anbusathaiah, S.-H. Lim, V. Nagarajan, C. J. Fennie, M. Wuttig, L. Salamanca-Riba, and I. Takeuchi. Combinatorial discovery of a lead-free morphotropic phase boundary in a thin-film piezoelectric perovskite. *Applied Physics Letters*, 92(20):202904, 2008.
- [42] J. B. Neaton, C. Ederer, U. V. Waghmare, N. A. Spaldin, and K. M. Rabe. First-principles study of spontaneous polarization in multiferroic BiFeO_3 . *Physical Review B*, 71(1):014113, 2005.
- [43] Y.-H. Chu, L. W. Martin, M. B. Holcomb, M. Gajek, S.-J. Han, Q. He, N. Balke, C.-H. Yang, D. Lee, W. Hu, et al. Electric-field control of local ferromagnetism using a magnetoelectric multiferroic. *Nature Materials*, 7(6):478–482, 2008.
- [44] I. Levin, M. G. Tucker, H. Wu, V. Provenzano, C. L. Dennis, S. Karimi, T. Comyn, T. Stevenson, R. I. Smith, and I. M. Reaney. Displacive phase transitions and magnetic structures in Nd-substituted BiFeO_3 . *Chemistry of Materials*, 23(8):2166–2175, 2011.
- [45] A. Chen, H. Zhou, Z. Bi, Y. Zhu, Z. Luo, A. Bayraktaroglu, J. Phillips, E.-M. Choi, J. L. MacManus-Driscoll, S. J. Pennycook, et al. A new class of room-temperature multiferroic thin films with bismuth-based supercell structure. *Advanced Materials*, 25(7):1028–1032, 2013.
- [46] D. M. Evans, A. Schilling, A. Kumar, D. Sanchez, N. Ortega, M. Arredondo, R. S. Katiyar, J. M. Gregg, and J. F. Scott. Magnetic switching of ferroelectric domains at room temperature in multiferroic PZTFT. *Nature Communications*, 4:1534, 2013.
- [47] P. Yu, W. Luo, D. Yi, J. X. Zhang, M. D. Rossell, C.-H. Yang, L. You, G. Singh-Bhalla, S. Y. Yang, Q. He, et al. Interface control of bulk ferroelectric polarization. *Proceedings of the National Academy of Sciences*, 109(25):9710–9715, 2012.
- [48] Z. Liao, R. J. Green, N. Gauquelin, S. Macke, L. Li, J. Gonnissen, R. Sutarto, E. P. Houwman, Z. Zhong, S. Van Aert, J. Verbeeck, G. A. Sawatzky, M. Huijben, G. Koster, and G. Rijnders. Long-range domain structure and symmetry engineering by interfacial oxygen octahedral coupling at heterostructure interface. *Advanced Functional Materials*, 2016.
- [49] L. W. Martin, Y.-H. Chu, and R. Ramesh. Advances in the growth and characterization of magnetic, ferroelectric, and multiferroic oxide thin films. *Materials Science and Engineering: R: Reports*, 68(4):89–133, 2010.

- [50] C. Kisielowski, C. J. D. Hetherington, Y. C. Wang, R. Kilaas, M. A. Okeefe, and A. Thust. Imaging columns of the light elements carbon, nitrogen and oxygen with sub Ångstrom resolution. *Ultramicroscopy*, 89(4):243–263, 2001.
- [51] K. Yoshida, T. Kawai, T. Nambara, S. Tanemura, K. Saitoh, and N. Tanaka. Direct observation of oxygen atoms in rutile titanium dioxide by spherical aberration corrected high-resolution transmission electron microscopy. *Nanotechnology*, 17(15):3944, 2006.
- [52] C. L. Jia, S. B. Mi, K. Urban, I. Vrejoiu, M. Alexe, and D. Hesse. Atomic-scale study of electric dipoles near charged and uncharged domain walls in ferroelectric films. *Nature Materials*, 7:57–61, 2008.
- [53] Z. Zhang, W. Sigle, F. Phillipp, and M. Rühle. Direct atom-resolved imaging of oxides and their grain boundaries. *Science*, 302(5646):846–849, 2003.
- [54] C. L. Jia, M. Lentzen, and K. Urban. Atomic-resolution imaging of oxygen in perovskite ceramics. *Science*, 299(5608):870–873, 2003.
- [55] S. D. Findlay, N. Shibata, H. Sawada, E. Okunishi, Y. Kondo, T. Yamamoto, and Y. Ikuhara. Robust atomic resolution imaging of light elements using scanning transmission electron microscopy. *Applied Physics Letters*, 95, 191913, 2009.
- [56] E. Okunishi, I. Ishikawa, H. Sawada, F. Hosokawa, M. Hori, and Y. Kondo. Visualization of light elements at ultrahigh resolution by STEM annular bright field microscopy. *Microscopy and Microanalysis*, 15:164–165, 2009.
- [57] S. D. Findlay, N. R. Lugg, N. Shibata, L. J. Allen, and Y. Ikuhara. Prospects for lithium imaging using annular bright field scanning transmission electron microscopy: A theoretical study. *Ultramicroscopy*, 111:1144–1154, 2011.
- [58] Y. Zhu, R. L. Withers, L. Bourgeois, C. Dwyer, and J. Etheridge. Direct mapping of Li-enabled octahedral tilt ordering and associated strain in nanostructured perovskites. *Nature Materials*, 2015.
- [59] H. Fujita and N. Sumida. Usefulness of electron microscopy. In *Physics of New Materials*, pages 226–263. Springer, 1994.
- [60] D. Van Dyck, S. Van Aert, A. J. den Dekker, and A. van den Bos. Is atomic resolution transmission electron microscopy able to resolve and refine amorphous structures? *Ultramicroscopy*, 98(1):27–42, 2003.
- [61] D. van Dyck. High-resolution electron microscopy. *Advances in Imaging and Electron Physics*, 123:105–171, 2002.
- [62] M. De Graef. *Introduction to conventional transmission electron microscopy*. Cambridge University Press, 2003.
- [63] D. B. Williams and C. B. Carter. *Transmission electron microscopy: a textbook for materials science*. Springer 2nd Edition, 2009.

- [64] D. Van Dyck and J. H. Chen. Towards an exit wave in closed analytical form. *Acta Crystallographica Section A: Foundations of Crystallography*, 55(2):212–215, 1999.
- [65] P. Geuens and D. Van Dyck. The S-state model: a work horse for HRTEM. *Ultramicroscopy*, 93:179–198, 2002.
- [66] P. D. Nellist and S. J. Pennycook. The principles and interpretation of annular dark-field Z-contrast imaging. *Advances in imaging and electron physics*, 113:147–203, 2000.
- [67] S. J. Pennycook and P. D. Nellist. *Scanning transmission electron microscopy: imaging and analysis*. Springer Science & Business Media, 2011.
- [68] N. Shibata, Y. Kohno, S. D. Findlay, H. Sawada, Y. Kondo, and Y. Ikuhara. New area detector for atomic-resolution scanning transmission electron microscopy. *Journal of Electron Microscopy*, 59(6):473–479, 2010.
- [69] R. Hovden and D. A. Muller. Efficient elastic imaging of single atoms on ultrathin supports in a scanning transmission electron microscope. *Ultramicroscopy*, 123:59–65, 2012.
- [70] H. Yang, T. J. Pennycook, and P. D. Nellist. Efficient phase contrast imaging in STEM using a pixelated detector. Part II: Optimisation of imaging conditions. *Ultramicroscopy*, 151:232–239, 2015.
- [71] S. J. Pennycook and L. A. Boatner. Chemically sensitive structure-imaging with a scanning transmission electron microscope. *Nature*, 336(6199):565–567, 1988.
- [72] P. Hartel, D. Rose, and C. Dinges. Conditions and reasons for incoherent imaging in STEM. *Ultramicroscopy*, 63:63–114, 1996.
- [73] P. D. Nellist and S. J. Pennycook. Incoherent imaging using dynamically scattered coherent electrons. *Ultramicroscopy*, 78(1):111–124, 1999.
- [74] D. O. Klenov and S. Stemmer. Contributions to the contrast in experimental high-angle annular dark-field images. *Ultramicroscopy*, 106(10):889–901, 2006.
- [75] S. Van Aert, K. J. Batenburg, M. D. Rossell, R. Erni, and G. Van Tendeloo. Three dimensional atomic imaging of crystalline nanoparticles. *Nature*, 470:374–377, 2011.
- [76] S. Van Aert, A. De Backer, G. T. Martinez, B. Goris, S. Bals, G. Van Tendeloo, and A. Rosenauer. *Physical Review B*, 87:064107, 2013.
- [77] A. De Backer, G. T. Martinez, A. Rosenauer, and S. Van Aert. Atom counting in HAADF STEM using a statistical model-based approach: methodology, possibilities, and inherent limitations. *Ultramicroscopy*, 134:23–33, 2013.
- [78] T. Grieb, K. Mueller, R. Fritz, M. Schowalter, N. Neugebohrn, N. Knaub, K. Volz, and A. Rosenauer. Determination of the chemical composition of GaNAs using STEM HAADF imaging and STEM strain state analysis. *Ultramicroscopy*, 117:15–23, 2012.

- [79] T. Grieb, K. Müller, R. Fritz, V. Grillo, M. Schowalter, K. Volz, and A. Rosenauer. Quantitative chemical evaluation of dilute GaNAs using ADF STEM: Avoiding surface strain induced artifacts. *Ultramicroscopy*, 129:1–9, 2013.
- [80] M. Ohtsuka, T. Yamazaki, Y. Kotaka, I. Hashimoto, and K. Watanabe. Imaging of light and heavy atomic columns by spherical aberration corrected middle-angle bright-field STEM. *Ultramicroscopy*, 120:48–55, 2012.
- [81] R. F. Egerton. Electron energy-loss spectroscopy in the TEM. *Reports on Progress in Physics*, 72(1):016502, 2008.
- [82] F. J. G. De Abajo. Optical excitations in electron microscopy. *Reviews of Modern Physics*, 82(1):209, 2010.
- [83] H. Tan, S. Turner, E. Yücelen, J. Verbeeck, and G. Van Tendeloo. 2D atomic mapping of oxidation states in transition metal oxides by scanning transmission electron microscopy and electron energy-loss spectroscopy. *Physical Review Letters*, 107(10):107602, 2011.
- [84] P. E. Batson. Electron microscopy: Hydrogen brightens up. *Nature Materials*, 10(4):270–271, 2011.
- [85] S. D. Findlay, N. Shibata, H. Sawada, E. Okunishi, Y. Kondo, and Y. Ikuhara. Dynamics of annular bright field imaging in scanning transmission electron microscopy. *Ultramicroscopy*, 110:903–923, 2010.
- [86] E. Okunishi, H. Sawada, and Y. Kondo. Experimental study of annular bright field (ABF) imaging using aberration-corrected scanning transmission electron microscopy (STEM). *Micron*, 43:538–544, 2012.
- [87] M. Varela, A. Lupini, K. Van Benthem, A. Borisevich, M. Chisholm, N. Shibata, E. Abe, and S. J. Pennycook. Do smaller probes in a STEM result in more precise measurement of the distances between atom columns? *Annual Review of Materials Research*, 35:539, 2005.
- [88] K. Mkhoyan, P. Baston, J. Cha, W. Schaff, and J. Silcox. Retrieval of crystal defect structures from HREM images by simulated evolution i. basic technique. *Science*, 312:1354, 2006.
- [89] J. M. Cowley. Image contrast in a transmission scanning electron microscope. *Applied Physics Letters*, 15:58–59, 1969.
- [90] R. Huang and Y. Ikuhara. STEM characterization for lithium-ion battery cathode materials. *Current opinion in Solid State and Materials Science*, 16:31–38, 2012.
- [91] M. Knoll and E. Ruska. Das Elektronenmikroskop. *Zeitschrift für Physik*, 78(5-6):318–339, 1932.
- [92] M. Knoll and E. Ruska. Aufladepotential und Sekundäremission Elektronenbestrahlter Körper. *Zeitschrift für Technische Physik*, 16:467–475, 1935.
- [93] M. Von Ardenne. Das Elektronen-Rastermikroskop. *Zeitschrift für Physik*, 109(9-10):553–572, 1938.

- [94] A. V. Crewe. Scanning electron microscopes: is high resolution possible? *Science*, 154(3750):729–738, 1966.
- [95] A. V. Crewe, J. Wall, and L. M. Welter. A high-resolution scanning transmission electron microscope. *Journal of Applied Physics*, 39(13):5861–5868, 1968.
- [96] A. V. Crewe, J. Wall, and J. Langmore. Visibility of single atoms. *Science*, 168(3937):1338–1340, 1970.
- [97] I. R. M. Wardell and P. E. Bovey. A History of Vacuum Generators’ 100-kV Scanning Transmission Electron Microscope. *Advances in Imaging and Electron Physics*, 159:221–285, 2009.
- [98] O. Scherzer. Über einige Fehler von Elektronenlinsen. *Zeitschrift für Physik*, 101(9-10):593–603, 1936.
- [99] O. Scherzer. The theoretical resolution limit of the Electron Microscope. *Journal of Applied Physics*, 20:20–29, 1949.
- [100] O. Scherzer. Sphärische und chromatische Korrektur von Elektronenlinsen. *Optik*, 2:114–132, 1947.
- [101] R. Seeliger. Über die justierung sphärisch korrigierter elektronenoptischer Systeme. *Optik*, 10(1-3):29–41, 1953.
- [102] G. Möllenstedt. Elektronenmikroskopische Bilder mit einem nach O. Scherzer sphärisch korrigierten Objektiv. *Optik*, 13:209–215, 1956.
- [103] H. Rose. Abbildungseigenschaften sphärisch korrigierter elektronenoptischer Achromate. *Optik*, 33(1):1–24, 1971.
- [104] G. D. Archard. Two new simplified systems for the correction of spherical aberration in electron lenses. *Proceedings of the Physical Society. Section B*, 68(3):156, 1955.
- [105] D. F. Hardy. *Combined magnetic and electrostatic quadrupole electron lenses*. PhD thesis, University of Cambridge, 1969.
- [106] V. D. Beck. Hexapole spherical-aberration corrector. *Optik*, 53(4):241–255, 1979.
- [107] J. Zach and M. Haider. Correction of spherical and chromatic aberration in a low voltage SEM. *Optik*, 98(3):112–118, 1995.
- [108] M. Haider, G. Braunshausen, and E. Schwan. Correction of the spherical aberration of a 200 kV TEM by means of a hexapole-corrector. *Optik*, 99(4):167–179, 1995.
- [109] M. Lentzen, B. Jahnen, C. L. Jia, A. Thust, K. Tillmann, and K. Urban. High-resolution imaging with an aberration-corrected transmission electron microscope. *Ultramicroscopy*, 92(3):233–242, 2002.
- [110] O. L. Krivanek, N. Dellby, and A. R. Lupini. Towards sub-Å electron beams. *Ultramicroscopy*, 78(1):1–11, 1999.

- [111] M. Haider, H. Rose, S. Uhlemann, B. Kabius, and K. Urban. Towards 0.1 nm resolution with the first spherically corrected transmission electron microscope. *Journal of Electron Microscopy*, 47(5):395–405, 1998.
- [112] M. Haider, S. Uhlemann, E. Schwan, H. Rose, B. Kabius, and K. Urban. Electron microscopy image enhanced. *Nature*, 392:768–769, 1998.
- [113] C. L. Jia, M. Lentzen, and K. Urban. High-resolution transmission electron microscopy using negative spherical aberration. *Microscopy and Microanalysis*, 10(02):174–184, 2004.
- [114] R. Erni, M. D. Rossell, C. Kisielowski, and U. Dahmen. Atomic-resolution imaging with a sub-50-pm electron probe. *Physical Review Letters*, 102(9):096101, 2009.
- [115] H. Sawada, Y. Tanishori, N. Ohashi, T. Tomita, F. Hosokawa, T. Kaneyama, Y. Kondo, and K. Takayanagi. STEM imaging of 47-pm separated atomic columns by a spherical aberration-corrected electron microscope with a 300-kV cold field emission gun. *Journal of Electron Microscopy*, 58:357–361, 2009.
- [116] T. Akashi, Y. Takahashi, T. Tanigaki, T. Shimakura, T. Kawasaki, T. Furutsu, H. Shinada, H. Müller, M. Haider, N. Osakabe, et al. Aberration corrected 1.2-MV cold field-emission transmission electron microscope with a sub-50-pm resolution. *Applied Physics Letters*, 106(7):074101, 2015.
- [117] H. Lichte. Electron holography approaching atomic resolution. *Ultramicroscopy*, 20(3):293–304, 1986.
- [118] D. Van Dyck, M. Op de Beeck, and W. Coene. A new approach to object wavefunction reconstruction in electron microscopy. *Optik*, 93:103–103, 1993.
- [119] A. I. Kirkland, W. O. Saxton, K.-L. Chau, K. Tsuno, and M. Kawasaki. Super-resolution by aperture synthesis: tilt series reconstruction in CTEM. *Ultramicroscopy*, 57(4):355–374, 1995.
- [120] M. Op de Beeck, D. Van Dyck, and W. Coene. Wave function reconstruction in HRTEM: The parabola method. *Ultramicroscopy*, 64:167–183, 1996.
- [121] W.-K. Hsieh, F.-R. Chen, J.-J. Kai, and A. I. Kirkland. Resolution extension and exit wave reconstruction in complex HREM. *Ultramicroscopy*, 98(2):99–114, 2004.
- [122] S. J. Haigh, H. Sawada, and A. I. Kirkland. Optimal tilt magnitude determination for aberration-corrected super resolution exit wave function reconstruction. *Philosophical Transactions of the Royal Society of London A: Mathematical, Physical and Engineering Sciences*, 367(1903):3755–3771, 2009.
- [123] C. Kisielowski, B. Freitag, M. Bischoff, H. Van Lin, S. Lazar, G. Knippels, P. Tiemeijer, M. van der Stam, S. von Harrach, M. Stekelburg, et al. Detection of single atoms and buried defects in three dimensions by aberration-corrected electron microscope with 0.5-Å information limit. *Microscopy and Microanalysis*, 14(05):469–477, 2008.

- [124] M. Haider, P. Hartel, H. Müller, S. Uhlemann, and J. Zach. Information transfer in a TEM corrected for spherical and chromatic aberration. *Microscopy and Microanalysis*, 16(04):393–408, 2010.
- [125] N. Alem, O. V. Yazyev, C. Kisielowski, P. Denes, U. Dahmen, P. Hartel, M. Haider, M. Bischoff, B. Jiang, S. G. Louie, et al. Probing the out-of-plane distortion of single point defects in atomically thin hexagonal boron nitride at the picometer scale. *Physical Review Letters*, 106(12):126102, 2011.
- [126] Lord Rayleigh. On the theory of optical images, with special reference to the microscope. *Philosophical Magazine*, 42:167–195, 1896.
- [127] P. E. Batson, N. Dellby, and O. L. Krivanek. Sub-Ångstrom resolution using aberration corrected electron optics. *Nature*, 418(6898):617–620, 2002.
- [128] P. D. Nellist, M. F. Chisholm, N. Dellby, O. L. Krivanek, M. F. Murfitt, Z. S. Szilagyi, A. R. Lupini, A. Borisevich, W. H. Sides Jr., and S. J. Pennycook. Direct sub-Ångstrom imaging of a crystal lattice. *Science*, 305:1741, 2004.
- [129] S. Van Aert, D. Van Dyck, and A. J. den Dekker. Resolution of coherent and incoherent imaging systems reconsidered-Classical criteria and a statistical alternative. *Optics Express*, 14(9):3830–3839, 2006.
- [130] D. H. Shin, E. J. Kirkland, and J. Silcox. Annular dark field electron microscope images with better than 2 Å resolution at 100 kV. *Applied Physics Letters*, 55(23):2456–2458, 1989.
- [131] G. Van Tendeloo and D. Van Dyck. The past, the Present, and the Future of Nanoscopy. *Handbook of Nanoscopy, Volume 1&2*, pages 1–8, 2012.
- [132] S. Van Aert, A. J. den Dekker, A. van den Bos, and D. Van Dyck. High-Resolution Electron Microscopy: From Imaging Toward Measuring. *IEEE Transactions on Instrumentation and Measurement*, 51(4):611–615, 2002.
- [133] Lord Rayleigh. Wave theory of light. In *Scientific Papers by John William Strutt, Baron Rayleigh*, volume 3, pages 47–189, Cambridge, 1902. Cambridge University Press.
- [134] A. J. den Dekker and A. van den Bos. Resolution: a survey. *Journal of the Optical Society of America A*, 14(3):547–557, 1997.
- [135] D. Van Dyck, E. Bettens, J. Sijbers, M. Op de Beeck, A. van den Bos, and A. J. den Dekker. From high resolution image to atomic structure: how far are we? *Scanning Microscopy*, 11:467–478, 1997.
- [136] D. A. Muller. Why changes in bond lengths and cohesion lead to core-level shifts in metals, and consequences for the spatial difference method. *Ultramicroscopy*, 78:163–174, 1999.
- [137] C. Kisielowski, E. Principe, B. Freitag, and D. Hubert. Benefits of microscopy with super resolution. *Physica B*, 308-310:1090–1096, 2001.
- [138] J. P. Locquet, J. Perret, J. Fompeyrine, E. Machler, J. W. Seo, and G. Van Tendeloo. Doubling the critical temperature of $\text{La}_{1.9}\text{Sr}_{0.1}\text{CuO}_4$. *Nature*, 394:453–456, 1998.

- [139] A. J. den Dekker, J. Sijbers, and V. Van Dyck. How to optimize the design of a quantitative HREM experiment so as to attain the highest precision? *Journal of Microscopy*, 194:95–104, 1999.
- [140] E. Bettens, D. Van Dyck, A. J. den Dekker, J. Sijbers, and A. van den Bos. Model-Based Two-Object Resolution from Observations Having Counting Statistics. *Ultramicroscopy*, 77:37–48, 1999.
- [141] S. Van Aert, A. J. den Dekker, A. van den Bos, D. Van Dyck, and J. H. Chen. Maximum likelihood estimation of structure parameters from high resolution electron microscopy images. Part II: a practical example. *Ultramicroscopy*, 104(2), 2005.
- [142] S. Bals, S. Van Aert, G. Van Tendeloo, and D. Ávila-Brande. Statistical estimation of atomic positions from exit wave reconstruction with a precision in the picometer range. *Physical Review Letters*, 96:096106, 2006.
- [143] S. Van Aert, S. Turner, R. Delville, D. Schryvers, G. Van Tendeloo, and E. K. H. Salje. Direct observation of ferroelectricity at ferroelastic domain boundaries in CaTiO_3 by electron microscopy. *Advanced Materials*, 24:523–527, 2012.
- [144] A. J. den Dekker, S. Van Aert, D. Van Dyck, and A. van den Bos. Maximum likelihood estimation of structure parameters from high resolution electron microscopy image. Part I: a theoretical framework. *Ultramicroscopy*, 104(2):83–106, 2005.
- [145] J. Verbeeck and S. Van Aert. Model based quantification of EELS spectra. *Ultramicroscopy*, 101:207–224, 2004.
- [146] S. Van Aert, J. Verbeeck, R. Erni, S. Bals, M. Luysberg, D. Van Dyck, and G. Van Tendeloo. Quantitative atomic resolution mapping using high-angle annular dark field scanning transmission electron microscopy. *Ultramicroscopy*, 109:1236–1244, 2009.
- [147] A. De Backer, K. H. W. van den Bos, W. Van den Broek, J. Sijbers, and S. Van Aert. StatSTEM: An efficient approach for accurate and precise model-based quantification of atomic resolution electron microscopy images. *Ultramicroscopy*, 171:104–116, 2016.
- [148] A. van den Bos and A. J. den Dekker. Resolution Reconsidered - Conventional Approaches and an Alternative. In P. W. Hawkes, editor, *Advances in Imaging and Electron Physics*, volume 117, pages 241–360. Academic Press, 2001.
- [149] S. Van Aert and D. Van Dyck. Do smaller probes in a STEM result in more precise measurement of the distances between atom columns? *Philosophical Magazine B*, 81:1833–1846, 2001.
- [150] A. J. den Dekker, S. Van Aert, D. Van Dyck, A. van den Bos, and P. Geuens. *Ultramicroscopy*, 89:275–290, 2001.
- [151] S. Van Aert, A. J. den Dekker, D. Van Dyck, and A. van den Bos. High-resolution electron microscopy and electron tomography: resolution versus precision. *Journal of Structural Biology*, 138:21–33, 2002.

- [152] S. Van Aert. *Statistical Experimental Design for Quantitative Atomic Resolution Transmission Electron Microscopy*. PhD thesis, Delft University of Technology, 2003.
- [153] S. Van Aert, A. J. den Dekker, and D. Van Dyck. How to optimize the experimental design of quantitative atomic resolution TEM experiments? *Micron*, 35:425–429, 2004.
- [154] S. Van Aert, A. J. den Dekker, A. van den Bos, and D. Van Dyck. *Statistical Experimental Design for Quantitative Atomic Resolution Transmission Electron Microscopy*, volume 130 of *Advances in Imaging and Electron Physics*, pages 1–164. Academic Press, San Diego, USA, 2004.
- [155] W. Van den Broek, S. Van Aert, P. Goos, and D. Van Dyck. Throughput maximization of particle radius measurements through balancing size versus current of the electron probe. *Ultramicroscopy*, 111:940–947, 2011.
- [156] S. M. Kay. *Fundamentals of Statistical Signal Processing. Volume II Detection Theory*. Prentice-Hall, Inc., New Jersey, 2009.
- [157] A. J. den Dekker, J. Gonnissen, A. De Backer, J. Sijbers, and S. Van Aert. Estimation of unknown structure parameters from high-resolution (S)TEM: What are the limits? *Ultramicroscopy*, 134:34–43, 2013.
- [158] J. Gonnissen, A. De Backer, A. J. den Dekker, G. T. Martinez, A. Rosenauer, J. Sijbers, and S. Van Aert. Optimal experimental design for the detection of light atoms from high-resolution scanning transmission electron microscopy images. *Applied Physics Letters*, 105(6):063116, 2014.
- [159] J. Gonnissen, A. De Backer, A. J. den Dekker, J. Sijbers, and S. Van Aert. Atom-counting in High Resolution Electron Microscopy: TEM or STEM—that’s the question. *Ultramicroscopy*, 2016.
- [160] S. Van Aert, A. J. den Dekker, D. Van Dyck, and A. van den Bos. Optimal experimental design of STEM measurement of atom column positions. *Ultramicroscopy*, 90(4):273–289, 2002.
- [161] A. Wang, S. Van Aert, P. Goos, and D. Van Dyck. Precision of three-dimensional atomic scale measurements for HRTEM images: what are the limits? *Ultramicroscopy*, 114:20–30, 2012.
- [162] A van den Bos. Parameter estimation. In P. H. Sydenham, editor, *Handbook of Measurement Science*, volume 1, pages 331–377, Chichester, 1982. Wiley.
- [163] B. R. Frieden. *Physics from Fisher Information - A Unification*. Cambridge University Press, Cambridge, United Kingdom, 1998.
- [164] A. Stuart and K. Ord. *Kendall’s Advanced Theory of Statistics*. Arnold, London, 1994.
- [165] R. I. Jennrich. *An Introduction to Computational Statistics - Regression Analysis*. Prentice Hall, Englewood Cliffs, NJ, 1995.

- [166] N. H. Dekkers and H. D. Lang. Differential phase contrast in a STEM. *Optik*, 41:452–456, 1974.
- [167] H. Rose. Image-formation by Inelastically Scattered Electrons in Electron-Microscopy. *Optik*, 45:139158, 1976.
- [168] H. Yang, R. N. Rutte, L. Jones, M. Simson, R. Sagawa, H. Ryll, M. Huth, T. J. Pennycook, M. L. H. Green, H. Soltau, Y. Kondo, B. G. Davis, and P. D. Nellist. Simultaneous atomic-resolution electron ptychography and Z-contrast imaging of light and heavy elements in complex nanostructures. *Nature Communications*, 7, 2016.
- [169] Earl J. Kirkland. *Advanced Computing in Electron Microscopy*. Springer, New York and London, 1998.
- [170] K. Fujiwara. Relativistic dynamical theory of electron diffraction. *Journal of the Physical Society of Japan*, 16:2226–2238, 1961.
- [171] H. A. Ferwerda, B. J. Hoendersa, and C. H. Slumpa. Fully relativistic treatment of electron-optical image formation based on the dirac equation. *Optica Acta*, 33:145–157, 1986.
- [172] H. A. Ferwerda, B. J. Hoendersa, and C. H. Slumpa. The Fully Relativistic Foundation of Linear Transfer Theory in Electron Optics Based on the Dirac Equation. *Optica Acta*, 33:159–183, 1986.
- [173] R. Jagannathan, R. Simon, and E. C. G. Sudarshan. Quantum theory of magnetic electron lenses based on the dirac equation. *Physics Letters A*, 134:457464, 1989.
- [174] R. Jagannathan. Quantum theory of electron lenses based on the dirac equation. *Physical Review A*, 42:66746689, 1990.
- [175] A. Rother and K. Scheerschmidt. Relativistic effects in elastic scattering of electrons in TEM. *Ultramicroscopy*, 109(2):154–160, 2009.
- [176] R. Brydson. *Aberration-corrected analytical transmission electron microscopy*, volume 3. John Wiley & Sons, 2011.
- [177] A. Howie and Z. S. Basinski. Approximations of the dynamical theory of diffraction contrast. *Philosophical Magazine*, 17:1039–1063, 1968.
- [178] D. Van Dyck. The importance of backscattering in high-energy electron diffraction calculations. *physica status solidi (a)*, 77:301308, 1975.
- [179] D. Van Dyck and W. Coene. The real space method for dynamical electron diffraction calculations in high resolution electron microscopy: I. Principles of the method. *Ultramicroscopy*, 15:29–40, 1984.
- [180] H. Bethe. Theorie der Beugung von Elektronen an Kristallen. *Annalen der Physik*, 392:55–129, 1928.

- [181] A. Howie and M. J. Whelan. Diffraction contrast of electron microscope images of crystal lattice defects, II. The development of a dynamical theory. *Proceedings of the Royal Society A*, 263:217237, 1961.
- [182] D. Van Dyck. The path integral formalism as a new description for the diffraction of high-energy electrons in crystals. *physica status solidi (b)*, 72:321336, 1975.
- [183] B. Jap and R. Glaeser. The scattering of high-energy electrons. I. Feynman pathintegral formulation. *Acta Crystallographica Section A*, 34:94–102, 1978.
- [184] J. M. Cowley. *Diffraction physics*. Elsevier, 1995.
- [185] P. G. Self, M. A. O’Keefe, P. R. Buseck, and A. E. C. Spargo. Practical computation of amplitudes and phases in electron diffraction. *Ultramicroscopy*, 11:3552, 1983.
- [186] D. Van Dyck. Image calculations in high-resolution electron microscopy: Problems, progress, and prospects. *Hawkes PW (ed.) Advances in electronics and electron physics*, 65:295355, 1985.
- [187] K. Watanabe. n-Beam dynamical calculations. *Advances in electronics and electron physics*, 86:173–224, 1993.
- [188] J. M. Cowley and A. F. Moodie. The Scattering of Electrons by Atoms and Crystals. I. A New Theoretical Approach. *Acta Crystallographica*, 10:609–619, 1957.
- [189] M. Born and E. Wolf. *Principles of optics: electromagnetic theory of propagation, interference and diffraction of light*. Elsevier, 1980.
- [190] P. Goodman and A. F. Moodie. Numerical evaluations of N-beam wave functions in electron scattering by the multi-slice method. *Acta Crystallographica Section A*, 30:280–290, 1974.
- [191] Y. Yang and Y. Kawazoe. Characterization of zero-point vibration in one-component crystals. *Europhysics Letters*, 98(6):66007, 2012.
- [192] Z. L. Wang. Thermal diffuse scattering in sub-angstrom quantitative electron microscopy Phenomenon, effects and approaches. *Micron*, 34(3):141–155, 2003.
- [193] P. Rez. Does phonon scattering give high-resolution images? *Ultramicroscopy*, 52(3):260–266, 1993.
- [194] A. Rosenauer, M. Schowalter, J. T. Titantah, and D. Lamoen. An emission-potential multi-slice approximation to simulate thermal diffuse scattering in high-resolution transmission electron microscopy. *Ultramicroscopy*, 108:1504–1513, 2009.
- [195] H. Yoshioka. Effect of inelastic waves on electron diffraction. *Journal of the Physical Society of Japan*, 12:618–628, 1957.
- [196] R. F. Loane, P. Xu, and J. Silcox. Thermal vibrations in convergent-beam electron diffraction. *Acta Crystallographica Section A*, 47:267–278, 1991.

- [197] D. Van Dyck. Is the frozen phonon model adequate to describe inelastic phonon scattering? *Ultramicroscopy*, 109:677–682, 2009.
- [198] D. A. Muller, B. Edwards, E. J. Kirkland, and J. Silcox. Simulation of thermal diffuse scattering including a detailed phonon dispersion curve. *Ultramicroscopy*, 86:371380, 2001.
- [199] L. J. Allen, S. D. Findlay, M. P. Oxley, and C. J. Rossouw. Lattice-resolution contrast from a focused coherent electron probe. Part I. *Ultramicroscopy*, 96:47–63, 2003.
- [200] K. Ishizuka. A practical approach for STEM image simulation based on the FFT multislice method. *Ultramicroscopy*, 90:71–83, 2002.
- [201] A. Rosenauer and M. Schowalter. STEMSIM—a New Software Tool for Simulation of STEM HAADF Z-Contrast Imaging. In *Microscopy of Semiconducting Materials 2007*, volume 120, pages 170–172. Springer Netherlands, 2008.
- [202] S. D. Findlay, L. J. Allen, M. P. Oxley, and C. J. Rossouw. Lattice-resolution contrast from a focused coherent electron probe. Part II. *Ultramicroscopy*, 96:65–81, 2003.
- [203] M. D. Croitoru, D. Van Dyck, S. Van Aert, S. Bals, and J. Verbeeck. An efficient way of including thermal diffuse scattering in simulation of scanning transmission electron microscopic images. *Ultramicroscopy*, 106(10):933–940, 2006.
- [204] A. Weickenmeier and H. Kohl. Computation of absorptive form factors for high-energy electron diffraction. *Acta Crystallographica Section A*, 47:590597, 1991.
- [205] G. T. Martinez. *Quantitative model-based High Angle Annular Dark Field Scanning Transmission Electron Microscopy*. PhD thesis, Univeristy of Antwerp, 2015.
- [206] M. A. O’Keefe and J. V. Sanders. n-beam lattice images. VI. degradation of image resolution by a combination of incident-beam divergence and spherical aberration. *Acta Crystallographica Section A: Crystal Physics, Diffraction, Theoretical and General Crystallography*, 31(3):307–310, 1975.
- [207] A. van den Bos. *Parameter Estimation for Scientists and Engineers*. John Wiley and Sons, Inc., 2007.
- [208] A. De Backer, A. de Wael, J. Gonnissen, and S. Van Aert. Optimal experimental design for nano-particle atom-counting from high-resolution stem images. *Ultramicroscopy*, 151:46–55, 2015.
- [209] J. Gonnissen, A. De Backer, A. J. den Dekker, J. Sijbers, and S. Van Aert. Detecting and locating light atoms from high-resolution STEM images: The quest for a single optimal design. *Ultramicroscopy*, 170:128–138, 2016.
- [210] A. Papoulis. *Probability, Random Variables, and Stochastic Processes*. McGraw-Hill, New York, 1965.
- [211] K.-H. Herrmann. Image recording in microscopy. In S. Amelinckx, D. Van Dyck, J. Van Landuyt, and G. Van Tendeloo, editors, *Handbook of Microscopy - Applications in Materials Science, Solid-State Physics and Chemistry, Methods II*, pages 885–921. Weinheim: VCH, 1997.

- [212] J. M. Hammersley. On estimating restricted parameters. *Journal of the Royal Statistical Society. Series B (Methodological)*, 12(2):192–240, 1950.
- [213] D. G. Chapman and H. Robbins. Minimum variance estimation without regularity assumptions. *The Annals of Mathematical Statistics*, pages 581–586, 1951.
- [214] S. Zacks. *Parametric statistical inference: Basic theory and modern approaches*, volume 4. Elsevier, 2014.
- [215] I. J. Myung. Tutorial on maximum likelihood estimation. *Journal of Mathematical Psychology*, 47(1):90–100, 2003.
- [216] A. Mood, F. A. Graybill, and D. C. Boes. *Introduction to the Theory of Statistics*. McGraw-Hill, New York, NY, 1974.
- [217] P. S. de Laplace. *Théorie analytique des probabilités*, volume 7. Courcier, 1820.
- [218] M. A. O. Miedema, A. van den Bos, and A. H. Buist. Experimental design of exit wave reconstruction from a transmission electron microscope defocus series. *IEEE Transactions on Instrumentation and Measurement*, 43(2):181–186, 1994.
- [219] I. Lobato and D. Van Dyck. MULTEM: A new multislice program to perform accurate and fast electron diffraction and imaging simulations using Graphics Processing Units with CUDA. *Ultramicroscopy*, 156:9–17, 2015.
- [220] H. E. K. E. MacArthur, T. J. Pennycook, E. Okunishi, A. J. D’Alfonso, N. R. Lugg, L. J. Allen, and P. D. Nellist. Probe integrated scattering cross sections in the analysis of atomic resolution HAADF STEM images. *Ultramicroscopy*, 133:109–119, 2013.
- [221] H. Fischer. *A history of the central limit theorem: From classical to modern probability theory*. Springer Science & Business Media, 2010.
- [222] S. Kullback and R. A. Leibler. On information and sufficiency. *The Annals of Mathematical Statistics*, 22:79–86, 1951.
- [223] S. Kullback. *Information theory and statistics*. John Wiley and Sons, 1959.
- [224] M. Huijben, G. Rijnders, D. H. A. Blank, S. Bals, S. van Aert, J. Verbeeck, G. van Tendeloo, A. Brinkman, and H. Hilgenkamp. Electronically coupled complementary interfaces between perovskite band insulators. *Nature Materials*, 5:556–560, 2006.
- [225] J. M. LeBeau, S. D. Findlay, L. J. Allen, and S. Stemmer. Quantitative atomic resolution scanning transmission electron microscopy. *Physical Review Letters*, 100:206101, 2008.
- [226] A. Rosenauer, K. Gries, K. Müller, A. Pretorius, M. Schowalter, A. Avramescu, K. Engl, and S. Lutgen. Measurement of specimen thickness and composition in $\text{Al}_x\text{Ga}_{1-x}\text{N}/\text{GaN}$ using high-angle annular dark field images. *Ultramicroscopy*, 109:1171–1182, 2009.
- [227] T. Kume, H. Ohura, T. Takeichi, A. Ohmura, A. Machida, T. Watanuki, K. Aoki, S. Sasaki, H. Shimizu, and K. Takemura. High-pressure study of ScH_3 : Raman, infrared, and visible absorption spectroscopy. *Physical Review B*, 84:064132, 2011.

- [228] J. N. Huiberts, R. Griessen, J. H. Rector, R. J. Wijngaarden, J. P. Dekker, D. G. De Groot, and N. J. Koeman. Yttrium and lanthanum hydride films with switchable optical properties. 380:231 – 234, 1996.
- [229] P. Van der Sluis and V. M. M. Mercier. Solid state Gd–Mg electrochromic devices with ZrO_2H_x electrolyte. *Electrochimica Acta*, 46(13):2167–2171, 2001.
- [230] Y. A. Abramov and V. G. Tsirelson. The chemical bond and atomic displacements in $SrTiO_3$ from X-ray diffraction analysis. *Acta Crystallography B*, 51:942–951, 1995.
- [231] L.-M. Peng. Anisotropic thermal vibrations and dynamical electron diffraction by crystals. *Acta Crystallography A*, 53:663–672, 1997.
- [232] R. A. Blessing, D. Y. Guo, and D. A. Langs. Statistical Expectation Value of the Debye-Waller Factor and $E(hkl)$ Values for Macromolecular Crystals. *Acta Crystallography D*, 52:257–266, 1996.
- [233] M. M. Thackeray, A. De Kock, M. H. Rossouw, D. Liles, R. Bittihn, and D. Hoge. Spinel Electrodes from the Li-Mn-O System for Rechargeable Lithium Battery Applications. *Journal of The Electrochemical Society*, 139(2):363–366, 1992.
- [234] G. X. Wang, D. H. Bradhurst, S. X. Dou, and H. K. Liu. Spinel $Li[Li_{1/3}Ti_{5/3}]O_4$ as an anode material for lithium ion batteries. *Journal of Power Sources*, 83(1):156–161, 1999.
- [235] L. Jones and P. D. Nellist. Identifying and correcting scan noise and drift in the scanning transmission electron microscope. *Microscopy and Microanalysis*, 19(04):1050–1060, 2013.
- [236] E. Anguiano and M. Aguilar. A cross-measurement procedure (cmp) for near noise-free imaging in scanning microscopes. *Ultramicroscopy*, 76(1):39–47, 1999.
- [237] B. S. Salmons, D. R. Katz, and M. L. Trawick. Correction of distortion due to thermal drift in scanning probe microscopy. *Ultramicroscopy*, 110(4):339–349, 2010.
- [238] B. Berkels, P. Binev, D. A. Blom, W. Dahmen, R. C. Sharples, and T. Vogt. Optimized imaging using non-rigid registration. *Ultramicroscopy*, 138:46–56, 2014.
- [239] L. Jones, H. Yang, T. Pennycook, M. Marshall, S. Van Aert, N. Browning, M. Castell, and P. D. Nellist. Smart Align - a new tool for robust non-rigid registration of scanning microscope data. *Advanced Structural and Chemical Imaging*, 1:8–23, 2015.
- [240] X. Sang and J. M. LeBeau. Revolving Scanning Transmission Electron Microscopy: Correcting Sample Drift Distortion without Prior Knowledge. *Ultramicroscopy*, 138:28–35, 2013.
- [241] C. Ophus, J. Ciston, and C. T. Nelson. Correcting nonlinear drift distortion of scanning probe and scanning transmission electron microscopies from image pairs with orthogonal scan directions. *Ultramicroscopy*, 162:1–9, 2016.
- [242] S. Bals, M. Casavola, M. A. van Huis, S. Van Aert, K. J. Batenburg, G. Van Tendeloo, and D. Vanmaekelbergh. Three-dimensional atomic imaging of colloidal core-shell nanocrystals. *Nano Letters*, 11(8):3420–3424, 2011.

- [243] S. Bals, S. Van Aert, C. P. Romero, K. Lauwaet, M. J. Van Bael, B. Schoeters, B. Partoens, E. Yücelen, P. Lievens, and G. Van Tendeloo. Atomic scale dynamics of ultrasmall germanium clusters. *Nature Communications*, 3:897, 2012.
- [244] P. Kundu, S. Turner, S. Van Aert, N. Ravishankar, and S. Van Tendeloo. Atomic Structure of Quantum Gold Nanowires: Quantification of the Lattice Strain. *ACS Nano*, 8:599–606, 2014.
- [245] R. Erni, H. Heinrich, and G. Kostorz. Quantitative characterisation of chemical inhomogeneities in Al-Ag using high-resolution Z-contrast STEM. *Ultramicroscopy*, 94:125–133, 2003.
- [246] J. M. LeBeau, S. D. Findlay, L. J. Allen, and S. Stemmer. Standardless atom counting in scanning transmission electron microscopy. *Nano Letters*, 10:4405–4408, 2010.
- [247] J. M. LeBeau and S. Stemmer. Experimental quantification of annular dark-field images in scanning transmission electron microscopy. *Ultramicroscopy*, 108:1653–1658, 2008.
- [248] J. M. LeBeau, A. J. Alfonso, S. D. Findlay, S. Stemmer, and L. J. Allen. Quantitative comparisons of contrast in experimental and simulated bright-field scanning transmission electron microscopy images. *Physical Review B*, 80:174106, 2009.
- [249] J. M. LeBeau, S. D. Findlay, X. Wang, A. J. Jacobson, L. J. Allen, and S. Stemmer. High-angle scattering of fast electrons from crystals containing heavy elements: simulation and experiment. *Physical Review B*, 79:214110, 2010.
- [250] K. J. Batenburg. A network flow algorithm for reconstructing binary images from discrete X-rays. *Journal of Mathematical Imaging and Vision*, 27:175–191, 2007.
- [251] J. R. Jinschek, K. J. Batenburg, H. A. Calderon, R. Kilaas, V. Radmilovic, and C. Kisielowski. 3-D reconstruction of the atomic positions in a simulated gold nanocrystal based on discrete tomography: prospects of atomic resolution electron tomography. *Ultramicroscopy*, 108:589–604, 2008.
- [252] W. Van den Broek, S. Van Aert, and D. Van Dyck. A model based atomic resolution tomographic algorithm. *Ultramicroscopy*, 109(12):1485–1490, 2009.
- [253] G. T. Martinez, A. De Backer, A. Rosenauer, J. Verbeeck, and S. Van Aert. The effect of probe inaccuracies on the quantitative model-based analysis of high angle annular dark field scanning transmission electron microscopy images. *Micron*, 63:57–63, 2014.
- [254] C. L. Jia, S. B. Mi, J. Barthel, D. W. Wang, R. E. Dunin-Borkowski, K. W. Urban, and A. Thust. Determination of the 3D shape of a nanoscale crystal with atomic resolution from a single image. *Nature Materials*, 13:1044, 2014.
- [255] I. Lobato, S. Van Aert, and J. Verbeeck. Progress and new advances in simulating electron microscopy datasets using MULTEM. *Ultramicroscopy*, 168:17–27, 2016.
- [256] R.S. Ruskin, Z. Yu, and N. Grigorieff. Quantitative characterization of electron detectors for transmission electron microscopy. *Journal of Structural Biology*, 184:3, 2013.

- [257] R.N. Clough, G. Moldovan, and A.I. Kirkland. Direct Detectors for Electron Microscopy. In *Journal of Physics: Conference Series*, volume 522, page 012046. IOP Publishing, 2014.
- [258] A. Thust. High-resolution transmission electron microscopy on an absolute contrast scale. *Physical Review Letters*, 102(22):220801, 2009.
- [259] D. Van Dyck. Is the frozen phonon model adequate to describe inelastic phonon scattering? *Ultramicroscopy*, 109(6):677–682, 2009.
- [260] D. Van Dyck. Persistent misconceptions about incoherence in electron microscopy. *Ultramicroscopy*, 111(7):894–900, 2011.
- [261] D. Van Dyck, I. Lobato, F.-R. Chen, and C. Kisielowski. Do you believe that atoms stay in place when you observe them in HREM? *Micron*, 68:158–163, 2015.
- [262] K. E. MacArthur, A. J. D’Alfonso, D. Ozkaya, L. J. Allen, and P. D. Nellist. Optimal ADF STEM imaging parameters for tilt-robust image quantification. *Ultramicroscopy*, 156:1–8, 2015.
- [263] P. D. Nellist. Scanning transmission electron microscopy. In *Science of Microscopy*, pages 65–132. Springer, 2007.
- [264] A. M. Glazer. The classification of tilted octahedra in perovskites. *Acta Crystallographica Section B: Structural Crystallography and Crystal Chemistry*, 28(11):3384–3392, 1972.
- [265] P. M. Woodward. Octahedral tilting in perovskites. I. Geometrical considerations. *Acta Crystallographica Section B: Structural Science*, 53(1):32–43, 1997.
- [266] C. J. Howard and H. T. Stokes. Group-theoretical analysis of octahedral tilting in perovskites. *Acta Crystallographica Section B: Structural Science*, 54(6):782–789, 1998.
- [267] V. Gopalan and D. B. Litvin. Rotation-reversal symmetries in crystals and handed structures. *Nature Materials*, 10(5):376–381, 2011.
- [268] A. Vailionis, H. Boschker, W. Siemons, E. P. Houwman, D. H. A. Blank, G. Rijnders, and G. Koster. Misfit strain accommodation in epitaxial ABO_3 perovskites: Lattice rotations and lattice modulations. *Physical Review B*, 83(6):064101, 2011.
- [269] Z. Liao, M. Huijben, Z. Zhong, N. Gauquelin, S. Macke, R. J. Green, S. Van Aert, J. Verbeeck, G. Van Tendeloo, K. Held, et al. Controlled lateral anisotropy in correlated manganese heterostructures by interface-engineered oxygen octahedral coupling. *Nature Materials*, 15(4):425–431, 2016.
- [270] D. G. Schlom, L.-Q. Chen, C.-B. Eom, K. M. Rabe, S. K. Streiffer, and J.-M. Triscone. Strain tuning of ferroelectric thin films. *Annual Review of Materials Research*, 37:589–626, 2007.
- [271] D. L. Proffit, H. W. Jang, S. Lee, C. T. Nelson, X. Q. Pan, M. S. Rzchowski, and C. B. Eom. Influence of symmetry mismatch on heteroepitaxial growth of perovskite thin films. *Applied Physics Letters*, 93(11):111912, 2008.

- [272] P. F. Chen, B. B. Chen, X. L. Tan, H. R. Xu, X. F. Xuan, Z. Guo, F. Jin, and W. B. Wu. High-TC ferromagnetic order in $\text{CaRuO}_3/\text{La}_{2/3}\text{Ca}_{1/3}\text{MnO}_3$ superlattices. *Applied Physics Letters*, 103(26):262402, 2013.
- [273] F. Johann, A. Morelli, D. Biggemann, M. Arredondo, and I. Vrejoiu. Epitaxial strain and electric boundary condition effects on the structural and ferroelectric properties of BiFeO_3 films. *Physical Review B*, 84(9):094105, 2011.
- [274] C. M. Folkman, S. H. Baek, H. W. Jang, C. B. Eom, C. T. Nelson, X. Q. Pan, Y. L. Li, L. Q. Chen, A. Kumar, V. Gopalan, et al. Stripe domain structure in epitaxial (001) BiFeO_3 thin films on orthorhombic TbScO_3 substrate. *Applied Physics Letters*, 94(25):251911, 2009.
- [275] Z. Liao, N. Gauquelin, R. J. Green, S. Macke, J. Gonnissen, S. Thomas, Z. Zhong, L. Li, L. Si, S. Van Aert, P. Hansmann, K. Held, J. Xia, J. Verbeeck, G. Van Tendeloo, G. A. Sawatzky, G. Koster, M. Huijben, and G. Rijnders. Thickness dependent properties in oxide heterostructures driven by structurally induced metal-oxygen hybridization variations. *Accepted to Advanced Functional Materials*, 2016.
- [276] J. M. Rondinelli, S. J. May, and J. W. Freeland. Control of octahedral connectivity in perovskite oxide heterostructures: An emerging route to multifunctional materials discovery. *MRS Bulletin*, 37(03):261–270, 2012.
- [277] A. Vailionis, H. Boschker, Z. Liao, J. R. A. Smit, G. Rijnders, M. Huijben, and G. Koster. Symmetry and lattice mismatch induced strain accommodation near and away from correlated perovskite interfaces. *Applied Physics Letters*, 105(13):131906, 2014.
- [278] M. Ohgaki, K. Tanaka, and F. Marumo. Structure refinement of lithium (I) niobium (V) trioxide, LiNbO_3 , with anharmonic thermal vibration model. *Mineralogical Journal*, 16(3):150–160, 1992.
- [279] E. A. Eliseev, A. N. Morozovska, G. S. Svechnikov, V. Gopalan, and V. Y. Shur. Static conductivity of charged domain walls in uniaxial ferroelectric semiconductors. *Physical Review B*, 83(23):235313, 2011.
- [280] M. Schröder, A. Haußmann, A. Thiessen, E. Soergel, T. Woike, and L. M. Eng. Conducting domain walls in lithium niobate single crystals. *Advanced Functional Materials*, 22(18):3936–3944, 2012.
- [281] M. Schröder, X. Chen, A. Haußmann, A. Thiessen, J. Poppe, D. A. Bonnell, and L. M. Eng. Nanoscale and macroscopic electrical ac transport along conductive domain walls in lithium niobate single crystals. *Materials Research Express*, 1(3):035012, 2014.
- [282] T. Kämpfe, P. Reichenbach, M. Schröder, A. Haußmann, L. M. Eng, T. Woike, and E. Soergel. Optical three-dimensional profiling of charged domain walls in ferroelectrics by cherenkov second-harmonic generation. *Physical Review B*, 89(3):035314, 2014.
- [283] P. Lerner, C. Legras, and J. P. Dumas. Stoechiometrie des monocristaux de metaniobate de lithium. *Journal of Crystal Growth*, 3:231–235, 1968.

- [284] V. Aristov and L. Kokhanchik. Scanning electron microscopy investigation of lithium niobate properties. *Ferroelectrics*, 126(1):353–358, 1992.
- [285] H. Xu, D. Lee, S. B. Sinnott, V. Gopalan, V. Dierolf, and S. R. Phillpot. Interactions of Defects and Domain Walls in LiNbO₃—Insights from Simulations. In *IOP Conference Series: Materials Science and Engineering*, volume 15, page 012003. IOP Publishing, 2010.
- [286] G. Stone, D. Lee, H. Xu, S. R. Phillpot, and V. Dierolf. Local probing of the interaction between intrinsic defects and ferroelectric domain walls in lithium niobate. *Applied Physics Letters*, 102(4):042905, 2013.
- [287] V. Gopalan, V. Dierolf, and D. A. Scrymgeour. Defect-domain wall interactions in trigonal ferroelectrics. *Annual Review of Materials Research*, 37:449–489, 2007.
- [288] K. Shapovalov, P. V. Yudin, A. K. Tagantsev, E. A. Eliseev, A. N. Morozovska, and N. Setter. Elastic coupling between nonferroelastic domain walls. *Physical Review Letters*, 113(20):207601, 2014.
- [289] G. F. Nataf, O. Aktas, T. Granzow, and E. K. H. Salje. Influence of defects and domain walls on dielectric and mechanical resonances in LiNbO₃. *Journal of Physics: Condensed Matter*, 28(1):015901, 2015.
- [290] D. Lee, H. Xu, V. Dierolf, V. Gopalan, S. R. Phillpot, et al. Structure and energetics of ferroelectric domain walls in LiNbO₃ from atomic-level simulations. *Physical Review B*, 82(1):014104, 2010.
- [291] J. Gonnissen, D. Batuk, G. F. Nataf, L. Jones, A. M. Abakumov, S. Van Aert, D. Schryvers, and E. K. H. Salje. Direct Observation of Ferroelectric Domain Walls in LiNbO₃: Wall-Meanders, Kinks, and Local Electric Charges. *Advanced Functional Materials*, 2016.
- [292] E. K. H. Salje. Ferroelastic materials. *Annual Review of Materials Research*, 42:265–283, 2012.
- [293] X.-K. Wei, A. K. Tagantsev, A. Kvasov, K. Roleder, C.-L. Jia, and N. Setter. Ferroelectric translational antiphase boundaries in nonpolar materials. *Nature Communications*, 5, 2014.
- [294] Y. Sheng, A. Best, H.-J. Butt, W. Krolikowski, A. Arie, and K. Koynov. Three-dimensional ferroelectric domain visualization by čerenkov-type second harmonic generation. *Optics Express*, 18(16):16539–16545, 2010.
- [295] T. Kämpfe, P. Reichenbach, A. Haußmann, T. Woike, E. Soergel, and L. M. Eng. Real-time three-dimensional profiling of ferroelectric domain walls. *Applied Physics Letters*, 107(15):152905, 2015.
- [296] A. Tselev, P. Yu, Y. Cao, L. R. Dedon, L. W. Martin, S. V. Kalinin, and P. Maksymovych. Microwave ac conductivity of domain walls in ferroelectric thin films. *Nature Communications*, 7, 2016.
- [297] T. Jach, S. Kim, V. Gopalan, S. Durbin, and D. Bright. Long-range strains and the effects of applied field at 180 ferroelectric domain walls in lithium niobate. *Physical Review B*, 69(6):064113, 2004.

List of Symbols and Abbreviations

Roman characters

Character	Page	Explanation
a_0	47	Bohr radius
a_i	47	set of three constant parameters for potential parametrisation of a specific atomic number Z
$A(\mathbf{g})$	39	aperture function
b_i	47	set of three constant parameters for potential parametrisation of a specific atomic number Z
B_n	32	Debye-Waller factor of atom n
c_i	47	set of three constant parameters for potential parametrisation of a specific atomic number Z
C_s	39	spherical aberration constant
C_5	39	spherical aberration of 5th order
CS_n	58	expected scattering cross-section for n atoms in a column
d_i	47	set of three constant parameters for potential parametrisation of a specific atomic number Z
$D(\mathbf{g})$	35	detector function
$D(p_{\mathcal{H}_1}, p_{\mathcal{H}_0})$	62	Kullback-Leibler divergence from $p_{\mathcal{H}_1}$ to $p_{\mathcal{H}_0}$
D_{STEM}	46	incoming electron dose per pixel in STEM
D_{TEM}	46	incoming electron dose per pixel in TEM
e	23	magnitude of the electron charge
\mathbb{E}	45	expected value
E_0	23	incident electron energy
f	39	defocus
f_{kl}	46	fraction of detected intensity at pixel (k, l)

F	48	Fisher information matrix
F_{rs}	49	(r, s) th element of the Fisher information matrix
F^{-1}	49	inverse of the Fisher information matrix
$F(x; \lambda)$	57	cumulative distribution function of the Poisson distribution with parameter λ evaluated at x
$f_{kl}(\boldsymbol{\theta})$	52	expectation model as a function of the unknown parameters
$f_{\mathbf{q}}^n$	32	scattering factor of atom n with scattering vector \mathbf{q}
\mathbf{g}	32	reciprocal lattice vector
\mathbf{g}_{β}	37	one illumination angle in the condenser aperture
$g(\boldsymbol{\theta})$	50	an arbitrary scalar function of the unknown true parameter vector $\boldsymbol{\theta}$
\mathcal{H}_0	54	null hypothesis
\mathcal{H}_1	54	alternative hypothesis
\mathcal{H}_i^s	66	sorted hypotheses according to the expectation values of the scattering cross-sections or peak intensities
h	23	Planck's constant
\hbar	23	the Planck's constant h divided by 2π
$I(\mathbf{R})$	37	intensity in the image plane
$I^{(n)}(\mathbf{R})$	33	intensity of the wave function entering slice n
$I_{TDS}^{(n)}$	33	for slice n , the intensity of the TDS scattered electrons that reach the detector
$I_{TDS}^{(total)}$	34	total TDS intensity on the detector
K	44	number of pixels in x -direction of a HR(S)TEM image
k	44	index
$K_0(x)$	47	modified Bessel function
k_0	23	wave vector of the incident electron
\mathbf{k}_0	23	three-dimensional wave vector of the incident electron
\mathbf{k}_x	25	one-dimensional wave vector of the incident electron perpendicular to the optical axis
\mathbf{k}_y	25	one-dimensional wave vector of the incident electron perpendicular to the optical axis
\mathbf{k}_z	25	one-dimensional wave vector of the incident electron parallel to the optical axis
\mathbf{k}_{xy}	26	the two-dimensional vector given by $(\mathbf{k}_x, \mathbf{k}_y)$
k_{β}	40	$1/e$ half-width value of the Gaussian distribution of illumination angles

L	44	number of pixels in y -direction of a HR(S)TEM image
$L(\mathbf{t})$	51	likelihood function
l	44	index
$\ln LR(\mathbf{w})$	55	log likelihood ratio of the observations \mathbf{w}
m	23	relativistic mass of the electron
M	64	number of hypotheses in a multiple hypothesis test
N	22	total number of atoms in the specimen
	46	incoming electron dose per square ångström
	52	total number of pixel observations, equal to $K \times L$
N_a	108	number of unit cells in the a -direction of the supercell
N_b	108	number of unit cells in the b -direction of the supercell
n	28	index: n th slice
	32	index: n th atom
	54	number of atoms in a projected atomic column
$n_{\mathcal{H}_0}$	54	number of atoms in a column under the null hypothesis
$n_{\mathcal{H}_1}$	54	number of atoms in a column under the alternative hypothesis
$\mathcal{O}(\Delta z^2)$	29	big O notation
$p(\mathbf{R})$	46	probe function
$p(x, y, \Delta z)$	29	propagation function of the electron wave
P_e	55	probability of error
P_c	65	probability of a correct decision
$P(\mathcal{H}_i)$	55	prior probability associated with \mathcal{H}_i
$P(\mathcal{H}_i \mathcal{H}_j)$	55	conditional probability of deciding \mathcal{H}_i when \mathcal{H}_j is true
$p(\boldsymbol{\omega})$	44	joint probability (density) function
$p(\delta_f)$	37	normalised distribution function of the defocus
$p(\mathbf{g}_\beta)$	37	normalised distribution function of the illumination angle
$p_{kl,STEM}$	46	the probability that an electron hits pixel (k, l) in a HRSTEM image
$p_{kl,TEM}$	46	the probability that an electron hits pixel (k, l) in a HRTEM image
$p(\mathbf{w}; \mathcal{H}_i)$	55	conditional probability function assuming \mathcal{H}_i to be true
\mathbf{r}	22	three-dimensional coordinate vector
\mathbf{r}_i	22	three-dimensional coordinate vector of atom i
\mathbf{R}	24	two-dimensional coordinate vector in a plane perpendicular to the optical axis z
\mathbf{S}	32	scattering vector
$T_{cc}^{coh}(\mathbf{g}, \mathbf{g}')$	38	coherent transmission cross coefficient

$T_{cc}^{pc}(\mathbf{g}, \mathbf{g}')$	38	partially coherent transmission cross coefficient
$T(\mathbf{R})$	24	transmission operator
	38	coherent point spread function
$T(\mathbf{R}, f + \delta_f)$	37	point spread function
$t(x, y, z)$	29	transmission function of the electron wave
\mathbf{u}_n	32	atomic displacement vector
$V(\mathbf{r})$	22	the specimen potential
$V_i(\mathbf{r} - \mathbf{r}_i)$	22	the spherically symmetric potential of atom i
$V_p(\mathbf{R})$	32	total projected potential of a crystal slice
$V_{Coul}(\mathbf{R})$	32	electrostatic Coulomb potential
$V_{TDS}(\mathbf{R})$	32	TDS absorptive potential
$v_z(\mathbf{R})$	24	projected electrostatic atomic potential along the optical axis z
V_0	23	accelerating voltage
\mathbf{w}	44	vector of the available observations
w_{kl}	44	observation at the pixel value (k, l)
x_k	44	x -coordinate at the pixel value (k, l)
x_p	34	x -coordinate of the probe position
x	22	spatial coordinate
y_l	44	y -coordinate at the pixel value (k, l)
y_p	34	y -coordinate of the probe position
y	22	spatial coordinate
Z	8	atomic number
Z_H	2	atomic number of hydrogen
Z_{Li}	2	atomic number of lithium
Z_O	4	atomic number of oxygen
z	22	spatial coordinate
Δz	29	slice thickness

Greek characters

Character	Page	Explanation
α	8	objective aperture angle
β	40	beam semi-divergence angle
β_1	8	inner collection angle
β_2	8	outer collection angle
γ	55	proportion of prior probabilities under both hypotheses

$\gamma(\boldsymbol{\theta})$	49	function of the parameters $\boldsymbol{\theta}$
$\widehat{\gamma}$	49	unbiased estimator of $\gamma(\boldsymbol{\theta})$
$\widehat{\delta}$	50	unbiased estimator of an arbitrary scalar function g
δ_f	37	defocus spread
Δ	23	three-dimensional Laplacian operator
	40	$1/e$ half-width value of the Gaussian distribution of defocus values
	50	difference in the true parameter $\boldsymbol{\theta}$
Δ_{xy}	26	two-dimensional Laplacian operator
Δx	44	pixel size in x -direction
Δy	44	pixel size in y -direction
$\Delta\alpha$	137	relative tilt angle
\emptyset	54	the empty set
$\boldsymbol{\theta}$	45	vector of the (unknown) true parameters
$\widehat{\boldsymbol{\theta}}$	49	unbiased estimator of $\boldsymbol{\theta}$
$\widehat{\boldsymbol{\theta}}_{ML}$	51	maximum likelihood estimator
$\widehat{\boldsymbol{\theta}}_{LS}$	53	least squares estimator
λ	23	relativistically corrected electron wavelength
λ_{kl}	45	expected value of the Poisson distribution at pixel (k, l)
λ_{kl}^{TEM}	46	expected value of pixel (k, l) in a HRTEM image
λ_{kl}^{STEM}	46	expected value of pixel (k, l) in a HRSTEM image
$\lambda_{\mathcal{H}_i}^{PI}$	57	expectation value of the peak intensity under \mathcal{H}_i
$\lambda_{\mathcal{H}_i, kl}$	58	expectation values for the pixel intensities of a HRTEM image under \mathcal{H}_i
μ	45	expected value
$\mu_{\mathcal{H}_i}$	60	expected value of normal distribution of $\ln \text{LR}(\boldsymbol{\omega}^{Im})$ under \mathcal{H}_i
∇	25	three-dimensional gradient operator
∇_{xy}	26	two-dimensional gradient operator
σ	24	interaction parameter
σ^2	45	variance
$\sigma_{\mathcal{H}_i}^2$	60	variance of normal distribution of $\ln \text{LR}(\boldsymbol{\omega}^{Im})$ under \mathcal{H}_i
$\Phi(x)$	61	cumulative distribution function of the standard normal distribution evaluated at x
$\chi(\mathbf{g})$	39	aberration function
$\Psi(\mathbf{r})$	23	wave function of the electron in the specimen
$\psi_0(\mathbf{R})$	24	wave function of the incident electron

ψ_n	29	wave function of the electron at the entrance of slice n
ω	44	vector of the stochastic variables of the observations \mathbf{w}
ω_{kl}	44	stochastic variable for the pixel (k, l)
ω^{PI}	56	stochastic variable for the peak intensities
ω^{CS}	56	stochastic variable for the scattering cross-sections
ω^{Im}	56	stochastic variable for HR(S)TEM image pixel values of a projected atom column
Ω	32	volume of the crystal unit cell

Abbreviation	Page	Explanation
2D	17	Two-dimensional
3D	26	Three-dimensional
4D	17	Four-dimensional
ABF	2	Annular Bright Field
ADF	6	Annular Dark Field
BF	4	Bright Field
CBED	6	Convergent Beam Electron Diffraction
CCD	6	Charged Coupled Device
CFEG	9	Cold Field Emission Fun
CRLB	14	Cramér-Rao lower bound
CSHG	136	Cherenkov Second Harmonic generation
CTEM	3	Conventional Transmission Electron Microscopy
FIB	129	Focused ion beam
FOV	42	Field of View
HAADF	3	High Angle Annular Dark Field
HR(S)TEM	15	High Resolution (Scanning) Transmission Electron Microscopy
HRSTEM	15	High Resolution Scanning Transmission Electron Microscopy
HRTEM	1	High Resolution Transmission Electron Microscopy
LAADF	5	Low Angle Annular Dark Field
LNT	4	$\text{Li}_{0.5-3x}\text{Nd}_{0.5+x}\text{TiO}_3$
LR	54	Likelihood ratio
LS	51	Least squares
LSMO	123	$\text{La}_{2/3}\text{Sr}_{1/3}\text{MnO}_3$
MAADF	8	Medium Angle Annular Dark Field
ML	49	Maximum Likelihood

MTF	109	Modulation Transfer Function
NGO	123	NdGaO ₃
OOC	123	Oxygen octahedral coupling
OOR	123	Oxygen octahedral rotation
PDF	14	Probability density function
P(D)F	14	Probability (density) function
PF	14	Probability function
PI	54	Peak intensity
SCS	54	Scattering cross-section
SNR	6	Signal-to-noise ratio
STEM	2	Scanning Transmission Electron Microscopy
TCC	35	Transmission cross coefficient
TDS	28	Thermal diffuse scattering
TEM	3	Transmission Electron Microscopy
UC	123	Unit cell

Samenvatting

In het laatste decennium is de interesse in het in beeld brengen van lichte atomen zoals lithium en waterstof enorm gegroeid door hun belangrijke rol bij de ontwikkeling van nieuwe materialen die energie kunnen opslaan en bewaren. De optimalisatie van verschillende technieken binnen de transmissie-elektronenmicroscopie is dan ook erg belangrijk geworden voor zulke toepassingen. Het is echter enorm moeilijk om systemen bestaande uit lichte atomen in beeld te brengen en hun structuur en chemische compositie te kwantificeren op atomaire schaal, aangezien de interactie met de elektronenbundel verzwakt naarmate het atoom lichter wordt. Het hoofddoel van dit onderzoek bestond erin de experimentele opstelling van de elektronenmicroscopie te optimaliseren om nanostructuren bestaande uit lichte atomen te kunnen karakteriseren en dit gebruik makend van nieuwe technieken binnen de kwantitatieve transmissie-elektronenmicroscopie. Het doel is dan om de atomaire structuur vanuit experimentele beelden te kunnen bepalen voor nanokristallen bestaande uit lichte atomen.

Atomen kunnen gevisualiseerd worden met behulp van hoge resolutie donkerbeeldvorming via raster transmissie elektronenmicroscopie (High Resolution High-Angle Annular Dark Field Scanning Transmission Electron Microscopy of HR HAADF STEM). In deze techniek scant een gefocusseerde elektronenbundel over een voor elektronen transparant materiaal. Door gebruik te maken van een ringvormige detector met grote binnenstraal worden bijna uitsluitend incoherent verstrooide elektronen gedetecteerd. Het zo verkregen signaal schaalt dan benaderd kwadratisch met het atoomgetal Z en geeft dus een relatief hoge gevoeligheid voor de chemische samenstelling. Een directe, kwalitatieve interpretatie van experimentele beelden leidt echter tot onbetrouwbare resultaten wanneer het verschil in atoomgetal Z van de aanwezige atoomkolommen klein is of wanneer de signaal-ruis verhouding van de beelden slecht is. Voor de chemische karakter-

isatie van systemen met lichte atomen is daarom het gebruik van kwantitatieve methoden noodzakelijk. Hiervoor wordt statistische parameterschattingstheorie toegepast in combinatie met detectietheorie.

Elektronenmicroscopische waarnemingen fluctueren rond verwachtingswaarden. Het verwachtingswaardenmodel, het fysische model dat de verwachtingswaarden beschrijft, bevat de te meten parameters. De parameters die geschat zullen worden in deze thesis zijn het atoomgetal (van een geïsoleerd atoom en van geprojecteerde atoomkolommen in een kristal), de posities van geprojecteerde atoomkolommen en de dikte ervan (het aantal atomen in een kolom). Voor het schatten van continue parameters, zoals de atoomkolomposities, kan gebruik gemaakt worden van de zogenaamde *Cramér-Rao ondergrens*, die een maat is voor de haalbare precisie op deze geschatte parameter. Detectietheorie biedt een alternatieve methode voor het schatten van discrete parameters, zoals het atoomgetal Z , omdat hiervoor de Cramér-Rao ondergrens niet gedefinieerd is. Hierbij wordt een schattingsprobleem geformuleerd als een binaire of meervoudige hypothesetoets, waarbij de verschillende hypothesen bijvoorbeeld overeenkomen met verschillende mogelijke atoomgetallen. De kans op het kiezen van een foute hypothese, de zogenaamde *probability of error*, kan dan berekend worden en geminimaliseerd worden als functie van de experimentele opstelling.

Het doel is uiteindelijk om de optimale experimentele proefopzet te vinden waarvoor de kans op een foute hypothesekeuze minimaal is, of de haalbare precisie maximaal. Zowel conventionele TEM als STEM zullen bestudeerd en vergeleken worden voor het detecteren en lokaliseren van lichte atomen, alsook voor het tellen van atomen in een geprojecteerde atoomkolom. Voor HRSTEM worden hierbij de detector binnen- en buitenhoek geoptimaliseerd, maar HRTEM wordt geoptimaliseerd in termen van de sferische aberratie en defocus.

Voor het detecteren en lokaliseren van lichte atomen, blijkt HRSTEM een meer geschikte techniek in vergelijking met HRTEM, voor dezelfde inkomende elektronendosis. Bovendien wordt eenzelfde optimale proefopzet gevonden voor de STEM detector voor zowel het detecteren als lokaliseren van lichte atomen. Daarnaast wordt er gevonden dat voor dezelfde inkomende elektronendosis en onder de optimale settings HRSTEM een lagere kans op een telfout geeft dan HRTEM, wanneer men verstrooiingsdoorsnedes als prestatie maat gebruikt voor STEM en piekintensiteiten voor HRTEM, zoals voorgesteld in de literatuur. Wanneer echter een beslissing genomen wordt op basis van de zogenaamde gezamenlijke kansdichtheidsfunctie van alle pixelobservaties in een HR(S)TEM beeld, wordt HRTEM voordeliger voor het tellen van atomen.

Als praktische toepassing in het onderzoek naar technieken om nanostructuren bestaande uit lichte atomen kwantitatief te karakteriseren, wordt de lokale koppeling van de zuurstof-octaëders aan het raakvlak met heterogene perovskietstructuren in verschillende epitaxiale dunne films bepaald. Daarnaast wordt ook het raakvlak tussen twee domeinen in het kristal LiNbO_3 onderzocht en wordt de verschuiving van de atomen aan beide zijden van dit raakvlak, alsook de breedte van de overgang tussen beide domeinen gekwantificeerd met behulp van statistische parameterschattingstheorie.

List of publications

Contributions to Scientific Journals

- A. J. den Dekker, **J. Gonnissen**, A. De Backer, J. Sijbers, S. Van Aert, *Estimation of unknown structure parameters from high-resolution (S)TEM images: what are the limits?*, Ultramicroscopy 134, 34-43 (2013).
- **J. Gonnissen**, A. J. den Dekker, A. De Backer, G. T. Martinez, A. Rosenauer, J. Sijbers, and S. Van Aert, *Optimal experimental design for the detection of light atoms from high-resolution STEM images*, Applied Physical Letters 105, 6 (2014).
- A. De Backer, A. De wael, **J. Gonnissen** and S. Van Aert, *Optimal experimental design for nano-particle atom-counting from high-resolution STEM images*, Ultramicroscopy 151, 46-55 (2015).
- A. De Backer, A. De wael, **J. Gonnissen**, G.T. Martinez, A. Béché, K. E. MacArthur, L. Jones, P. D. Nellist, S. Van Aert, *Quantitative annular dark field scanning transmission electron microscopy for nano particle atom-counting: What are the limits?*, Journal of Physics: Conference Series 644 (1), 012034 (2015).
- Z. L. Liao, R. J. Green, N. Gauquelin, S. Macke, L. Lin, **J. Gonnissen**, R. Surtarto, E. P. Houwman, Z. Zhong, S. Van Aert, J. Verbeeck, G. A. Sawatzky, M. Huijben, G. Koster, G. Rijnders, *Long-Range Domain Structure and Symmetry Engineering by Interfacial Oxygen Octahedral Coupling at Heterostructure Interface*, Advanced Functional Materials (2016) Wiley Online Library.
- **J. Gonnissen**, A. De Backer, A. J. den Dekker, J. Sijbers and S. Van Aert, *Detecting and locating light atoms from High Resolution Scanning Transmission*

Electron Microscopy Images: The quest for a single optimal design, Ultramicroscopy 170, 128-138 (2016).

- **J. Gonnissen**, D. Batuk, G. F. Nataf, L. Jones, A. M. Abakumov, S. Van Aert, D. Schryvers, E.K.H. Salje, *Direct Observation of Ferroelectric Domain Walls in LiNbO₃: Wall-Meanders, Kinks, and Local Electric Charges*, Advanced Functional Materials, (2016), Wiley Online Library.
- **J. Gonnissen**, A. De Backer, A. J. den Dekker, J. Sijbers and S. Van Aert, *Atom-counting in High Resolution Electron Microscopy: TEM or STEM - that's the question*, Ultramicroscopy (2016), DOI: 10.1016/j.ultramic.2016.10.011.
- Z. L. Liao, N. Gauquelin, R. J. Green, S. Macke, L. Lin, **J. Gonnissen**, S. Thomas, Z. Zhong, L. Li, L. Si, S. Van Aert, P. Hansmann, K. Held, J. Xia, J. Verbeeck, G. A. Sawatzky, G. Koster, M. Huijben, G. Rijnders, *Thickness dependent properties in oxide heterostructures driven by structurally induced metal-oxygen hybridization variations*, accepted for publication in Advanced Functional Materials (2017).

Contributions to Scientific Meetings

- S. Van Aert, A. De Backer, G.T. Martinez, E. Mudry, **J. Gonnissen**, K.J. Batenburg, and S. Bals, Model-based scanning transmission electron microscopy: from 2D images toward 3D atomic structures, 13^{ème} colloque de la Société Française des Microscopies, July 2-5, 2013.
- **J. Gonnissen**, A. J. den Dekker, A. De Backer, J. Sijbers, and S. Van Aert, Estimation of atomic numbers from STEM images: what are the limits?, Microscopy Conference MC 2013, Regensburg, Germany, August 25-30, 2013, IM.1.P010, *Poster presentation - received the prize for Best Poster in the category Quantitative High-Resolution TEM/STEM and Diffraction (IM1)*.
- S. Van Aert, **J. Gonnissen**, A. De Backer, J. Sijbers, and A.J. den Dekker, Measuring structure parameters from electron microscopy images: what are the limits?, International 18th Microscopy Congress IMC 2014, Prague, Czech Republic, September 7-12, 2014, IT-16-O-2356.
- S. Van Aert, A. De Backer, A. De wael, **J. Gonnissen**, G. Martinez, A. Béché, K. MacArthur, L. Jones, and P. Nellist, Quantitative annular dark field scan-

ning transmission electron microscopy for nano-particle atom-counting: What are the limits?, PICO 2015 - 3rd Conference on Frontiers of Aberration Corrected Electron Microscopy, Kasteel Vaalsbroek, The Netherlands, April 19-23, 2015.

- A. De Backer, A. De wael, **J. Gonnissen**, G.T. Martinez, A. Béch , K.E. MacArthur, L. Jones, P.D. Nellist, and S. Van Aert, Quantitative annular dark field scanning transmission electron microscopy for nanoparticle atom-counting: What are the limits?, MMC 2015 incorporating EMAG 2015, Manchester, UK, June 29 - July 2, 2015.
- **J. Gonnissen**, A. De Backer, G.T. Martinez, I. Lobato, A.J. den Dekker, J. Sijbers, and S. Van Aert, Optimal experiment design for atom-counting in atomic resolution TEM and STEM: possibilities and limitations to the precision for both imaging methods, MMC 2015 incorporating EMAG 2015, Manchester, UK, June 29 - July 2, 2015, *Oral presentation*.
- S. Van Aert, A. De wael, K. van den Bos, **J. Gonnissen**, A. De Backer, L. Jones, G. T. Martinez, P. D. Nellist, Maximum structural information of beam-sensitive nanoparticles for a minimum electron budget using quantitative STEM, MRS Spring Meeting, Phoenix, Arizona, March 28 - April 1, 2016.
- S. Van Aert, A. De wael, K. van den Bos, **J. Gonnissen**, A. De Backer, L. Jones, M. Alania, G. T. Martinez, P. D. Nellist, Minimum electron budget for maximum structural information of beam-sensitive nanoparticles using quantitative scanning transmission electron microscopy, ACMM 2016, Melbourne, Australia, January 31 - February 4, 2016.
- **J. Gonnissen**, A. De Backer, A.J. den Dekker, J. Sijbers, S. Van Aert, Optimal detectability combined with picometre range precision to position light atoms from HR STEM images, EMC Lyon, France, August 29 - September 2, 2016, *Poster*.
- **J. Gonnissen**, A. De Backer, A.J. den Dekker, J. Sijbers, S. Van Aert, Detecting and locating light atoms from HRSTEM images: The quest for a single optimal design, RBSM - Golden Jubilee Meeting of the Royal Belgian Society for Microscopy, Brussels, Belgium, September 8-9, 2016, *Poster presentation - received the 2016 RBSM Best Poster Award*.

Dankwoord

Zo'n vijftal jaar geleden kwam ik toevallig Annick tegen op de fiets, beiden kwamen we nog van dezelfde middelbare school en fietsten we elke dag richting de universiteit. Geïnteresseerd geraakt door de uitleg over haar doctoraat, kwam ik een tijdje later bij Sandra aankloppen om meer informatie te vragen over haar onderzoek. Ik was dan ook enorm blij dat Sandra me de mogelijkheid bood aan een doctoraat te starten bij haar. De tijd is voorbij gevlogen en nu, vier en een half jaar later, zou ik graag enkele mensen persoonlijk willen bedanken zonder wie ik dit doctoraat nooit tot een goed einde had kunnen brengen.

In de eerste plaats zou ik dan ook Sandra enorm willen bedanken, niet alleen voor jouw enthousiaste begeleiding als promotor, het delen van zoveel kennis en nieuwe ideeën en de vele inhoudelijke verbeteringen van mijn werk, maar vooral ook omdat je me de motivatie en het vertrouwen gaf om mijn doctoraat af te maken nadat ik bijna zelf beslist had ermee te stoppen. Ik weet dat het niet altijd gemakkelijk zal geweest zijn voor jou om als promotor alles gepland en georganiseerd te krijgen, zeker als je twee keer op rij te horen krijgt dat je doctoraatsstudente een kindje verwacht en 15 weken afwezig zal zijn. Ik waardeer het dan ook enorm dat je me hierin hebt gesteund en de kans hebt gegeven om mijn doctoraat een half jaar later dan oorspronkelijk voorzien af te ronden. Mijn mede-promotor professor Jan Sijbers verdient hier ook een oprechte dankuwel, voor de enthousiaste steun en de vele opmerkingen en suggesties bij mijn thesis die ze tot een beter werk hebben gemaakt.

Daarnaast wil ik graag professor dr. ir. Arjan den Dekker bedanken voor de vele boeiende inzichten en waardevolle discussies die geleid hebben tot de meeste resultaten die ik tijdens mijn onderzoek heb behaald.

I would like to express my sincere thanks to all members of the jury, for their time spent reading my thesis and all the useful comments and questions during

the defence which have led to a deeper understanding of some of my results.

To all (ex-)members of “Sandra’s group” within EMAT: Annick, Karel, Ivan, Marcos, Gerardo, Jarmo, Annelies and Knut, thank you so much for all the useful discussions, your support and friendship during the past years and the nice chats that made every day more pleasant! Also special thanks to all my friends at EMAT, I will not explicitly write down names as I would probably forget people. It was a pleasure working in such a diverse and friendly group, thank you for all the nice conversations, the Greek and Iranian dinners, the badminton- and squash-games during lunch time, the coffee-breaks and so much more. Karel wil ik nog speciaal bedanken voor Figuur 1.1 en Liesbet voor de heel mooie cover!

Mijn klasgenoten wil ik ook graag bedanken voor de toffe voorbije 9,5 jaar. Jullie hebben mijn studiejaren op de universiteit tot de meest plezierige jaren van mijn jonge leven gemaakt. Ik heb met jullie de grappigste momenten en meest bizarre gesprekken meegemaakt en kijk dan ook nostalgisch terug op onze vele leuke jaren samen in een toch wel unieke klasgroep.

In het bijzonder wil ik graag nog enkele vrienden bedanken die me extra na aan het hart liggen, mijn soulsister Ann in de eerste plaats: of we nu via mail, de telefoon of in het echt ons hart bij elkaar luchten, jij begrijpt me altijd meteen en hebt me dan ook, meer dan je misschien beseft, enorm gesteund de voorbije jaren. Ook Stéphanie en Cedric wil ik speciaal bedanken voor jullie waardevolle vriendschap en steun. Stéphanie, jij bent altijd een enorm voorbeeld voor mij geweest en jouw doctoraatsverdediging was er geen als een ander! Bedankt om me altijd aan te moedigen en ook voor de leuke en ontspannende momenten die echt deugd deden tijdens de soms toch wel stressvolle periodes.

Uiteraard gaat een enorme dank ook uit naar mijn familie. In de eerste plaats naar mijn ouders, die me alle kansen en steun in mijn leven hebben gegeven om te staan waar ik nu sta. Zonder jullie in de eerste plaats was ik nooit kunnen worden wie ik nu ben. Bedankt voor al jullie goede raad en vele hulp die ik soms als te vanzelfsprekend acht. Ook wil ik mijn schoonouders bedanken om altijd voor ons klaar te staan, mijn (schoon-)zussen en (schoon-)broers, neefjes en nichtjes, en mijn grootouders, voor de warme familie die jullie vormen en in wiens aanwezigheid ik me altijd goed en thuis voel.

Speciale dank gaat nog uit naar pater Patrick Annaert O.F.M.Cap. voor uw onvoorwaardelijke steun en vriendschap die ik mocht ervaren tijdens de voorbije jaren. Ik ben enorm dankbaar u te hebben mogen leren kennen en hoop u nog vele jaren onder ons te mogen hebben.

Tenslotte wil ik nog mijn kleine kapoenen, Samuel en Eveline bedanken. Ook al geven jullie je mama misschien niet zoveel nachtrust, elke morgen zorgen jullie er toch voor dat ik vrolijk aan mijn dag kan beginnen. Dankzij jullie kreeg ik een enorm relativiseringsvermogen waardoor alles in het niets valt als ik nog maar aan jullie denk. En mijn eeuwige steun en toeverlaat, Thomas, dank je voor zoveel! Jij geeft me de energie die me gaande houdt. Niet alleen kon ik dankzij jouw steun mijn doctoraat afronden, maar ondertussen hebben we samen nog zoveel meer kunnen verwezenlijken. Ik kijk uit naar de toekomst die nog voor ons ligt en alles wat we samen nog gaan beleven, te beginnen met onze derde spruit die er binnen enkele weken aankomt. Bedankt om er altijd voor ons gezinnetje te zijn!

Julie Gonnissen